

Chemical exfoliation of graphene and its application in organic electronics and energy storage devices

Dissertation

zur Erlangung des Grades
„Doktor der Naturwissenschaften“

im Fachbereich Chemie, Pharmazie, und
Geowissenschaften der Johannes Gutenberg-Universität
Mainz und in Kooperation mit dem Max-Planck-Institut
für Polymerforschung Mainz

vorgelegt von

Khaled Parvez

geboren in Gazipur / Bangladesh

Mainz, 2014

Die vorliegende Arbeit wurde in der Zeit von September 2010 bis April 2014 im Max-Planck-Institut für Polymerforschung in Mainz unter der Betreuung von [REDACTED] durchgeföhrt.

Ich danke [REDACTED] für seine wissenschaftliche und persönliche Unterstützung sowie für seine ständige Diskussionsbereitschaft.

Table of Contents

Chapter 1. Introduction	1
1.1. Graphene	2
1.2 Production of graphene.....	4
1.2.1 Micromechanical cleavage	4
1.2.2 Liquid-phase exfoliation.....	5
1.2.3 Graphene from graphite oxide.....	8
1.2.4 Chemical vapor deposition.....	11
1.3 Graphene characterization methods	14
1.3.1 Quantitative analysis	14
1.3.2 Qualitative analysis	17
1.4 Applications of graphene	19
1.4.1 Field-effect transistors	19
1.4.2 Electrocatalysts for oxygen reduction reaction	21
1.4.2.1 Heteroatom doped graphene.....	23
1.4.2.2 Graphene-nitrogen-metal hybrid electrocatalysts	24
1.4.3 Supercapacitors	25
1.5 Motivation and objectives.....	27
1.7 References	33
Chapter 2. Nitrogen-doped graphene as metal-free electrocatalysts for oxygen reduction reaction (ORR)	41
2.1 Introduction	42
2.2 Synthesis of nitrogen doped graphene (NG)	43
2.3 Morphology of GO and NG.....	45
2.4 Chemical structure of NG.....	49
2.5 Electrochemical properties of NG.....	54
2.5.1 Alkaline conditions.....	54
2.5.2 Acidic conditions	59
2.6 Electrochemical stability of NG	60
2.7 Conclusion.....	62
2.8 References	63
Chapter 3. Iron incorporated nitrogen-doped graphene as non-noble metal electrocatalysts for oxygen reduction reaction (ORR)	67
3.1 Introduction	68
3.2 Synthesis of NG/Fe_x composites	70
3.3 Structure and morphology of of NG/Fe_x composites.....	71
3.4 Electrochemical property of NG/Fe_x composites.....	76
3.4.1 Alkaline conditions.....	76
3.4.2 Effect of annealing temperature	79
3.4.3 Acidic conditions.....	81
3.5 Stability fof NG/Fex composites	83
3.6 Conclusion.....	84
3.7 References	85

Chapter 4. Methane plasma assisted reduction of graphene oxide films for high-performance micro-supercapacitors	89
4.1 Introduction.....	90
4.2 Fabrication of GO films	91
4.3 Methane plasma reduction of GO films.....	93
4.4 Morphology and structural characterizations	95
4.5 Optoelectronic properties.....	102
4.6 Graphene based in-plane micro-supercapacitors	106
4.6.1 Fabrication of graphene based micro-supercapacitors.....	107
4.6.2 Electrochemical characterization	109
4.6.3 Flexible MPG-MSCs	116
4.6.4 Ragone plot.....	119
4.7 Conclusion	122
4.8 References.....	123
Chapter 5. Electrochemically exfoliated graphene as solution processable, highly conductive electrodes for organic electronics	127
5.1 Introduction.....	128
5.2 electrochemical exfoliation of graphite	130
5.2.1 Exfoliation mechanism	132
5.2.2 Role of water and electrolyte concentration	133
5.3 Morphology of exfoliated graphene	134
5.4 Structural characterizations	136
5.5 Electronic properties	138
5.6 Fabrication of transparent EG films.....	141
5.7 Exfoliated graphene based electrodes for OFETs.....	144
5.8 Flexible OFETs based on graphene electrodes.....	148
5.9 Conclusion	151
5.10 References.....	152
Chapter 6. Electrochemical exfoliation of graphite into graphene in aqueous solutions of inorganic salts	157
6.1 Introduction.....	158
6.2 electrochemical exfoliation of graphite in aqueous inorganic salt	159
6.2.1 Exfoliation in different types of salt electrolytes.....	161
6.2.2 Exfoliation mechanism	163
6.2.3 Effect of electrolyte concentration.....	168
6.3 Morphology characterizations.....	169
6.4 Structural characterizations	174
6.5 Electronic properties	177
6.6 Fabrication of exfoliated graphene based thin films	181
6.7 Graphene ink.....	183
6.8 Graphene paper based supercapacitors.....	185
6.9 Conclusion	188
6.10 References.....	189

Chapter 7. Conclusion and Outlook193
 7.1 Conclusion..... 193
 7.2 Outlook..... 197

List of Publications201

Curriculum Vitae.....204

Acknowledgements205

Chapter 1. Introduction

Carbon (from Latin word ‘*carbo*’ meaning *coal*) forms more known stable allotropes than any other element. Elemental carbon with sp^3 -bond builds up a tetrahedral lattice, giving rise to diamond, while sp^2 -bonded carbon networks form the graphite (Figure 1.1). Both sp^2 - and sp^3 -bond structures have been known from the ancient times (the word diamond comes from the ancient Greek, ‘*adamad*’ meaning impossible to tame) and possess unique physical properties like hardness, thermal conductivity, etc.

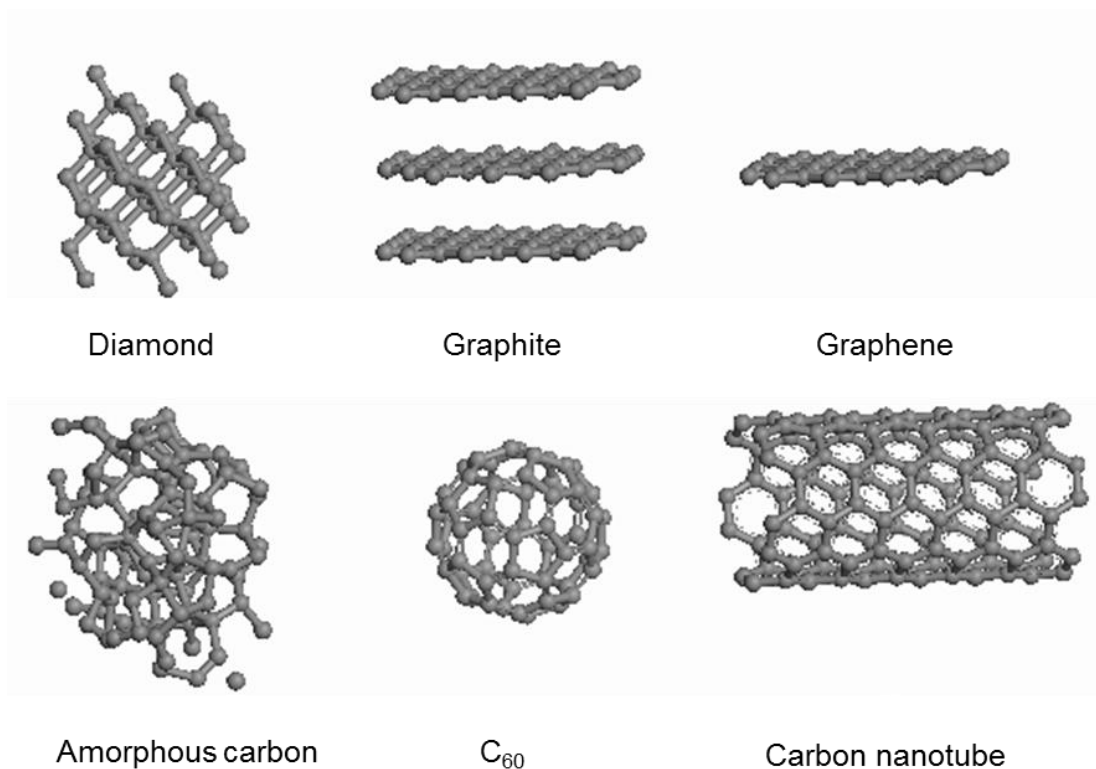


Figure 1.1 Schematic representations of carbon allotropes including, diamond, graphite, graphene, C₆₀ (Buckminsterfullerene) and carbon nanotube. (Source: <http://cnx.org/content/m22963/latest/?collection=col10699/latest>)

Many other allotropes of carbon have been discovered over the last 30 years. Among them the most famous allotropes are fullerene (C_{60}), carbon nanotube (CNT) and graphene. Fullerene was discovered in 1985 by Kroto, Smalley, Heath, Curl and O'Brian at the Rice University.¹ They observed that laser ablation of graphite led to the formation of closed cages consisting of carbon atoms connected in pentagonal and hexagonal rings (Figure 1.1). The discovery was awarded with the Nobel Prize in Chemistry in 1996. Parallel with the rise of fullerene research, carbon nanotube (CNT) was discovered by Iijima in 1991.² The discovery of CNTs gave a new turn on the carbon research opening broad space for further applications. In particular, single walled CNTs have drawn a lot of attention due to their one-dimensional cylindrical nanostructure unveiling compelling mechanical and electronic properties.

There are many more allotropes of carbon like, amorphous carbon, carbon fibers which show captivating physical properties depending on the crystalline structure and chemical bonding nature. Nevertheless, a big revolution of carbon arises with the discovery of graphene, the first stable two dimensional (2D) materials ever found with unprecedented physical, chemical and electronic properties.

1.1 Graphene

Graphene is a two-dimensional sheet of atomically thick sp^2 -hybridized carbon arranged in a honeycomb lattice. Although graphene has been studied over 40 years,³⁻⁵ this exceptional 2D system was believed to be thermodynamically unstable and not to exist in free state. A ground breaking experiment in graphene research was achieved in 2004, when

A. Geim and K. Novoselov at the University of Manchester first isolated monolayer graphene by mechanical exfoliation of highly oriented pyrolytic graphite (HOPG).⁶

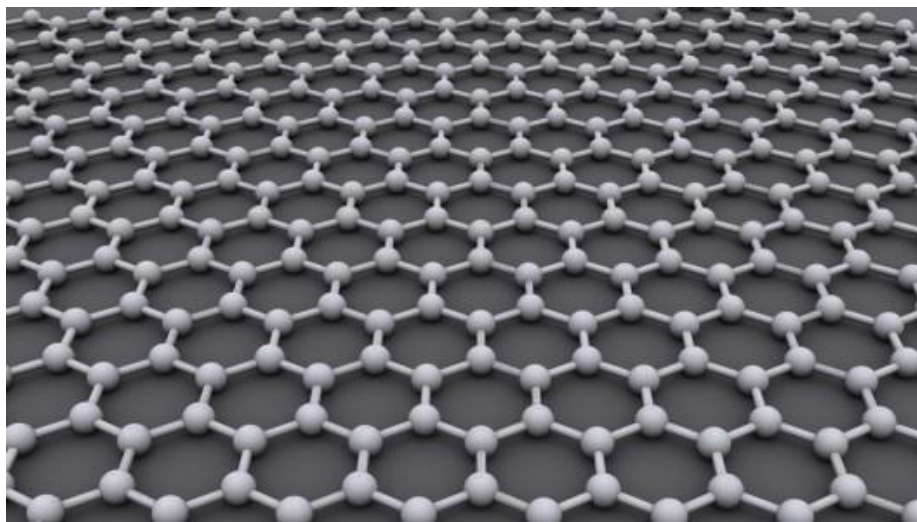


Figure 1.2 Schematic structure of graphene. (Source:

<http://gizmodo.com/5988977/9-incredible-uses-for-graphene>)

Long range π -conjugation in graphene yields extraordinary physical properties such as, high intrinsic mobility (theoretically $200,000 \text{ cm}^2 \text{ V}^{-1} \text{ s}^{-1}$),^{7,8} large theoretical specific surface area ($2630 \text{ m}^2 \text{ g}^{-1}$), high thermal conductivity ($\sim 5000 \text{ Wm}^{-1} \text{ K}^{-1}$)⁹ and Young's modulus ($\sim 1.0 \text{ TPa}$)¹⁰. Moreover, a single-layer graphene absorbs only 2.3% of incident light and therefore, it has a transparency of 97.7%.¹¹ The combination of high electrical conductivity, chemical and thermal stability,^{12,13} as well as excellent stretchability¹⁴⁻¹⁶ offers tremendous advantages for using graphene as transparent conductor in organic electronic devices such as, solar cells,^{13,15,17} organic light emitting diodes (OLEDs),^{18,19} touch screens,²⁰ field effect transistors (FETs),^{21,22} photodetectors^{23,24} etc. Moreover, graphene also proved to be a promising material as the catalyst support or as a metal-free catalyst for fuel cells,^{25,26} supercapacitors,^{27,28} and lithium-ion batteries due to its excellent

electrical conductivity and high surface area.^{29,30} The physical, chemical and electronic properties of graphene are so remarkable that A. K. Geim and K. Novoselov were awarded the Nobel Prize in Physics in 2010, within just 7 years of their first report on this material. Nevertheless, the scientific researchers are still ongoing to show the promise of graphene both in fundamental as well as technological and applied science.

1.2 Production of graphene

Several approaches have been developed to prepare graphene with the final aim for industrial-scale production. These approaches include micromechanical cleavage, epitaxial growth from silicon carbide (SiC),³¹ liquid-phase exfoliation,³² chemical vapor deposition (CVD),²⁰ electrochemical exfoliation,²² reduction of graphene oxide (GO),³³ bottom-up organic synthesis,³⁴ etc.

1.2.1 Micromechanical cleavage

The ‘micromechanical cleavage’ also known as, ‘Scotch tape’ method developed by A. Geim and K. Novoselov, involves peeling off a piece of graphite by means of adhesive tape.⁶ The process has been optimized to produce single layer graphene (SLG) with high structural quality and can be more than $100 \mu\text{m}^2$ in size.³⁵ In fact, this approach still provides the best graphene in terms of purity, defects, electronic and optoelectronic properties.^{36,37} So far, ultra-high carrier mobility of $100,000 \text{ cm}^2 \text{ V}^{-1} \text{ s}^{-1}$ for a single layer exfoliated graphene suspended between gold contacts has been reported.³⁸ Unfortunately,

this method is impractical for large scale applications and thus is limited to fundamental researches only.

1.2.2 Liquid-phase exfoliation

Graphene flakes can be produced by ultrasonication of natural graphite in a range of organic solvents such as N-methyl-pyrrolidone (NMP), N,N-dimethylformamide (DMF), *ortho*-dichlorobenzene (*o*-DCB), etc. (Figure 1.3a).³² Exfoliation of graphite layer occurs because of the strong interaction between graphitic basal planes and the solvent. The solvent that can minimize the interfacial tension (γ) between liquid and graphene flakes (i.e. the force that minimizes the area of the surfaces in contact) is considered to be ideal. Interfacial tension plays a crucial role when a solid is immersed in a liquid medium. Solvents with a surface tension of $\sim 40 \text{ mJ m}^{-2}$ such as, NMP, DMF, γ -butyrolactone (GBL) etc. have been demonstrated as the best medium for graphite exfoliation (Figure 1.3b and c). Although the concentration at which graphene can be dispersed has increased from $\sim 0.01 \text{ mg mL}^{-1}$ to 1.2 mg mL^{-1} in NMP with low power sonication, the average flake size reduces significantly.^{32,39} On the other hand, majority of organic solvents with $\gamma \sim 40 \text{ mJ m}^{-2}$ such as, NMP (40 mJ m^{-2} , b.p. $203 \text{ }^\circ\text{C}$), DMF (37.1 mJ m^{-2} , b.p. $154 \text{ }^\circ\text{C}$) and *o*-DCB (37 mJ m^{-2} , $181 \text{ }^\circ\text{C}$) are toxic and have high boiling point, which limit their viability for manipulation, in particular for thin film fabrications. Therefore, stable dispersions of graphene in low boiling point solvents such as, water, ethanol, etc. are highly desirable. Despite of the low yield and small flake size, the liquid-phase exfoliated graphene is of high quality and the field-effect mobility measured for single-layer graphene sheet was reported to be as high as $95 \text{ cm}^2 \text{ V}^{-1} \text{ s}^{-1}$.^{32,40}

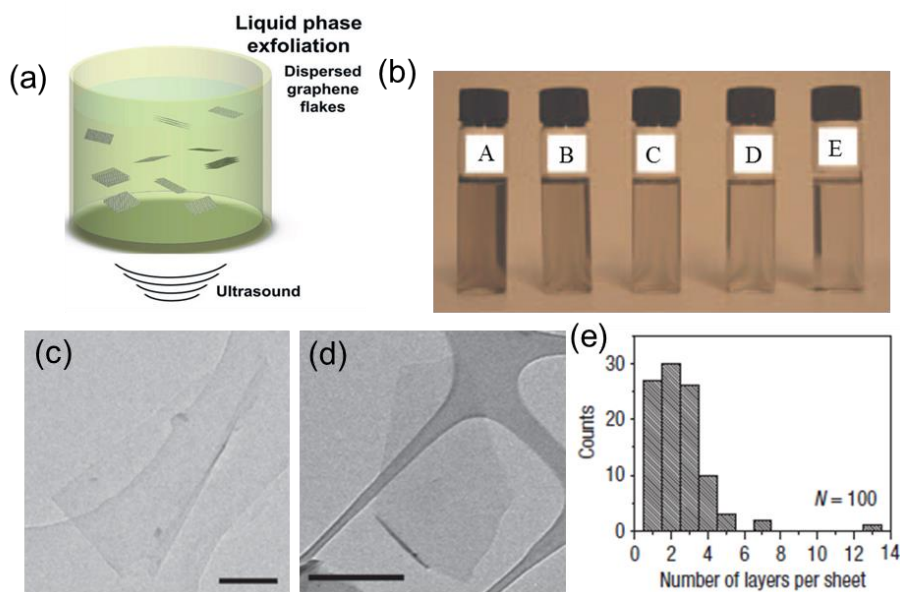


Figure 1.3(a) Schematic illustration of graphene preparation by liquid-phase exfoliation⁴¹; (b) dispersions of graphene flakes in NMP, at a range of concentrations ranging from $6 \mu\text{g mL}^{-1}$ (A) to $4 \mu\text{g mL}^{-1}$ (E) after centrifugation; (c) and (d) TEM images of monolayer graphene flakes deposited from GBL and NMP, respectively; (e) histogram of the number of visual observations of flakes as a function of the number of monolayers per flake for NMP dispersions.³²

Several attempts of producing graphene by liquid-phase exfoliation in low boiling point solvents have been reported. One approach is the solvothermal-assisted exfoliation of expanded graphite in polar organic solvent, i.e. acetonitrile.⁴² It has been proposed that the dipole-induced interactions between graphene and acetonitrile facilitate the exfoliation and dispersion of graphene. The solvothermal-assisted exfoliation process resulted in yield of ~ 10 wt% graphene. Recently, the dispersion of graphene in ethanol was reported by solvent exchange from NMP.⁴³ The exfoliated graphene in NMP was first filtered through a polytetrafluoroethylene (PTFE) membrane followed by re-dispersing the filtered cake into

ethanol. After several times of centrifugation and washing steps, a stable dispersion of graphene in ethanol (0.04 mg/mL) was obtained. Nevertheless, about 20% sedimentation of dispersion was observed after one week.

Water is a natural choice of solvents because of its non-toxicity, low boiling point etc. However, the exfoliation of graphene in water is challenging because of its high γ ($\sim 72 \text{ mJm}^{-2}$) and incompatibility with the hydrophobic nature of graphene sheets. This can be partially overcome by using anionic surfactants such as, 4-dodecylbenzenesulfonic acid (SDBS),⁴⁴ sodium deoxycholate (SDC),⁴⁵ and sodium cholate (SC)^{46,47} A concentration up to 0.3 mg/mL of exfoliated graphene in water was achieved by sonicating graphite into these surfactant solutions. Nevertheless, depending on the final application the presence of surfactant may be a troublesome issue e.g. compromising or decreasing the conductivity of graphene.

In addition to organic solvent and surfactant based liquid-phase exfoliation, ionic-liquids have emerged as promising solvents to aid sonication based graphite exfoliation. Ionic-liquids are salts in liquid state below 100 °C and often have surface energies (i.e. 40 mJ m^{-2}) close to that of graphene. One of the first ionic liquid used for graphite exfoliation was 1-butyl-3-methylimidazolium bis(trifluoro-methane-sulfonyl)imide, which led to 0.95 mg/mL stable dispersion of graphene nanosheets with 1 h of sonication.⁴⁸ The majority of sheets were less than 5 layers; however no rigorous analysis was carried out in this work. Recently, prolonged sonication (24 h) of graphite flakes in 1-hexyl-3-methyl-imidazolium hexafluorophosphate (HMIH) yielded stable graphene dispersion with concentration as high as 5.33 mg mL^{-1} and an average thickness of 2 nm for the graphene flakes. However, the reported exfoliation yield is only about 1 to 2 wt%.⁴⁹

1.2.3 Graphene from graphite oxide

One of the low cost methods of producing graphene on a large scale is the reduction of graphite oxide or graphene oxide to graphene. Graphite oxide was first prepared almost 150 years ago by Brodie, who treated graphite repeatedly with potassium chlorate and nitric acid.⁵⁰ Hummers and Offeman later demonstrated a less hazardous and more efficient method for graphite oxidation, which involves a mixture of sodium nitrate, potassium permanganate and sulfuric acid.⁵¹ Their modified protocols are presently the most commonly used methods for the oxidation of graphite. Nowadays, the existence of monolayers of graphite oxide is widely acknowledged and recognized as graphene oxide (GO).⁵² The term “platelets” is often used to describe thick multilayers of GO, while “sheets” usually indicate a monolayer to few layers.⁵³ Individual sheets of GO can be viewed as graphene decorated with oxygen functional groups (c.a. hydroxyl, carbonyl, epoxy etc.) on both sides of the plane and around the edges.^{54,55} Due to the presence of these functional groups, GO shows negatively charged feature and can be electrostatically stabilized to form a colloidal suspension in water, alcohols and certain organic solvents without surfactants.^{56,57} The maximum lateral size of the GO sheets is dependent on the size of initial graphite crystals, but the average size can be adjusted to some degree by the extent of oxidation procedure or by ultrasonication process.

The determination of GO structure has been challenging because of its non-stoichiometric chemical composition, which depends on the synthetic methods. It is generally agreed that oxygen is present in GO mostly in the form of hydroxyl and epoxy groups on the basal plane, whereas smaller amounts of carboxyl, carbonyl, lactone and

quinone are located primarily at the sheet edges. The chemical structure of GO was recently confirmed by the solid-state NMR characterization of ^{13}C -labeled GO.⁵⁸

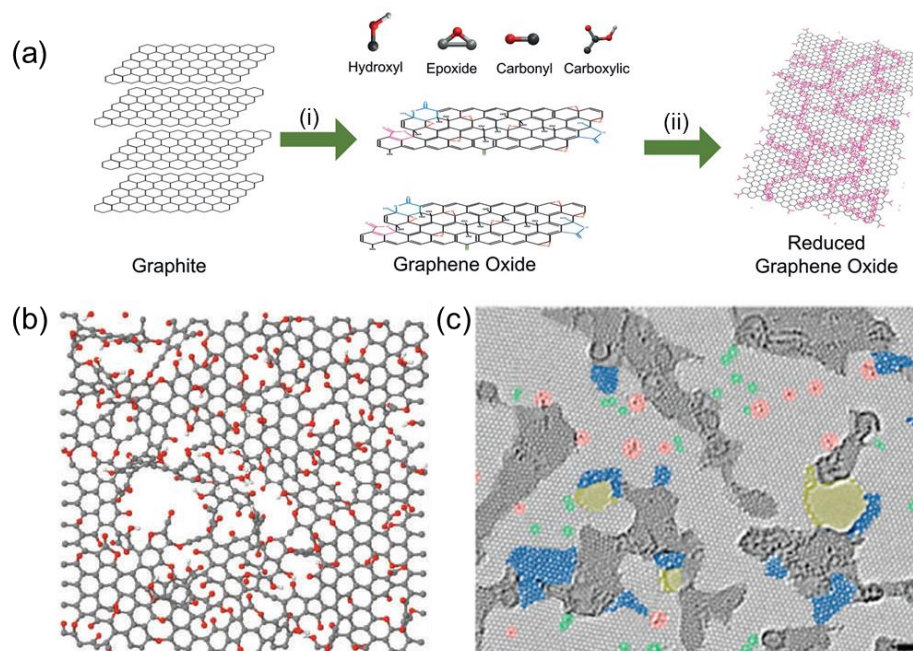


Figure 1.4 (a) GO synthesis and reduction which involve (i) oxidation of graphite to graphene oxide layers where the flakes are functionalized with epoxy, hydroxyl, carbonyl groups and (ii) conversion of GO to rGO through chemical and/or thermal treatment; (b) atomic model schematically illustrating disordered rGO basal plane consisting of holes, topological defects and remnants of oxygen groups.⁵⁹ (c) high resolution transmission electron micrograph of a single-layer rGO membrane. Color scheme highlighting the different structural features: dark grey, contaminated regions; blue, disordered single-layer carbon networks or extended topological defects; red, individual substitutions; green, isolated topological defects; yellow, holes and their edge constructions. Scale bar: 1 nm.⁶⁰

Although GO can form homogeneous colloidal suspensions, it is electrically insulating owing to the disruption of the ‘graphitic’ networks. Therefore, to restore the

electronic property of graphene, chemical or thermal reduction of GO is required to partially remove the oxygen functional groups (Figure 1.4a). Chemical reduction of GO sheets has been performed with reducing agents including hydrazine (N_2H_4),³³ sodium borohydride (NaBH_4)⁶¹, dimethyl hydrazine,⁶² hydriodic acid (HI),^{63,64} etc. Until now, N_2H_4 is the most commonly used reducing agent in both solution and gas phase.⁶⁵ During the reduction process, the brown colored dispersion of GO in water turns black and the reduced sheets aggregate and/or precipitate.⁶⁶ The reduced GO (i.e. rGO) becomes less hydrophilic due to the partial removal of oxygen containing functional groups. Unfortunately, the chemical reduction of GO has shortcomings such as, chemical toxicity and long processing time that requires several hours to one day to complete the reduction process. Furthermore, the most widely used reducing agent N_2H_4 incorporates nitrogen impurities into graphene.⁶⁷ On the other hand, reduction of GO with NaBH_4 in aqueous solution is more effective than N_2H_4 .⁶⁵ Such reduction produces rGO with a C/O ratio of 13.4 compared to 6.2 for using N_2H_4 .⁶⁸ Other chemical reduction methods including hydroquinone,⁶⁹ solvothermal,⁷⁰ electrochemical⁷¹ and ultraviolet-assisted^{72,73} reduction have been developed over the last few years. Besides chemical reduction methods, thermal reduction of GO at high temperature (900 to 1100 °C), particularly under ultra-high vacuum (UHV), has been found to be highly efficient in producing rGO with a remarkable C/O ratio (~ 12.5 to 14.1)^{74,75}. Nevertheless, simulations based on density functional theory (DFT) have indicated that it becomes increasingly difficult to reduce GO with C/O ratio above 16.⁷⁶

The downside of producing graphene from GO is that, after reduction, the sp^2 carbon network can be irreversibly destroyed in many places, leaving sp^3 carbons and vacancies which behave as electron traps (Figure 1.4b and c).⁶⁰ Due to the merits of large-

scale production and solution processability, a great number of attempts have been made to improve the electronic properties of the rGO, such as chemical doping,⁷⁷ defect repairing,^{78,79} etc.

1.2.4 Chemical vapor deposition

The formation of few layered graphene on transition metal surfaces has been known for nearly 50 years.⁸⁰ Layers of graphite were first observed on Ni^{80,81} surfaces when they were exposed to carbon sources in the form of hydrocarbons at high temperature (i.e. 1000 – 1050 °C). However, the first attempt to synthesize monolayer graphene can be traced back to 1975 via the thermal decomposition of carbon on single crystal platinum (Pt) surface.⁸² Unfortunately, the process was not studied extensively due to the lack of characterization and application for such kind of graphitic materials. The interest in graphene has led to the reevaluation of this chemical vapor deposition (CVD) method for controlled growth of graphene layers. Graphene growth has been demonstrated on a variety of transition metals such as, Ru,⁸³ Ir,⁸⁴ Co,⁸⁵ Pt,⁸⁶ etc. Recent results of growth on relatively inexpensive polycrystalline Ni^{87,88} and Cu^{89,90} substrates have triggered remarkable interests in optimizing CVD conditions for the large-area synthesis of high quality graphene. Graphene deposited on polycrystalline Ni substrate, exhibits mobility value up to 3650 cm² V⁻¹ s⁻¹.⁹¹ However, the fundamental limitation on utilizing Ni as the catalyst is that single- and few- layered graphene are formed over few tens of microns regions, rather than over the entire substrate.⁹² The lack of control over the number of layers is partially attributed to the fact that the segregation of carbon from the metal carbide upon cooling, occurs at different rate within the Ni grains and at the grain boundaries.⁹³ In contrast, uniform

growth of high quality single layer graphene (SLG) over large areas has been recently achieved on polycrystalline Cu foils (Figure 1.5a-c). The subsequent studies conducted by Samsung Electronics demonstrated the growth of SLG over area as large as 30-inch with 95% coverage (Figure 1.5d).²⁰ CVD growth of graphene on Cu is generally attributed to the thermal decomposition of hydrocarbons on the surface and subsequent surface diffusion of carbon atoms due to their low solubility (< 0.001 at%) in Cu. Very recently, R. S. Rouff *et al.* reported 1 cm-sized single crystal of CVD graphene on Cu with a carrier mobility ranging from 15,000 to 30,000 $\text{cm}^2 \text{V}^{-1} \text{s}^{-1}$ at room temperature (Figure 1.5e).⁹⁴

The major drawback of CVD grown graphene lies in tedious steps required to transfer graphene from metallic surface to arbitrary substrates like, quartz, PET, SiO_2 etc. for device fabrications. In general, a polymer solution such as, poly (methyl methacrylate) (PMMA)^{95,96} or polydimethylsiloxane (PDMS)⁹¹ is spin coated on CVD graphene as a support, followed by wet chemical etching of Cu or Ni foil using $\text{Fe}(\text{NO}_3)_3$ or FeCl_3 . After the PMMA/graphene has been placed over a target substrate, the PMMA layer can be dissolved with acetone (Figure 1.5f). Nevertheless, a complete removal of the PMMA layer remains a great challenge, and thus p-doping of graphene was commonly observed for such samples.^{95,96}

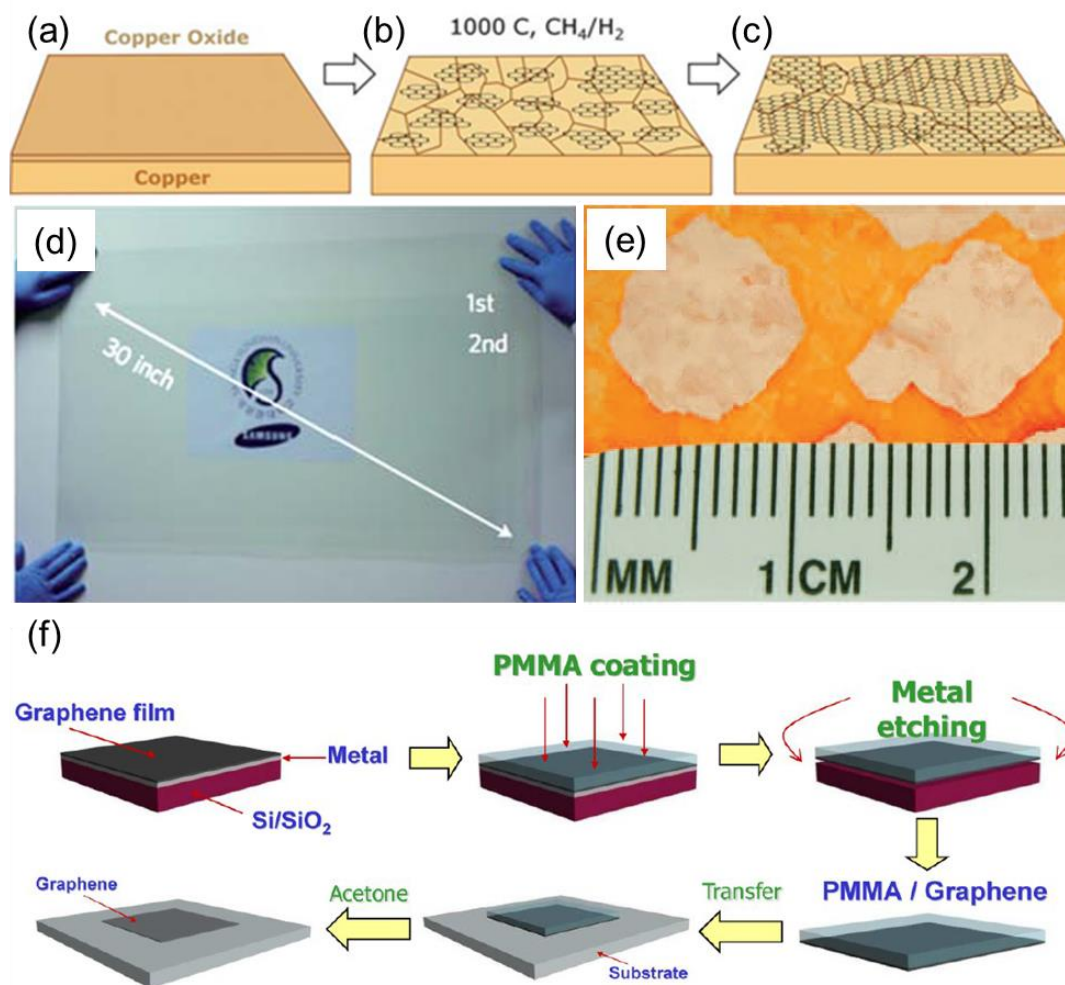


Figure 1.5 (a-c) Schematic illustrations of three main strategies of graphene growth on Cu by CVD: (a) Cu foil with native oxide, (b) exposure of the Cu foil to CH_4/H_2 atmosphere at $1000\text{ }^\circ\text{C}$ leading to nucleation of graphene islands, (c) enlargement of the graphene flakes with different lattice orientations.⁹⁷ (d) Transparent graphene film on a 35-inch PET.⁹⁸ (e) Optical microscopic image of centimeter-scale graphene domains on Cu.⁹⁴ (f) Schematic illustration of the CVD graphene transfer process.⁹⁹

1.3 Graphene characterization methods

Characterizations of graphene are generally based on various microscopic and spectroscopic studies. The determination of the number of layers and the purity of graphene in terms of defects is essential to achieve unique physical properties of graphene. The following part will summarize the important characterization methods with a particular emphasis on the identification of graphene.

1.3.1 Quantitative analysis

The yield of chemically exfoliated graphene can be described by different analytical approaches such as, the yield by weight, yield by percentage etc. The yield by weight is defined as the ratio between the weight of starting graphite and that of the dispersed graphitic material. For the yield of single-layered graphene (SLG) by percentage, it is defined as the ratio between the number of SLG and the total number of graphitic flakes in the dispersion. The yield of SLG by weight is expressed by the ratio between the total mass of dispersed SLG and the total mass of all dispersed flakes. Thus, the yield by weight does not give information on the amount of SLG but only on the total amount of exfoliated graphitic material. In order to determine the yield by weight, it is necessary to calculate the concentration ' c ' (g L^{-1}) of dispersed graphene. The value of ' c ' is usually calculated via the optical absorption spectroscopy, by exploiting Beer-Lambert Law: $A = \alpha cl$, where A is the absorbance, ' l ' (m) is the length of the optical path, and ' α ' ($\text{L g}^{-1} \text{m}^{-1}$) is the absorption coefficient. The ' α ' can be experimentally determined by filtering a known volume dispersion, e.g. via vacuum filtration, onto a filter of known mass and measuring the

resulting mass using a microbalance. The identification of graphene layers down to single-layer in thickness was first realized through optical microscopy (OM) *via* the color contrast caused by the light interference effect of micromechanically exfoliated graphene on SiO₂ substrate, or simply by the color difference of different layers of graphene. The contrast depends on the thickness of SiO₂, the wavelength of light used and the angle of illumination.¹⁰⁰ This feature of graphene is useful for the quick identification of single- to few-layer graphene sheets. Figure 1.5a-c show the optical contrast of one, two and three layers of exfoliated graphene under different wavelengths of illumination and different thickness of SiO₂.

Scanning electron microscope (SEM) is also useful to identify graphene. The secondary electron intensity from the graphene sample operating at low electron acceleration voltage has a linear relationship with the number of graphene layers.¹⁰¹ A quantitative estimation of the layer thickness is obtained using attenuated secondary electrons emitted from the substrate with an in-column low energy electron detector.¹⁰² From the color depth, the layer of graphene can be estimated. The major advantage of SEM over OM is that, the graphene gives more clear contrast in SEM.

The thickness of graphene layers can be directly probed by atomic force microscopy (AFM).¹⁰³ On the basis of interlayer distance of graphite (3.4 Å), the thickness of a graphene flake or the number of layers can be determined. As shown in Figure 1.5d, from the step of graphene on substrate, it is possible to estimate the number of graphene layer. However, the height of a SLG via AFM usually depends on the substrate and on the environmental conditions such as relative humidity. The height of a SLG on SiO₂ is in a range from ~ 0.6 to ~ 1.0 nm, while on mica it amounts to ~ 0.4 nm.¹⁰⁴ On the other hand,

the thickness of a single layer GO sheet is approximately 1.0 – 1.4 nm, which is thicker than the pristine graphene due to the presence of functional groups and adsorbed molecules.^{52,105}

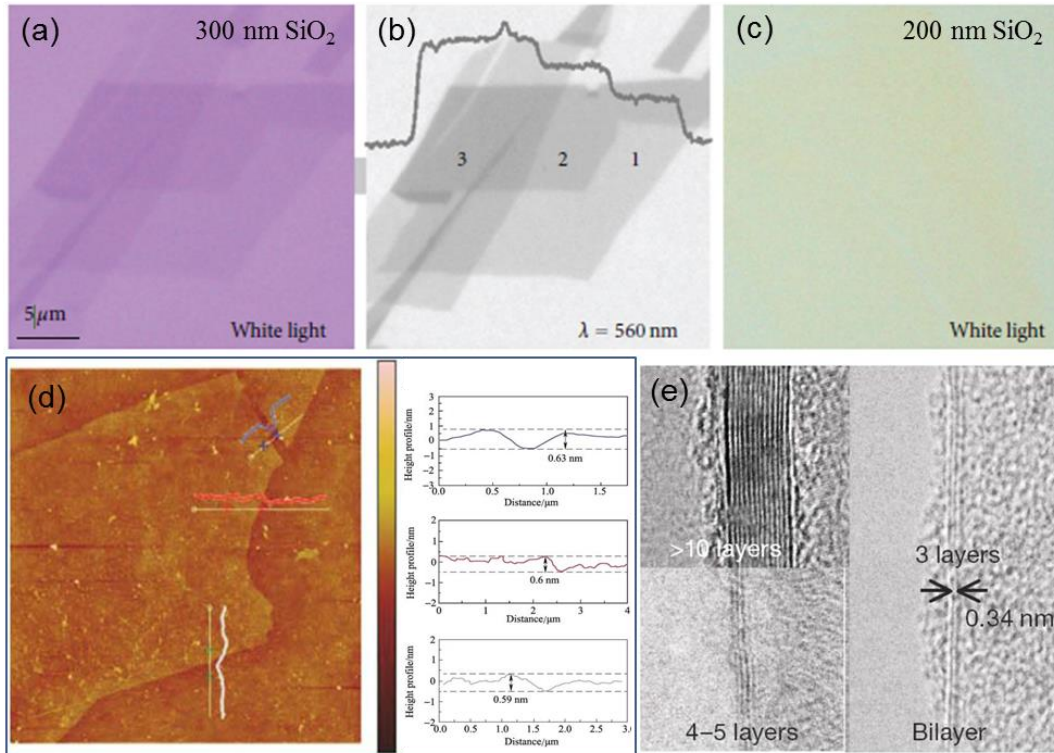


Figure 1.5 (a), (b) and (c) Optical microscopic images of graphene. Multilayer graphene sheet on Si/SiO₂ showing optical contrast at different wavelengths.¹⁰⁰ (d) AFM image of graphene on SiO₂ substrate and its corresponding height profile.¹⁰³ (e) High-magnification TEM image of graphene.⁹¹

High resolution transmission electron microscopy (HRTEM) not only allows one to identify the morphological feature of graphene but also to accurately identify the number of layers on viewing the edges of the sample, each layers corresponding to a dark line (Figure 1.5e).⁹¹ In addition, HRTEM is often assisted with electron diffraction pattern, which shows a hexagonal pattern arises from the crystal structure of graphene. Moreover, the relative

intensities of the electron diffraction pattern from the (2-110) and (1-110) planes can be used to determine the number of layers. For example, if $I_{(1-110)}/I_{(2-110)}$ is > 1 , it is recognized as single layer graphene, whereas it is referred to multilayer graphene if the ratio is < 1 .

1.3.2 Qualitative analysis

Raman spectroscopy can provide a quick and effective way for structure and quality characterization of graphene.^{32,106,107} The major features of the Raman spectra for graphite and graphene are the G band located at $\sim 1580 \text{ cm}^{-1}$ and 2D band (also called as G' band) at $\sim 2700 \text{ cm}^{-1}$. A third feature, the D band at $\sim 1350 \text{ cm}^{-1}$, is not Raman active for pristine graphene but can be observed where symmetry is broken at the edges of graphene. The D band is also known as a defect-induced band. Therefore, an intense D band in Raman spectrum signifies the presence of certain amount of defects on graphene layer. The G band results from in-plane vibration of sp^2 carbon atoms and is the most prominent feature of most graphitic materials. The 2D band is a double resonance Raman process, which involves the scattering of two phonons with opposite momentum around the high symmetry K point in the first Brillouin zone of graphene.

From Raman spectroscopy, one can deduce the layers of graphene.¹⁰⁶ As shown in Figure 1.6, an increase in layer leads to a significant decrease in the relative intensity of the 2D band. At the same time, the 2D band shifts to higher wavenumber and saturates to that of HOPG, whereas the intensity ratio I_{2D}/I_G reduces gradually. Thus Raman spectroscopy can clearly distinguish a single layer from a bilayer or few (less than 5) layers graphene. Moreover, the intensity ratio of D to G (*i.e.* I_D/I_G) band can be used to estimate the density

of defects in a graphene sample. For example, the higher the I_D/I_G ratio is, the higher the number of defects are present in graphene.¹⁰⁸

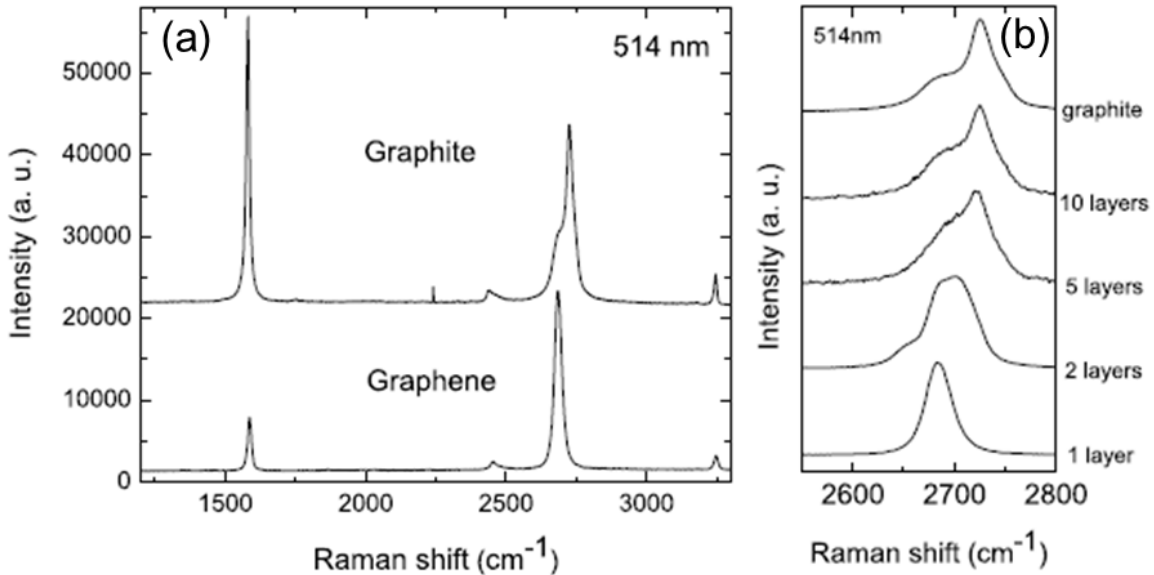


Figure 1.6 (a) Comparison of Raman spectra at 514 nm of bulk graphite and graphene. (b) Evolution of the 2D peak at 514 nm with the number of layers.¹⁰⁶

In addition to the Raman spectroscopy, several other techniques are frequently used to examine the quality of graphene such as, X-ray photoelectron spectroscopy (XPS). The XPS is a powerful technique to identify the elements present in graphene especially in GO and reduced GO. The carbon-to-oxygen ratio (C/O) is generally used to estimate the reduction efficiency of GO or the quality of graphene. A high C/O ratio indicates low amount of oxygen functional groups decorated on graphene and therefore, good quality of the sample.

1.4 Applications of Graphene

Due to the high electrical conductivity, chemical stability and mechanical flexibility, graphene and its derivatives have been investigated extensively in various electronics and energy storage/conversion devices. Here, we emphasize two important categories of the applications of graphene: the first area is the use of graphene as an electrode or active component in electronic devices. The second field is about the application of graphene and/or graphene based composites as electrode materials in energy storage/conversion devices. In the following section, we will mainly introduce the state-of-the-art application of graphene in field-effect transistors (FETs), fuel cells and supercapacitors which are related to this thesis.

1.4.1 Field-effect transistors (FETs)

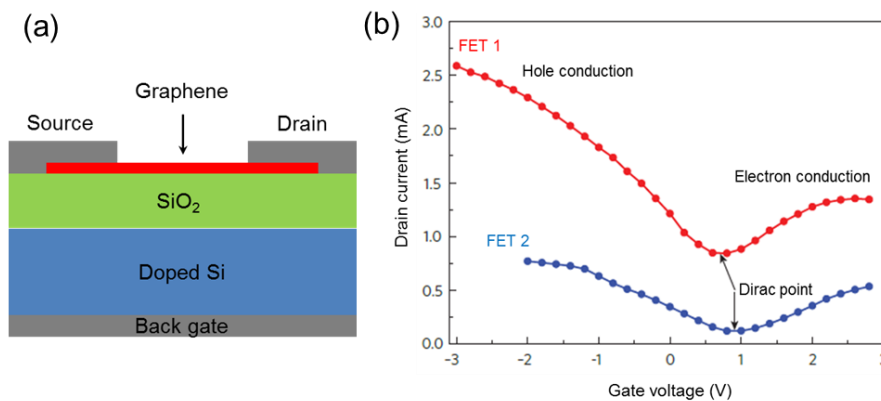


Figure 1.7 (a) Schematic illustration of back-gated graphene FETs. The channel shown in red consists of either large-area graphene or graphene nanoribbons. (b) Typical transfer characteristics for two FETs with large-area graphene channels.¹⁰⁹

Owing to its unique band structure, graphene exhibits remarkable electron and/or hole transport properties such as ambipolar field effect and minimum conductivity which are absent in most conventional semiconducting materials. Graphene based FET devices generally consist of a 300 nm SiO₂ layer underneath the graphene serving as a back-gate dielectric and a doped silicon substrate as a back-gate (Figure 1.7a).^{6,110} The most frequently stated advantage of graphene is its ultrahigh carrier mobility at room temperature. Large-area graphene transistors have a unique-current voltage transfer characteristic (Figure 1.7b). The carrier density and the type of carrier (electrons or holes) in the channel are governed by the potential differences between the channel and gates (top-gate and/or back gate). Large positive gate voltages promote an electron accumulation in the channel (n-type channel) and large negative gate voltage leads to a p-type channel. Such behavior gives rise to two branches of transfer characteristics separated by the Dirac point (Figure 1.7b).¹⁰⁹ The position of the Dirac point depends on several factors: the difference between work functions of the gate and the graphene, the type and density of the charges at the interfaces and bottom of the channel as well as any doping effect of the graphene. Mobilities of 10,000 – 15,000 cm² V⁻¹ s⁻¹ are routinely measured for mechanically exfoliated graphene on SiO₂ covered silicon wafers.^{6,111} Recently, a mobility of 1000,000 cm² V⁻¹ s⁻¹ is recently reported for suspended graphene.³⁸ In contrast, rGO only shows a mobility value of 0.01~15.0 cm²/V·s depending on the level of reduction.^{103,112,113} Moreover, rGO rarely shows ambipolar field-effect characteristics because the residual oxygen groups provide deep trap states for electrons and limit any gate modulation to that of states for holes.

In addition to the use of graphene as active material in FETs, another application of graphene in FETs is as source/drain (S/D) electrodes. Gold (Au) is the most commonly used material for S/D electrodes in organic FETs (*i.e.* OFETs) due to its favorable work function. Compared to Au based S/D electrodes, graphene has great advantage of low contact resistance with organic semiconductors and thereby, can enhance the overall performance of OFETs. For example, solution-based polymer transistors employing thermally reduced GO patterns as S/D electrodes and P3HT as semiconductor layer yielded an average hole mobility of $0.04 \text{ cm}^2 \text{ V}^{-1} \text{ s}^{-1}$, which was about two times higher than that of Au based devices.²¹ Several other organic semiconductors such as, pentacene,¹¹⁴ copper phthalocyanine (CuPc)¹¹⁵ etc. also show enhanced mobility based on graphene electrodes. In addition, graphene can be used to tune the work function of Cu and/or Ag S/D electrodes for OFETs.¹¹⁶ The modification of the electrodes can be carried out by depositing thin graphene layers on their surface via heating the patterned Cu or Ag electrodes under ethanol/H₂/Ar at 700-800 °C. The mobilities of pentacene FETs with the Cu (or Ag)/graphene as the S/D electrodes were 10 times higher than that of pure Cu or Ag electrodes.

1.4.2 Electrocatalyst for oxygen reduction reaction

Polymer electrolyte fuel cells (PEFCs) are generally viewed as one of the most promising energy conversion technologies. Development of the state-of-the-art electrocatalysts with inexpensive and commercially available materials to facilitate cathodic oxygen reduction reaction (ORR) is a key issue for the future commercialization of fuel cells. In general, there are two electrochemical pathways to reduce oxygen to water

in aqueous electrolytes. As illustrated in Figure 1.8, O_2 can be electrochemically reduced either directly to water (rate constant k_1) without intermediate formation of $H_2O_{2,ad}$ (one step four electron reduction) or to $H_2O_{2,ad}$ with the rate constant k_2 (two step two electron reduction). The adsorbed H_2O_2 can be electrochemically reduced to water with the rate constant k_3 , catalytically decomposed on the electrode surface (k_4) or desorbed into the bulk solution (k_5).¹¹⁷

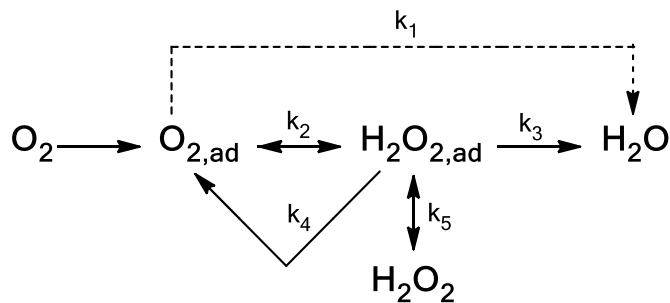
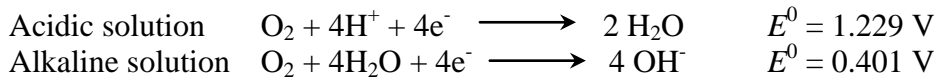


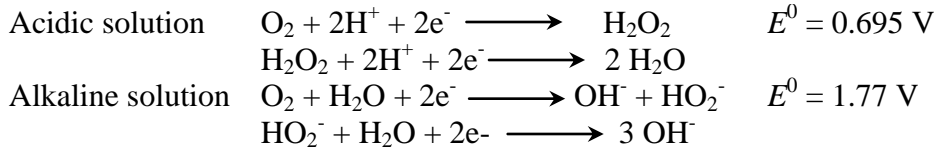
Figure 1.8 Kinetic pathway of reduction from O_2 to water.¹¹⁷

On the other hand, ORR proceeds quite differently from each other when acid or alkaline electrolytes are used, as follows:

Four electron reduction



Two electron reduction



In fuel cell processes, the four electron direct pathway is highly preferred. The two electron reduction pathway is used in the industry for H_2O_2 production.

Currently, Pt-nanoparticle catalysts, supported on high-surface area carbonaceous materials represent the state-of-the-art electrocatalysts for the oxygen reduction reaction (ORR) at the fuel cell cathode. However, at least two important issues must be addressed before Pt-based catalysts can be commercialized for practical applications. First, the fact that the sluggish ORR kinetics require high loading of Pt in the electrode for acceptable power density. In addition, the Pt-based electrode materials suffer from their susceptibility to time-dependent drift and CO deactivation, which greatly decrease the cathode potential and reduce fuel cell efficiency. Second, the high cost of the Pt-based catalysts together with limited reserve in nature, hinder the mass production of fuel cells.¹¹⁸ Thereby, the development of cathode catalysts with enhanced ORR activity is highly desired.

Given the high surface area and excellent electrical conductivity of graphene, considerable efforts have been made to synthesize graphene based nanomaterials with high ORR performance.^{26,119} In principle, graphene based electrocatalysts for ORR can be classified in two main categories: i) heteroatom doped graphene as metal free electrocatalysts and ii) N-doped graphene/carbon supported metal hybrids such as, M-N-C catalysts (where, M = Fe, Co, Ni etc.).

1.4.2.1 Heteroatom doped graphene

Both theoretical and experimental studies have revealed that heteroatom (nitrogen, boron and sulfur) doped graphene materials can tailor their electronic property and chemical reactivity, as well as give rise to new functions. A prominent example is N-doped graphene (NG) that generally exhibits high electrocatalytic activity and CO tolerance for ORR in comparison to conventional Pt-based catalysts, and therefore holds great promise to

replace noble metal catalysts for fuel cells. NG can be synthesized by the chemical vapor deposition of methane in presence of NH_3 ,¹²⁰ exposing graphene into NH_3 plasma and/or high temperature annealing in NH_3 .^{77,121,122} Although, NG possesses excellent tolerance and durability, their electrochemical activities towards ORR remain to be much improved. Therefore, NG with unique nanostructures and enhanced ORR activity is a highly attractive synthetic target.

1.4.2.2 Graphene-nitrogen-metal hybrid electrocatalysts

Carbon supported transition metal/nitrogen (M-N-C) materials (M = Co, Fe, Ni, Mn etc.) have gained increasing attention due to their promising catalytic activity towards ORR. The incorporation of transition metal-nitrogen moieties on graphene surfaces of great concern in pursuit of high performance catalysts.^{26,119,123} One of the strategies is functionalization of graphene with transition metals such as iron or cobalt macrocycle compounds. For instance, graphene anchored with cobalt[tetrakis(o-aminophenyl)porphyrin] (CoTAPP) has been reported to show high electrocatalytic performance with almost four electron transfer towards ORR in acidic conditions.¹²⁴ For another strategy, high surface area NG provides abundant sites for coordination with transition metals. While NG is mostly active in alkaline solution, the poor catalytic activity of NG in acidic media can be overcome by incorporating transition metals into NG for constructing M-N-C based catalysts.^{26,125,126}

1.4.3 Supercapacitors

Supercapacitors are a class of electrochemical devices for storing and releasing energies rapidly and reversibly. In general, a supercapacitor is composed of two collectors, two electrodes, a separator and an electrolyte. The cell is assembled into a sandwich-like stacked configuration of a collector/electrode/separator/electrode/collector and is surrounded with sealing and packaging materials. The electrolyte mostly consists of a conductive liquid mixture of an aqueous or organic solvent that can migrate into and out of the two electrodes during the charge-discharge process. Depending on the charge-storage mechanism, supercapacitors are usually divided into three categories: i) electric double-layer capacitors (EDLCs) that electrostatically store charges on the interface of high surface area carbon electrodes, ii) pseudocapacitors that achieve electrochemical storage of electricity with high electron transfer during redox reactions, typically based on metal oxide and conducting polymers, and iii) hybrid supercapacitors that consist of special hybrid electrodes or asymmetric electrodes that have both the significant double-layer capacitance of carbon and the pseudocapacitance of electronically conducting polymer or transition metal oxide. The EDLCs can achieve rapid charge storage but deliver relatively low capacitance. Pseudocapacitors, on the other hand, offer high capacitance but suffer from poor rate capability and low cycle performance. Hybrid supercapacitors combine the advantageous features of EDLCs and pseudocapacitors, and thus are becoming a more attractive choice to achieve both high-energy and power densities in one device. Nevertheless, the performance of all the above supercapacitor devices strongly depends on the properties of active materials, fabrication process of electrodes, selection of electrolytes and geometry of the devices.¹²⁷⁻¹²⁹

Graphene based materials have been demonstrated as one class of the most promising electrode materials for supercapacitors because of their excellent conductivity, high surface area, exceptional intrinsic double-layer capacitance ($\sim 21 \mu\text{F cm}^{-2}$) and high theoretical capacitance ($\sim 550 \text{ F g}^{-1}$).^{130,131} For instance, conventional supercapacitors composed of curved graphene,¹³² activated graphene,¹³³ vertically oriented graphene,¹³⁰ doped graphene,¹²⁷ laser-scribed graphene,¹³⁴ and graphene/metal oxide hybrids as bulk electrodes¹³⁵ have shown excellent performance in terms of specific capacitance and energy density. More importantly, graphene based thin films hold great promise for developing new types of flexible, transparent and miniaturized ultrathin supercapacitors, such as micro-supercapacitors (MSCs).^{129,136} Notably, graphene based planar MSCs that provide electrolyte ions the ability to rapidly interact with all graphene layers in the horizontal direction are superior to conventional devices.^{27,28,136}

1.5 Motivation and objectives

As discussed above, graphene is optically transparent, chemically inert and an excellent electrical and thermal conductor. These intriguing properties make graphene a promising candidate for numerous applications in electronic, energy storage and conversion devices. Although, micromechanical exfoliation of graphite and the CVD method can produce high quality graphene, their widespread applications are hampered by limited production rate. Therefore, scalable protocol for graphene production via chemical exfoliation of graphite (such as rGO) is highly appealing. Moreover, the presence of oxygen containing functional groups in the exfoliated graphene materials, offers facile solution processing and further covalent and/or non-covalent functionalization with various organic and inorganic compounds. The bottleneck of rGO is the low conductivity, which is strongly governed by the degree of remaining functional groups after chemical or thermal reduction. Therefore, the development of a novel chemical exfoliation process which aims at high yield synthesis of high quality graphene while maintaining good solution processability is of great concern. In this thesis, we will focus on the solution production of high-quality graphene by wet-chemical exfoliation methods and address the applications of chemically exfoliated graphene as high performance fuel cell catalyst, supercapacitors and OFETs.

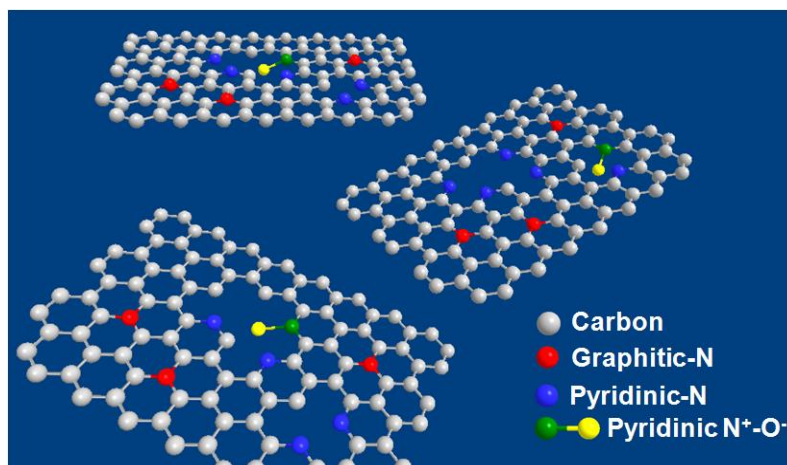


Figure 1.9 Schematic representation of nitrogen doped graphene (NG).

It is well known that doping in a carbon network with heteroatoms (e.g. N, B and P) can introduce electrocatalytic active sites. The functional groups on GO, offer a suitable platform for nitrogen doping due to their electrostatic or π - π interaction with various organic or inorganic nitrogen containing precursors. Therefore, nitrogen-doping enhances not only the electric conductivity but also the long-term operational stability of graphene when nitrogen-doped graphene (NG) is utilized as electrocatalyst for ORR. However, there are only a handful of studies on the preparation of NG. Motivated by this, we introduce a facile synthetic method to prepare NG in bulk scale in Chapter 2. For this purpose, we use chemically exfoliated GO and cyanamide as graphene and nitrogen-rich precursor respectively. Non-covalent functionalization of graphene by cyanamide which undergoes polymerization to form carbon nitride (CN) helps to prevent restacking of graphene sheets. High temperature pyrolysis of graphene/CN composites results in decomposition of CN and thereby introducing nitrogen moieties into graphene (Figure 1.9). As a result, NG sheets with nitrogen content from 4.0% to 12.0% are obtained by controlling the pyrolysis temperature from 800 to 1000 °C. As prepared NG shows a high electrocatalytic activity

with almost four-electron (i.e. 3.70) transfer process, high current density of 6.67 mA cm^{-2} , excellent methanol cross-over effect and durability ($\sim 87\%$ after 10,000 cycles) in alkaline conditions (i.e. 0.1 M KOH) which are superior to those of commercially available Pt-based catalysts.

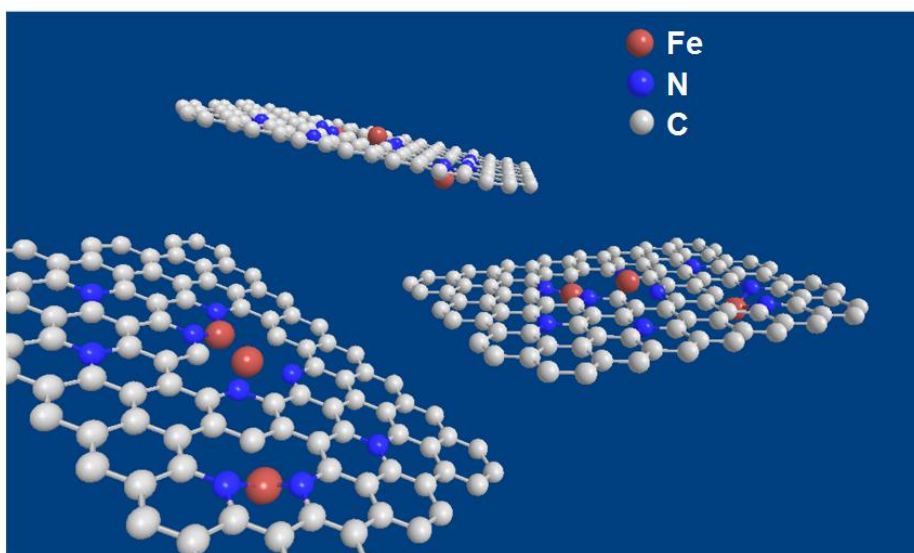


Figure 1.10 Illustration of the structure of NG/Fe composites

Non-precious metal catalysts, namely metal-nitrogen-carbon (M-N-C) catalysts (M = Fe and/or Co), can be obtained by pyrolyzing precursors of a transition metal, nitrogen and carbon. Therefore, following the synthesis of NG, we further extend our synthetic method to coordinate non-precious iron (Fe) with NG, as will be discussed in Chapter 3. Fe nanoparticles can be incorporated into NG with the aid of Fe (III) chloride in the synthetic process. As a result, NG supported with only 5 wt% Fe nanoparticles displays an excellent methanol cross-over effect and high current density of 8.20 mA cm^{-2} in alkaline solution. Moreover, Fe incorporated NG shows almost four electron transfer process and superior stability in both alkaline ($\sim 94\%$) and acidic ($\sim 85\%$) solution, which outperform the Pt/C and NG-based catalysts.



Figure 1.11 Plasma reduced flexible and transparent graphene film.

High electrical conductivity is one of the most important requirements for applying graphene in various electronic devices. As discussed above, GO is an insulating material due to the presence of significant amount of oxygen containing functional groups and structural defects. Generally, GO is reduced by chemical and/or thermal reduction methods. However, these methods are hampered by lengthy experimental time and high temperature requirement. Therefore, searching for an efficient reduction protocol to prepare highly reduced GO (rGO) remains a great challenge. In Chapter 4, we will discuss an ultrafast and highly effective method for the reduction of GO by exposing GO film to methane plasma treatment at a relative low temperature (700 °C) for only few seconds. By this means, methane plasma reduced GO (PrGO) films show low sheet resistance (i.e. $4.12 \text{ k}\Omega \text{ sq.}^{-1}$) compared to the conventional thermally and/or chemically reduced GO films ($> 20 \text{ k}\Omega \text{ sq.}^{-1}$). Moreover, PrGO films with various thicknesses can be readily transferred to the flexible substrates (Figure 1.11). All-solid-state micro-supercapacitors fabricated from PrGO films deliver a high power density and energy density of 495 W cm^{-3} and 2.5 mWh cm^{-3} , respectively, which are comparable to lithium thin-film batteries. Importantly, the devices

can be operated at ultrahigh rate up to 1000 V s^{-1} , three orders of magnitude larger than that of conventional supercapacitors.

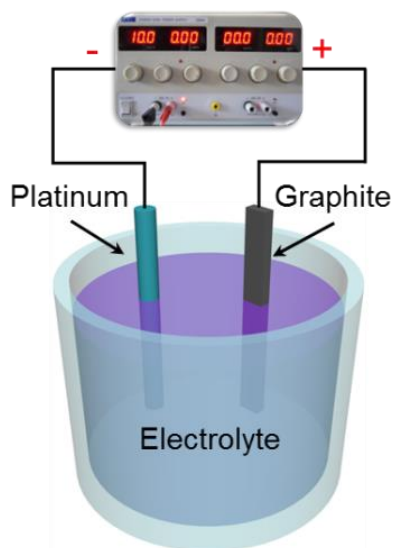


Figure 1.12 Schematic illustration of electrochemical exfoliation of graphite.

Although GO can be produced in bulk scale, large amount of defect density and low electrical conductivity are the major drawbacks. More critically, the production of GO involves the use of large amounts of toxic chemicals (such as, H_2SO_4 , KMnO_4 , H_2O_2 etc.) which requires tedious purification and reduction processes, thus preventing GO from practical industrial applications. To overcome these limitations of chemically exfoliated GO, in Chapter 5 we demonstrate the electrochemical exfoliation of graphite in aqueous H_2SO_4 as an alternative pathway to produce high quality graphene. The electrochemically exfoliated graphene (EG) contains a high yield ($> 80\%$) of one-to-three layer graphene flakes with high C/O ratio of 12.3. As-fabricated EG shows a low sheet resistance of $4.8 \text{ k}\Omega \text{ sq.}^{-1}$ for a single sheet compared to that of reduced GO. Profiting from the easy solution processability of EG in DMF, a vacuum filtration method in association with dry transfer are developed to fabricate large area and highly conducting graphene films on various

substrates. The patterned EG can be used as high performance source/drain electrodes for organic field-effect transistors (OFETs).

Although, electrochemical exfoliation of graphite in acidic electrolytes yields graphene with better quality than reduced GO, a large amount of oxygen containing groups cannot be avoided due to the over-oxidation of graphite by the acid. Therefore, to improve the quality of graphene, acid electrolytes used in electrochemical exfoliation can be replaced by aqueous inorganic salts such as, ammonium sulfate ($(\text{NH}_4)_2\text{SO}_4$), potassium sulfate (K_2SO_4), sodium sulfate (Na_2SO_4) etc. As will be discussed in Chapter 6, exfoliation in these electrolytes results in graphene with high yield (> 80% of 1 to 3 layers), large lateral size (up to 44 μm), low oxidation degree (a C/O ratio of 17.2) and remarkable hole mobility of $310 \text{ cm}^2 \text{ V}^{-1} \text{ s}^{-1}$. The process can be produced on a scale of over 10 gram in less than one hour, demonstrating the great potential for industrial scale-up production. Furthermore, such high quality graphene allows formulating graphene ink with high concentration. Large area, highly conductive graphene can be fabricated on commercial Xerox paper by brush painting. All-solid-state flexible supercapacitors manufactured from such graphene films deliver high area capacitance and excellent rate capability.

1.6 References

- (1) Kroto, H. W.; Heath, J. R.; O'Brien, S. C.; Curl, R. F.; Smalley, R. E. *Nature* **1985**, *318*, 162.
- (2) Iijima, S. *Nature* **1991**, *354*, 56.
- (3) Boehm, H. P.; Setton, R.; Stumpp, E. *Carbon* **1986**, *24*, 241.
- (4) Lu, X. K.; Yu, M. F.; Huang, H.; Ruoff, R. S. *Nanotechnology* **1999**, *10*, 269.
- (5) Lu, X. K.; Huang, H.; Nemchuk, N.; Ruoff, R. S. *Appl. Phys. Lett.* **1999**, *75*, 193.
- (6) Novoselov, K. S.; Geim, A. K.; Morozov, S. V.; Jiang, D.; Zhang, Y.; Dubonos, S. V.; Grigorieva, I. V.; Firsov, A. A. *Science* **2004**, *306*, 666.
- (7) Bolotin, K. I.; Sikes, K. J.; Jiang, Z.; Klima, M.; Fudenberg, G.; Hone, J.; Kim, P.; Stormer, H. L. *Solid State Commun.* **2008**, *146*, 351.
- (8) Morozov, S. V.; Novoselov, K. S.; Katsnelson, M. I.; Schedin, F.; Elias, D. C.; Jaszczak, J. A.; Geim, A. K. *Phys. Rev. Lett.* **2008**, *100*.
- (9) Balandin, A. A.; Ghosh, S.; Bao, W. Z.; Calizo, I.; Teweldebrhan, D.; Miao, F.; Lau, C. N. *Nano Lett.* **2008**, *8*, 902.
- (10) Lee, C.; Wei, X. D.; Kysar, J. W.; Hone, J. *Science* **2008**, *321*, 385.
- (11) Nair, R. R.; Blake, P.; Grigorenko, A. N.; Novoselov, K. S.; Booth, T. J.; Stauber, T.; Peres, N. M. R.; Geim, A. K. *Science* **2008**, *320*, 1308.
- (12) Blake, P.; Brimicombe, P. D.; Nair, R. R.; Booth, T. J.; Jiang, D.; Schedin, F.; Ponomarenko, L. A.; Morozov, S. V.; Gleeson, H. F.; Hill, E. W.; Geim, A. K.; Novoselov, K. S. *Nano Lett.* **2008**, *8*, 1704.
- (13) Wang, X.; Zhi, L. J.; Mullen, K. *Nano Lett.* **2008**, *8*, 323.
- (14) Son, D. I.; Kim, T. W.; Shim, J. H.; Jung, J. H.; Lee, D. U.; Lee, J. M.; Il Park, W.; Choi, W. K. *Nano Lett.* **2010**, *10*, 2441.
- (15) De Arco, L. G.; Zhang, Y.; Schlenker, C. W.; Ryu, K.; Thompson, M. E.; Zhou, C. W. *ACS Nano* **2010**, *4*, 2865.
- (16) Gunes, F.; Han, G. H.; Kim, K. K.; Kim, E. S.; Chae, S. J.; Park, M. H.; Jeong, H. K.; Lim, S. C.; Lee, Y. H. *Nano* **2009**, *4*, 83.
- (17) Su, Q.; Pang, S. P.; Alijani, V.; Li, C.; Feng, X. L.; Mullen, K. *Adv. Mater.* **2009**, *21*, 3191.

- (18) Matyba, P.; Yamaguchi, H.; Eda, G.; Chhowalla, M.; Edman, L.; Robinson, N. D. *ACS Nano* **2010**, *4*, 637.
- (19) Jo, G.; Choe, M.; Cho, C. Y.; Kim, J. H.; Park, W.; Lee, S.; Hong, W. K.; Kim, T. W.; Park, S. J.; Hong, B. H.; Kahng, Y. H.; Lee, T. *Nanotechnology* **2010**, *21*.
- (20) Bae, S.; Kim, H.; Lee, Y.; Xu, X. F.; Park, J. S.; Zheng, Y.; Balakrishnan, J.; Lei, T.; Kim, H. R.; Song, Y. I.; Kim, Y. J.; Kim, K. S.; Ozyilmaz, B.; Ahn, J. H.; Hong, B. H.; Iijima, S. *Nat. Nanotechnol.* **2010**, *5*, 574.
- (21) Pang, S. P.; Tsao, H. N.; Feng, X. L.; Mullen, K. *Adv. Mater.* **2009**, *21*, 3488.
- (22) Parvez, K.; Li, R. J.; Puniredd, S. R.; Hernandez, Y.; Hinkel, F.; Wang, S. H.; Feng, X. L.; Mullen, K. *ACS Nano* **2013**, *7*, 3598.
- (23) Cao, Y.; Liu, S.; Shen, Q.; Yan, K.; Li, P. J.; Xu, J.; Yu, D. P.; Steigerwald, M. L.; Nuckolls, C.; Liu, Z. F.; Guo, X. F. *Adv. Funct. Mater.* **2009**, *19*, 2743.
- (24) Pang, S. P.; Yang, S. B.; Feng, X. L.; Mullen, K. *Adv. Mater.* **2012**, *24*, 1566.
- (25) Lee, K. R.; Lee, K. U.; Lee, J. W.; Ahn, B. T.; Woo, S. I. *Electrochem. Commun.* **2010**, *12*, 1052.
- (26) Parvez, K.; Yang, S. B.; Hernandez, Y.; Winter, A.; Turchanin, A.; Feng, X. L.; Mullen, K. *ACS Nano* **2012**, *6*, 9541.
- (27) Wu, Z. S.; Parvez, K.; Feng, X.; Mullen, K. *Nat. Commun.* **2013**, *4*, 2487.
- (28) Yoo, J. J.; Balakrishnan, K.; Huang, J. S.; Meunier, V.; Sumpter, B. G.; Srivastava, A.; Conway, M.; Reddy, A. L. M.; Yu, J.; Vajtai, R.; Ajayan, P. M. *Nano Lett.* **2011**, *11*, 1423.
- (29) Bi, H.; Chen, J.; Zhao, W.; Sun, S. R.; Tang, Y. F.; Lin, T. Q.; Huang, F. Q.; Zhou, X. D.; Xie, X. M.; Jiang, M. H. *Rsc Adv.* **2013**, *3*, 8454.
- (30) Wu, Z. S.; Ren, W. C.; Xu, L.; Li, F.; Cheng, H. M. *ACS Nano* **2011**, *5*, 5463.
- (31) Ruan, M.; Hu, Y. K.; Guo, Z. L.; Dong, R.; Palmer, J.; Hankinson, J.; Berger, C.; de Heer, W. A. *Mrs. Bull.* **2012**, *37*, 1138.
- (32) Hernandez, Y.; Nicolosi, V.; Lotya, M.; Blighe, F. M.; Sun, Z. Y.; De, S.; McGovern, I. T.; Holland, B.; Byrne, M.; Gun'ko, Y. K.; Boland, J. J.; Niraj, P.; Duesberg, G.; Krishnamurthy, S.; Goodhue, R.; Hutchison, J.; Scardaci, V.; Ferrari, A. C.; Coleman, J. N. *Nat. Nanotechnol* **2008**, *3*, 563.
- (33) Park, S.; Ruoff, R. S. *Nat. Nanotechnol* **2009**, *4*, 217.
- (34) Sun, Z. Z.; Yan, Z.; Yao, J.; Beitler, E.; Zhu, Y.; Tour, J. M. *Nature* **2010**, *468*, 549.

-
- (35) Allen, M. J.; Tung, V. C.; Kaner, R. B. *Chemical reviews* **2010**, *110*, 132.
- (36) Geim, A. K.; Novoselov, K. S. *Nat. Mater.* **2007**, *6*, 183.
- (37) Novoselov, K. S.; Jiang, D.; Schedin, F.; Booth, T. J.; Khotkevich, V. V.; Morozov, S. V.; Geim, A. K. *P. Natl. Acad. Sci.* **2005**, *102*, 10451.
- (38) Geim, A. *Bull. Am. Phys. Soc.* **2010**, *55*, abstr.J21.0004.
- (39) Khan, U.; O'Neill, A.; Lotya, M.; De, S.; Coleman, J. N. *Small* **2010**, *6*, 864.
- (40) Torrisi, F.; Hasan, T.; Wu, W. P.; Sun, Z. P.; Lombardo, A.; Kulmala, T. S.; Hsieh, G. W.; Jung, S. J.; Bonaccorso, F.; Paul, P. J.; Chu, D. P.; Ferrari, A. C. *ACS Nano* **2012**, *6*, 2992.
- (41) Bonaccorso, F.; Lombardo, A.; Hasan, T.; Sun, Z. P.; Colombo, L.; Ferrari, A. C. *Mater. Today* **2012**, *15*, 564.
- (42) Qian, W.; Hao, R.; Hou, Y. L.; Tian, Y.; Shen, C. M.; Gao, H. J.; Liang, X. L. *Nano Res.* **2009**, *2*, 706.
- (43) Zhang, X. Y.; Coleman, A. C.; Katsonis, N.; Browne, W. R.; van Wees, B. J.; Feringa, B. L. *Chem. Commun.* **2010**, *46*, 7539.
- (44) Lotya, M.; Hernandez, Y.; King, P. J.; Smith, R. J.; Nicolosi, V.; Karlsson, L. S.; Blighe, F. M.; De, S.; Wang, Z. M.; McGovern, I. T.; Duesberg, G. S.; Coleman, J. N. *J. Am. Chem. Soc.* **2009**, *131*, 3611.
- (45) Marago, O. M.; Bonaccorso, F.; Saija, R.; Privitera, G.; Gucciardi, P. G.; Iati, M. A.; Calogero, G.; Jones, P. H.; Borghese, F.; Denti, P.; Nicolosi, V.; Ferrari, A. C. *ACS Nano* **2010**, *4*, 7515.
- (46) Green, A. A.; Hersam, M. C. *Nano Lett.* **2009**, *9*, 4031.
- (47) Lotya, M.; King, P. J.; Khan, U.; De, S.; Coleman, J. N. *Acs Nano* **2010**, *4*, 3155.
- (48) Wang, X. Q.; Fulvio, P. F.; Baker, G. A.; Veith, G. M.; Unocic, R. R.; Mahurin, S. M.; Chi, M. F.; Dai, S. *Chem. Commun.* **2010**, *46*, 4487.
- (49) Nuvoli, D.; Valentini, L.; Alzari, V.; Scognamillo, S.; Bon, S. B.; Piccinini, M.; Illescas, J.; Mariani, A. *J. Mater. Chem.* **2011**, *21*, 3428.
- (50) Brodie, B. C. *Ann. Chim. Phys.* **1860**, *59*, 466.
- (51) Hummers, W. S.; Offeman, R. E. *J. Am. Chem. Soc.* **1958**, *80*, 1339.
- (52) Stankovich, S.; Dikin, D. A.; Piner, R. D.; Kohlhaas, K. A.; Kleinhammes, A.; Jia, Y.; Wu, Y.; Nguyen, S. T.; Ruoff, R. S. *Carbon* **2007**, *45*, 1558.
- (53) Stankovich, S.; Piner, R. D.; Nguyen, S. T.; Ruoff, R. S. *Carbon* **2006**, *44*, 3342.

- (54) Lerf, A.; He, H. Y.; Forster, M.; Klinowski, J. *J. Phys. Chem. B* **1998**, *102*, 4477.
- (55) He, H. Y.; Klinowski, J.; Forster, M.; Lerf, A. *Chem. Phys. Lett.* **1998**, *287*, 53.
- (56) Cai, D. Y.; Song, M. *J. Mater. Chem.* **2007**, *17*, 3678.
- (57) Paredes, J. I.; Villar-Rodil, S.; Martinez-Alonso, A.; Tascon, J. M. D. *Langmuir* **2008**, *24*, 10560.
- (58) Cai, W. W.; Piner, R. D.; Stadermann, F. J.; Park, S.; Shaibat, M. A.; Ishii, Y.; Yang, D. X.; Velamakanni, A.; An, S. J.; Stoller, M.; An, J. H.; Chen, D. M.; Ruoff, R. S. *Science* **2008**, *321*, 1815.
- (59) Gomez-Navarro, C.; Meyer, J. C.; Sundaram, R. S.; Chuvilin, A.; Kurasch, S.; Burghard, M.; Kern, K.; Kaiser, U. *Nano Lett.* **2010**, *10*, 1144.
- (60) Bagri, A.; Mattevi, C.; Acik, M.; Chabal, Y. J.; Chhowalla, M.; Shenoy, V. B. *Nat. Chem.* **2010**, *2*, 581.
- (61) Shin, H. J.; Kim, K. K.; Benayad, A.; Yoon, S. M.; Park, H. K.; Jung, I. S.; Jin, M. H.; Jeong, H. K.; Kim, J. M.; Choi, J. Y.; Lee, Y. H. *Adv. Funct. Mater.* **2009**, *19*, 1987.
- (62) Stankovich, S.; Dikin, D. A.; Dommett, G. H. B.; Kohlhaas, K. M.; Zimney, E. J.; Stach, E. A.; Piner, R. D.; Nguyen, S. T.; Ruoff, R. S. *Nature* **2006**, *442*, 282.
- (63) Pei, S. F.; Zhao, J. P.; Du, J. H.; Ren, W. C.; Cheng, H. M. *Carbon* **2010**, *48*, 4466.
- (64) Moon, I. K.; Lee, J.; Ruoff, R. S.; Lee, H. *Nat. Commun.* **2010**, *1*, 73.
- (65) Singh, V.; Joung, D.; Zhai, L.; Das, S.; Khondaker, S. I.; Seal, S. *Prog. Mater. Sci.* **2011**, *56*, 1178.
- (66) Stankovich, S.; Piner, R. D.; Chen, X. Q.; Wu, N. Q.; Nguyen, S. T.; Ruoff, R. S. *J. Mater. Chem.* **2006**, *16*, 155.
- (67) Park, S.; Hu, Y. C.; Hwang, J. O.; Lee, E. S.; Casabianca, L. B.; Cai, W. W.; Potts, J. R.; Ha, H. W.; Chen, S. S.; Oh, J.; Kim, S. O.; Kim, Y. H.; Ishii, Y.; Ruoff, R. S. *Nat. Commun.* **2012**, *3*.
- (68) Bourlinos, A. B.; Gournis, D.; Petridis, D.; Szabo, T.; Szeri, A.; Dekany, I. *Langmuir* **2003**, *19*, 6050.
- (69) Wang, G. X.; Yang, J.; Park, J.; Gou, X. L.; Wang, B.; Liu, H.; Yao, J. *J. Phys. Chem. C* **2008**, *112*, 8192.
- (70) Dubin, S.; Gilje, S.; Wang, K.; Tung, V. C.; Cha, K.; Hall, A. S.; Farrar, J.; Varshneya, R.; Yang, Y.; Kaner, R. B. *ACS Nano* **2010**, *4*, 3845.
- (71) Ramesha, G. K.; Sampath, S. *J. Phys. Chem. C* **2009**, *113*, 7985.

-
- (72) Williams, G.; Seger, B.; Kamat, P. V. *ACS Nano* **2008**, *2*, 1487.
- (73) Kim, S. R.; Parvez, M. K.; Chhowalla, M. *Chem. Phys. Lett.* **2009**, *483*, 124.
- (74) Mattevi, C.; Eda, G.; Agnoli, S.; Miller, S.; Mkhoyan, K. A.; Celik, O.; Mostrogiovanni, D.; Granozzi, G.; Garfunkel, E.; Chhowalla, M. *Adv. Funct. Mater.* **2009**, *19*, 2577.
- (75) Yang, D.; Velamakanni, A.; Bozoklu, G.; Park, S.; Stoller, M.; Piner, R. D.; Stankovich, S.; Jung, I.; Field, D. A.; Ventrice, C. A.; Ruoff, R. S. *Carbon* **2009**, *47*, 145.
- (76) Boukhvalov, D. W.; Katsnelson, M. I. *J. Am. Chem. Soc.* **2008**, *130*, 10697.
- (77) Li, X. L.; Wang, H. L.; Robinson, J. T.; Sanchez, H.; Diankov, G.; Dai, H. J. *J. Am. Chem. Soc.* **2009**, *131*, 15939.
- (78) Liang, Y. Y.; Frisch, J.; Zhi, L. J.; Norouzi-Arasi, H.; Feng, X. L.; Rabe, J. P.; Koch, N.; Mullen, K. *Nanotechnology* **2009**, *20*, 434007.
- (79) Lopez, V.; Sundaram, R. S.; Gomez-Navarro, C.; Olea, D.; Burghard, M.; Gomez-Herrero, J.; Zamora, F.; Kern, K. *Adv. Mater.* **2009**, *21*, 4683.
- (80) Banerjee, B. C.; Walker, P. L.; Hirt, T. J. *Nature* **1961**, *192*, 450.
- (81) Robertso. *Sd Nature* **1969**, *221*, 1044.
- (82) Lang, B. *Surf Sci* **1975**, *53*, 317.
- (83) Sutter, P. W.; Flege, J. I.; Sutter, E. A. *Nat. Mater.* **2008**, *7*, 406.
- (84) Coraux, J.; N'Diaye, A. T.; Busse, C.; Michely, T. *Nano Lett.* **2008**, *8*, 565.
- (85) Hamilton, J. C.; Blakely, J. M. *Surf. Sci.* **1980**, *91*, 199.
- (86) Hu, Z. P.; Ogletree, D. F.; Vanhove, M. A.; Somorjai, G. A. *Surf. Sci.* **1987**, *180*, 433.
- (87) Reina, A.; Jia, X. T.; Ho, J.; Nezich, D.; Son, H. B.; Bulovic, V.; Dresselhaus, M. S.; Kong, J. *Nano Lett.* **2009**, *9*, 30.
- (88) Kumar, S.; McEvoy, N.; Lutz, T.; Keeley, G. P.; Nicolosi, V.; Murray, C. P.; Blau, W. J.; Duesberg, G. S. *Chem. Commun.* **2010**, *46*, 1422.
- (89) Wei, D. C.; Liu, Y. Q.; Wang, Y.; Zhang, H. L.; Huang, L. P.; Yu, G. *Nano Lett.* **2009**, *9*, 1752.
- (90) Li, X. S.; Cai, W. W.; An, J. H.; Kim, S.; Nah, J.; Yang, D. X.; Piner, R.; Velamakanni, A.; Jung, I.; Tutuc, E.; Banerjee, S. K.; Colombo, L.; Ruoff, R. S. *Science* **2009**, *324*, 1312.

- (91) Kim, K. S.; Zhao, Y.; Jang, H.; Lee, S. Y.; Kim, J. M.; Kim, K. S.; Ahn, J. H.; Kim, P.; Choi, J. Y.; Hong, B. H. *Nature* **2009**, *457*, 706.
- (92) Obraztsov, A. N.; Obraztsova, E. A.; Tyurnina, A. V.; Zolotukhin, A. A. *Carbon* **2007**, *45*, 2017.
- (93) Hou, J. B.; Shao, Y. Y.; Ellis, M. W.; Moore, R. B.; Yi, B. L. *Phys. Chem. Chem. Phys.* **2011**, *13*, 15384.
- (94) Hao, Y. F.; Bharathi, M. S.; Wang, L.; Liu, Y. Y.; Chen, H.; Nie, S.; Wang, X. H.; Chou, H.; Tan, C.; Fallahazad, B.; Ramanarayan, H.; Magnuson, C. W.; Tutuc, E.; Yakobson, B. I.; McCarty, K. F.; Zhang, Y. W.; Kim, P.; Hone, J.; Colombo, L.; Ruoff, R. S. *Science* **2013**, *342*, 720.
- (95) Lin, Y. C.; Jin, C. H.; Lee, J. C.; Jen, S. F.; Suenaga, K.; Chiu, P. W. *ACS Nano* **2011**, *5*, 2362.
- (96) Pirkle, A.; Chan, J.; Venugopal, A.; Hinojos, D.; Magnuson, C. W.; McDonnell, S.; Colombo, L.; Vogel, E. M.; Ruoff, R. S.; Wallace, R. M. *Appl. Phys. Lett.* **2011**, *99*.
- (97) Mattevi, C.; Kim, H.; Chhowalla, M. *J. Mater. Chem.* **2011**, *21*, 3324.
- (98) Bae, S.; Kim, H.; Lee, Y.; Xu, X.; Park, J.-S.; Zheng, Y.; Balakrishnan, J.; Lei, T.; Ri Kim, H.; Song, Y. I.; Kim, Y.-J.; Kim, K. S.; Ozyilmaz, B.; Ahn, J.-H.; Hong, B. H.; Iijima, S. *Nat. Nanotechnol.* **2010**, *5*, 574.
- (99) Zhang, Y.; Zhang, L. Y.; Zhou, C. W. *Accounts Chem. Res.* **2013**, *46*, 2329.
- (100) Blake, P.; Hill, E. W.; Neto, A. H. C.; Novoselov, K. S.; Jiang, D.; Yang, R.; Booth, T. J.; Geim, A. K. *Appl. Phys. Lett.* **2007**, *91*, 063124.
- (101) Hiura, H. M., Hisao; Tsukagoshi, Kazuhito *Appl. Phys. Express* **2010**, *3*, 095101.
- (102) Kochat, V.; Pal, A. N.; Sneha, E. S.; Sampathkumar, A.; Gairola, A.; Shivashankar, S. A.; Raghavan, S.; Ghosh, A. *J. Appl. Phys.* **2011**, *110*, 014315.
- (103) Tung, V. C.; Allen, M. J.; Yang, Y.; Kaner, R. B. *Nat. Nanotechnol.* **2009**, *4*, 25.
- (104) Valles, C.; Drummond, C.; Saadaoui, H.; Furtado, C. A.; He, M.; Roubeau, O.; Ortolani, L.; Monthieux, M.; Penicaud, A. *J. Am. Chem. Soc.* **2008**, *130*, 15802.
- (105) Jung, I.; Vaupel, M.; Pelton, M.; Piner, R.; Dikin, D. A.; Stankovich, S.; An, J.; Ruoff, R. S. *J. Phys. Chem. C* **2008**, *112*, 8499.
- (106) Ferrari, A. C.; Meyer, J. C.; Scardaci, V.; Casiraghi, C.; Lazzeri, M.; Mauri, F.; Piscanec, S.; Jiang, D.; Novoselov, K. S.; Roth, S.; Geim, A. K. *Phys. Rev. Lett.* **2006**, *97*.

-
- (107) Malard, L. M.; Pimenta, M. A.; Dresselhaus, G.; Dresselhaus, M. S. *Phys. Rep.* **2009**, *473*, 51.
- (108) Pimenta, M. A.; Dresselhaus, G.; Dresselhaus, M. S.; Cancado, L. G.; Jorio, A.; Saito, R. *Phys. Chem. Chem. Phys.* **2007**, *9*, 1276.
- (109) Kedzierski, J.; Hsu, P. L.; Healey, P.; Wyatt, P. W.; Keast, C. L.; Sprinkle, M.; Berger, C.; de Heer, W. A. *Ieee T Electron. Dev.* **2008**, *55*, 2078.
- (110) Zhang, Y. B.; Tan, Y. W.; Stormer, H. L.; Kim, P. *Nature* **2005**, *438*, 201.
- (111) Chen, J. H.; Jang, C.; Xiao, S. D.; Ishigami, M.; Fuhrer, M. S. *Nat. Nanotechnol.* **2008**, *3*, 206.
- (112) Eda, G.; Fanchini, G.; Chhowalla, M. *Nat. Nanotechnol.* **2008**, *3*, 270.
- (113) Yang, J.; Kim, J. W.; Shin, H. S. *Adv. Mater.* **2012**, *24*, 2299.
- (114) Lee, S.; Jo, G.; Kang, S. J.; Wang, G.; Choe, M.; Park, W.; Kim, D. Y.; Kahng, Y. H.; Lee, T. *Adv. Mater.* **2011**, *23*, 100.
- (115) Liu, W.; Jackson, B. L.; Zhu, J.; Miao, C. Q.; Chung, C. H.; Park, Y. J.; Sun, K.; Woo, J.; Xie, Y. H. *ACS Nano* **2010**, *4*, 3927.
- (116) Di, C. A.; Wei, D. C.; Yu, G.; Liu, Y. Q.; Guo, Y. L.; Zhu, D. B. *Adv. Mater.* **2008**, *20*, 3289.
- (117) Wroblowa, H. S.; Pan, Y. C.; Razumney, G. *J. Electroanal. Chem.* **1976**, *69*, 195.
- (118) Snyder, J.; Fujita, T.; Chen, M. W.; Erlebacher, J. *Nat. Mater.* **2010**, *9*, 904.
- (119) Wu, Z. S.; Yang, S. B.; Sun, Y.; Parvez, K.; Feng, X. L.; Mullen, K. *J. Am. Chem. Soc.* **2012**, *134*, 9082.
- (120) Qu, L. T.; Liu, Y.; Baek, J. B.; Dai, L. M. *ACS Nano* **2010**, *4*, 1321.
- (121) Geng, D. S.; Chen, Y.; Chen, Y. G.; Li, Y. L.; Li, R. Y.; Sun, X. L.; Ye, S. Y.; Knights, S. *Energ. Environ. Sci.* **2011**, *4*, 760.
- (122) Lin, Y. C.; Lin, C. Y.; Chiu, P. W. *Appl. Phys. Lett.* **2010**, *96*.
- (123) Wu, Z. S.; Chen, L.; Liu, J.; Parvez, K.; Liang, H.; Shu, J.; Sachdev, H.; Graf, R.; Feng, X.; Mullen, K. *Adv. Mater.* **2013**.
- (124) Kim, S. K.; Jeon, S. *Electrochem. Commun.* **2012**, *22*, 141.
- (125) Byon, H. R.; Suntivich, J.; Shao-Horn, Y. *Chem. Mater.* **2011**, *23*, 3421.
- (126) Tsai, C. W.; Tu, M. H.; Chen, C. J.; Hung, T. F.; Liu, R. S.; Liu, W. R.; Lo, M. Y.; Peng, Y. M.; Zhang, L.; Zhang, J. J.; Shy, D. S.; Xing, X. K. *Rsc Adv.* **2011**, *1*, 1349.

- (127) Wu, Z. S.; Winter, A.; Chen, L.; Sun, Y.; Turchanin, A.; Feng, X. L.; Mullen, K. *Adv. Mater.* **2012**, *24*, 5130.
- (128) Wu, Z. S.; Sun, Y.; Tan, Y. Z.; Yang, S. B.; Feng, X. L.; Mullen, K. *J. Am. Chem. Soc.* **2012**, *134*, 19532.
- (129) Wu, Z.-S.; Parvez, K.; Feng, X.; Müllen, K. *Journal of Materials Chemistry A* **2014**.
- (130) Miller, J. R.; Outlaw, R. A.; Holloway, B. C. *Science* **2010**, *329*, 1637.
- (131) Xia, J. L.; Chen, F.; Li, J. H.; Tao, N. J. *Nat. Nanotechnol.* **2009**, *4*, 505.
- (132) Liu, C. G.; Yu, Z. N.; Neff, D.; Zhamu, A.; Jang, B. Z. *Nano Lett.* **2010**, *10*, 4863.
- (133) Zhu, Y. W.; Murali, S.; Stoller, M. D.; Ganesh, K. J.; Cai, W. W.; Ferreira, P. J.; Pirkle, A.; Wallace, R. M.; Cychosz, K. A.; Thommes, M.; Su, D.; Stach, E. A.; Ruoff, R. S. *Science* **2011**, *332*, 1537.
- (134) El-Kady, M. F.; Strong, V.; Dubin, S.; Kaner, R. B. *Science* **2012**, *335*, 1326.
- (135) Wu, Z. S.; Zhou, G. M.; Yin, L. C.; Ren, W.; Li, F.; Cheng, H. M. *Nano Energy* **2012**, *1*, 107.
- (136) Wu, Z. S.; Parvez, K.; Winter, A.; Vieker, H.; Liu, X.; Han, S.; Turchanin, A.; Feng, X.; Mullen, K. *Adv. Mater.* **2014**, *26*, 4552.

Chapter 2

Nitrogen-doped graphene as metal-free electrocatalyst for oxygen reduction reaction (ORR)

The high cost of platinum-based electrocatalysts for the oxygen reduction reaction (ORR) has hindered the practical applications of fuel cells. Thanks to its unique chemical and structural properties, nitrogen-doped graphene (NG) is among the most promising metal-free catalysts for replacing platinum (Pt). In this chapter, we describe a simple, cost-effective and scalable method for the preparation of NG by using cyanamide as a nitrogen source and graphene oxide (GO) as a precursor. The nitrogen doping content in NG can be controlled by varying the annealing temperature. Moreover, the ratio of graphitic-type nitrogen is found to play an important role in the ORR process. The NG thermally treated at 900 °C shows a stable methanol crossover effect, almost four-electron (i.e. 3.70) transfer processes, high current density and durability of ~ 87% after 10,000 cycles, which outperformed the Pt based catalysts in alkaline (0.1 M KOH) solution.

2.1 Introduction

The oxygen reduction reaction (ORR) at the cathode plays a key role in controlling the performance of a fuel cell. Thus, the development of efficient electrocatalysts is essential for the practical applications of fuel cells.^{1,2} The ORR can proceed through either (i) a four-electron process to combine oxygen with electrons and protons directly, or (ii) a less efficient two-step, two-electron pathway involving the formation of hydrogen peroxide ions as an intermediate.³ Platinum (Pt) is the most commonly used catalyst for the ORR; however, in addition to its prohibitive cost and scarcity, Pt-based catalysts generally suffer from surface oxide formation, particle dissolution and aggregation in alkaline electrolytes, during the long term electrochemical process.⁴⁻⁸ Therefore, electrocatalysts with inexpensive and commercially available materials to facilitate sluggish cathodic ORR is a key issue for the development of fuel cells. Numerous efforts have been devoted to finding a suitable substitute for Pt-based catalysts including nitrogen-doped carbon nanotubes (NCNTs)^{3,9,10}, nitrogen-doped mesoporous graphitic arrays¹¹ and carbon nanosheets,¹² enzymatic electrocatalytic systems¹³, and even conducting poly(3,4-ethylenedioxythiophene) (PEDOT) coated membranes¹⁴.

Recently, nitrogen-doped graphene (NG) has been shown to possess high electrocatalytic activity and long-term operational stability when catalyzing the ORR.¹⁵ However, there are only a handful of studies on the preparation of NG, including treating graphene in ammonia at high temperature,^{16,17} using ammonia or nitrogen plasma,¹⁷⁻¹⁹ and growth of NG on Ni substrates by chemical vapor deposition.²⁰ All these processes to produce NG require vacuum conditions and are difficult to scale up.

In this chapter, we describe a facile synthesis of NG by immobilizing graphitic carbon nitride (CN) on graphene sheets to form a carbon nitride-graphene (CN-G) composite. The CN-G is then subjected to thermal treatment and thereby introducing nitrogen moieties into graphene. In this way, NG sheets with nitrogen content from 4.0% to 12.0% are obtained by controlling the pyrolysis temperature from 800 to 1000 °C. As-prepared NG shows a high electrocatalytic activity, low onset potential, excellent methanol cross-over effect and durability compared to the commercially available Pt-based electrodes (30 wt% Pt on Vulcan XC72).

2.2 Synthesis of Nitrogen-doped graphene (NG)

Towards the synthesis of NG, graphene oxide (GO) was first prepared by Hummer's method.²¹ For a typical procedure, natural graphite flakes (10 g, Aldrich) and NaNO₃ (7.5 g) were mixed with 300 mL of concentrated H₂SO₄ under continuous stirring. After 10 minutes, 40 g of KMnO₄ was slowly added to the reaction mixture over 1 hour. The mixture was stirred at room temperature for 3 days. Afterwards, 2 L of deionized (DI) water was added into the dark brown paste. Later on, 100 mL of H₂O₂ solution (1% in water) was added to the reaction mixture followed by continuous stirring for 2 hours. The resulting solution was then centrifuged 5 times at 4,000 rpm for 10 minutes to remove unreacted graphite flakes. After removal of large graphite flakes, the thick brown dispersion was repeatedly washed with DI water by centrifugation (10,000 rpm for 15 minutes) to remove residual salts and acid until the pH of the dispersion reached 7.0. Thus, a GO dispersion in water was obtained (Figure 2.1). The resulting homogeneous brown dispersion was stable for several months. The concentration of the GO dispersion was

measured by vacuum drying and measuring the weight of a small volume of the as-prepared GO.

Subsequently, as-prepared GO sheets were used for the synthesis of NG. As illustrated in Figure 2.1, graphene-carbon nitride (G-CN) composites were prepared by electrostatic interaction between anionic surfactant modified GO and cyanamide (CH_2N_2) precursor for synthesizing CN. Although several precursors such as, melamine ($\text{C}_3\text{H}_6\text{N}_6$),²² ethylenediamine ($\text{C}_2\text{H}_4(\text{NH}_2)_2$),²³ s-heptazine triazide ($\text{C}_6\text{N}_7(\text{N}_3)_3$)²⁴ etc. has been reported for the synthesis of CN, cyanamide was selected for this work due to its superior solubility in in water. Therefore, it is expected that cyanamide would provide better electrostatic interaction with negatively charged GO in water. In a typical synthesis, 0.1 g of the surfactant sodium dodecylbenzene sulfonic acid (SDBS) was mixed with 100 mL of GO dispersion (1 mg/mL) in water and sonicated for 30 min. Addition of SDBS enhanced the dispersion of GO in water. Then, 4 mL of cyanamide solution (50 wt% in water) was added dropwise. The mixture was continuously stirred and heated at 100 °C to remove water. The resulting solid was calcined in two different steps. In the first step, the solid products were heated to 550 °C at a rate of 2 °C/min and tempered at this temperature for another 4 h to form CN. In second step, the resulting CN-G composites were further heated to 800, 900, and 1000 °C and thus NG samples were obtained, which are denoted as NG-800, NG-900 and NG-1000, respectively. During the second step annealing, the effective reduction of GO occurs and the CN could decompose into nitrogen-containing species (e.g. C_2N_2^+ , C_3N_2^+ , C_3N_3^+)^{25,26} that provide nitrogen sources for finally evolving into NGs. All the annealing and cooling processes were carried out under argon flow. For comparison,

undoped and reduced GO (rGO) were also prepared by treating GO under the same annealing processes.

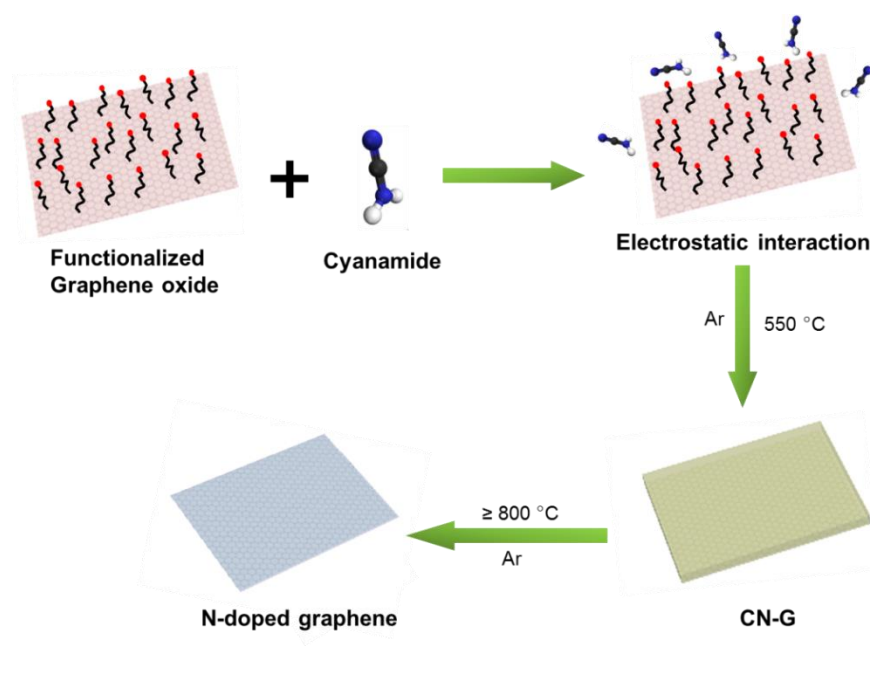


Figure 2.1 Preparation of nitrogen-doped graphene for oxygen reduction reaction (ORR).

2.3 Morphology of GO and NG

The morphology of the prepared GO was first characterized prior to the synthesis of CN-G and/or NG. As shown in Figure 2.2, the lateral size of the GO sheets is less than 5 μm as shown in the transmission electron microscopy (TEM) and atomic force microscopy (AFM) images (Figure 2.2b and c). The dark lines in Figure 2.2b are attributed to the wrinkled structures of GO sheets, which are formed due to the hydrophobic feature of the underlying carbon film on the TEM copper grids. These wrinkled structures disappeared when GO sheets were deposited on the hydrophilic SiO_2 substrate (Figure 2.2c). The height

profile in Figure 2.1c shows that the thickness of GO sheets is about 1 nm, which is in good agreement with the value of monolayer GO sheets reported previously.^{27,28}

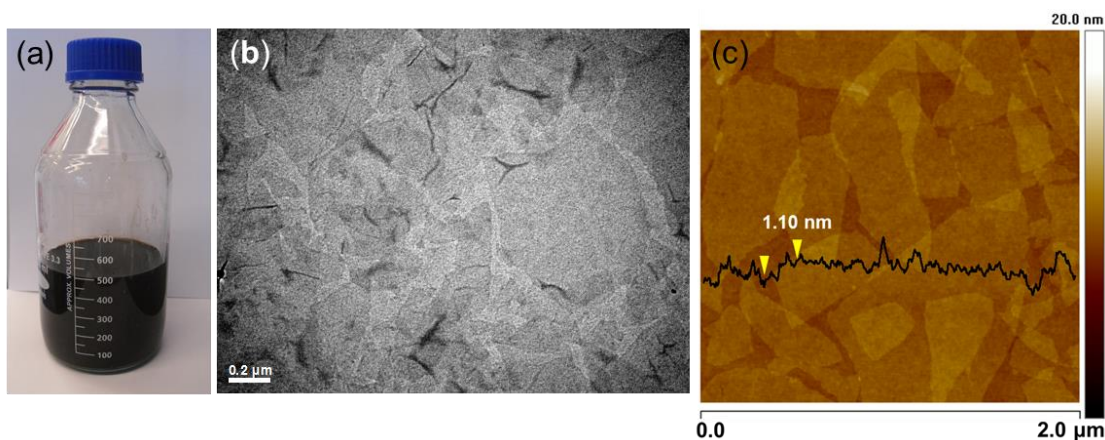


Figure 2.2 Photograph of GO dispersion in water. (b) TEM image of GO sheets. (c) AFM image of GO on SiO₂ substrates. The height profile is indicated by the black line showing the thickness of ~ 1 nm.

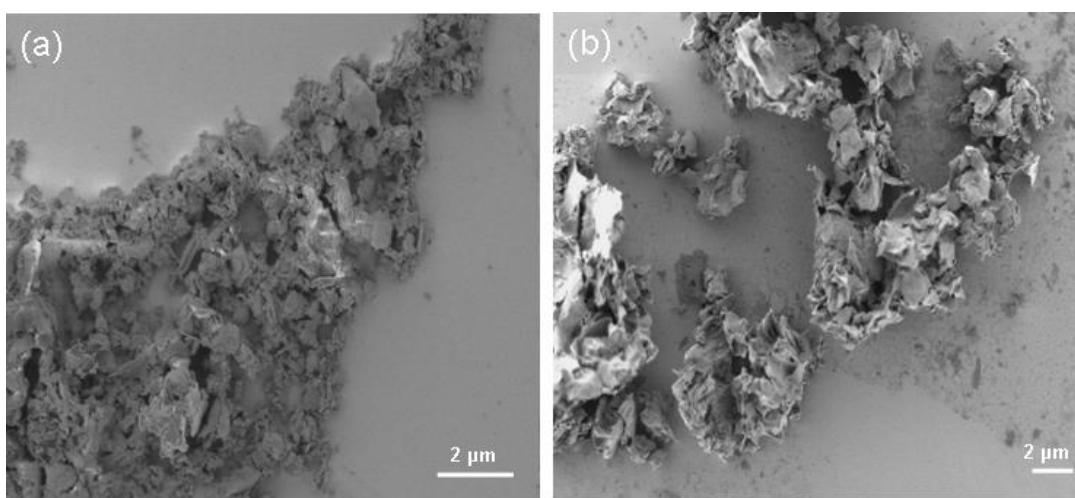


Figure 2.3 Typical SEM images of (a) CN and (b) CN-G composite.

The morphology and structure of CN-G were firstly investigated by transmission electron microscope (TEM) and scanning electron microscope (SEM). As shown in Figure 2.3a, the CN without incorporation of graphene sheets exhibit a typical slate like morphology.²⁹ Whereas, the CN-G composite becomes crumpled (Figure 2.3b) due to the adsorbed cyanamide on graphene which undergoes polymerization under thermal treatment. As indicated by the TEM images in Figure 2.4a, graphene sheets were not distinctively visible in CN-G due to thick layer of CN adsorbed on the graphene surface.

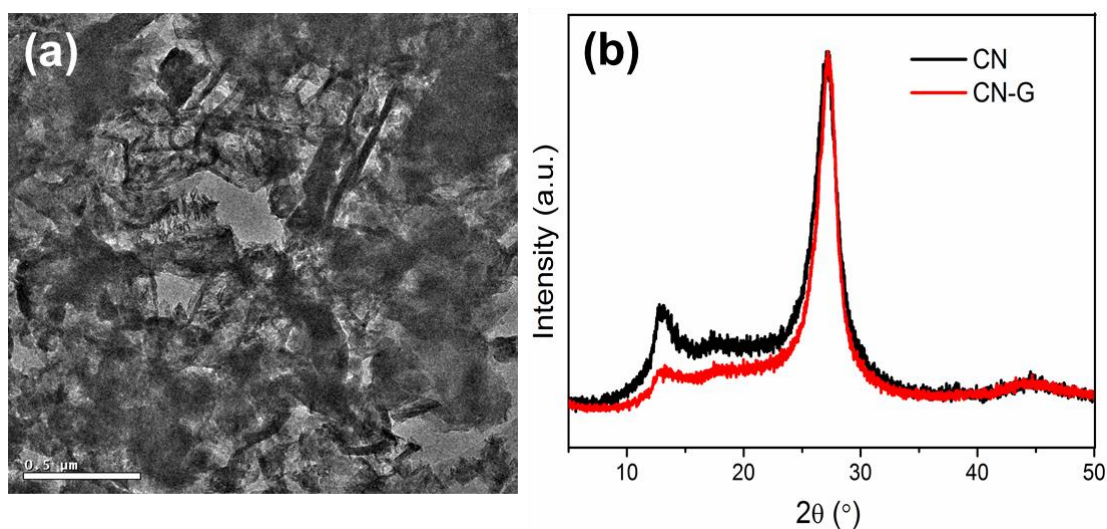


Figure 2.4 (a) TEM image of CN-G; (b) XRD pattern of CN and CN-G composite

The XRD patterns of CN, which stacks like graphite with tri-s-triazine unit, feature two diffraction peaks at around 27.2° and 13.1°.³⁰ The intense peak at 27.2° (d -spacing = 3.28 Å) is a characteristic interplanar stacking peak of aromatic system. Meanwhile, the peak at 13.1° with a d -spacing of 6.76 Å corresponds to repeated tri-s-triazine (i.e. the distance of the nitride pores), which is smaller than one tri-s-triazine unit (~ 7.13 Å).³¹ After the introduction of graphene, the unchanged XRD pattern suggests that graphene

sheets are homogeneously distributed in CN without disrupting their solid state packing (Figure 2.4b). Thermogravimetric analysis (TGA) of CN-G containing 5.0 wt% of graphene reveals that weight loss starts at around 600 °C (Figure 2.5a) which can be assigned to the decomposition of CN. It has been reported previously that the decomposition of CN occurs between 700 to 750 °C and decomposes completely without leaving any residue.³² After treatment at 800 °C, a total of ~ 95% weight loss of the composite suggests that only graphene remains.

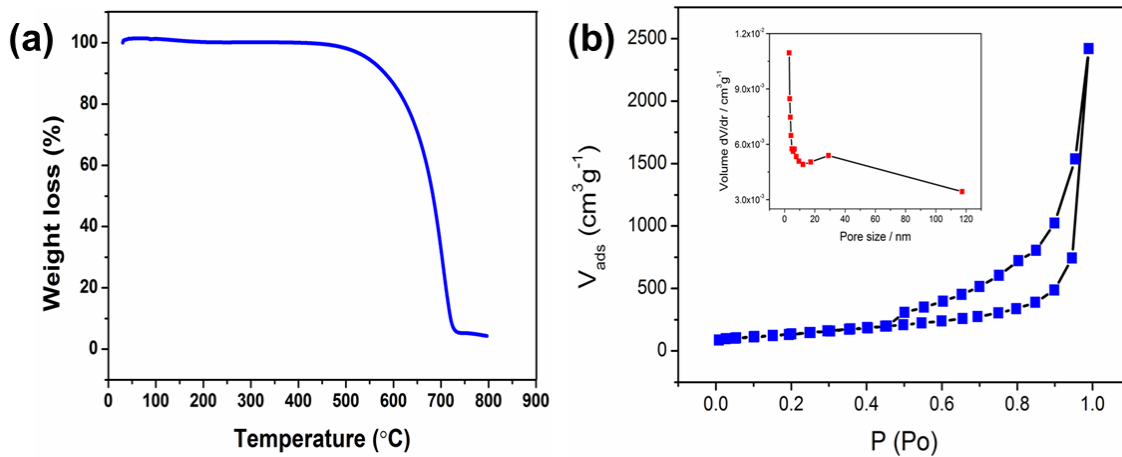


Figure 2.5 (a) TGA plot of CN-G composite and; (b) nitrogen adsorption-desorption isotherm of NG-900. Inset of (b) shows the pore size distribution.

A Brunauer-Emmett-Teller (BET) surface area of $508 \text{ m}^2 \text{ g}^{-1}$ for NG-900 (Figure 3.4b) was obtained which is higher than that of NG produced by other methods.^{33,34} In addition, a narrow pore-size distribution centered at about 3.1 nm and a total pore volume of $3.674 \text{ cm}^3 \text{ g}^{-1}$ can be derived from the adsorption branch of the isotherms based on the Barrett-Joyner-Halenda (BJH) model. Moreover, TEM images (Figure 2.6) of the NG-800, NG-900 and NG-1000 demonstrate transparent graphene sheets without the presence of any

residual CN. Therefore, it can be concluded that, no carbon and/or nitrogen species are left from CN as residues. Nevertheless, the optical contrast of NG sheets is low compared with un-doped graphene, which is a common phenomenon in NG.^{20,35}

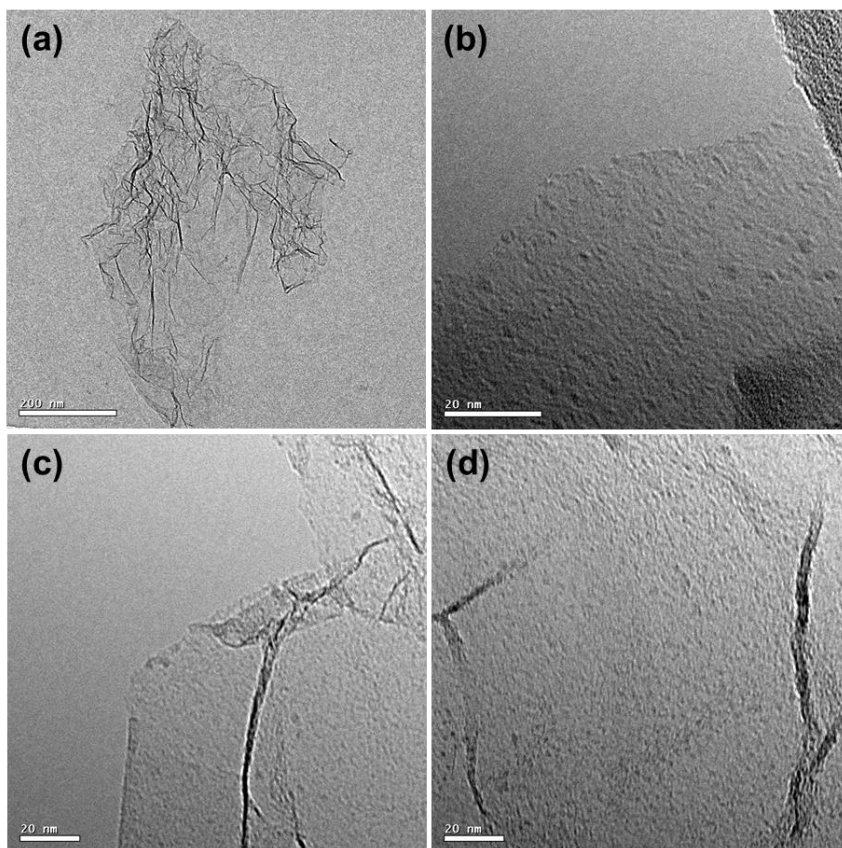


Figure 2.6 HRTEM images of (a) large NG flake representing the absence of any residual CN, (b) NG-800, (c) NG-900 and (d) NG-1000.

2.4 Chemical structure of NG

To probe the chemical composition and content of nitrogen in NG, X-ray photoelectron spectroscopic (XPS) measurements are carried out for NG-800, NG-900 and NG-1000 (Figure 2.7a). The XPS of NG samples were measured by the group of Dr.

Andrey Turchanin at the University of Bielefeld, using an Omicron Multiprobe spectrometer with Al K α radiation. For these measurements, NG powder samples were ultrasonicated in ethanol and then drop-casted on Au substrates (30 nm Au films thermally evaporated on Si-wafer). As shown in Figure 3.6a, the survey spectra of NG samples reveal the presence of C, O and N with a nitrogen content of 12.0, 5.0 and 4.0% in NG-800, NG-900 and NG-1000, respectively. However, elemental analysis of NG samples for bulk powder show the nitrogen content of 13.2%, 9.2% and 7.5% in NG-800, NG-900 and NG-1000, respectively (Figure 2.7b) which are much higher than the results obtained by XPS measurement on a film. Nevertheless, both the elemental analysis and XPS characterizations suggest that the nitrogen content decreases with the increase of annealing temperature suggesting that nitrogen is not very stable at high temperature. The decrease in nitrogen content is probably due to the decomposition of carbon-nitrogen bonds in graphene.

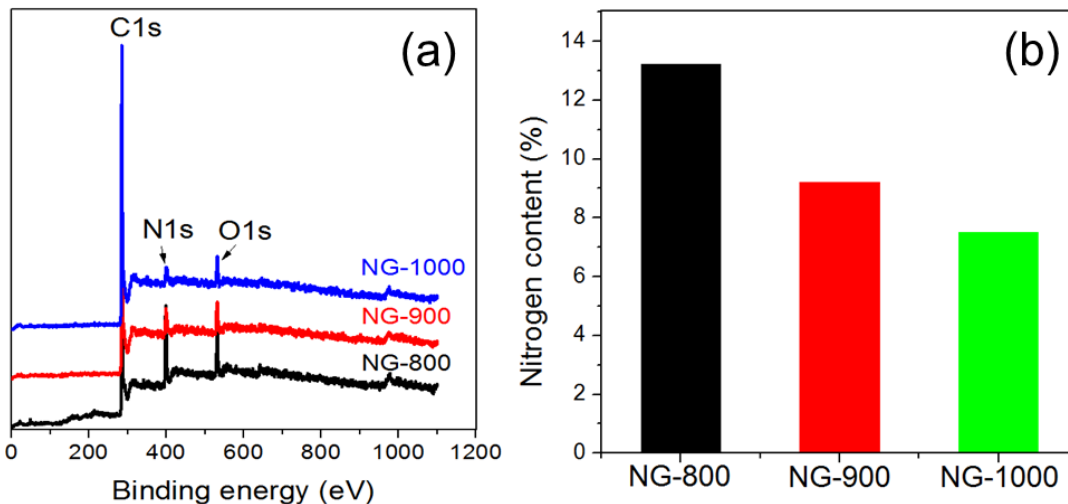


Figure 2.7 (a) XPS survey spectra of NG sample and, (b) content of nitrogen in NG samples by elemental analysis.

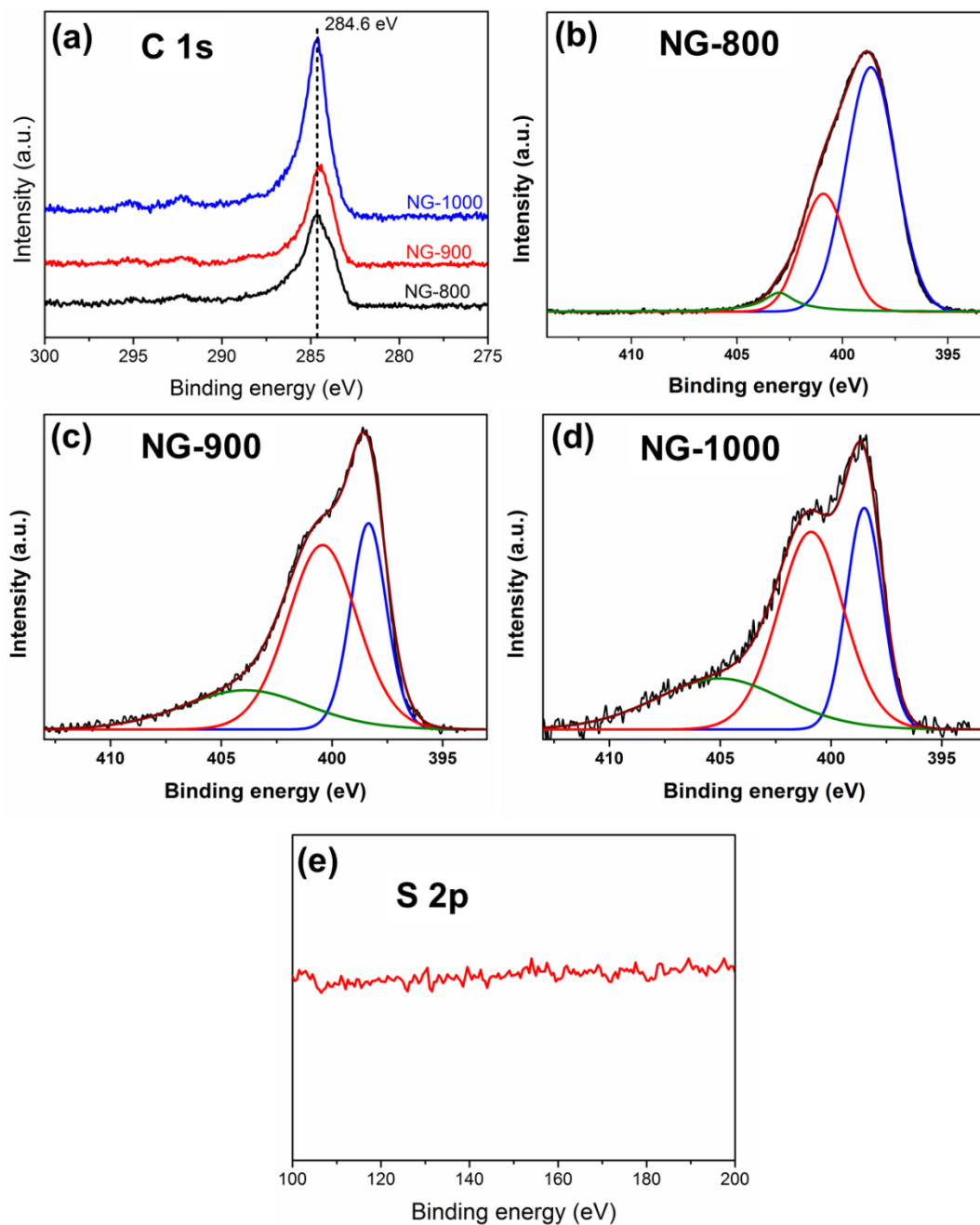


Figure 2.8 (a) C1s regions and the high resolution N1s XPS spectra of (b) NG-800, (c) NG-900, (d) NG-1000 and, (e) S 2p peak in NG-900, showing the absence of sulphur. The N1s peaks in (b), (c) and (d) are fitted into three energy components centered around 398.5, 401.0 and 403.6 eV, corresponding to pyridinic-N (red line), graphitic-N (blue line), and pyridinic N⁺-O⁻(green line,) respectively.

The C 1s peaks for the NG samples (Figure 2.8a) center at approximately 284.6 eV and are slightly asymmetric. This is a common effect for nitrogen doped carbon materials.³⁶ The width of C 1s peaks become smaller as the pyrolysis temperature increases from 800 to 1000 °C, suggesting an enhanced graphitization degree at higher temperature.¹¹ Furthermore, absence of S 2p peak at 165.0 eV (Figure 2.8e) indicates that, the surfactant (SDBS) was completely decomposed during pyrolysis.

Analysis of N1s spectra reveals the presence of pyridinic- and graphitic- nitrogen corresponding to their binding energies of 398.4 and 401.0 eV, respectively (Figure 2.8b to d).³⁷ In addition, the reaction between oxygen containing groups in GO and nitrogen species during the synthesis results in the formation of pyridinic N⁺-O⁻ at 402.0-404.0 eV.³⁸ As depicted in Figure 2.9b, the nitrogen functional groups are usually in the following molecular structures (chemical states): pyridinic-N refers to the nitrogen atoms at the edge of the graphene planes, each of which is bonded to two carbon atoms and donates one p-electron to the aromatic π -system; graphitic-N also called quaternary-N, is incorporated into the graphene layer and bonded to the three neighboring carbon atoms within a graphene plane; pyridinic N⁺-O⁻ is bonded to two carbon atoms and one oxygen atom. In the case of NG-800, pyridinic-N is dominant over graphitic-N with a content of 7.92% and 3.45%, respectively (Figure 2.9a). Upon raising the pyrolysis temperature to 900 and 1000 °C, the overall nitrogen content decreases dramatically. Interestingly, the pyridinic-N content largely drops to 1.47% at 900 °C and 1.14% at 1000 °C, whereas, the graphitic-N slowly decreases to 2.56% at 900 °C and 1.92% at 1000 °C, respectively. However, the content of graphitic-N is higher than that of pyridinic-N at 900 and 1000 °C. Furthermore, the ratio of graphitic-N to pyridinic-N content in NG-800, NG-900 and NG-1000 shows significant

differences (*i.e.* 0.44, 1.73 and 1.66, respectively). On the other hand, slight increase in pyridinic N⁺-O⁻ is observed from NG-800 to NG-900 and remains unchanged in NG-1000. Nevertheless, this type of nitrogen species does not contribute to ORR performance significantly and is unstable in fuel cell operating conditions.³⁹ Therefore, such different amount of nitrogen bonding configurations in NG samples is expected to play a crucial role on the ORR performance.⁴⁰

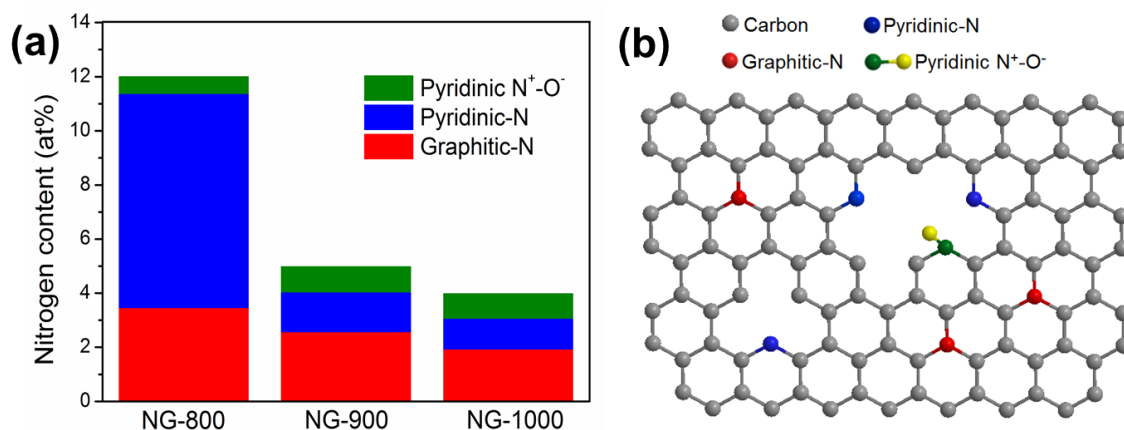


Figure 2.9 (a) The content of three types of nitrogen in NG and, (b) Schematic representation of NG.

The Raman spectra of NG samples in Figure 2.10a reveal that the G band becomes sharper and the intensity ratio of the G to the D band (I_G/I_D) increases, further supporting that the graphitization degree increases upon increasing temperature.⁴¹ Furthermore, the X-ray diffraction (XRD) of NG samples in Figure 2.10b exhibits a broad (002) peak at 26.1° , which can be attributed to the π -stacking of the graphene sheets.¹⁵ The absence of diffraction peak at 13.1° also suggests that CN is successfully removed upon pyrolysis. As the nitrogen content decreases from NG-800 to NG-1000, the peaks became sharper and shifted to higher diffraction angle from 25.6° to 26.1° , respectively. Thus, the d -spacing of

NG samples shows a decreasing order of 3.47, 3.44 and 3.41 Å for NG-800, NG-900 and NG-1000, respectively, further suggesting that the graphitization degree increases upon increasing temperatures.

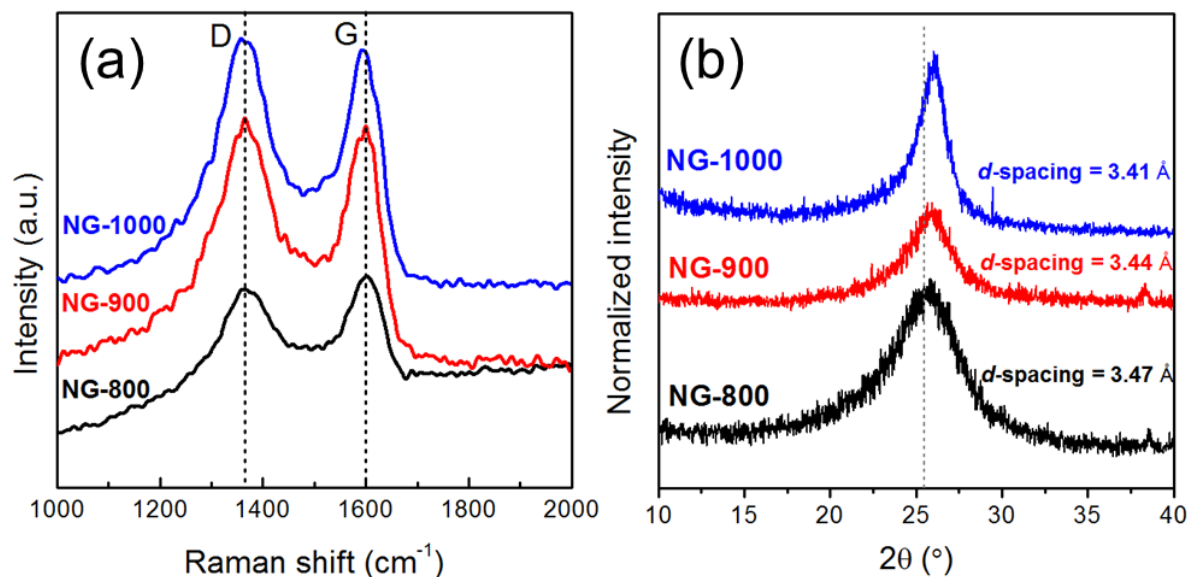


Figure 2.10 (a) Raman spectra and, (b) X-ray diffraction (XRD) of NG samples.

2.5 Electrochemical properties of NG

2.5.1 Alkaline conditions

The electrocatalytic activity of NG for ORR was first examined by cyclic voltammetry (CV) in 0.1 M KOH solution saturated with argon or oxygen at a scan rate of 100 mV s^{-1} . As presented in Figure 2.11a, featureless voltammetric currents within the potential range from -1.2 to +0.2 V were observed for NG-900 in argon saturated solution (dotted curve). In contrast, when the electrolyte was saturated with O_2 , a well-defined cathodic peak centered at -0.16 V was detected, suggesting a pronounced electrocatalytic

activity of NG-900 for oxygen reduction. A possible cross over effect of NG-900 and Pt/C against the electrooxidation of methanol in O₂ saturated 0.1M KOH in the presence of methanol (3.0 M) was also detected. Apparently, the Pt/C shows a pair of peaks at -0.15 V and -0.08 V for methanol oxidation in the CV curve, whereas the cathodic peak for the ORR disappears (Figure 2.11b). In contrast, no noticeable change was seen in the oxygen reduction current on NG-900 under the same experimental conditions (Figure 2.11a), suggesting high selectivity and good stability of NG-900 for ORR with respect to Pt/C.

To further evaluate the electrocatalytic activity of NG, both rotating ring disk electrodes (RRDE) and rotating disk electrodes (RDE) were employed. The RRDE and RDE measurements were carried out using a CHI Electrochemical Station (model 760D) in a conventional three-electrode electrochemical cell. Platinum wire and an Ag/AgCl, (KCl, 3 M) electrodes were used as the counter and reference electrode, respectively. A glassy carbon working electrode was employed to investigate the electrocatalytic nature of NG samples. Prior to use, the working electrode was polished mechanically with 0.05 μm alumina slurry to obtain mirror like surface, then washed with Mill-Q water and acetone and allowed to dry. One milligram of prepared NG sample was dispersed in 1 mL solvent mixture of Nafion (5 wt%) and water (v/v ratio = 1:9) using sonication. The dispersion was then drop-casted on pre-cleaned glassy carbon and allowed to dry overnight before any measurements. For comparison, a commercially available catalyst of 30 wt% Pt supported on carbon black (fuel cell grade) was used and 1 mg/mL of Pt/C suspension was prepared according to the process described above. The loading of both Pt/C and NG catalysts was 50.91 $\mu\text{g cm}^{-2}$. All the electrochemical measurements of NG were repeated at least three times and reproducible results were obtained.

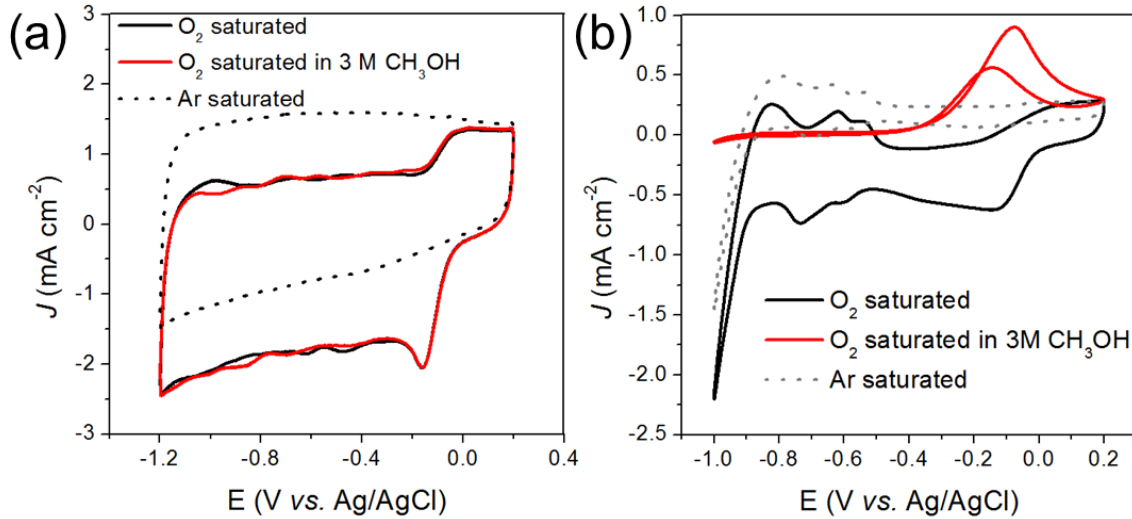


Figure 2.11 Cyclic voltammograms of (a) NG-900 and (b) Pt/C at a scan rate of 100 mV cm^{-1} in O_2 and Ar-saturated 0.1M KOH solution as well as O_2 -saturated 0.1M KOH solution with 3M CH_3OH .

Figure 2.12a displays the steady state voltammograms for different NG samples loaded on a glassy carbon electrode in O_2 saturated 0.1 M KOH. The corresponding ring current (I_R) for the oxidation of hydrogen peroxide ions (HO_2^-) was measured with a Pt ring electrode at an applied potential of 0.5 V. The electron transfer number per oxygen molecule involved in the ORR was calculated to be 3.35, 3.70 and 3.48 on the basis of Eq. 1³ for the NG-800, NG-900 and NG-1000 electrode at the potential of -0.4 V, respectively.

$$n = 4I_D / (I_D + I_R/N) \quad (1)$$

where, $N = 0.36$ is the collection efficiency, I_D is the disk current, and I_R is the ring current. The lower ring current of NG-900 compared to NG-800 and NG-1000 suggests that a small amount of HO_2^- reached the ring electrode under increasing negative potentials. The onset potential of NG-900 was determined to be -0.03 V which is close to that identified from CV

measurements (-0.04 V, Figure 2.11a). Different from a Pt/C electrode, the NG-900 electrode exhibited enhanced steady-state diffusion current over a large potential range.

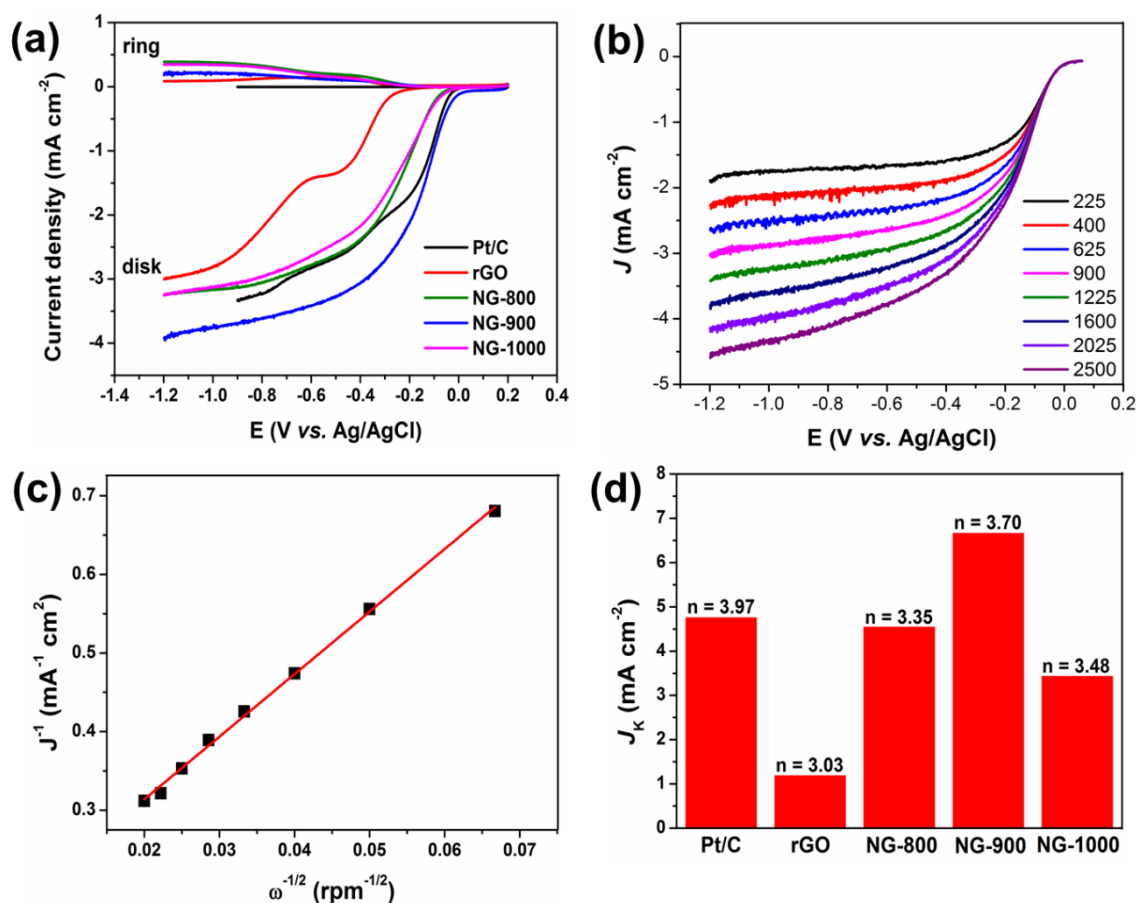


Figure 2.12 (a) RRDE voltammetric response for ORR in O₂ saturated 0.1M KOH at a scan rate of 10 mVs⁻¹. The electrode rotation rate was 1600 rpm and the Pt ring electrode was polarized at 0.5 V; (b) RDE voltammograms recorded for NG-900 supported on a GC electrode in an O₂-saturated 0.1M KOH at a scan rate of 10 mVs⁻¹ and different rotation rates; (c) Koutecky-Levich plot of J^{-1} vs $\omega^{-1/2}$ at -0.4 V obtained from (b); and (d) Electrochemical activity given as the kinetic-limiting current density (J_K) at -0.4 V for Pt/C, rGO and all three NG electrodes.

The current density (J_K) of NG samples was analyzed by RDE and calculated on the basis of the Koutecky-Levich equations [Eq. (2) – (4)].¹¹

$$\frac{1}{J} = \frac{1}{J_L} + \frac{1}{J_K} = \frac{1}{B\omega^{1/2}} + \frac{1}{J_K} \quad (2)$$

$$B = 0.62nFC_0(D_0)^{2/3}\nu^{-1/6} \quad (3)$$

$$J_K = nFkC_0 \quad (4)$$

where J is the measured current density, J_K and J_L are the kinetic and diffusion limiting current densities, ω is the angular velocity of the disk ($\omega = 2\pi N$, N is the linear rotation speed), n is the overall number of electrons transferred in the oxygen reduction, F is the Faraday constant (96485 C mol⁻¹), C_0 is the bulk concentration of O₂, ν is the kinematic viscosity of the electrolyte, and k is the electron transfer rate constant. The Koutecky-Levich plot of J^{-1} vs. $\omega^{-1/2}$ at a potential of -0.40 V on NG-900 electrode exhibited good linearity (Figure 2.12c). As shown in Figure 2.12d, the calculated J_K value of 6.67 mA cm⁻² at -0.40 V is much higher than that of Pt/C (4.76 mA cm⁻² at -0.40 V) and is comparable to or even higher than previous reports on N-doped graphene, CNTs and other types of carbon materials.^{15,42-44} In association with the XPS and electrochemical results described for NG-800, NG-900 and NG-1000, the content of pyridinic-N among the different nitrogen species does not play a significant role in ORR performance. In contrast, the electrochemical performance is dependent on the content of graphitic-N, for which a higher ratio of graphitic-N over pyridinic-N in NG-900 than NG-800 and NG-1000 might be responsible for the high catalytic performance in ORR.

2.5.2 Acidic conditions

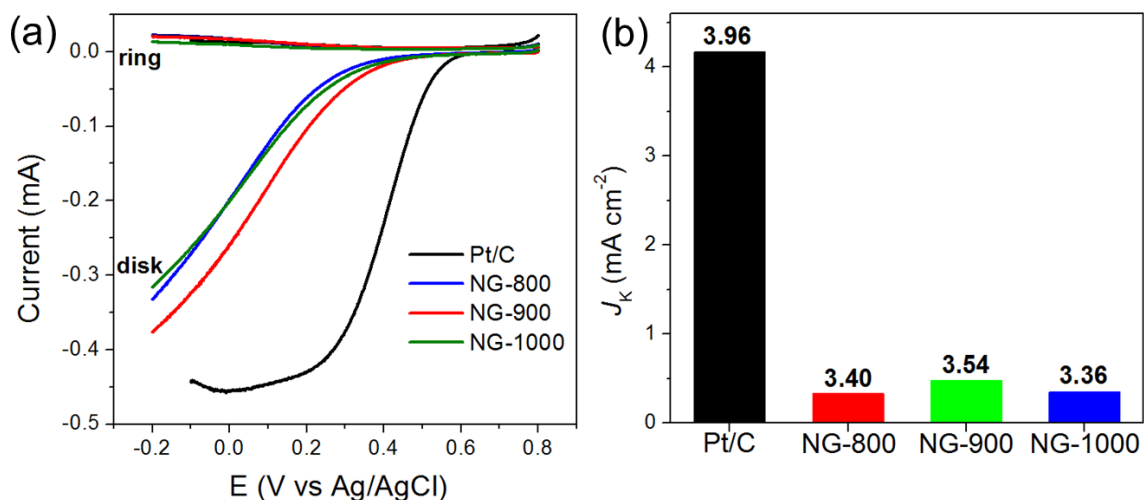


Figure 2.13 (a) RRDE polarization curves of Pt/C and NG samples in O_2 -saturated 0.5 M H_2SO_4 at a scan rate of 10 mV s^{-1} and 1600 rpm electrode rotation rate; (b) electrochemical activity given as the kinetic-limiting current density (J_K) of Pt/C and NG samples supported on GC electrodes at -0.4 V . The electron transfer number (n) in (b) was obtained from RRDE.

The electrochemical catalytic activity of NG towards ORR was further investigated in acidic conditions. To this end, the RRDE experiments in acidic conditions were performed in O_2 -saturated 0.5 M H_2SO_4 solution within the potential range of $+0.8$ to -0.2 V at a potential sweep of 10 mV s^{-1} and a ring potential of 0.1 V . As shown in Figure 2.13a, the onset potential of NG-800, NG-900 and NG-1000 were 0.25 , 0.31 and 0.27 , respectively, which is much lower than the Pt/C (0.52 V). Although, the electron transfer number (n) of NG samples in acidic conditions were similar to that of in alkaline conditions, the current density (J_K) values were significantly lower (Figure 2.13b). As mentioned earlier, Pyridinic-N bonds with two carbon atoms in the graphene plane with a lone pair of

electrons. Since the lone pair of electrons is not delocalized into the aromatic π -system, the pyridinic-N can be protonated to pyridinic-N-H (the pyridinium cation) in the acidic environment. In addition, pyridinic-N⁺-O⁻ can also be initially converted to pyridinic-N and then to pyridinic-N-H in the acidic conditions.⁴⁵ On the other hand, there is no lone pair of electrons in the graphitic-N that is bonded with three neighboring carbon atoms. Therefore, graphitic-N is less susceptible to protonation reaction. Figure 2.14 shows the schematic representation of the protonation reaction on the NG catalysts. The pyridinic-N-H group is not active for the ORR⁴⁶ and might be attributed to the significantly low catalytic activity of NG. Nevertheless, the J_K values for NG obtained in this work is well comparable with that of the nitrogen-doped CNTs in acidic medium.⁴⁴

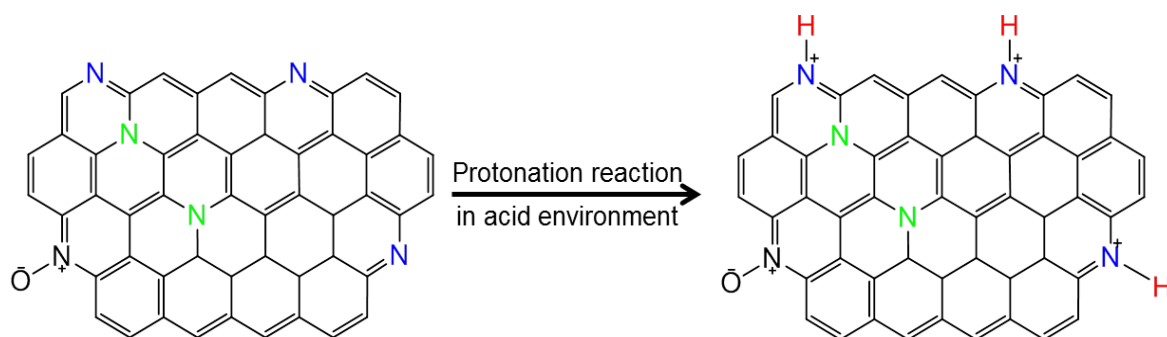


Figure 2.14 Schematic representation of the protonation reaction on the NG catalyst in the acidic conditions.

2.6 Electrochemical stability of NG

The stability of Pt/C and NG-900 electrodes towards ORR was examined by continuous potential cycling between + 0.2 and -1.2 V in O₂-saturated 0.1 M KOH electrolyte for 10,000 cycles (Figure 2.15). As indicated in Figure 2.13a, the deterioration

of the Pt/C electrode resulted in $\sim 58\%$ drop in the current density. In contrast, NG-900 showed only a slight decay of $\sim 13\%$ at -0.15 V (Figure 2.14b). Therefore, the NG-900 has higher durability for ORR than the Pt/C based catalysts.

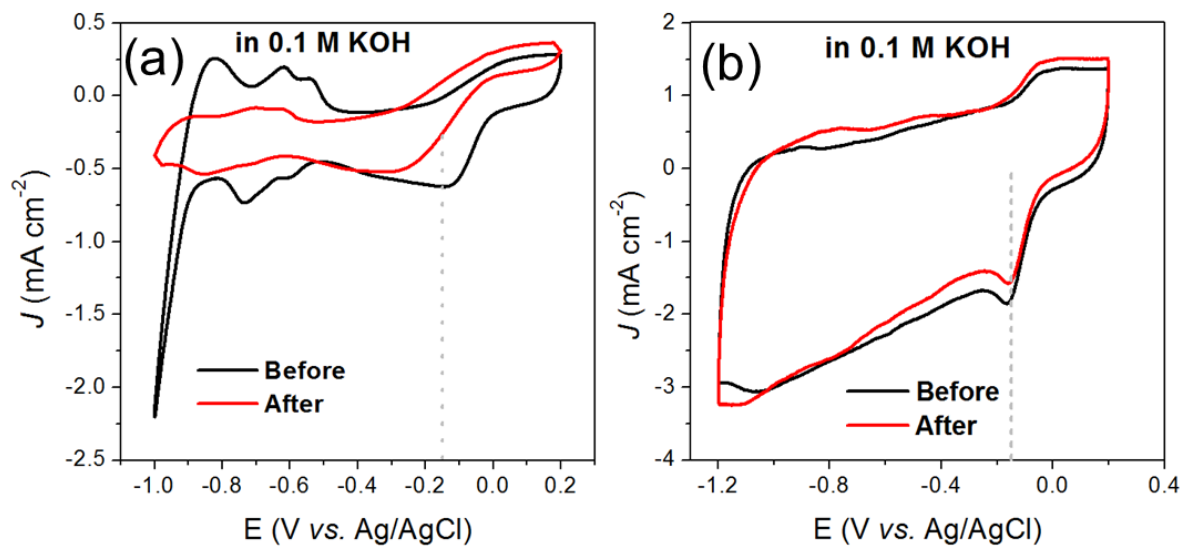


Figure 2.15 Cyclic voltammetry curves for the ORR at (a) Pt/C, (b) NG-900 electrode in O₂-saturated 0.1M KOH before and after a continuous potentiodynamic swept for 10,000 cycles at room temperature and at a scan rate of 100 mVs⁻¹. The wave like bands over -1.0 to -0.5 V seen for the pristine Pt/C electrode are attributed to the hydrogen adsorption/desorption.

2.7 Conclusion

A simple and scalable process has been demonstrated to prepare NG as a metal-free catalyst for ORR. Thermal annealing of surfactant modified GO with cyanamide at 550 °C produced graphene-carbon nitride composites, while further treatment of G-CN at 800~1000 °C resulted in NG. As-prepared NG exhibited high surface area and nitrogen content up to 12.0% after annealing. The NG prepared at 900 °C (i.e. NG-900) revealed an electron transfer number of 3.70 and high current density of 6.67 mA cm⁻² and superior durability in alkaline condition compared to that of the Pt/C (4.76 mA cm⁻²) based catalysts. In association with XPS and electrochemical performance, the high catalytic performance of NG-900 compared to that of NG-800 and NG-1000, might be attributed the higher ratio of graphitic-N over pyridinic-N where O₂ molecule is preferentially adsorbed at carbon sites when a graphitic-N is located nearby. Unfortunately, the ORR performance of NG samples was poor in the acidic conditions, due to the protonation of pyridinic-N in acidic conditions. This can be overcome by incorporating non-precious transition metal into NG and thereby forming a M-N-C based catalyst. In the next chapter we will describe the synthesis of NG/iron composites as well as their electrochemical performance towards ORR in both acidic and alkaline conditions.

2.8 Reference

- (1) Steele, B. C. H.; Heinzl, A. *Nature* **2001**, *414*, 345.
- (2) Zhu, C. Z.; Dong, S. J. *Nanoscale* **2013**, *5*, 1753.
- (3) Gong, K. P.; Du, F.; Xia, Z. H.; Durstock, M.; Dai, L. M. *Science* **2009**, *323*, 760.
- (4) Gewirth, A. A.; Thorum, M. S. *Inorg. Chem.* **2010**, *49*, 3557.
- (5) Jin, W.; Du, H.; Zheng, S. L.; Xu, H. B.; Zhang, Y. *J. Phys. Chem. B* **2010**, *114*, 6542.
- (6) Shao, Y. Y.; Liu, J.; Wang, Y.; Lin, Y. H. *J. Mater. Chem.* **2009**, *19*, 46.
- (7) Chen, W.; Chen, S. *Angew. Chem. Int. Ed.* **2009**, *48*, 4386.
- (8) Chen, W.; Kim, J. M.; Sun, S. H.; Chen, S. W. *J. Phys. Chem. C* **2008**, *112*, 3891.
- (9) Yu, D. S.; Zhang, Q.; Dai, L. M. *J. Am. Chem. Soc.* **2010**, *132*, 15127.
- (10) Feng, L. Y.; Yan, Y. Y.; Chen, Y. G.; Wang, L. J. *Energ. Environ. Sci.* **2011**, *4*, 1892.
- (11) Liu, R. L.; Wu, D. Q.; Feng, X. L.; Mullen, K. *Angew. Chem. Int. Edit.* **2010**, *49*, 2565.
- (12) Wei, W.; Liang, H.; Parvez, K.; Zhuang, X.; Feng, X.; Mullen, K. *Angew. Chem. Int. Ed.* **2014**.
- (13) Collman, J. P.; Devaraj, N. K.; Decreau, R. A.; Yang, Y.; Yan, Y. L.; Ebina, W.; Eberspacher, T. A.; Chidsey, C. E. D. *Science* **2007**, *315*, 1565.
- (14) Winther-Jensen, B.; Winther-Jensen, O.; Forsyth, M.; MacFarlane, D. R. *Science* **2008**, *321*, 671.
- (15) Qu, L. T.; Liu, Y.; Baek, J. B.; Dai, L. M. *ACS Nano* **2010**, *4*, 1321.
- (16) Wang, X. R.; Li, X. L.; Zhang, L.; Yoon, Y.; Weber, P. K.; Wang, H. L.; Guo, J.; Dai, H. J. *Science* **2009**, *324*, 768.
- (17) Lin, Y. C.; Lin, C. Y.; Chiu, P. W. *Appl. Phys. Lett.* **2010**, *96*.
- (18) Wang, Y.; Shao, Y. Y.; Matson, D. W.; Li, J. H.; Lin, Y. H. *ACS Nano* **2010**, *4*, 1790.
- (19) Shao, Y. Y.; Zhang, S.; Engelhard, M. H.; Li, G. S.; Shao, G. C.; Wang, Y.; Liu, J.; Aksay, I. A.; Lin, Y. H. *J. Mater. Chem.* **2010**, *20*, 7491.

- (20) Wei, D. C.; Liu, Y. Q.; Wang, Y.; Zhang, H. L.; Huang, L. P.; Yu, G. *Nano Lett.* **2009**, *9*, 1752.
- (21) Hummers, W. S.; Offeman, R. E. *J. Am. Chem. Soc.* **1958**, *80*, 1339.
- (22) Yan, H. J.; Chen, Y.; Xu, S. M. *Int J Hydrogen Energ.* **2012**, *37*, 125.
- (23) Yang, S. B.; Feng, X. L.; Wang, X. C.; Mullen, K. *Angew. Chem. Int. Edit.* **2011**, *50*, 5339.
- (24) Miller, D. R.; Holst, J. R.; Gillan, E. G. *Inorg. Chem.* **2007**, *46*, 2767.
- (25) Fischer, A.; Antonietti, M.; Thomas, A. *Adv. Mater.* **2007**, *19*, 264.
- (26) Fischer, A.; Muller, J. O.; Antonietti, M.; Thomas, A. *ACS Nano* **2008**, *2*, 2489.
- (27) Gomez-Navarro, C.; Meyer, J. C.; Sundaram, R. S.; Chuvilin, A.; Kurasch, S.; Burghard, M.; Kern, K.; Kaiser, U. *Nano Lett.* **2010**, *10*, 1144.
- (28) Eda, G.; Fanchini, G.; Chhowalla, M. *Nat. Nanotechnol.* **2008**, *3*, 270.
- (29) Zhang, Y. J.; Thomas, A.; Antonietti, M.; Wang, X. C. *J. Am. Chem. Soc.* **2009**, *131*, 50.
- (30) Wang, X. C.; Maeda, K.; Thomas, A.; Takanabe, K.; Xin, G.; Carlsson, J. M.; Domen, K.; Antonietti, M. *Nat. Mater.* **2009**, *8*, 76.
- (31) Guo, Q. X.; Xie, Y.; Wang, X. J.; Lv, S. C.; Hou, T.; Liu, X. M. *Chem. Phys. Lett.* **2003**, *380*, 84.
- (32) Zhao, Y. C.; Liu, Z.; Chu, W. G.; Song, L.; Zhang, Z. X.; Yu, D. L.; Tian, Y. J.; Xie, S. S.; Sun, L. F. *Adv. Mater.* **2008**, *20*, 1777.
- (33) Lee, K. R.; Lee, K. U.; Lee, J. W.; Ahn, B. T.; Woo, S. I. *Electrochem. Commun.* **2010**, *12*, 1052.
- (34) Sheng, Z. H.; Shao, L.; Chen, J. J.; Bao, W. J.; Wang, F. B.; Xia, X. H. *ACS Nano* **2011**, *5*, 4350.
- (35) Lin, Z.; Waller, G.; Liu, Y.; Liu, M.; Wong, C.-P. *Adv. Energy Mater.* **2012**, *2*, 884.
- (36) Cote, R.; Lalonde, G.; Guay, D.; Dodelet, J. P.; Denes, G. *J. Electrochem. Soc.* **1998**, *145*, 2411.
- (37) Yang, S. B.; Feng, X. L.; Ivanovici, S.; Mullen, K. *Angew. Chem. Int. Edit.* **2010**, *49*, 8408.
- (38) Chen, Z.; Higgins, D.; Tao, H. S.; Hsu, R. S.; Chen, Z. W. *J. Phys. Chem. C* **2009**, *113*, 21008.
- (39) Liu, G.; Li, X. G.; Lee, J. W.; Popov, B. N. *Catal. Sci. Technol.* **2011**, *1*, 207.

-
- (40) Rao, C. V.; Cabrera, C. R.; Ishikawa, Y. *J. Phys. Chem. Lett.* **2010**, *1*, 2622.
- (41) Kim, T. W.; Park, I. S.; Ryoo, R. *Angew. Chem. Int. Edit.* **2003**, *42*, 4375.
- (42) Geng, D. S.; Chen, Y.; Chen, Y. G.; Li, Y. L.; Li, R. Y.; Sun, X. L.; Ye, S. Y.; Knights, S. *Energ. Environ. Sci.* **2011**, *4*, 760.
- (43) Jeon, I. Y.; Yu, D. S.; Bae, S. Y.; Choi, H. J.; Chang, D. W.; Dai, L. M.; Baek, J. B. *Chem. Mater.* **2011**, *23*, 3987.
- (44) Mo, Z. Y.; Liao, S. J.; Zheng, Y. Y.; Fu, Z. Y. *Carbon* **2012**, *50*, 2620.
- (45) Liu, G.; Li, X. G.; Ganesan, P.; Popov, B. N. *Electrochim. Acta* **2010**, *55*, 2853.
- (46) Choi, C. H.; Chung, M. W.; Park, S. H.; Woo, S. I. *Rsc Adv.* **2013**, *3*, 4246.

Chapter 3

Iron incorporated nitrogen-doped graphene as non-noble metal electrocatalyst for oxygen reduction reaction (ORR)

The prohibitive cost of platinum for catalyzing the cathodic oxygen reduction reaction (ORR) has hampered the widespread use of polymer electrolyte fuel cells. In the previous chapter, we discussed the synthesis of nitrogen-doped graphene (NG) as high performance electrocatalyst for ORR in alkaline media. Unfortunately, the fabricated NG showed poor catalytic behavior in acidic condition, mostly due to the protonation by acid. To overcome the bottleneck of NG applied in acidic media, in this chapter, we describe non-precious iron (Fe) incorporated NG based catalysts. The Fe nanoparticles can be embedded into NG with the aid of Fe(III) chloride during the synthesis of NG from carbon nitride-graphene composites. Remarkably, we found that as-synthesized NG supported with 5 wt% of Fe nanoparticles displayed an excellent methanol crossover effect and high current density of 8.20 mA cm^{-2} at -0.4 V compared to Pt based catalysts (4.76 mA cm^{-2} at -0.4 V) in alkaline solution (i.e. 0.1 M KOH). Moreover, Fe-incorporated NG showed almost four-electron transfer processes and superior stability in both alkaline ($\sim 94\%$) and acidic ($\sim 85\%$) solutions, which outperformed both Pt and NG-based catalysts.

3.1 Introduction:

The performance of a carbon supported transition metal-nitrogen (M-N-C) materials (M = Fe, Co, Ni, Mn etc.) catalyst (i.e. activity, stability and selectivity) is directly related to the catalyst structure, which varies greatly according to preparation conditions, including synthesis method, metal precursor, carbon support and heat treatment.¹⁻⁴ In general, these catalysts can be prepared by thermal annealing of precursors containing nitrogen, Fe and/or Co salts adsorbed on carbon materials under optimized conditions or by direct use of Fe or Co macrocycles on carbon support. Although, Fe or Co macrocycles adsorbed on carbon black (CB) shows four-electron transfer process towards ORR in alkaline conditions,⁵⁻⁸ a major drawback of these types of catalysts is the low stability in acidic media.^{9,10} This can be attributed primarily to the loss of active sites caused by the attack of hydrogen peroxide that generates during the ORR process.¹¹⁻¹³ Therefore, significant efforts have been undertaken to replace the expensive macrocycles by combining nitrogen-containing compounds and Fe or Co inorganic salts with carbon supports, which exhibited considerable improvements in ORR activity but relatively little progress in stability.¹⁴⁻¹⁷ Moreover, the most commonly used carbon supports such as, CB suffer from gasification in presence of NH_3 when the pyrolysis temperature is higher than 800 °C, resulting in mass loss of carbon and consequently shortens the lifespan of these catalysts.^{18,19} Besides the preparation methods of the catalysts, proper metal-nitrogen coordination is of great concern for achieving active M-N-C catalysts with high performance.^{10,20,21} The content and relative ratios among different types of doped nitrogen in both Fe and Co based catalysts can be controlled by tuning the heat-treatment temperature.²²⁻²⁴ Although the nature of the active ORR catalytic sites in M-N-C catalysts continues to be at the center of an ongoing

debate,^{5,21,25,26} experimental results indicate that the presence of Fe or Co can indeed drastically affect the electrochemical properties of nitrogen doped carbon.^{27,28}

As discussed in the last chapter, NG has been shown to possess high electrocatalytic activity and long-term durability when catalyzing the ORR in alkaline conditions.¹⁷ The high surface area of NG provides abundant active sites for coordination with transition metals, which may lead to synergistic properties from both components and thus enhanced electrochemical performance towards ORR. However, there is only handful of studies on the optimization and investigation of the metal content on M-N-C based catalysts as well as their electrocatalytic performance for ORR.

In Chapter 2, we describe a facile approach to synthesize NG with controllable nitrogen contents. Although, the catalytic performance of NG was significantly higher than that of Pt/C in alkaline conditions, they exhibited low activity in acidic media. Therefore, we turn our attention to fabricating metal incorporated NG given that high content of pyridinic-N sites in NG is highly beneficial for coordinating transition metals. To this end, we extend our synthetic approach to the successful incorporation of non-precious metal Fe into NG which is named as NG/Fe_x. The optimization of preparation of NG/Fe_x catalysts as well as their detailed electrocatalytic studies will be presented. Notably, NG/Fe_x containing only 5.0 wt% of Fe exhibits four-electron transfer processes, excellent methanol crossover effect and superior stability in both alkaline (~ 94%) and acidic (~ 85%) solutions, which outperform both Pt and NG-based catalysts. These traits represent clear advantages over commercially available Pt/C based for the fuel cells.

3.2 Synthesis of NG/Fe_x composites

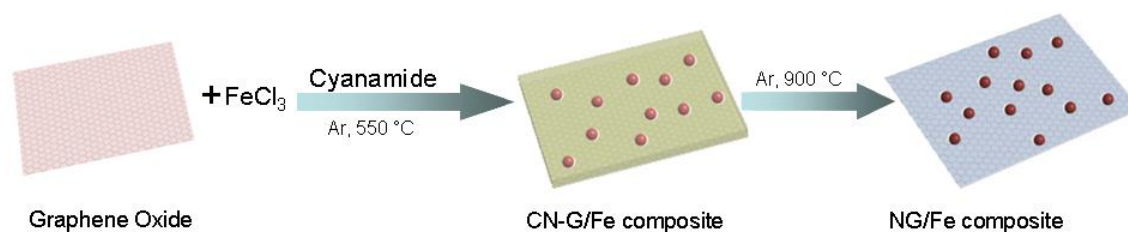


Figure3.1 Schematic illustration of the preparation of NG and Fe nanoparticle composite.

The NG decorated with Fe nanoparticles was prepared by mixing FeCl₃ with the precursors GO and cyanamide followed by high temperature treatment (Figure3.1). Briefly, desired amount (*i.e.* 2, 5, 10 and 15 mg) of FeCl₃ was added into 100 mg of aqueous GO dispersion (1 mg mL⁻¹). The mixture was sonicated for 1 h. The content of Fe (*i.e.* 2.0, 5.0, 10.0 and 15.0 wt%) in the composites was calculated with respect to the total mass of GO into the dispersion. Subsequently, 4 mL of cyanamide solution was added dropwise. The reaction mixture was heated at 100 °C with continuous stirring to remove water. The resulting solid was then calcined at 550 °C for 4 h to form carbon nitride (CN) and subjected to pyrolysis at 800, 900, and 1000 °C, respectively for 1 h to decompose the CN. All the annealing processes were carried under argon atmosphere. NG samples with different Fe content were prepared in this work and are denoted as NG/Fe_x (where x = 2.0, 5.0, 10.0 and 15.0 wt%).

3.3 Structure and morphology of NG/Fe_x composites

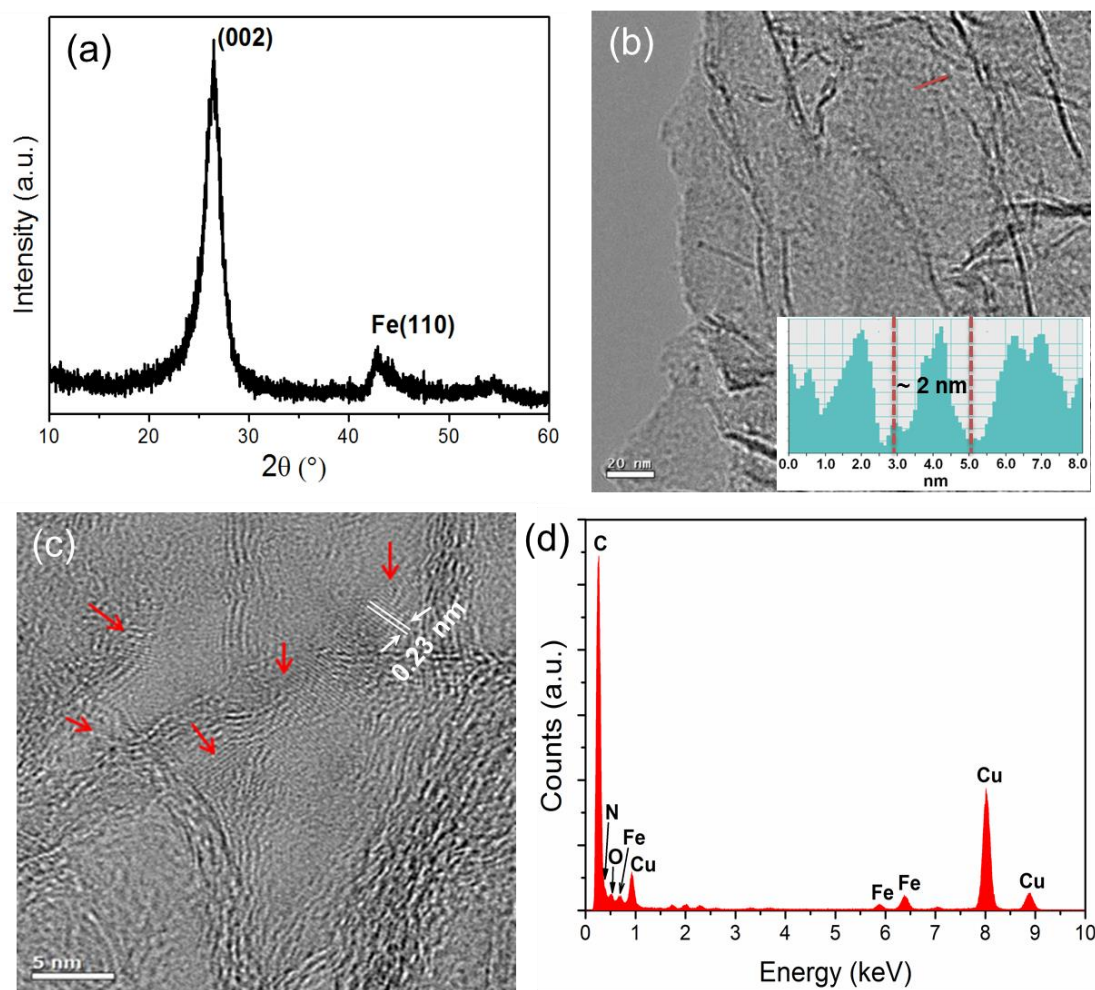


Figure 3.2(a) XRD pattern of NG/Fe_{5.0} composite; (b) TEM image of NG/Fe_{5.0} with particle size distribution of the area indicated by small red line (inset); (c) HRTEM images of NG/Fe_{5.0} showing the presence of crystalline Fe nanoparticles (indicated by arrows) on NG; (d) corresponding EDX spectra of NG/Fe_{5.0}.

Figure 3.2a represents the X-ray diffraction pattern (XRD) pattern of NG/Fe_{5.0}. The diffraction peak at 42.8° is characteristic for Fe(110). In addition, HRTEM images display

the presence of small (2-4 nm) crystalline Fe nanoparticles on NG with a lattice d-spacing of ~ 0.23 nm, which is slightly larger than the standard value of 0.203 nm (JCPDS database) (Figure 3.2b and c). The increased d-spacing value may be attributed to Fe nanoparticles incorporated into the nitrogen lattice, which enlarges the lattice constant.²⁹ The presence of N and Fe in the composite can be further validated by the corresponding energy dispersive spectra (EDX) (Figure 3.2d).

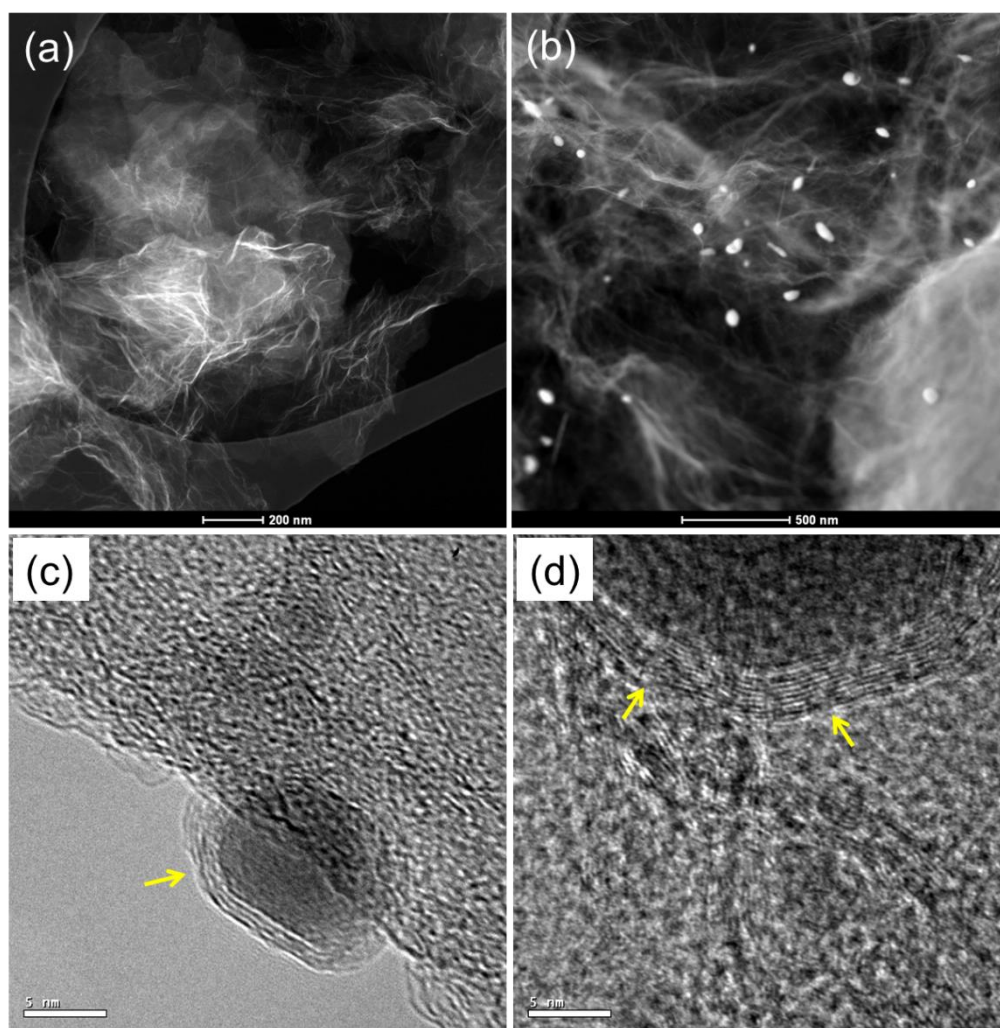


Figure 3.3 (a) and (b) Dark field TEM images of NG/Fe_{5.0} and NG/Fe_{15.0}, respectively. (c) and (d) HRTEM images of the NG/Fe_{15.0} indicating well-defined graphitic nanoshells (yellow colored arrows) encapsulated large Fe nanoparticles.

The dark field TEM images in Figure 3.3 reveal that, increasing the Fe content to 15.0 wt% (*i.e.* NG/Fe_{15.0}) results in the agglomeration of ~50 nm Fe nanoparticles. As evident from HRTEM images in Figure 3.3c and d, these large nanoparticles are encapsulated in well-defined graphitic carbon nanoshells. In contrast, no large nanoparticles are identified in NG/Fe_{5.0} (Figure 3.3a and 3.2b). As shown in Figure 3.4a, NG/Fe_{5.0} revealed a BET surface area of 317 m² g⁻¹. Although the surface area of iron incorporated NG is lower than that of NG (*i.e.* 508 m² g⁻¹), it is significantly higher than that of Fe supported NG (*i.e.* 110 m² g⁻¹) reported previously.³⁰ In addition, a narrow pore-size distribution centered at about 3.1 nm and a total pore volume of 1.11 cm³ g⁻¹ can be derived from the adsorption branch of the isotherms based on Barrett-Joyner-Halenda (BJH) model (Figure 3.4b).

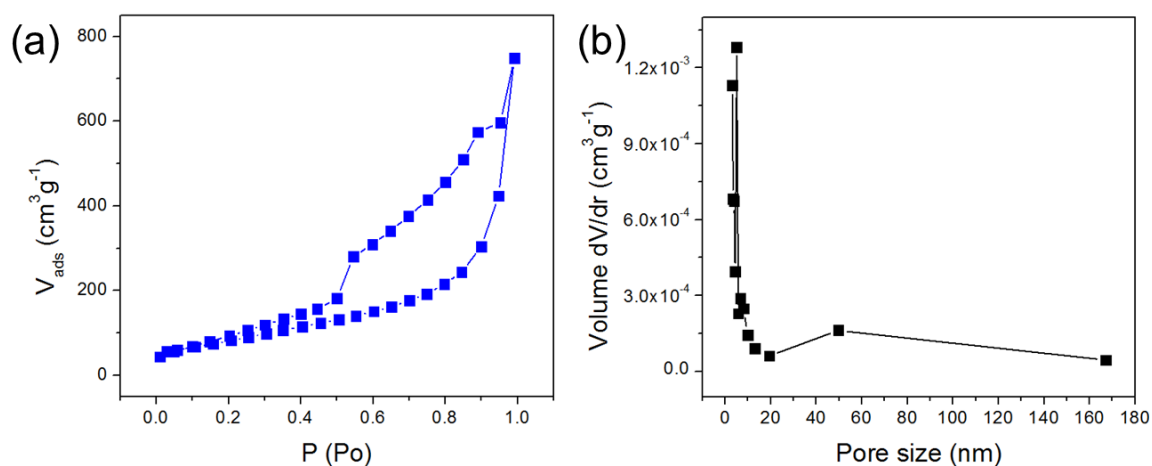


Figure 3.4 (a) Nitrogen adsorption-desorption isotherm and (b) pore-size distribution of NG/Fe_{5.0}.

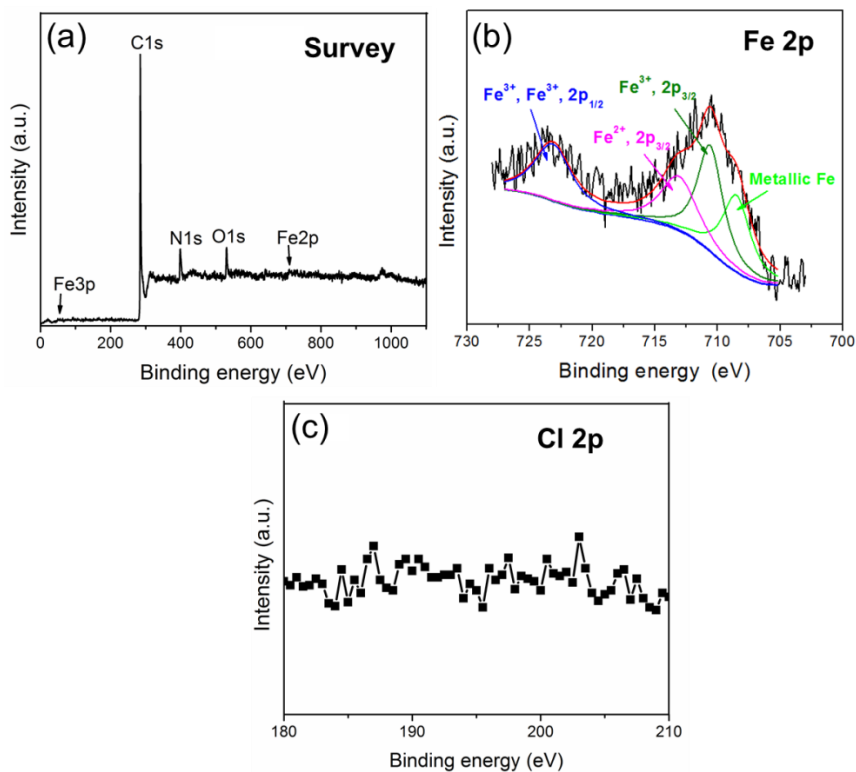


Figure 3.5 XPS spectra of NG/Fe_{5.0} where, (a) survey; (b) Fe 2p and (c) Cl 2p binding energy regions.

To investigate the structure of NG/Fe_x catalysts, X-ray photoelectron spectroscopy (XPS) measurements were carried out. The XPS survey spectra of NG/Fe_{5.0} show the presence of Fe 2p and Fe 3p, in addition to N 1s, C 1s, and O 1s peaks (Figure 3.5a). As presented in Figure 3.5b, the Fe 2p spectrum can be deconvoluted into four peaks, for which the peaks at 710.7 and 713.6 eV can be assigned to the binding energy of 2p_{3/2} of Fe³⁺ and Fe²⁺ ions, respectively.^{31,32} The peak at 723.5 eV corresponds to the binding energies of 2p_{1/2} of both Fe²⁺ and Fe³⁺ ions.³³ These results indicate that the Fe²⁺ and Fe³⁺ co-exist in the NG/Fe_x catalysts. Unfortunately, the Fe 3p peak (~ 52-56 eV) is too weak to be determined. Nevertheless, the formation of small crystalline Fe nanoparticles in NG/Fe_x

composites might be explained as: when the cyanamide and Fe^{3+} adsorbed GO is slowly heated up to 550 °C, cyanamide starts to polymerize. The reaction is a combination of polyaddition and polycondensation where the precursors are first condense towards melamine. The second step is a condensation where ammonia is eliminated. Up to 350 °C, melamine based products are found, while tri-s-triazine (i.e. melem) forms via melamine rearrangements at ~ 335 °C.³⁴ Condensation of this unit to polymers occurs around the Fe^{3+} ions adsorbed on graphene and potentially the final polymeric CN occurs at around 550 °C.³⁵ The distance of the nitride pores is ~0.681 nm, which is sufficient to hold Fe^{3+} ions inside.³⁴ Therefore, Fe^{3+} ions are embedded into pores of CN structure and thus preventing the formation of large, aggregated Fe nanoparticles (Figure 3.6).

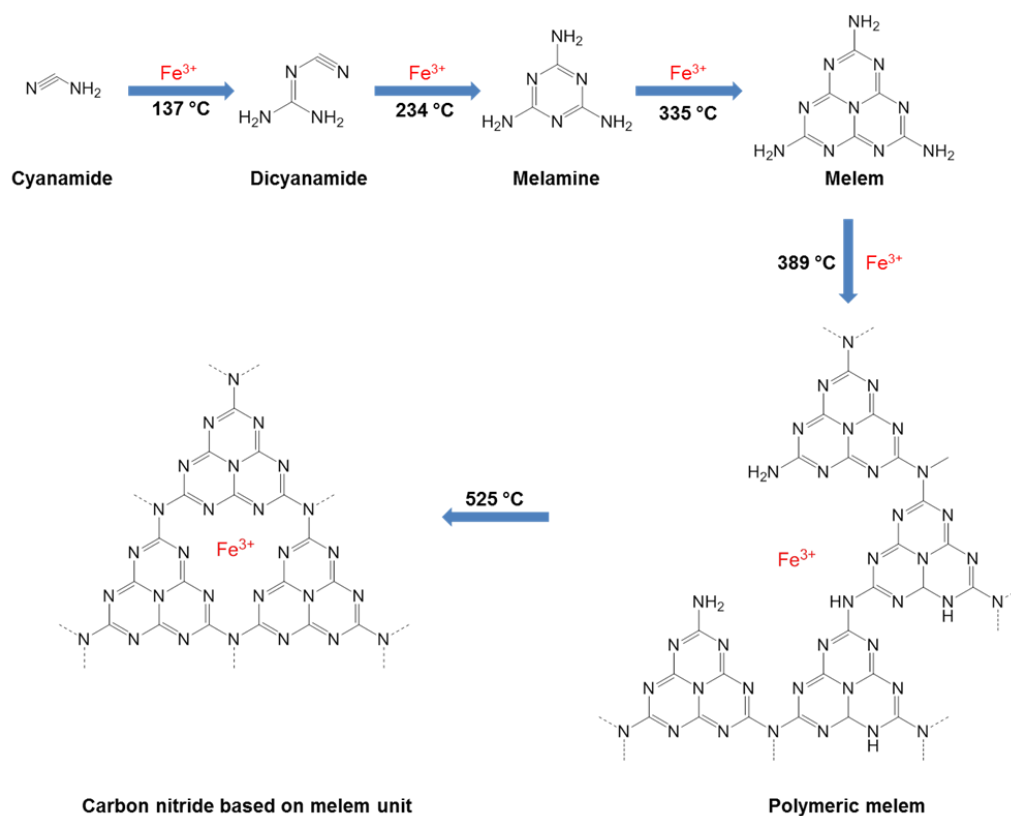


Figure 3.6 Proposed reaction mechanism of the formation of carbon nitride (CN) in presence of iron chloride (FeCl_3).

3.4 Electrochemical property of NG/Fe_x composites

3.4.1 Alkaline conditions

The catalytic properties of NG/Fe_x samples were first assessed with cyclic voltammetry (CV) in a 0.1 M KOH solution. The NG/Fe_{5.0} shows a featureless voltammetric current within the potential range of -1.2 to +0.2 V in an Ar-saturated alkaline solution (Figure 3.7). Saturating the electrolyte with O₂ results in a well-defined cathodic peak centered at ~ 0.20 V that emerges in the CV, suggesting a pronounced electrocatalytic activity of NG/Fe_{5.0} for oxygen reduction. Remarkably, when the CV measurement of NG/Fe_{5.0} was carried out in an O₂ saturated alkaline solution in the presence of 3.0 M methanol, no current drop can be identified, indicating that the catalyst has high stability against crossover effects. Two additional peaks are observed at -0.61 and -0.93 V, which are associated with the reversible redox reaction of the iron nanoparticles.³⁶

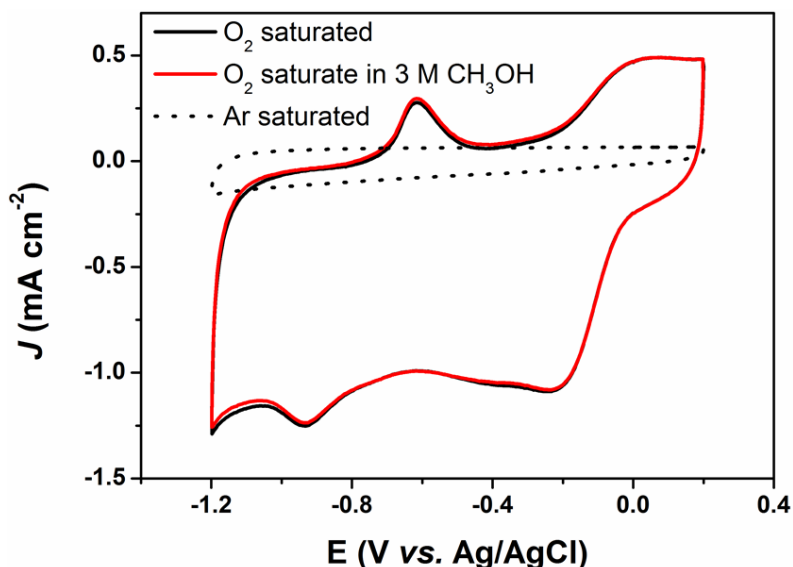


Figure 3.7 Cyclic voltammogram of NG/Fe_{5.0} in O₂ and Ar-saturated 0.1 M KOH, as well as O₂ saturated 0.1 M KOH solution with 3 M CH₃OH.

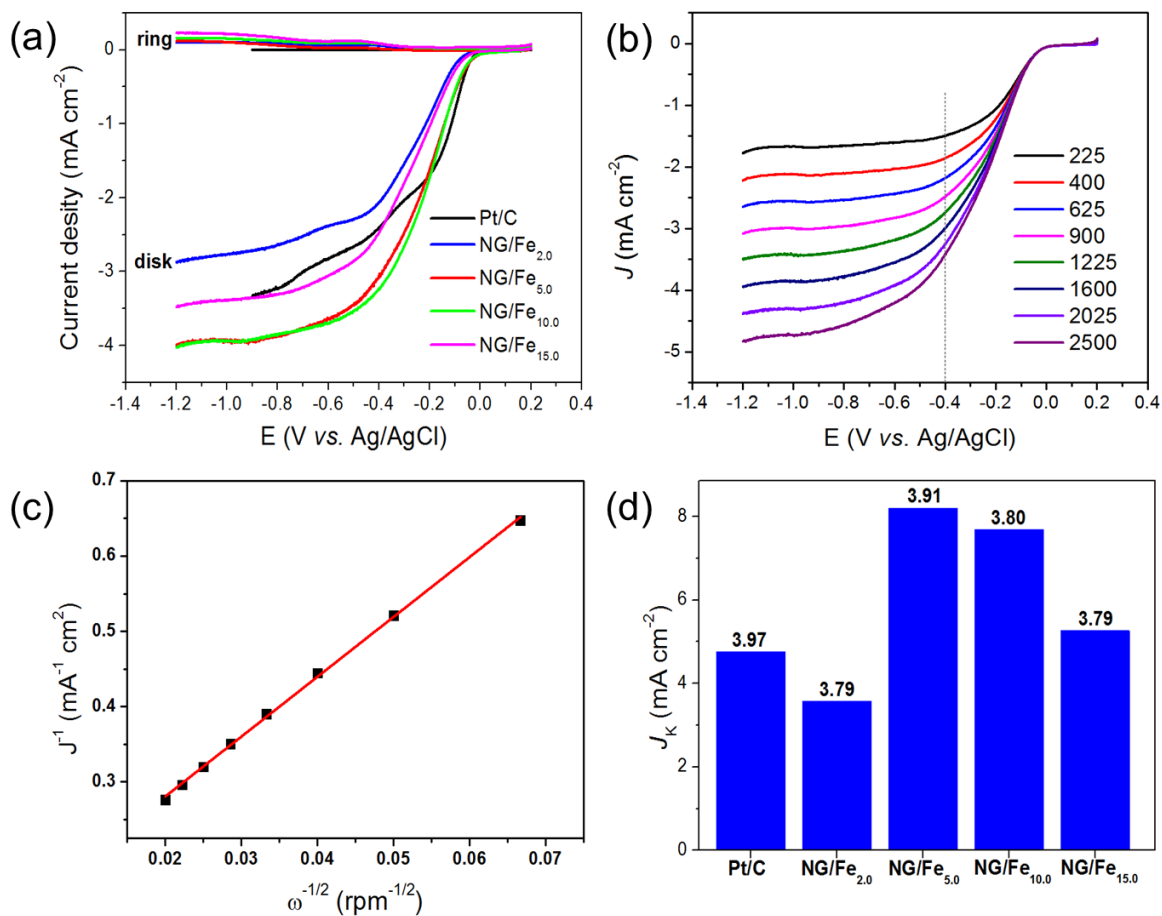


Figure 3.8 (a) RRDE polarization curves of Pt/C and NG/Fe_x samples in O₂-saturated 0.1 M KOH at a scan rate of 10 mVs⁻¹ and 1600 rpm electrode rotation rate; (b) RDE voltammograms recorded for NG/Fe_{5.0} supported on a glassy carbon (GC) electrode at a scan rate of 10 mVs⁻¹ and different rotation rates; (c) Koutecky-Levich plot of J^{-1} vs. $\omega^{-1/2}$ at -0.4 V using the data obtained from (b); and (d) electrochemical activity given as the kinetic-limiting current density (J_k) of the NG/Fe_x series supported on GC electrodes at -0.4 V.

The electrochemical behavior of NG/Fe_x catalysts with various content of Fe (i.e. 2.0, 5.0, 10.0 and 15.0 wt%) nanoparticles were further assessed by both rotating ring disk electrodes (RRDE) and rotating disk electrodes (RDE). Figure 3.8a shows the RRDE

polarization curves of NG/Fe_x composites supported on a glassy carbon electrode in O₂ saturated 0.1 M KOH. The electron transfer number for NG/Fe_x samples, at the potential of -0.4 V, was calculated to be 3.79, 3.91, 3.80, and 3.79 for the NG/Fe_{2.0}, NG/Fe_{5.0}, NG/Fe_{10.0}, and NG/Fe_{15.0}, respectively. Apparently, compared to NG itself, the incorporation of Fe nanoparticles greatly enhanced the electrochemical performance leading to the mainly four electron transfer process towards ORR.

Although the onset potential for the ORR at the NG/Fe_{5.0} electrode is similar (*i.e.* -0.04 V) to that of Pt/C, the reduction current is significantly higher (Figure 3.8a). Moreover, the calculated kinetic current density (J_K) value of NG/Fe_{2.0}, NG/Fe_{5.0}, NG/Fe_{10.0}, and NG/Fe_{15.0} is 3.57, 8.20, 7.69, and 5.26 mA cm⁻² at -0.4 V, respectively (Figure 3.8d). This result suggests that increasing the Fe content leads to an increase in the concentration of active catalytic sites until all pyridinic-N is coordinated (at 5.0 wt%). Increasing the Fe content further from 5.0 wt% to 10.0 and 15.0 wt% produces large Fe metal (and/or carbide) particles (~50 nm) that induce graphitization around them (as evident from Figure 3.3b).^{3,37} These large Fe nanoparticles do not provide any additional catalytic sites and therefore, catalytically inactive towards ORR.³⁸ Nevertheless, increasing the Fe content from 5.0 wt% to 10.0 and 15.0 wt% produces uncoordinated large metal particles (~50 nm) as evident from Figure 3.3b, which do not provide additional catalytic sites.³⁹ Therefore, no enhancement of the current density or electron transfer number was observed for NG/Fe_{10.0} and NG/Fe_{15.0}. It is remarkable to note that NG/Fe_{5.0} has a current density almost two times higher than that of Pt/C (4.76 mA cm⁻²). The current density achieved in this work is of the highest value reported on Fe and/or Co macrocycles and metal incorporated graphene based catalysts for ORR.^{30,40,41}

3.4.2 Effect of annealing temperature

To further investigate the effect of annealing temperature on the ORR process, another set of NG/Fe_{5.0} samples was prepared by annealing at 800 °C and 1000 °C. Similar to the NG/Fe_{5.0} prepared at 900 °C, they also revealed the presence of 2 – 6 nm sized crystalline Fe nanoparticles (Figure 3.9). Figure 3.10 shows the summarized results of electron transfer number and J_K values obtained from both RRDE and RDE measurements. The catalytic performance of NG/Fe_{5.0} prepared at 800 °C and 1000 °C (Figure 3.10b) is slightly lower than that of NG/Fe_{5.0} prepared at 900 °C (Figure 3.8d), suggesting that the oxygen reduction rate increases with heat treatment temperature of the catalysts, reaching a plateau at ≤ 1000 °C.^{42,43} As discussed in Chapter 2 (Figure 2.8 and 2.9), the NG synthesized at 800 °C has a higher content of pyridinic-N (i.e. 7.92%) than the NG samples prepared at 900 and 1000 °C (1.47 and 1.14%, respectively). Therefore, it is expected that NG/Fe_{5.0} prepared at 800 °C would result in high catalytic activity towards ORR. However, the catalytic performance of NG/Fe_{5.0} prepared at 800 °C was lower than that of the NG/Fe_{5.0} prepared at 900 and 1000 °C. One can conclude that the higher content of pyridinic-N alone (at lower temperature) does not necessarily lead to high catalytic performance. Instead, the temperature for catalyst preparation also plays an important role in the synergistic coupling between Fe (a non-noble metal) and nitrogen.

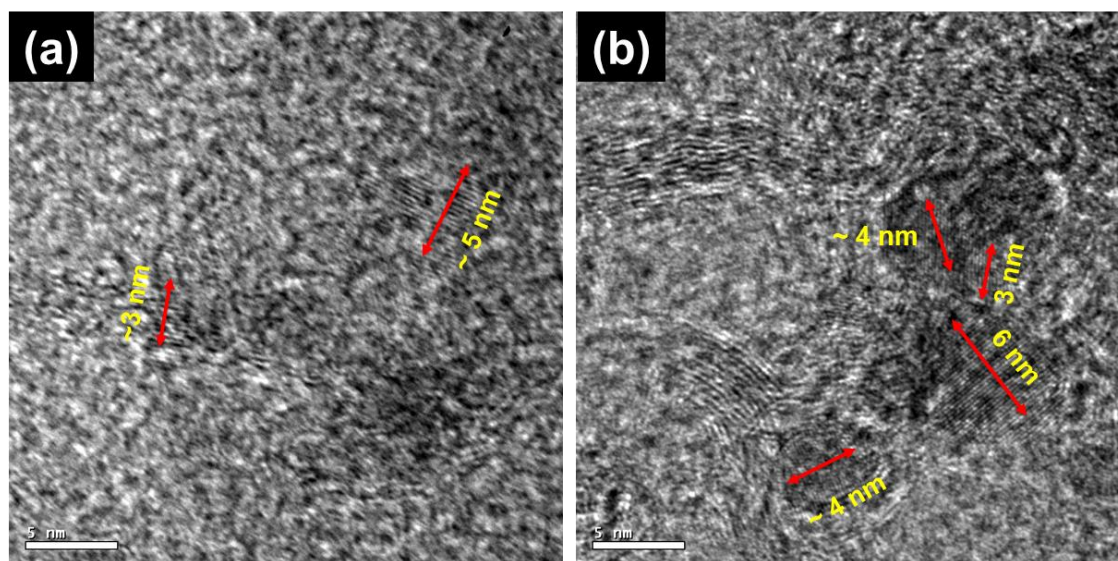


Figure 3.9 HRTEM images of NG/Fe_{5.0} samples prepared by annealing at (a) 800 °C and; (b) 1000 °C, respectively. Crystalline Fe nanoparticles with size distributions are indicated by arrows.

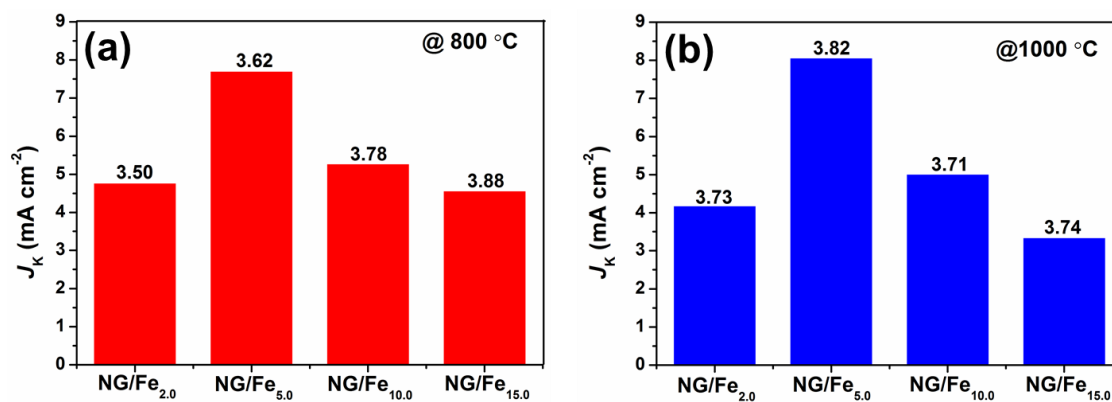


Figure 3.10 Electrochemical activity given as the kinetic-limiting current density (J_k) obtained from RDE curves at -0.4V in O₂-saturated 0.1M KOH solution for NG/Fe_x series obtained at (a) 800 °C and, (b) 1000 °C, respectively. The electron transfer number (n) was obtained from RRDE curves.

3.4.3 Acidic conditions

Next, the activity of NG/Fe_x hybrids in acidic media was examined. Both RRDE and RDE measurements were carried out in 0.5M H₂SO₄ solution (Figure 3.11a and b). All four NG samples containing 2.0, 5.0, 10.0 and 15.0 wt% of Fe nanoparticles again showed higher electron transfer numbers compared to NG (discussed in Chapter 2) samples at the potential of 0.2V vs Ag/AgCl. At 1600 rpm, NG/Fe_{5.0} prepared at 900 °C exhibited a maximum J_K of about 1.47 mA cm⁻² with almost four-electron transfer ($n = 3.82$) process and the lowest onset potential (0.47V vs Ag/AgCl). Although, the electron transfer number of NG/Fe_x catalysts in acidic medium was similar to that of the alkaline medium, the current density was significantly lower in acidic conditions.

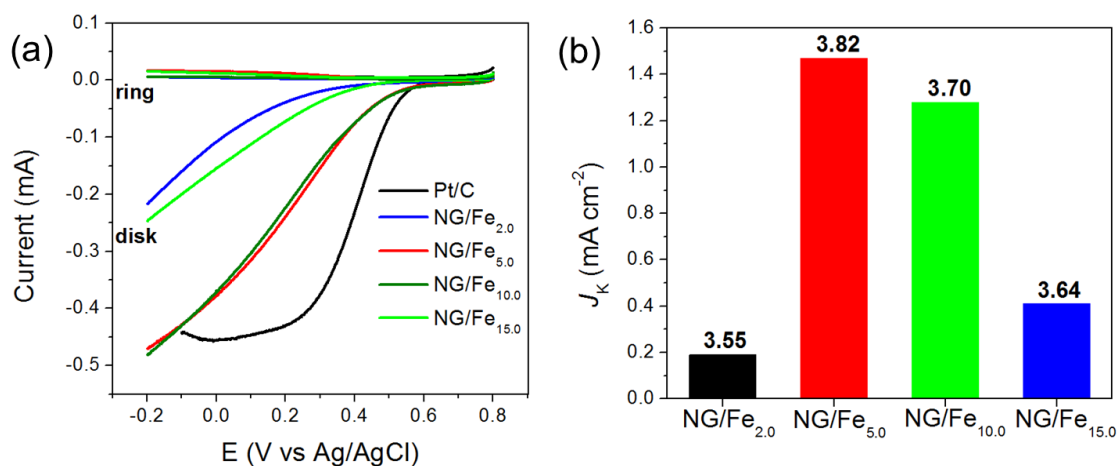


Figure 3.11 (a) RRDE curves of Pt/C and NG/Fe_x electrocatalyst series in O₂-saturated 0.5 M H₂SO₄ at a scan rate of 10 mV s⁻¹ and 1600 rpm electrode rotation rate; (b) electrochemical activity given as the kinetic-limiting current density (J_K) of NG/Fe_x series supported on GC electrodes at 0.2 V. The electron transfer number (n) was obtained from RRDE.

To examine the influence of any un-coordinated Fe (*i.e.* Fe residues) in the NG/Fe_x composites on the electrocatalytic performance, NG/Fe_{5.0} was first treated in 2M H₂SO₄ at 80 °C for 3 h and again subjected to ORR measurements in alkaline and acidic solutions. Remarkably, the acid treated NG/Fe_{5.0} displayed almost the same ORR catalytic activity with untreated NG/Fe_{5.0} in both acidic and alkaline media (Figure 3.12). This result suggests that Fe residues do not significantly contribute to the ORR performance.

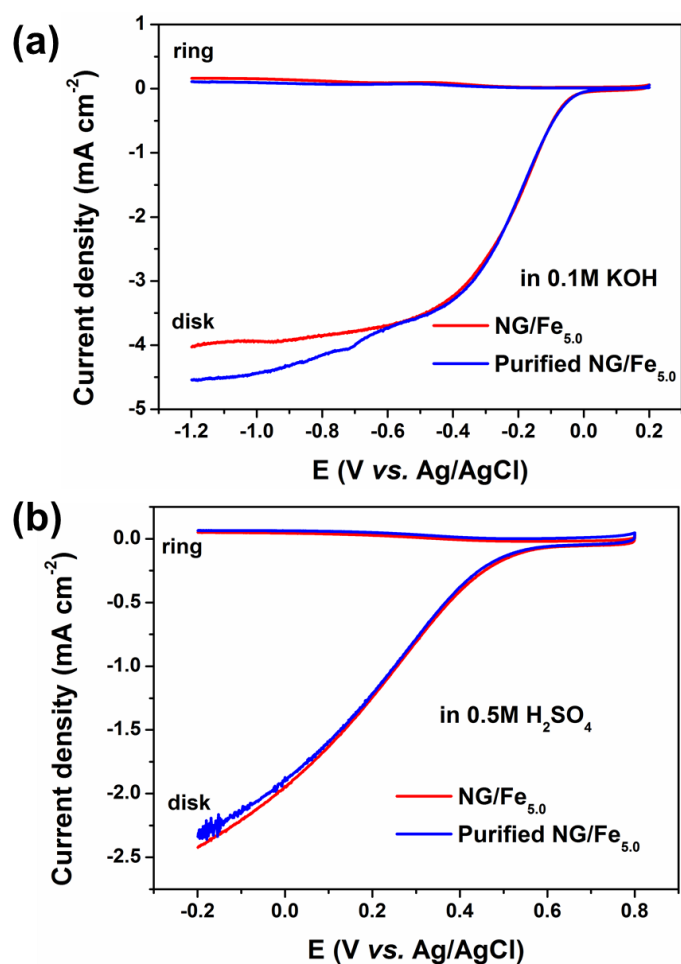


Figure 3.12 RRDE Polarization curves of purified and unpurified NG/Fe_{5.0} in O₂-saturated (a) 0.1 M KOH and (b) 0.5 M H₂SO₄ solution at a rotation rate of 1600 rpm.

3.5 Stability of NG/Fe_x composites

The stability of NG/Fe_{5.0} in alkaline solution towards the ORR was first evaluated by continuous potential cycling between +0.2 to -1.2 V in O₂ saturated 0.1M KOH for 10,000 cycles (Figure 3.12a). The NG/Fe_{5.0} catalyst prepared at 900 °C, exhibited only a slight decay of current density~ 6% at -0.15 V (Figure 3.12a). As shown in Figure 2.14a in Chapter 2, the deterioration of the Pt/C electrode resulted in a ~ 58% drop in current density. The voltammetric response of the electrodes remained unchanged after the continuous potential cycles. In contrast, only ~ 15% decay in the current density (at 0.38V) was observed for NG/Fe_{5.0} in acidic medium after 10,000 cycles (Figure 3.13b). Thereby, it can be concluded that NG/Fe_{5.0} exhibits superior durability over Pt/C based catalysts.

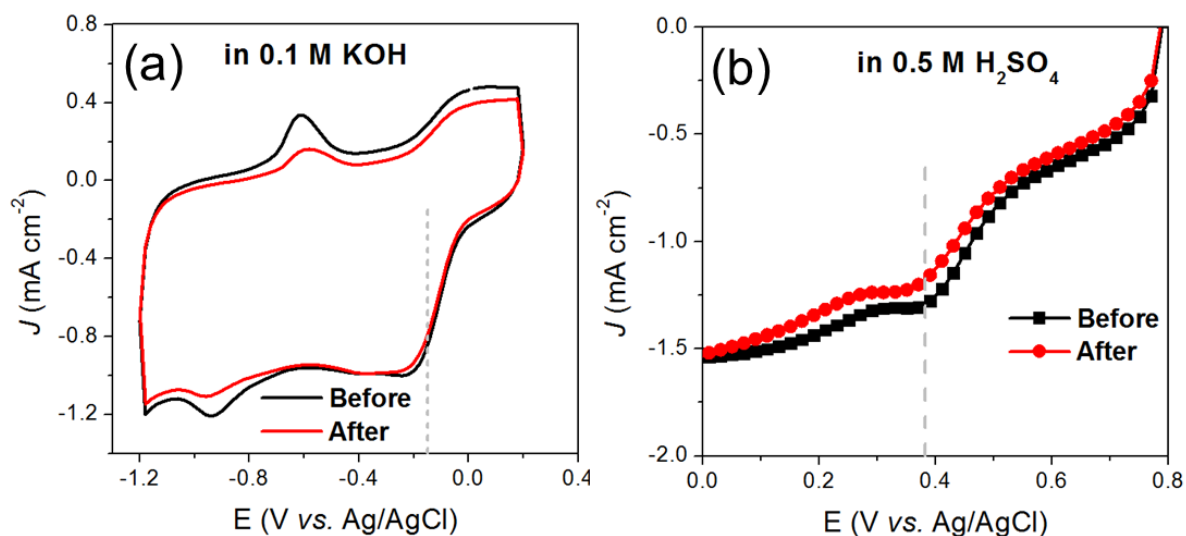


Figure 3.13 Cyclic voltammetry for the ORR at NG/Fe_{5.0} electrode in O₂-saturated (a) 0.1 M KOH and; (b) 0.5 M H₂SO₄ before and after continuous potentiodynamic swept for 10,000 cycles at room temperature and at a scan rate of 100 mVs⁻¹.

3.6 Conclusion

In summary, iron (Fe) nanoparticle decorated NG has been successfully prepared with the aid of Fe salt during the synthesis of NG from carbon nitride-graphene composites. Pyrolysis of Fe salt with CN-G composites at high temperature (≥ 800 °C) resulted in 2-4 nm size crystalline Fe incorporated NG. It is also found that the increasing the Fe content causes the formation of large (~ 50 nm) and aggregated Fe nanoparticles and does not necessarily enhance the catalytic performance. The NG supported with only 5 wt% Fe nanoparticles (i.e. NG/Fe_{5.0}) displayed stable methanol cross-over effect, almost four electron transfer process. Moreover, NG/Fe_{5.0} exhibited two times higher current density than that of Pt/C in alkaline condition and also is the highest value reported for Fe-N-C based catalysts. To confirm the catalytic effect of any Fe residues, acid leaching of NG/Fe_x was performed. However, no significant change in the catalytic performance was observed. Nevertheless, NG/Fe_x showed pronounced catalytic behavior in acidic condition towards ORR, with excellent durability compared to both commercial Pt/C and NG in both alkaline and acidic conditions. Therefore, the synthesized Fe-N-C based catalysts discussed in this chapter hold an enormous promise for their practical application in alkaline fuel cells. However, the current density of NG/Fe_x catalysts is still poor acidic media. In addition to different Fe based precursors for further optimization, Co based NG composites also needs to be investigated to improve the catalytic performance in acidic condition. Moreover, the surface area of the catalysts can be increased by the formation three-dimensional (3D) graphene networks which would allow the utilization of the unique features of graphene sheets, such as their rich macroporosity and multidimensional electron transport pathway.

3.7 References

- (1) Ohms, D.; Herzog, S.; Franke, R.; Neumann, V.; Wiesener, K.; Gamburgcev, S.; Kaisheva, A.; Iliev, I. *J. Power Sources* **1992**, *38*, 327.
- (2) Fournier, J.; Lalande, G.; Cote, R.; Guay, D.; Dodelet, J. P. *J. Electrochem. Soc.* **1997**, *144*, 218.
- (3) Faubert, G.; Cote, R.; Dodelet, J. P.; Lefevre, M.; Bertrand, P. *Electrochim. Acta* **1999**, *44*, 2589.
- (4) Maldonado, S.; Stevenson, K. J. *J. Phys. Chem. B* **2004**, *108*, 11375.
- (5) Wu, G.; More, K. L.; Johnston, C. M.; Zelenay, P. *Science* **2011**, *332*, 443.
- (6) Gupta, S.; Tryk, D.; Bae, I.; Aldred, W.; Yeager, E. *J. Appl. Electrochem.* **1989**, *19*, 19.
- (7) Schulenburg, H.; Stankov, S.; Schunemann, V.; Radnik, J.; Dorbandt, I.; Fiechter, S.; Bogdanoff, P.; Tributsch, H. *J. Phys. Chem. B* **2003**, *107*, 9034.
- (8) Li, W. M.; Yu, A. P.; Higgins, D. C.; Llanos, B. G.; Chen, Z. W. *J. Am. Chem. Soc.* **2010**, *132*, 17056.
- (9) Zhang, L.; Zhang, J. J.; Wilkinson, D. P.; Wang, H. J. *J. Power. Sources* **2006**, *156*, 171.
- (10) Bashyam, R.; Zelenay, P. *Nature* **2006**, *443*, 63.
- (11) Wang, B. *J. Power Sources* **2005**, *152*, 1.
- (12) Liu, H. S.; Song, C. J.; Tang, Y. H.; Zhang, J. L.; Zhang, H. J. *Electrochim. Acta* **2007**, *52*, 4532.
- (13) Fierro, C.; Anderson, A. B.; Scherson, D. A. *J. Phys. Chem.* **1988**, *92*, 6902.
- (14) Yuasa, M.; Yamaguchi, A.; Itsuki, H.; Tanaka, K.; Yamamoto, M.; Oyaizu, K. *Chem. Mater.* **2005**, *17*, 4278.
- (15) Yuan, X. X.; Zeng, X.; Zhang, H. J.; Ma, Z. F.; Wang, C. Y. *J. Am. Chem. Soc.* **2010**, *132*, 1754.
- (16) Bezerra, C. W. B.; Zhang, L.; Lee, K. C.; Liu, H. S.; Zhang, J. L.; Shi, Z.; Marques, A. L. B.; Marques, E. P.; Wu, S. H.; Zhang, J. J. *Electrochim. Acta* **2008**, *53*, 7703.
- (17) Parvez, K.; Yang, S. B.; Hernandez, Y.; Winter, A.; Turchanin, A.; Feng, X. L.; Mullen, K. *ACS Nano* **2012**, *6*, 9541.

- (18) Lefevre, M.; Dodelet, J. P. *Electrochim. Acta* **2008**, *53*, 8269.
- (19) Jaouen, F.; Lefevre, M.; Dodelet, J. P.; Cai, M. *J. Phys. Chem. B* **2006**, *110*, 5553.
- (20) Wu, Z. S.; Chen, L.; Liu, J.; Parvez, K.; Liang, H.; Shu, J.; Sachdev, H.; Graf, R.; Feng, X.; Mullen, K. *Adv. Mater.* **2013**.
- (21) Lefevre, M.; Proietti, E.; Jaouen, F.; Dodelet, J. P. *Science* **2009**, *324*, 71.
- (22) Wu, G.; Mack, N. H.; Gao, W.; Ma, S. G.; Zhong, R. Q.; Han, J. T.; Baldwin, J. K.; Zelenay, P. *ACS Nano* **2012**, *6*, 9764.
- (23) Wu, G.; Johnston, C. M.; Mack, N. H.; Artyushkova, K.; Ferrandon, M.; Nelson, M.; Lezama-Pacheco, J. S.; Conradson, S. D.; More, K. L.; Myers, D. J.; Zelenay, P. *J Mater. Chem.* **2011**, *21*, 11392.
- (24) Wu, G.; Nelson, M. A.; Mack, N. H.; Ma, S. G.; Sekhar, P.; Garzon, F. H.; Zelenay, P. *Chem. Commun.* **2010**, *46*, 7489.
- (25) Matter, P. H.; Zhang, L.; Ozkan, U. S. *J. Catal.* **2006**, *239*, 83.
- (26) Nallathambi, V.; Lee, J. W.; Kumaraguru, S. P.; Wu, G.; Popov, B. N. *J. Power Sources* **2008**, *183*, 34.
- (27) Ozaki, J.; Tanifuji, S.; Furuichi, A.; Yabutsuka, K. *Electrochim. Acta* **2010**, *55*, 1864.
- (28) Zhang, H. J.; Jiang, Q. Z.; Sun, L. L.; Yuan, X. X.; Shao, Z. P.; Ma, Z. F. *Int. J. Hydrogen Energ.* **2010**, *35*, 8295.
- (29) Herzog, B.; Herein, D.; Schlogl, R. *Appl. Catal. a-Gen.* **1996**, *141*, 71.
- (30) Wu, Z. S.; Yang, S. B.; Sun, Y.; Parvez, K.; Feng, X. L.; Mullen, K. *J. Am. Chem. Soc.* **2012**, *134*, 9082.
- (31) Siriwardane, R. V.; Cook, J. M. *J. Colloid. Interf. Sci.* **1985**, *108*, 414.
- (32) Marcus, P.; Grimal, J. M. *Corros. Sci.* **1992**, *33*, 805.
- (33) Li, Z.; Chen, H.; Bao, H. B.; Gao, M. Y. *Chem. Mater.* **2004**, *16*, 1391.
- (34) Wang, X. C.; Maeda, K.; Thomas, A.; Takanabe, K.; Xin, G.; Carlsson, J. M.; Domen, K.; Antonietti, M. *Nat. Mater.* **2009**, *8*, 76.
- (35) Thomas, A.; Fischer, A.; Goettmann, F.; Antonietti, M.; Muller, J. O.; Schlogl, R.; Carlsson, J. M. *J. Mater. Chem.* **2008**, *18*, 4893.
- (36) Gong, K. P.; Du, F.; Xia, Z. H.; Durstock, M.; Dai, L. M. *Science* **2009**, *323*, 760.
- (37) Lefevre, M.; Dodelet, J. P.; Bertrand, P. *J. Phys. Chem. B* **2002**, *106*, 8705.

-
- (38) Lalande, G.; Cote, R.; Guay, D.; Dodelet, J. P.; Weng, L. T.; Bertrand, P. *Electrochim. Acta* **1997**, *42*, 1379.
- (39) Dignardbailey, L.; Trudeau, M. L.; Joly, A.; Schulz, R.; Lalande, G.; Guay, D.; Dodelet, J. P. *J. Mater. Res.* **1994**, *9*, 3203.
- (40) Liang, Y. Y.; Li, Y. G.; Wang, H. L.; Zhou, J. G.; Wang, J.; Regier, T.; Dai, H. J. *Nat. Mater.* **2011**, *10*, 780.
- (41) Peng, H.; Mo, Z.; Liao, S.; Liang, H.; Yang, L.; Luo, F.; Song, H.; Zhong, Y.; Zhang, B. *Sci. Rep.* **2013**, *3*.
- (42) Gojkovic, S. L.; Gupta, S.; Savinell, R. F. *J. Electroanal. Chem.* **1999**, *462*, 63.
- (43) Subramanian, N. P.; Li, X. G.; Nallathambi, V.; Kumaraguru, S. P.; Colon-Mercado, H.; Wu, G.; Lee, J. W.; Popov, B. N. *J. Power Sources* **2009**, *188*, 38.

Chapter 4

Methane plasma assisted reduction of graphene oxide films for high-performance micro-supercapacitors

As discussed in the previous two chapters, the application of graphene as a fuel cell catalysts requires bulk scale use of GO and/or rGO. However, for the application in electronics and thin-film technologies, highly conductive graphene films are required. Here we develop a highly efficient one-pot reduction of graphene oxide (GO) films using methane (CH_4) plasma treatment. The reactive ion species produced in CH_4 plasma can facilitate the de-oxygenation and restoration of π -conjugation of GO films within a very short time. The as prepared plasma rGO film shows an oxygen content of 7.2% (C/O ratio of 12.9) and a hole transport mobility of $1.70 \text{ cm}^2 \text{ V}^{-1} \text{ s}^{-1}$. In addition, we demonstrate graphene based in-plane interdigital micro-supercapacitors (MSCs) on arbitrary substrates using plasma rGO films. Although the performance of MSCs has been significantly developed, their power or energy densities remain far from those of electrolytic capacitors or lithium thin-film batteries. Due to the high electrical conductivity of plasma rGO films (345 S cm^{-1}) and the in-plane geometry of the microdevices, the resulting micro-supercapacitors deliver an area capacitance of $80.7 \text{ }\mu\text{F cm}^{-2}$ and a stack capacitance of 17.9 F cm^{-3} . Further, they show a power density of 2.5 mWh cm^{-3} that is comparable to lithium thin-film batteries, in association with superior cycling stability. Such microdevices allow for operations at ultrahigh rate up to $1,000 \text{ V s}^{-1}$, three orders of magnitude higher than that of conventional supercapacitors.

4.1 Introduction

In Chapter 1, we discussed the chemical structure of graphene oxide (GO) containing over a range of C:O stoichiometries, with the oxygen bound to the carbon in the basal plane. Since GO is electrically insulating, the removal of oxygen containing functional groups is highly required to restore its electrical properties.¹ Until now, GO is typically reduced either by chemical and/or thermal reduction process. However, the chemical reduction of GO has shortcomings such as, chemical toxicity and a long processing time that requires several hours to one day to complete the reduction process.^{2,3} Moreover, chemical reduction often introduces heteroatom impurities into graphene.⁴ Alternatively, thermal annealing of GO in Ar, H₂ or ultra-high vacuum (UVH) can remove oxygen groups effectively but requires high temperature (~ 1100 °C), which limits the use of substrates especially flexible plastics.^{5,6} Recently, a hydrogen (H₂) plasma reduction method for GO has been reported to overcome the drawbacks of the chemical reduction methods.³ However, the rGO films with H₂ plasma treatment exhibits poor electrical conductivity due to partial removal of the functional groups. Therefore, it is highly desirable to develop new reduction protocol that involves eco-friendly and fast reduction process towards high-quality rGO films with low oxygen content.

In this chapter, we describe a novel protocol for the reduction of GO films applying methane (CH₄) plasma. The CH₄ plasma at 700 °C can be used to facilitate the de-oxygenation of GO within few seconds. As prepared reduced GO (named as PrGO) has a low oxygen content (i.e. 7.2 %), high electrical conductivity (~ 345 S cm⁻¹) and hole mobility up to 1.70 cm² V⁻¹ s⁻¹ which is comparable to the thermally and/or

chemically reduced GO. Moreover, in cooperation with Dr. Zhong-Shuai Wu in our group we developed a novel class of all solid-state graphene based in-plane interdigital micro-supercapacitors based on the PrGO films to overcome the limitations of carbon based micro-supercapacitors, such as low power and energy densities. The micro-supercapacitors can be fabricated on both rigid and flexible substrates through micropatterning of graphene films with a nanoscale thickness of 6-100 nm. Due to the high conductivity of the fabricated PrGO films and the in-plane geometry of the microdevices, the resulting all solid-state micro-supercapacitors deliver a maximum area capacitance of $80.7 \mu\text{F cm}^{-2}$ and a stack capacitance of 17.9 F cm^{-3} . Further, they show a power density of 495 W cm^{-3} , which is the highest value for reported supercapacitors and an energy density of 2.5 mWh cm^{-3} , which is comparable to that of lithium thin-film batteries, in association with superior cycling stability ($\geq 98.3\%$ capacitance retention after 100,000 cycles). Such in-plane microdevices allow for operations at an ultrahigh scan rate up to $1,000 \text{ V s}^{-1}$, three orders of magnitude higher than conventional supercapacitors.

4.2 Fabrication of GO films

Many methods have been explored to prepare homogeneous reduced graphene film on quartz or silicon substrates, such as spray coating,⁷ dip coating,⁸ spin coating⁹ etc. Each fabrication process has its own advantages depending on the final application purpose. Dip coating is a popular method to prepare thin GO film, for which the process consists of five different steps: immersion, start-up, deposition, evaporation and drainage of solvents. In order to obtain a uniform coating, the substrate is slowly dipped into/

withdrawn from a vessel containing GO dispersion at a constant velocity. For a thick GO film, the dip-coating deposition has to be repeated several times. Unfortunately, the roughness of the GO film increases with the repetition of dip-coating cycles. On the other hand, spray coating is also used to prepare GO film. The advantage of spray coating over spin coating is that the former has no thickness variation caused by directional effect of spinning and is applicable for large-area film preparation. The process consists of a spray-gun (also known as ‘Air brush’) to atomize the desired liquid sample into tiny droplets on a substrate. GO sheets in the sprayed droplets tend to aggregate and fold because of the fast evaporation speed of the solvent causing the film with large roughness.

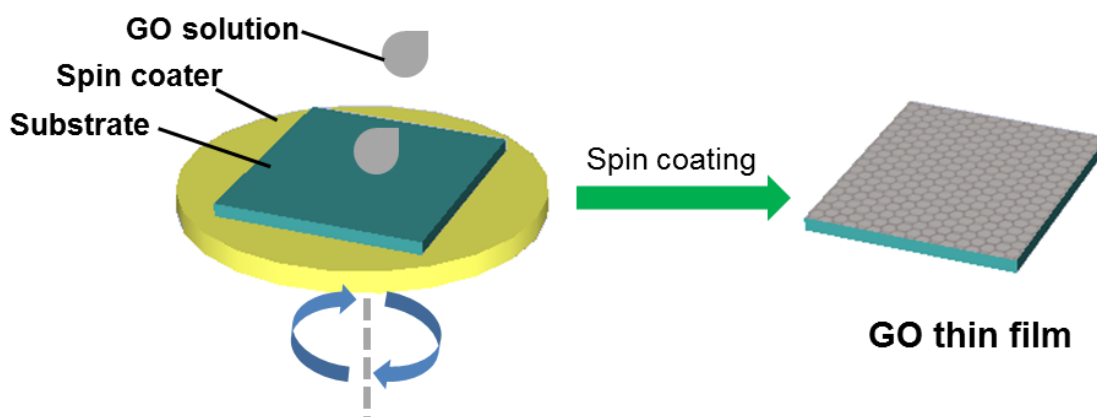


Figure 4.1 Schematic illustration of the spin coating of GO dispersion.

Spin coating is one of the most suitable methods to fabricate homogeneous GO films with a thickness ranging from several to tens of nanometers. Typically, an excess amount of GO dispersion is firstly dropped on a substrate, which is then rotated at high

speed in order to spread the fluid by centrifugal force. The thickness of the GO film can be adjusted via controlling the concentration of GO dispersion, rotation speed and time.

In our experiments, homogeneous GO films on quartz and/or silicon oxide substrates were prepared by spin coating GO dispersion. It should be noted that it is difficult to prepare homogeneous GO film from highly concentrated (i.e. $> 2 \text{ mg mL}^{-1}$) dispersion as wrinkles or aggregation of GO sheets can be easily seen. Therefore, the desirable GO concentration for the spin coating is kept at $0.5\sim 1.5 \text{ mg mL}^{-1}$. Prior to film fabrication, the surface of the substrates should be treated to form a hydrophilic surface in order to decrease the contact angle of GO dispersion. Nevertheless, the substrates such as quartz and Si/SiO₂ wafers are first cleaned with acetone and 2-propanol through sonication for 15 minutes in each solvent. Afterwards, the substrates are subjected to the oxygen plasma treatment using 300 W radio frequency (rf) power for 10 min (Plasma System 200-G, Technics). The GO dispersion of 1 mg mL^{-1} in water is then spin coated on the modified substrates at 1500 rpm for 60 sec. The as-prepared GO films are then used for direct CH₄ plasma reduction.

4.3 Methane (CH₄) plasma reduction of GO film

Plasma generally contains energetic species such as ions and offers a unique advantage because non-equilibrium reactions can be performed at low temperature and high purity. In the case of CH₄ plasma, the reactive species include ions such as, C⁺, CH_n⁺ (where n = 1 - 3) and radicals like H• and CH_n• etc. All these species can react with the GO and remove oxygen containing groups such as CO, -OH, -COOH etc. during ion

bombardment.¹⁰ In addition, CH₄ plasma can provide an additional carbon source to repair the defects of GO.¹¹



Figure 4.2 Photograph of a standard plasma enhanced chemical vapor deposition (PECVD) system.

The plasma reduction of GO was performed in a plasma-CVD system (AIXTRON, Nanoinstruments Black Magic) (Figure 4.3). The spin coated GO films with a thickness of ~5 nm were treated at 700 °C under the CH₄ plasma from 10 to 30 sec. The flow rate of CH₄ gas into the plasma chamber was 100 sccm. The plasma was operated with a 15-kHz waveform drive and ignited with a high voltage of 800 V. The chamber pressure during the plasma treatment was 6.20 Torr. The samples are named as PrGO-10, PrGO-20 and PrGO-30 for 10, 20 and 30 sec of plasma treatment, respectively.

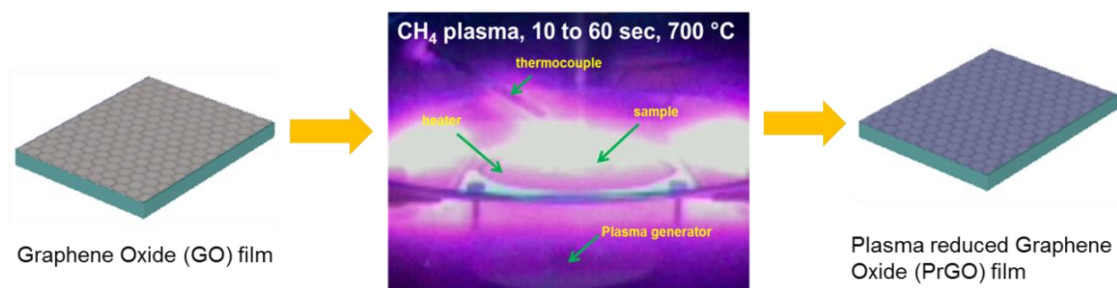


Figure 4.3 Schematic representation of CH₄ plasma reduction process of GO thin films. Spin coated GO films on quartz are exposed to CH₄ plasma at 700 °C for only 10 to 60 sec resulting in PrGO films.

4.4 Morphology and structural characterizations

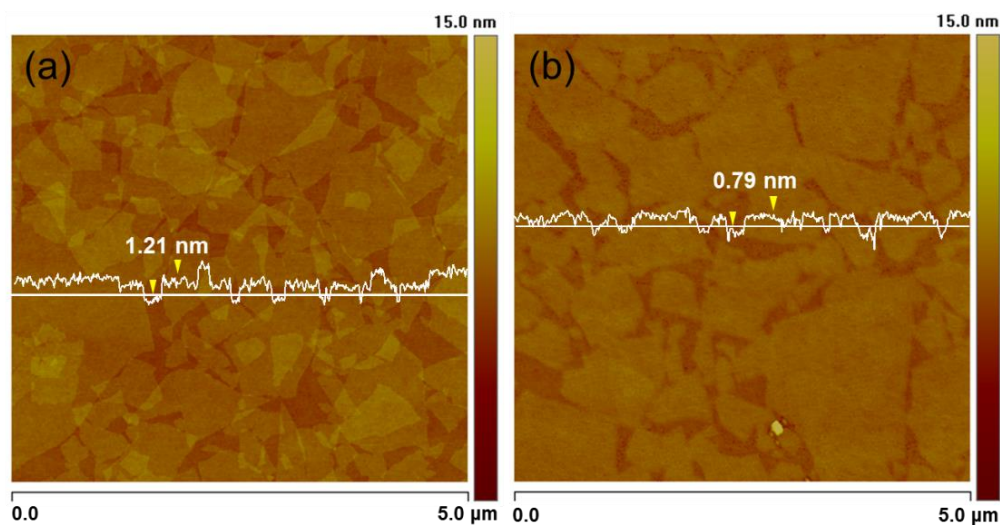


Figure 4.4 AFM image of (a) GO and (b) reduced GO after 10 sec of CH₄ plasma treatment on SiO₂ substrates. The white curves are AFM height profiles with each height value labeled.

As shown in Figure 4.4, the morphology of GO and PrGO sheets were first analyzed by the atomic force microscope (AFM). The single layer GO sheets deposited on SiO₂ substrates revealed a thickness of 1.2 nm with a lateral dimension of several micrometers (Figure 4.4a). The higher thickness of GO than the pristine graphene (thickness of ~ 0.7 nm) is mainly due to the presence of oxygen containing functional groups randomly decorated on both sides of GO sheet. However, after 10 sec of CH₄ plasma (i.e. PrGO10) treatment, the thickness of the graphene sheets decreased significantly to 0.79 nm, suggesting the effective removal of the functional groups.

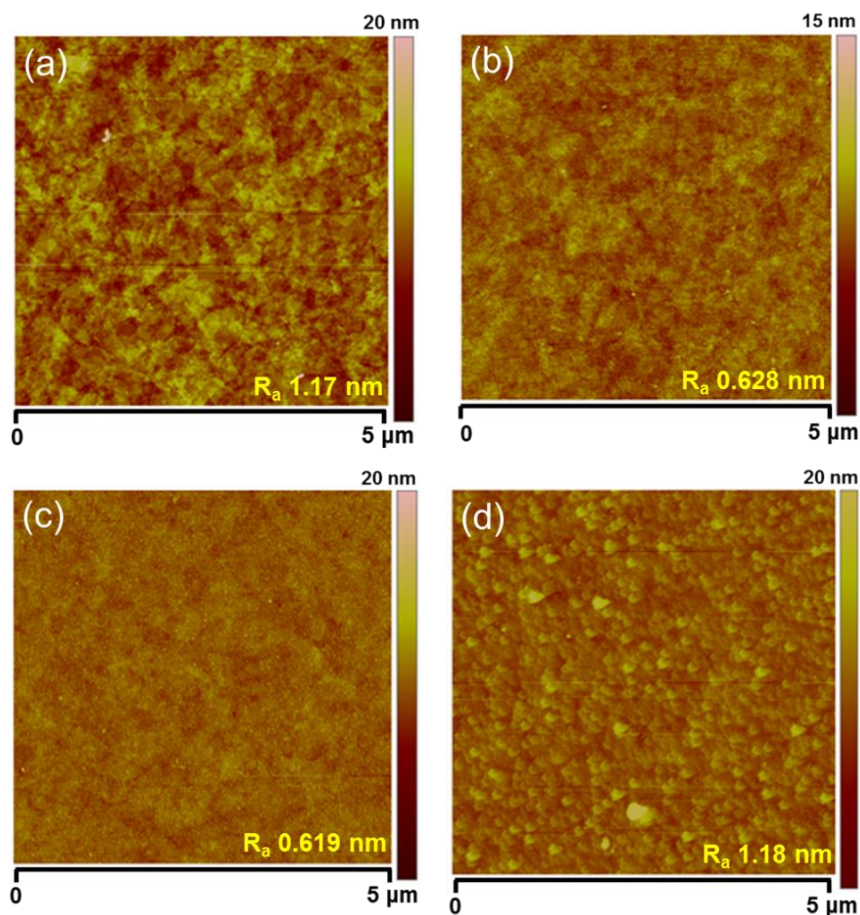


Figure 4.5 AFM images of (a) GO film, (b) PrGO-10, (c) PrGO-20 and (d) PrGO-30 films on SiO₂ substrates.

AFM characterizations further revealed that the roughness of the PrGO films decreased significantly after the CH₄ plasma treatment. As indicated in Figure 4.5a, the ~ 5 nm GO film showed an average Ra of 1.17 nm. After 10 and 20 sec of plasma treatment, the Ra decreased to 0.628 and 0.619 nm, respectively. Suggesting that, as the duration of plasma treatment increases the PrGO becomes thinner and smoother due to the reduction of oxygen functional groups and sp³ carbon domains. However, prolonged exposure to CH₄ plasma (≥ 30 sec) resulted in the formation of carbon nanoparticles on graphene surface (Figure 4.5d), which eventually affects the transmittance of the PrGO films (will be discussed later).

The X-ray diffraction (XRD) patterns of GO and PrGO films are presented in Figure 4.6a. The GO film reveals a sharp diffraction peak (002) at 9.92°, corresponding to a d-spacing of 8.92 Å. The large d-spacing in GO is mainly due to the presence of oxygen functional groups decorating both plane of a graphene acts as a spacer between neighboring graphene layers and results in a large d-spacing with lower 2θ angle compared to that of graphite ($2\theta = 26.7^\circ$, d-spacing ~ 3.34 Å).¹² After CH₄ plasma reduction for 20 sec (i.e. PrGO-20), the diffraction peak appears at 26.50°, with a interlayer d-spacing of 3.36 Å. This result suggests the pronounced reduction of GO. The sharp peak at around 33° is characteristics of Si (201) from the substrate (JCPDS No. 40-0932). The plasma reduced GO films are further assessed by their wettability. Figure 4.6b presents the water contact angle on PrGO-20 film is 62.8±1.1°, while that on HOPG surface is 81.1±1.8°. The relatively hydrophilic property of the PrGO film can be attributed to the remaining oxygen functional groups after reduction.

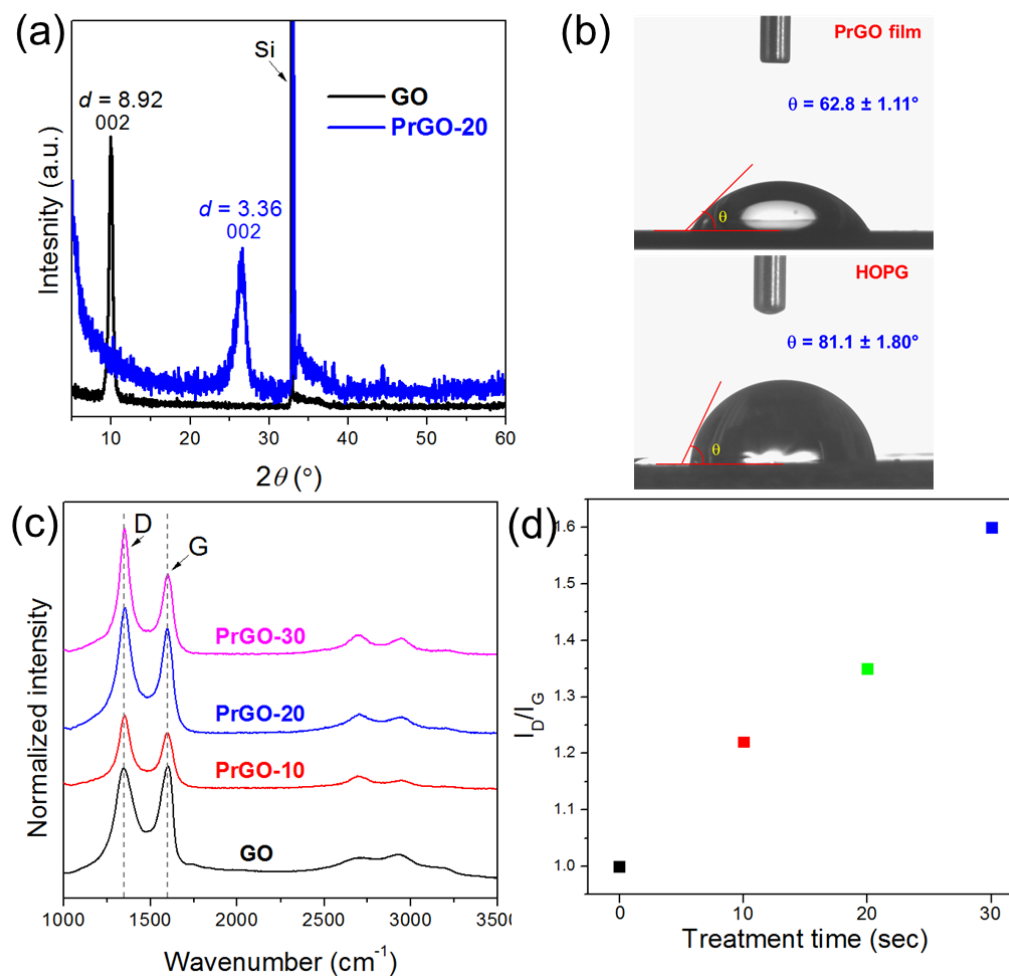


Figure 4.6 (a) XRD patterns of GO and PrGO films on silicon wafer, (b) water contact angle of HOPG and PrGO film, (c) Raman spectra and (d) I_D/I_G ratio of GO and PrGO thin films, respectively.

Structural changes of the GO films after CH_4 plasma treatment were evaluated by Raman spectroscopy. Raman spectra were collected with a Bruker RFS 100/S spectrometer at a laser excitation wavelength of 488 nm and 2 mW power. As displayed in Figure 4.6c, the Raman spectrum of as deposited GO film reveals a D peak at $\sim 1350 \text{ cm}^{-1}$ and a G peak at 1603 cm^{-1} . The G peak corresponds to the first-order scattering of the E_{2g} mode,¹³ while the D peak is due to structural defects and imperfections created

by oxygen functional groups in the basal plane of graphene sheet. After the plasma treatment, the G peak of the PrGO films red-shifts to 1594 cm^{-1} , which is consistent with previous reports on reduced GO.^{6,14,15} According to the Tunistra-Koenig relation,¹⁶ the in-plane sp^2 domain size can be estimated by the ratio of the intensity between the D and G peaks (I_D/I_G). Previous reports have shown that reduction of GO by hydrazine hydrate resulted in an increased I_D/I_G ratio because the sp^2 cluster size generally decreased during the removal of oxygen groups from the graphene sheets.^{15,17} Interestingly, PrGO films exhibit an approximately linear rise of I_D/I_G ratio, whereas the sheet resistance decreases with increasing plasma treatment time (will be discussed later) (Figure 4.6d).

Table 4.1 Atomic percentages of different carbon bonds identified by XPS in GO and PrGO films with plasma treatment time.

Samples	C=C/C-C (%)	C-OH (%)	C=O (%)	O=C-O (%)	π - π^* (%)
GO	60	18.09	11.39	10.53	--
PrGO-10	86.8	7.24	2.34	1.07	2.55
PrGO-20	90.7	3.88	2.33	0.95	2.08
PrGO-30	92.8	3.07	1.65	0.87	1.60

In order to investigate the chemical structure of the CH_4 plasma treated GO films, X-ray photoelectron spectroscopy (XPS) was performed by Dr. Xianjie Liu at Linköping University, Sweden. The XPS characterization was carried out by Scienta ESCA 200

spectrometer equipped with an Al ($K\alpha$) x-ray source. Figure 4.7a and 4.7b show the wide scan and C 1s core-level spectra collected from GO and PrGO films, respectively. The C 1s spectra of the fully oxidized GO can be deconvoluted into C=C/C-C (284.6 eV), C-OH (286.4 eV), C=O (287.2 eV), O=C-O (288.1 eV) and π - π^* satellite peak (290.6 eV), consistent with previous reports.¹⁸ Moreover, the atomic percentages of the various carbon bonds in the PrGO films were determined by analyzing the C 1s spectra, as summarized in Table 1. The majority of the oxygen species in the GO film is in the form of C-OH groups. Plasma reduction was found to be more effective in reducing the number of C-OH groups. Moreover, the C=O and O=C-O species that are believed to be more difficult to remove, was reduced significantly.¹⁹ Nevertheless, the CH₄ plasma treatment of GO films for 10 to 30 sec resulted in a decrease in the intensity of the O 1s peaks suggesting the elimination of oxygen species (Figure 4.7a). As shown in Figure 4.7c and d, the C/O ratio of untreated GO films is only 1.5. Whereas after CH₄ plasma treatment, the C/O ratio increases linearly to 6.58, 9.75 and 12.89 for PrGO-10, PrGO-20, PrGO-30 films, respectively (Figure 4.7d). The C/O ratio (12.89) obtained for PrGO-30 is significantly higher than H₂ plasma (~ 6.95)²⁰ and chemically reduced GO (~ 10.2)^{21,22} and comparable with thermally reduced GO (12.4) at 1000 °C.⁶

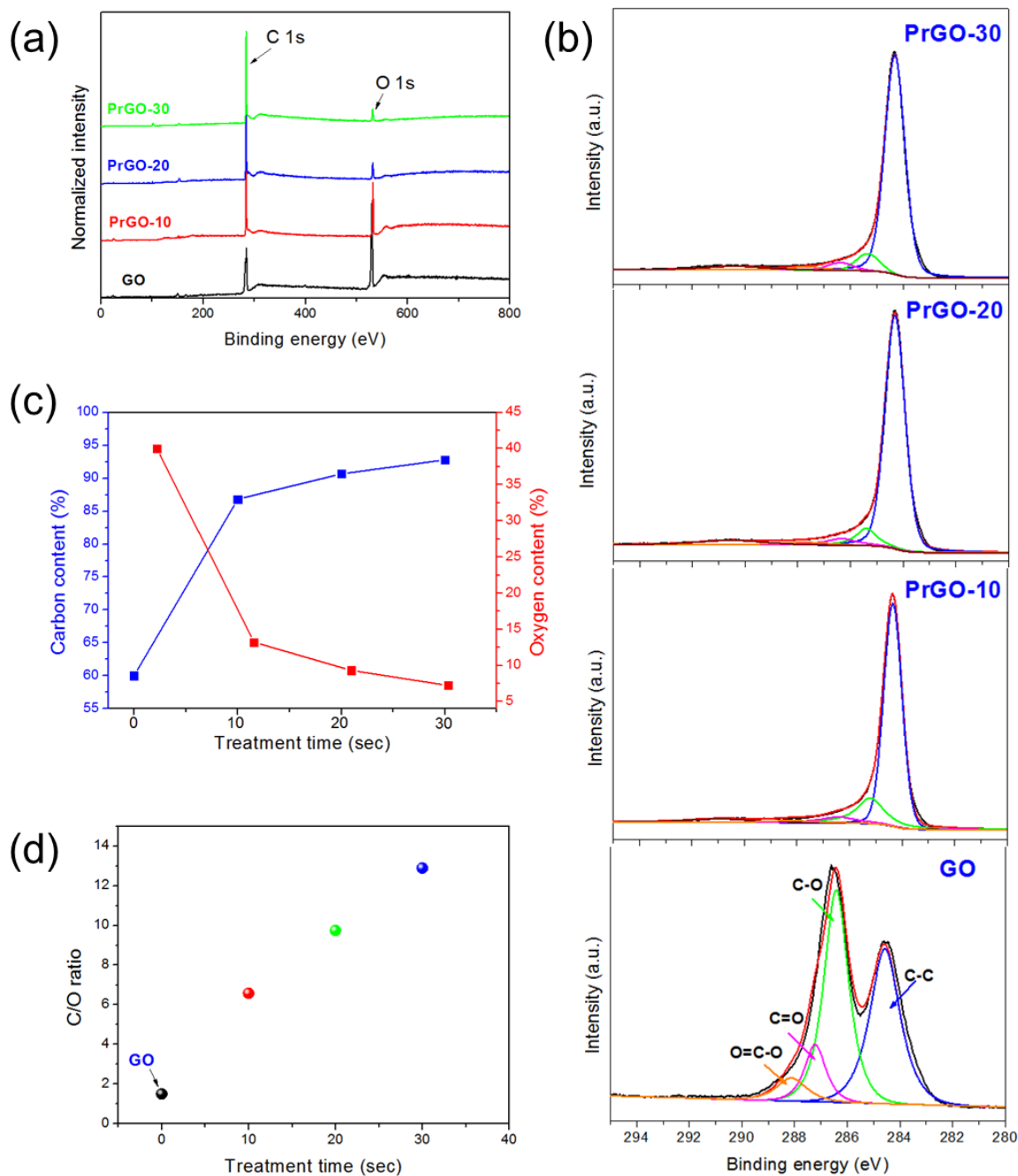


Figure 4.7 (a) Wide scan XPS profiles of GO and PrGO films recorded in the range of 0-800 eV, (b) high-resolution and deconvoluted C 1s spectra of GO and PrGO films, (c) atomic percentage of carbon and oxygen and (d) C/O ratio for the GO and PrGO films at various treatment time.

4.5 Optoelectronic properties

The electronic property of the PrGO films (thickness ~5 nm) was studied by fabricating field-effect transistors (FET). The FET devices were constructed using the standard technique of evaporating 50 nm thick Au electrodes on top of the PrGO thin films (thickness ~5.0 nm) on SiO₂/Si substrates (Figure 4.8a). The transfer curves of the FET devices based on thin PrGO films are presented in Figure 4.8b. All the FET devices based on PrGO-10, PrGO-20 and PrGO-30 films display a typical hole transport characteristic with no Dirac point observed between the gate voltage from -80 V to +80 V. Moreover, the transfer curves do not exhibit the ambipolar effect which is common phenomenon for high-quality graphene FETs. As reported previously, the presence of oxygen functional groups can act as electron traps and prohibit their function as free carriers.^{14,23} The hole carrier mobility was calculated from the linear region of the transfer curves using the following equation:

$$\mu = (L/WC_iV_d) \times (\Delta I_d/\Delta V_g)$$

Where C_i (11 nF cm⁻²) is the specific capacitance of the gate dielectric, L , W , I_d , V_d and V_g are channel length, width, drain-source current, drain-source voltage and gate voltage respectively. The derived hole mobilities for PrGO-10, PrGO-20 and PrGO-30 films were 0.51, 1.17 and 1.70 cm² V⁻¹ s⁻¹, respectively. It should be also noted that the contact resistance between the metal electrodes and PrGO films is not excluded in the mobility determination, which could lead to an underestimation. Nonetheless, the observed hole mobility of the PrGO based FETs is comparable with that of the chemically and/or thermally reduced GO films (~ 0.01-5.0 cm² V⁻¹ s⁻¹).^{14,24,25}

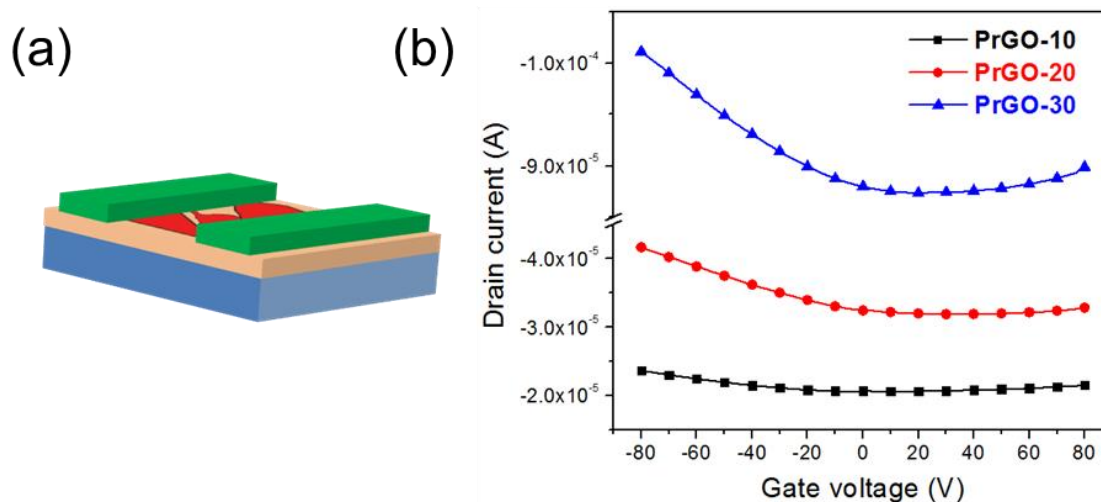


Figure 4.8 (a) Schematic illustration and (b) transfer curves of the FET devices based on the PrGO thin films.

The sheet resistance (R_s) and transmittance of PrGO films with different thickness were further investigated. To this end, the GO films were deposited on quartz substrates by spin coating aqueous GO solution at 1500 rpm for 60 sec. The thickness of the films was controlled by repeating the spin coating steps. After CH_4 plasma treatment for 30 sec, the R_s of PrGO films was recorded by a four-point probe system using a Keithly 2700 multimeter (probe spacing: 0.635 mm, $R_s = 4.532 \text{ V/I}$), whereas, the transmittance (at 550 nm wavelength) was monitored by UV-Vis spectrometer. As indicated in Figure 4.9a, the R_s of PrGO films decreased with increasing the film thickness. However, the transmittance of the films declined rapidly. After 30 sec of plasma exposure, the 5 nm and 15 nm thick graphene films delivered the R_s of 4.9 and 3.39 $\text{k}\Omega \text{ sq.}^{-1}$ respectively, while the transmittance was 75% and 69% at 550 nm, respectively. Notably, the achieved R_s values are significantly lower compared to the previously reported GO films reduced

by high temperature vacuum annealing in NH_3 and/or H_2 , pulse laser and N_2H_4 vapor etc.²⁶⁻²⁸

To achieve a balance between low R_s and high transmittance ($\geq 80\%$), thin graphene films with a thickness of ~ 5 nm were used for further optimization of the plasma reduction process. Thus, the GO films were exposed to CH_4 plasma for 10 to 60 sec. As shown in Figure 4.9b, the R_s of PrGO films decreased significantly from 4.12 to $1.31 \text{ k}\Omega \text{ sq.}^{-1}$, upon increasing plasma treatment time from 10 to 60 sec. However, the transmittance also declined rapidly, due to the formation of carbon nanoparticles as the treatment time proceeds (Figure 4.5d). Nevertheless, a R_s of $4.12 \text{ k}\Omega \text{ sq.}^{-1}$ with $\sim 80\%$ transmittance was achieved after only 10 sec of plasma treatment. Interestingly, doping of PrGO films with nitric acid (65% HNO_3) for 2 h led to $\sim 45\%$ decrease of R_s values without sacrificing the original transparency (Figure 4.9b, red line).

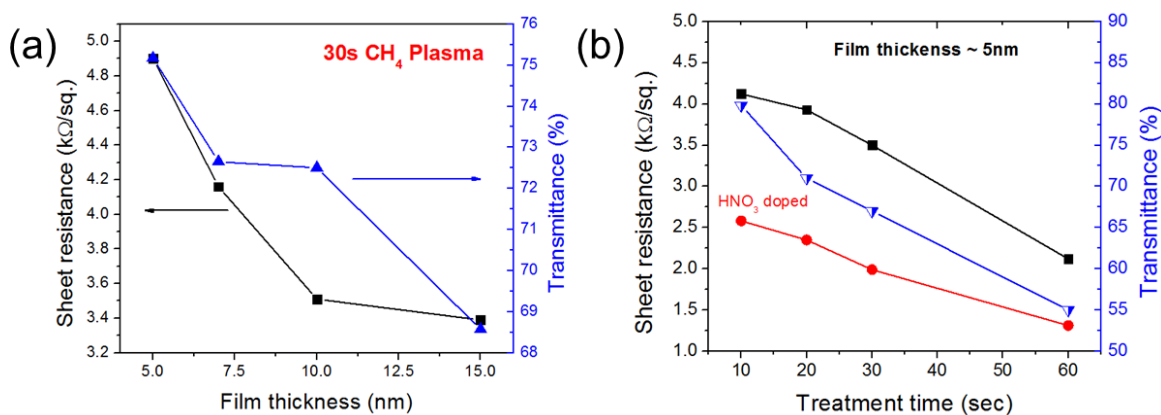


Figure 4.9 Sheet resistance and transmittance of graphene films of (a) 30 sec of plasma treatment with different film thickness, (b) different plasma treatment time on 5.0 nm films. The red line represents the sheet resistance of graphene films after HNO_3 doping.

In order to confirm that the reduction of GO occurred mainly due to the plasma exposure and not from the annealing, the GO films were annealed at 700 °C in Ar and H₂ gas mixtures, while the film thickness and treatment time (i.e. 10 to 60 sec) were kept the same (i.e. ~5 nm) as the plasma process. As can be seen from Figure 4.10a, thermal annealing of graphene films resulted in several magnitudes higher R_s than the plasma treated films. Therefore, it can be concluded that the effective reduction of GO is mainly attributed to the CH₄ plasma.

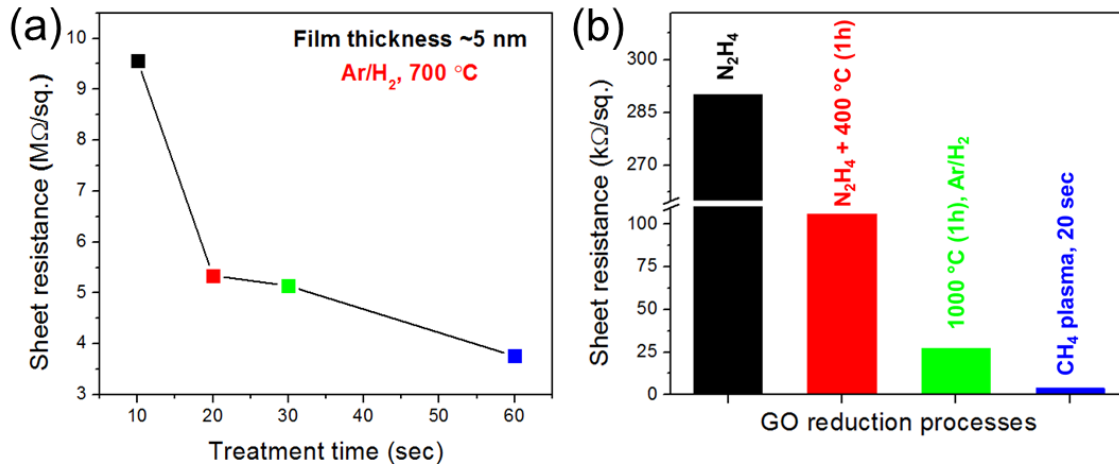


Figure 4.10 (a) Sheet resistance of the thermally reduced 5.0 nm thick GO films at 700 °C in Ar and H₂ gas mixtures; (b) comparison of sheet resistance of conventional GO reduction process with CH₄ plasma reduction.

We further compare the CH₄ plasma reduction with the widely reported conventional GO reduction methods. It is clear from Figure 4.10b that the CH₄ plasma reduced GO has a low R_s compared to the chemical reduction by hydrazine (N₂H₄), thermal annealing at 1000 °C and H₂ plasma reduced GO films. However, the R_s of the

PrGO films achieved are still significantly higher than that of the ITO. Nevertheless, the CH₄ plasma reduction possesses great advantage over other conventional chemical and/or thermal reduction methods due to very fast and effective removal of oxygen functional groups from GO.

4.6 Graphene based in-plane micro-supercapacitors

In cooperation with Dr. Zhong-Shuai Wu in our group, we further demonstrate the use of CH₄ plasma reduced GO film as an electrode material for the in-plane micro-supercapacitors (MSCs). MSCs represent one type of the newly developed miniaturized electrochemical energy storage devices. The term “micro” is used mainly because of the thickness of the active electrode material which is in the range of micrometer scale (i.e. $\leq 10 \mu\text{m}$). They offer power densities that are several orders of magnitude larger than those of conventional supercapacitors due to their short ion diffusion length.²⁹⁻³¹ Importantly, such on-chip microdevices can be directly integrated into other miniaturized electronic devices, such as microbatteries or energy-harvesting microsystems, thereby providing excellent nano-/micro-scale peak power.^{32,33} Nevertheless, MSCs that integrate the advantages of the ultrahigh power density of an electrolytic capacitor ($10^2\sim 10^3 \text{ W cm}^{-3}$) and the high-energy delivery of a thin-film battery ($10^{-3}\sim 10^{-2} \text{ Wh cm}^{-3}$) have not yet been achieved. To this end, it is essential to fabricate thin-film electrodes with a highly accessible electrochemically activated surface area, high electrical conductivity, superior interfacial integrity of the main components (electrode, separator, electrolyte, and substrate), and an elaborate device structure with short ion diffusion pathways.

4.6.1 Fabrication of graphene-based micro-supercapacitors

Figure 4.11 illustrates the fabrication process of the MSCs on a silicon wafer. First, a thin film of graphene oxide (GO) was obtained by spin-coating a GO dispersion (2 mg mL^{-1}) on a modified silicon wafer that was first treated with an oxygen plasma (Figure 4.11a,b). Next, the GO film was rapidly reduced by methane (CH_4) plasma treatment at $700 \text{ }^\circ\text{C}$ over a short time (20 s), as indicated by the color change of the film from yellow to grey (Figure 4.11c). Scanning electron microscopy (SEM) indicated that GO films composed of individually stacked sheets were readily transformed into large-area connected graphene films with a thickness of 15 nm (Figure 4.11h). The resulting plasma reduced graphene (named as MPG) films exhibited high electrical conductivity ($\sim 345 \text{ S cm}^{-1}$, Figure 4.11i), in contrast to $\sim 62 \text{ S cm}^{-1}$ for graphene (TG) film thermally reduced at $700 \text{ }^\circ\text{C}$ for 20 s. Subsequently, well-established photolithography techniques were applied to manufacture graphene-based interdigital microelectrode patterns through the deposition of gold current collectors, followed by oxidative etching in an oxygen plasma (Figure 4.11d,e). Optical (Figure 4.11j) and SEM (Figure 4.11k) images of the patterned films showed regular widths of $\sim 210 \text{ }\mu\text{m}$ and an interspace of $\sim 70 \text{ }\mu\text{m}$ between neighbouring electrode fingers. Atomic force microscopy (Figure 4.11l and m) further disclosed the uniform thickness and edge shape of MPG interdigital electrodes. A $5 \text{ }\mu\text{L}$ polymer gel electrolyte, such as H_2SO_4 /polyvinyl alcohol (H_2SO_4 /PVA), prepared by mixing 6 g H_2SO_4 and 6 g PVA ($M_w = 85,000\text{-}124,000$) in 60 mL deionized water followed by heating up to $80 \text{ }^\circ\text{C}$ for 1 h under vigorous stirring, was then drop-cast onto the interdigital electrodes and solidified overnight (Figure 4.11f). Notably, the gel electrolyte used here not only avoided the harmful leakage of liquid electrolytes, but also

reduced the microdevice thickness without additional packaging materials and thus simplified the entire fabrication process. Finally, all solid-state MPG-based MSCs (MPG-MSCs) with in-plane geometry (Figure 4.11g) were obtained. All the electrochemical measurements and data analysis of the fabricated MSCs mentioned in this work were performed by Dr. Zhong-Shuai Wu.

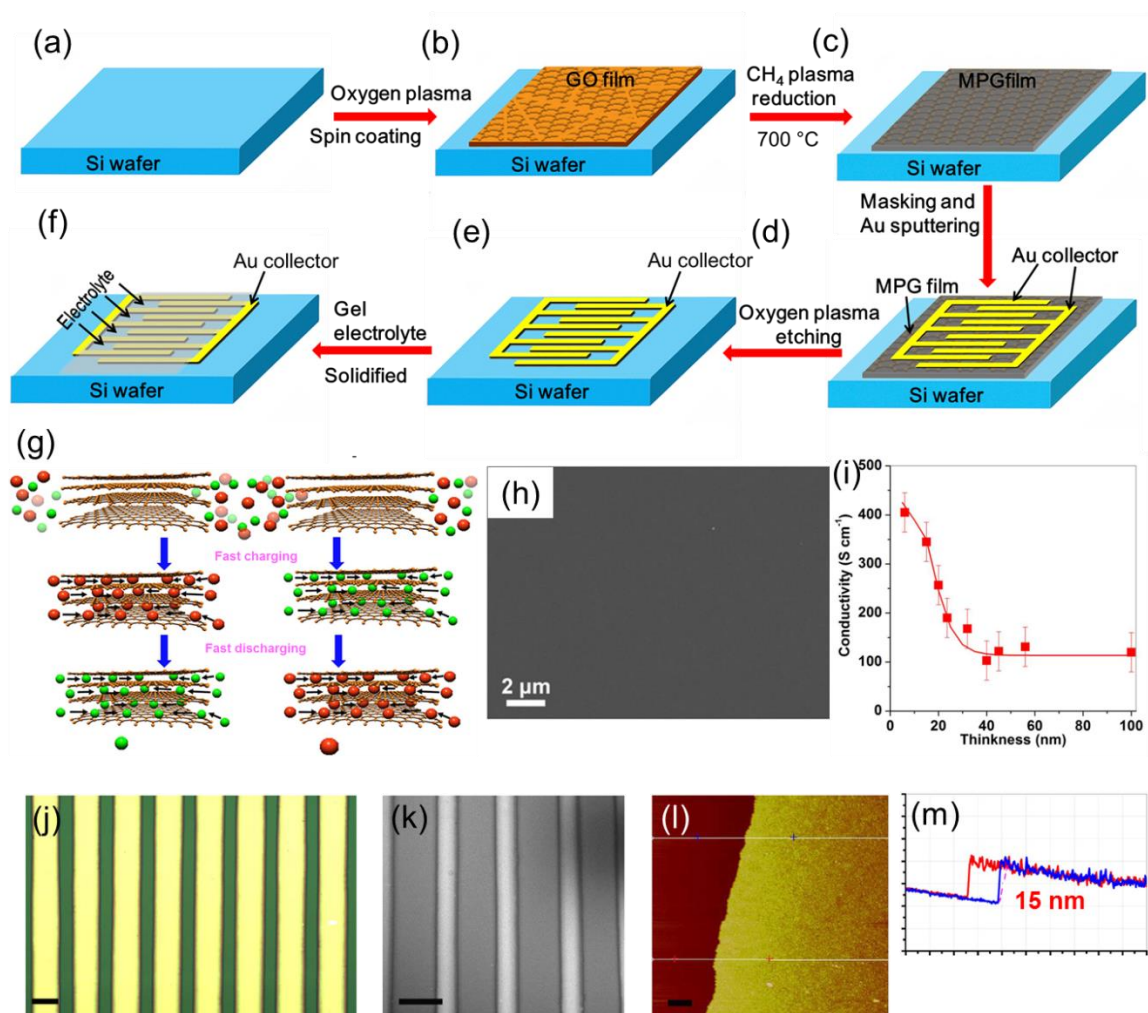


Figure 4.11 (a-f) Schematic illustration of the fabrication of MPG-MSC made up of 30 interdigital fingers integrated onto a silicon wafer. The fabrication process flow includes (a) oxygen plasma surface treatment of silicon, spin-coating of the GO solution on surface-modified silicon, (b) CH_4 plasma reduction, (c) masking pattern and

deposition of gold current collector, (d) oxidative etching in oxygen plasma, (e) drop casting of the H₂SO₄/PVA gel electrolyte and (f) solidification of the gel electrolyte. (g) In-plane geometry of MPG-MSCs, revealing that the ions between the electrode gaps can be rapidly transported along the planar graphene sheets with a short diffusion length. (h) SEM image reveals large-area continuous and uniform morphology of the graphene film. (i) The electrical conductivity of the MPG films as a function of film thickness. (j) Optical and (k) SEM images of the microelectrode patterns. Scale bars, 200 μm. (l) AFM image of the PrGO-20 film electrode after etching by oxygen plasma and removal of Au by a KI/I₂ aqueous solution. Scale bar, 1 μm. (m) Uniform thickness of ~ 15 nm, indicated by the height profile of the PrGO-20 film.

4.6.2 Electrochemical characterization

To evaluate the power capability of MPG-MSCs, cyclic voltammetry (CV) experiments were performed at scan rates ranging from 0.01 to 1000 V s⁻¹ with a CHI 760D electrochemical workstation. The capacitance values were calculated from the CV data according to the following equation:

$$C_{device} = \frac{1}{\nu(V_f - V_i)} \int_{V_i}^{V_f} I(V) dV$$

Where C_{device} is denoted as the capacitance contribution from graphene electrodes, ν is the scan rate (in V s⁻¹), V_f and V_i are the integration potential limits of the voltammetric curve, and $I(V)$ is the voltammetric discharge current (in amperes).

Specific capacitances were calculated based on the area or the volume of the device stack according to the following formula:

$$C_{area} = C_{device} / A$$

$$C_{stack} = C_{device} / V$$

Where C_{area} (in F cm⁻²) and C_{stack} (in F cm⁻³) refer to the area capacitance and volumetric stack capacitance of device, respectively. A and V are the total area (cm²) and volume (cm³) of the device, respectively. The area capacitances were calculated based on the entire projected surface area of the device, including the area of micro-electrodes and the interspaces between them. The volumetric stack capacitances were calculated by taking into account the whole volume of the device, including the volume of graphene electrodes, the interspaces between the electrodes, Au current collectors, gel electrolyte and electrolyte separators.

Compared with GO film-based MSCs (Figure 4.12a to c), MPG-MSCs exhibited an exceptionally enhanced electrochemical performance with a nearly rectangular CV shape, even at a high scan rate of 100 V s⁻¹ (Figure 4.12d to f), indicative of the typical double-layer capacitive behavior. A linear dependence of the discharge current on the scan rate was recognised at least up to 200 V s⁻¹ (Figure 4.12f). Remarkably, MPG-MSCs charged and discharged rapidly up to 1000 V s⁻¹ while maintaining excellent capacitance (Figure 4.12d to h), characteristic of a high instantaneous power. Such rate performance is three orders of magnitude higher than that of electric double-layer capacitors and comparable to any high-power microdevices previously reported¹¹. The cycling performance of MPG-MSCs was examined up to 100,000 cycles at a scan rate of 50 V s⁻¹ (Figure 4.13a).

The CV shapes remained almost unchanged and $\sim 98.3\%$ capacitance was retained, suggesting extremely stable capacitive behaviour (Figure 4.13b). In addition, MPG-MSCs show the self-discharge time of ~ 3.3 h from 1.0 to 0.5 V, indicating that the stored charges can be kept for a significant time in such devices (Figure 4.13c).

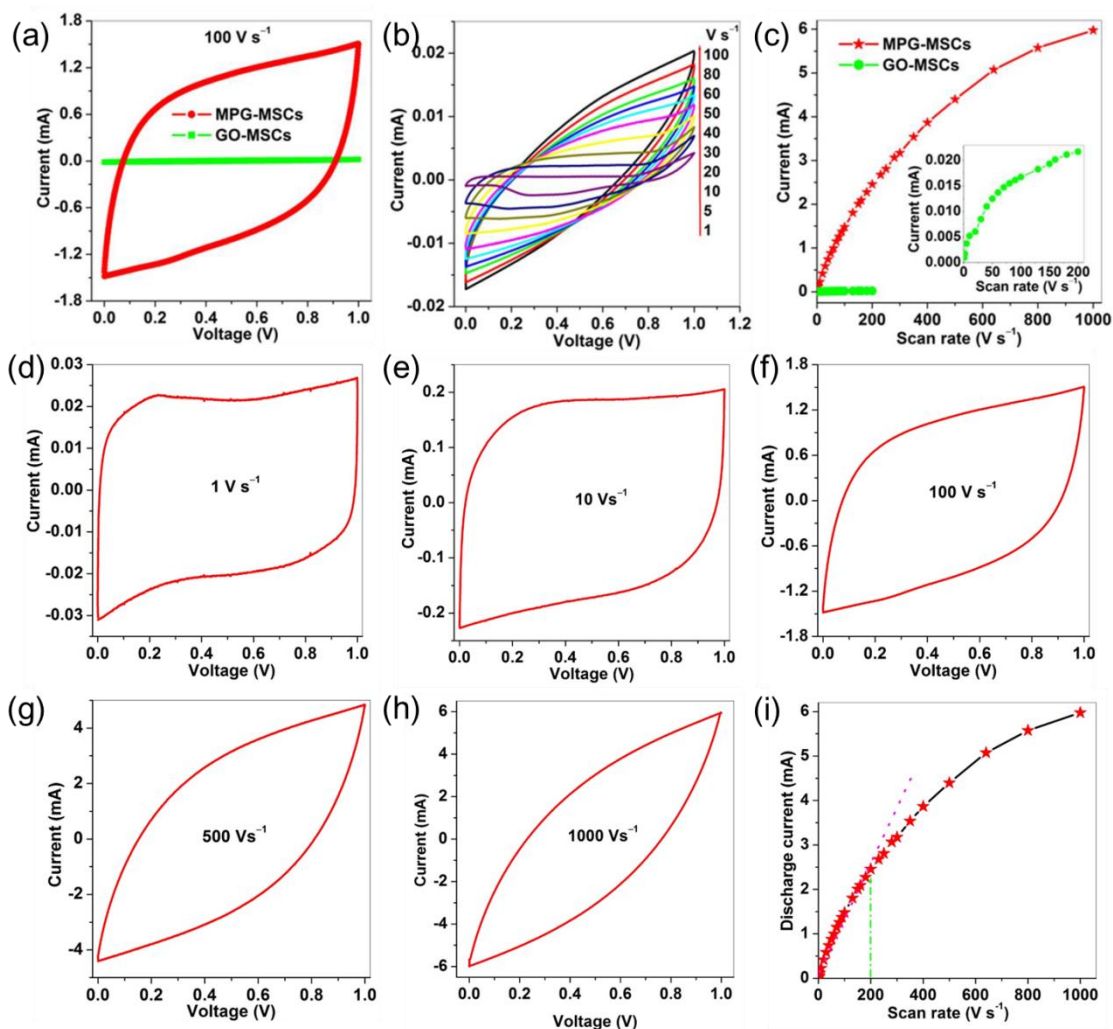


Figure 4.12 (a) Comparison of CV curves of GO-MSCs and MPG-MSCs with a thickness of 15 nm at 100 V s^{-1} in a $\text{H}_2\text{SO}_4/\text{PVA}$ gel electrolyte showing negligible capacitance of GO-MSCs. (b) CV curves of GO-MSCs at different scan rates. (c) Comparison of the discharge current vs. scan rate of GO-MSCs and MPG-MSCs. Inset is

the discharge current versus scan rate of GO-MSCs. (d-h) CV curves obtained at different scan rates from 1 to 1,000 V s^{-1} interdigital MSCs with a 15 nm thick MPG film, indicating a typical double layer capacitive behaviour even at different scan rates. (i) A plot of the discharge current as a function of the scan rate (red star line). Linear dependence (magenta dot line) is observed up to at least 200 V s^{-1} (green dash dot line), suggesting ultrahigh power ability of MPG-MSCs.

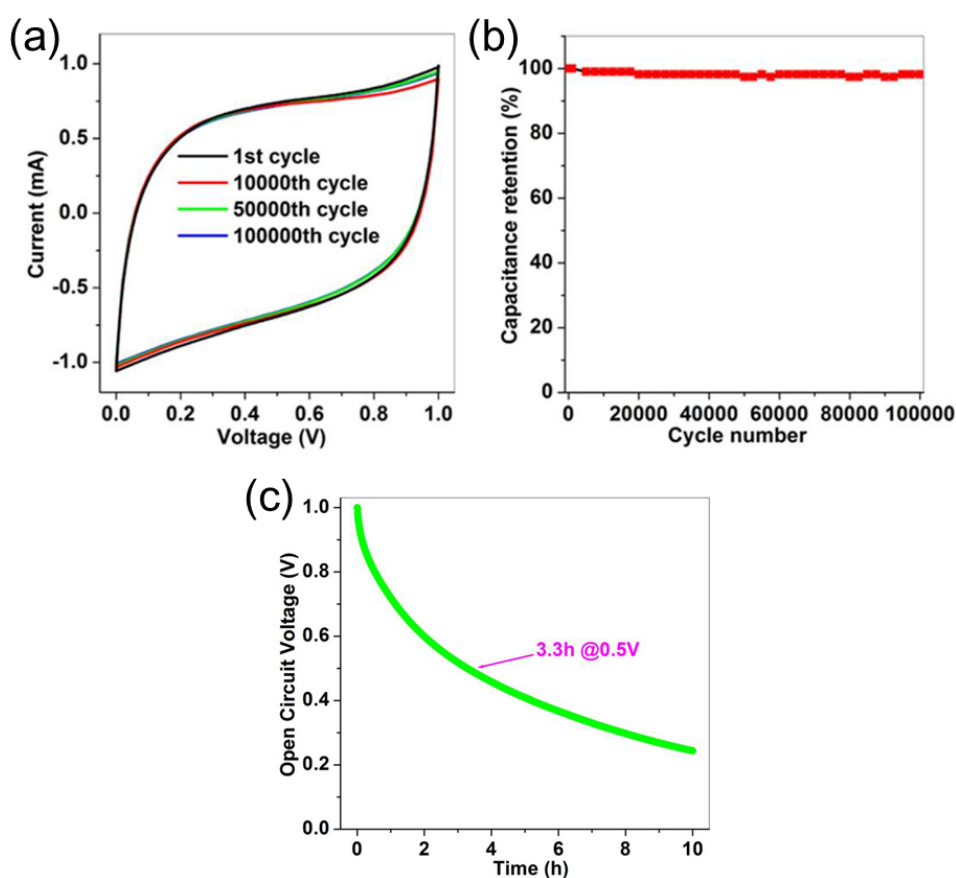


Figure 4.13 (a) CVs obtained at the 1st, 10000th, 50000th and 100000th measured at 50 V s^{-1} , showing similar curve shape before and after cycling. (b) The capacitance retention versus cycle number. The capacitance retention is about 98.3 % after 100000 cycles, revealing excellent cycling stability at ultrahigh charge and discharge rate of 50 V s^{-1} .

s⁻¹. (c) Self-discharge profile of MPG-MSCs in H₂SO₄/PVA gel electrolyte obtained immediately after charging to 1.0 V.

To further investigate the superiority of the in-plane device geometry for the performance of MPG-MSCs, classical sandwich-supercapacitors comprising H₂SO₄/PVA gel electrolytes between two MPG film electrodes (MPG-SSCs, Figure 4.14) with the same MPG film thickness were fabricated. The area capacitance and stack capacitance of the in-plane MPG-MSCs were calculated to be $\sim 80.7 \mu\text{F cm}^{-2}$ ($\sim 322.8 \mu\text{F cm}^{-2}$ in electrode) and $\sim 17.9 \text{ F cm}^{-3}$ ($\sim 71.6 \text{ F cm}^{-3}$ in electrode), respectively, both of which were much higher than those of MPG-SSCs ($\sim 64 \mu\text{F cm}^{-2}$ and $\sim 1.1 \text{ F cm}^{-3}$; Figure 4.13a and b). In addition, MPG-MSCs exhibited a rate capability superior to that of MPG-SSCs. Upon increasing the scan rates, the capacitances of the MPG-MSCs dropped very slowly. For example, $\sim 13.5 \mu\text{F cm}^{-2}$ and $\sim 3.0 \text{ F cm}^{-3}$ for area capacitance and stack capacitance, respectively, were obtained at 200 V s^{-1} . Even at an ultrafast rate of 1000 Vs^{-1} , MPG-MSCs still delivered an area capacitance of $\sim 4.5 \mu\text{F cm}^{-2}$ and a stack capacitance of $\sim 1.0 \text{ F cm}^{-3}$. In marked contrast, MPG-SSCs gave an area capacitance of only $\sim 0.9 \mu\text{F cm}^{-2}$ and a stack capacitance of $\sim 0.02 \text{ F cm}^{-3}$ at 200 V s^{-1} . Clearly, the much longer ion diffusion length of MPG-SSCs than that of MPG-MSCs ($< 180 \mu\text{m}$) should be responsible for the lower capacitance at ultrahigh rates (Figure 4.11g and Figure 4.13). To probe the influence of the electrical conductivity of the graphene film on the electrochemical performance of MPG-MSCs, we also fabricated in-plane MSCs based on TG film (TG-MSCs) without methane-plasma treatment, while keeping the film thickness and cell assembly the same as for MPG-MSCs. The maximum area and stack capacitances ($\sim 32.6 \mu\text{F cm}^{-2}$ and $\sim 7.3 \text{ F cm}^{-3}$) and rate capability ($\sim 4.9 \mu\text{F cm}^{-2}$ and $\sim 1.1 \text{ F cm}^{-3}$ at 400 V s^{-1})

obtained for TG-MSCs were much lower than those of MPG-MSCs, indicating that the conductivity of graphene also plays an important role in the electrochemical performance.

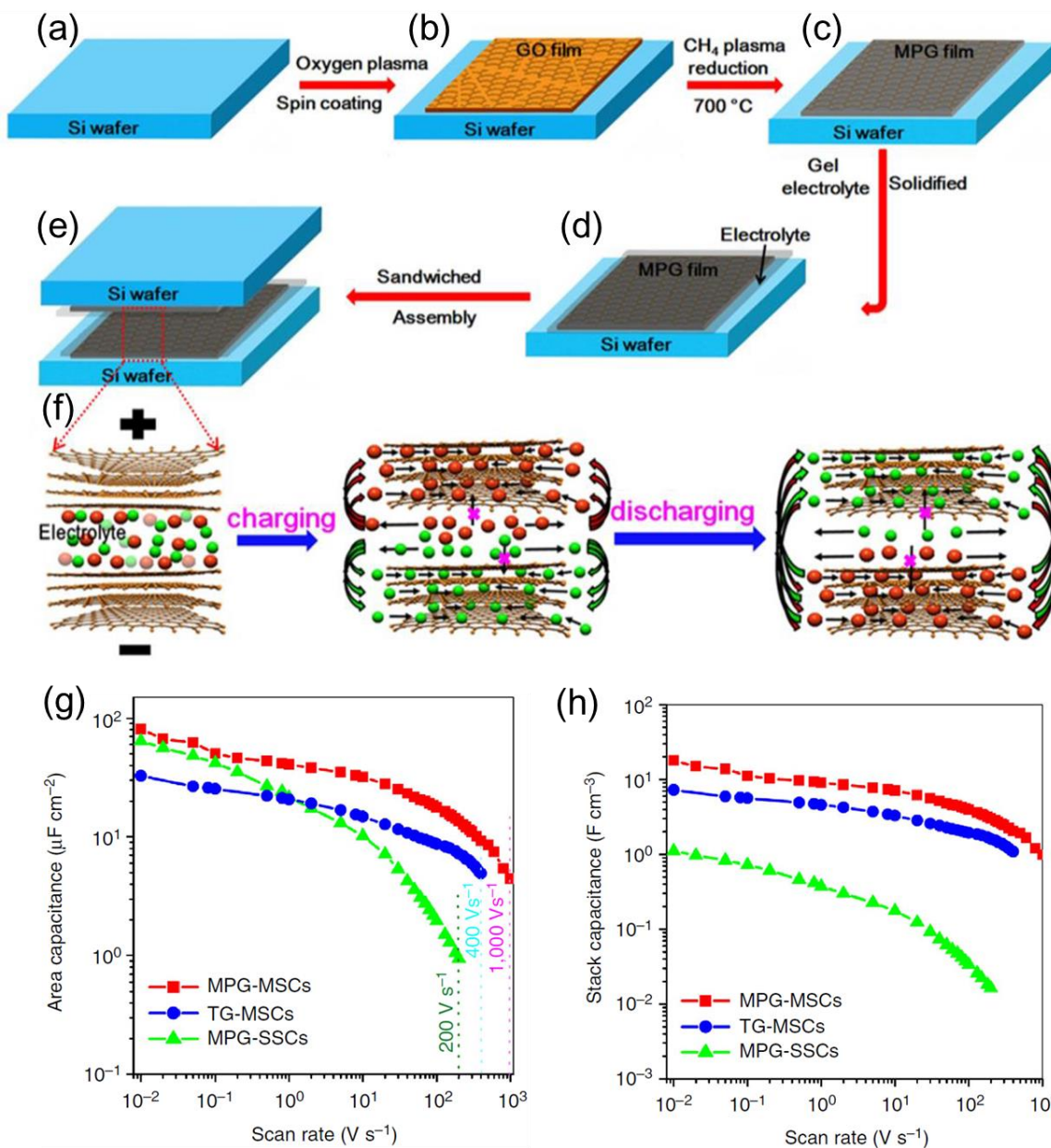


Figure 4.14 (a-f) Schematic illustration of the fabrication of MPG-SSCs. The fabrication process includes: (a) the oxygen plasma surface treatment of silicon wafer, spin coating of GO solution on surface-modified silicon, (b) CH₄ plasma reduction, (c)

drop casting and solidification of the solid-state gel electrolyte on the surface of MPG film, (d) assembly of two separated MPG films with gel electrolyte into one sandwiched device in (e). (f) The stack geometry of MPG-SSCs, revealing that the ions have to cross over from the electrode to the other electrode with a large diffusion distance via separator and electrode during charging and discharging process. (g,h) Evolution of the (g) area capacitance and (h) stack capacitance versus scan rate. The MPG-MSCs can operate at a higher scan rate of $1,000 \text{ V s}^{-1}$ and provide a capacitance 10 times larger than that of the sandwich device, for example at 200 V s^{-1} , indicating the potential for ultrahigh power delivery.

Despite the high stack capacitance, ultrahigh scan rate and cycling stability of the fabricated micro-supercapacitors, the area capacitance (which depends on the thickness of the electrode materials) is low compared to previously reported micro-supercapacitors based on carbide-derived carbon,³⁴ onion like carbon,³¹ ink-jet printed carbon,³⁵ and laser scribed graphene.³⁶ This is due to the fact that the thickness of the MPG-MSCs described in this work is only in terms of nanometre scale. Therefore, a major challenge remains to increase the thickness of the active materials in order to increase the area capacitance of MSCs without sacrificing the scan rate, stack capacitance and cycling stability in a given footprint of future micro-supercapacitor design.

4.6.3 Flexible MPG-MSCs

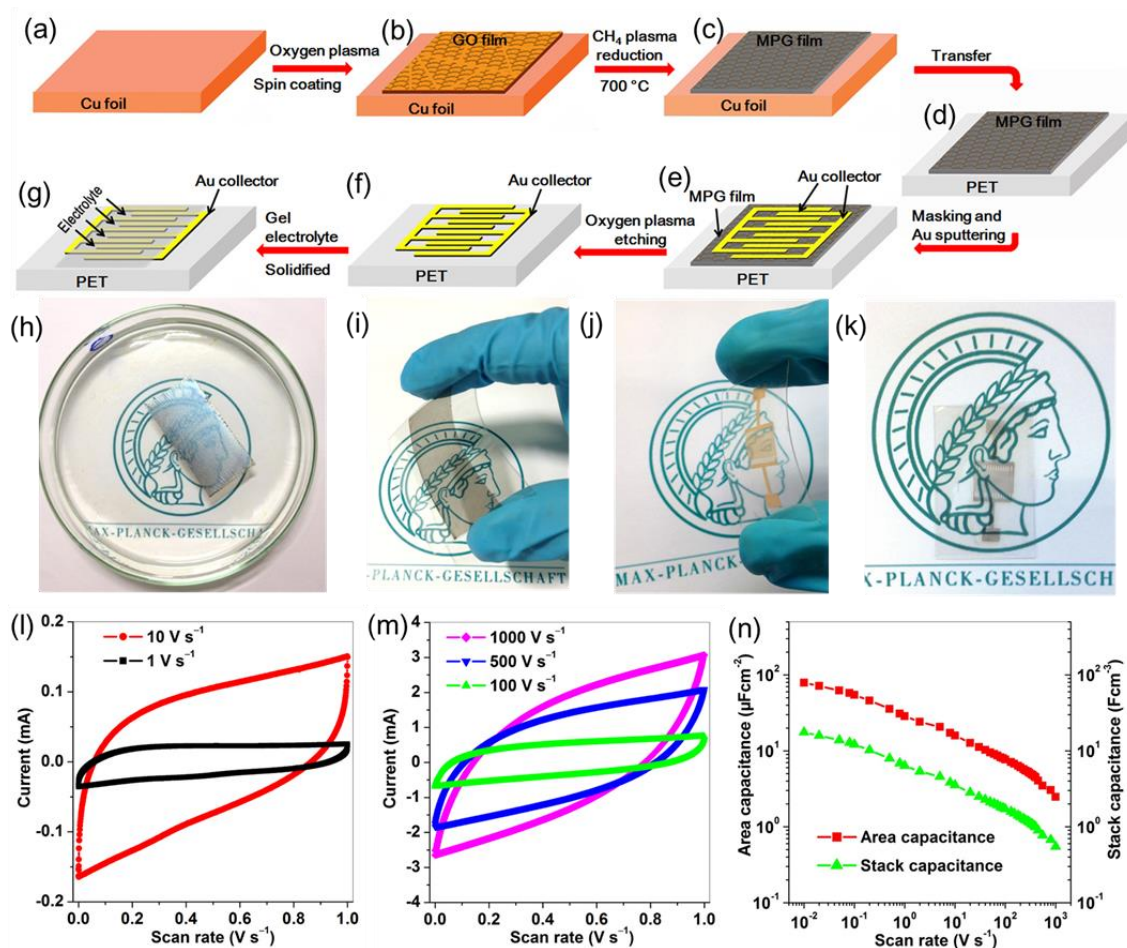


Figure 4.15 (a-g) Schematic illustration of the fabrication of flexible MPG-MSCs-PET. The fabrication process includes a sequence of (a) spin-coating of GO solution in Cu foil, (b) CH₄ plasma reduction, (c) transfer of MPG film from the Cu foil to PET substrate, (d) masking pattern and deposition of gold current collector, (e) oxidative etching, (f) drop casting of H₂SO₄/PVA gel electrolyte, and (g) solidification of gel electrolyte. (h-k) Optical images of (h) a 15-nm-thick MPG film (2×3 cm) on a polymethyl methacrylate (PMMA) support floated on the water surface after etching Cu foil by aqueous Fe(NO₃)₃ solution, (i) the MPG film transferred onto the PET substrate, (j),

k) the resulting MPG-MSCs-PET (j) with and (k) without Au collectors, displaying the flexible and transparent characteristics of the fabricated microdevices. (l, m) CV curves of the MPG-MSCs-PET obtained at different scan rates from (l) 1, 10, and (m) 100, 500, 1000 V s⁻¹ with a typical electric double-layer capacitive behavior, even at ultrahigh scan rates, demonstrating its ultrahigh power ability. (n) Area capacitance and stack capacitance of the MPG-MSCs-PET.

The fabrication method was further adapted to construct flexible MSCs on a polyethylene terephthalate (PET) substrate. Figure 4a-g illustrates the fabrication process of MPG-MSCs on a PET substrate (MPG-MSCs-PET). We first produced the MPG film from the spin-coated GO film on Cu foil, followed by CH₄ plasma treatment at 700 °C for 20 s (Figure 4.15a-c). Subsequently, the MPG film supported by PMMA film was transferred onto the PET substrate (PMMA/MPG/PET) via etching of Cu foil by a Fe(NO₃)₃ solution. The PMMA film was removed by acetone (Figure 4.15c,d). Other fabrication steps, including masking pattern, oxygen plasma etching, and addition/solidification of gel electrolyte (Figure 4.15e-g), were the same as for MPG-MSCs on a silicon wafer. The optical image of a typical PMMA-supported MPG film (15 nm thick) floated on the water surface is shown in Figure 4h. MPG film on the bent PET substrate (Figure 4.15i) positioned above a logo of the "Max-Planck Gesellschaft" shows the features of large-area uniformity, good transparency, and mechanical flexibility. The resulting MPG film had an electrical conductivity of ~297 S cm⁻¹. Importantly, the microdevices can be readily produced with (Figure 4.15j) and without Au collectors (removed by dropping in KI/I₂ solution, Figure 4.15k).

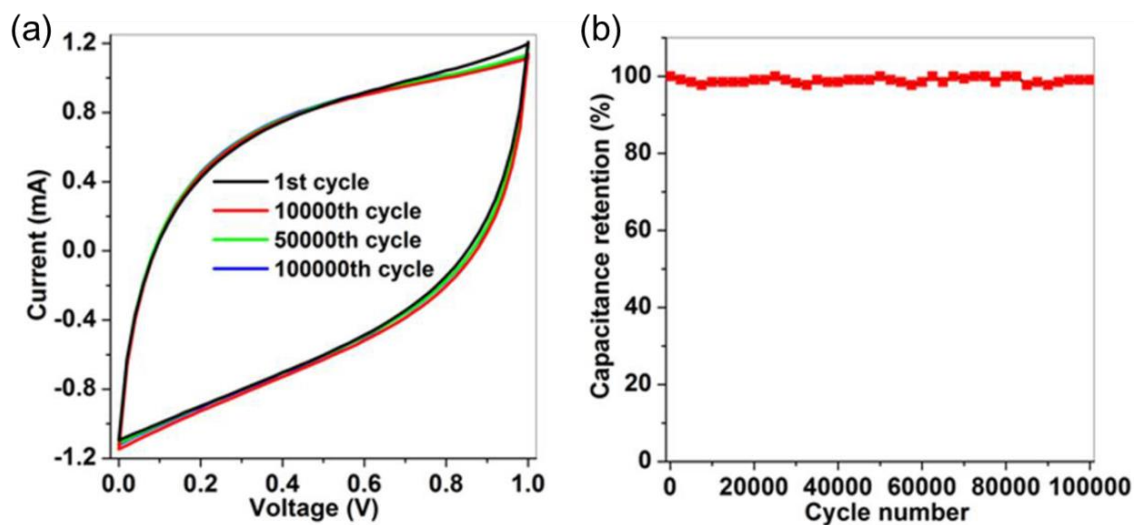


Figure 4.16 Cycling stability of flexible MPG-MSCs-PET. (a) CVs obtained at the 1st, 10000th, 50000th and 100,000th measure at 200 V s⁻¹, revealing almost similar curve shape. (b) The capacitance retention versus cycle number. The capacitance is retained as high as 99.1% after 100,000 cycles, revealing excellent cycling stability at ultrahigh charge/discharge rate of 200 V s⁻¹.

The electrochemical performance of MPG-MSCs-PET was first examined by CV measurement. Similar to MPG-MSCs, MPG-MSCs-PET can be also operated at an ultrahigh rate up to 1000 V s⁻¹ (Figure 4.15i,m). Furthermore, an area capacitance of ~78.9 $\mu\text{F cm}^{-2}$ and a stack capacitance of ~17.5 F cm⁻³ were obtained for MPG-MSCs-PET at 10 mV s⁻¹, comparable to the performance of MPG-MSCs on a silicon wafer. In addition, the flexible microdevices exhibited excellent cycling stability and mechanical stability. For example, up to ~99.1% of capacitance was maintained after 100,000 times at a scan rate of 200 V s⁻¹ (Figure 4.16b), and no capacity degradation was observed when the devices were bent for 100 times.

4.6.4 Ragone plot

Typically, a Ragone plot is used for performance comparisons of various energy-storage devices. On such a plot, the values of energy density are plotted versus power density. Both axes are logarithmic, which allows comparing performance of different types of devices (for example, Li-ion batteries, fuel cells, supercapacitors etc.). To demonstrate the overall performance of MPG-MSCs, a Ragone plot is shown in Figure 5. The data from MPG-SSCs and TG-MSCs, as well as a commercial high-energy lithium thin-film battery (4 V/500 μAh),³⁷ high-power aluminium electrolytic capacitor (3 V/300 μF)³⁸ and Panasonic Li-ion battery (780 mAh, 17 500)³⁷ are included for comparison. Remarkably, MPG-MSCs delivered a volumetric energy density of $\sim 2.5 \text{ mWh cm}^{-3}$, which is an order of magnitude higher than that of the typical supercapacitors of activated carbon ($< 1 \text{ mWh cm}^{-3}$), and well comparable to that of lithium thin-film batteries ($10^3 \sim 10^2 \text{ Wh cm}^{-3}$).³¹ In addition, MPG-MSCs manifest an ultrahigh power density of $\sim 495 \text{ W cm}^{-3}$ (even at a high energy density of 0.14 mWh cm^{-3}) discharged within an extremely short time ($\sim 1 \text{ ms}$). The powder density is at least 50 times higher than that of conventional supercapacitors (Figure 4.17), two times higher than that of the state-of-the-art MSCs, and comparable to that of high-power electrolytic capacitors ($10^1 \sim 10^3 \text{ W cm}^{-3}$).³⁸ To the best of our knowledge, this is the first report of MSCs with such excellent performance in terms of ultrahigh power and energy densities.

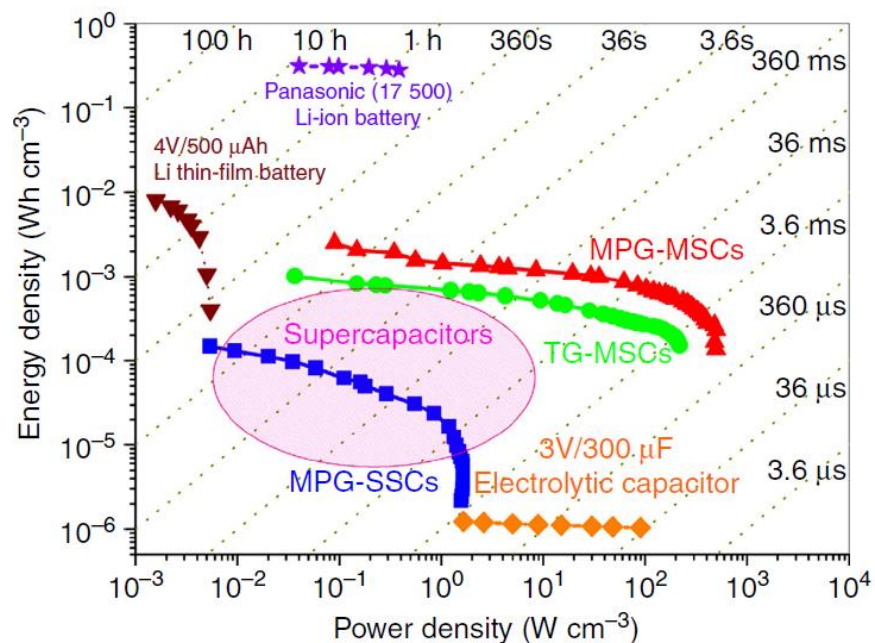


Figure 4.17 The comparison of energy and power density of MPG-MSCs with TG-MSCs, MPG-SSCs, commercially applied electrolytic capacitors,³⁸ lithium thin-film batteries,³¹ Panasonic Li-ion battery,³⁷ and conventional supercapacitors (indicated by the pink region), demonstrating that MPG-MSCs exhibit exceptional electrochemical energy storage with simultaneous ultrahigh energy density and power density.

The superior performance of graphene-based thin-film MSCs can be explained by the co-operative effects of the high conductivity of graphene materials and the in-plane geometry of the devices. First, interdigital microelectrodes in MPG-MSCs can maximise the use of the accessible surface area of graphene, which is responsible for the high-charge storage capacity. Second, the MPG film possesses high electrical conductivity which is another important factor for facilitating electron transport and thus generating high power supercapacitors. Last but not least, the in-plane interdigital electrodes in the

microdevices allow for ultrafast uptake of the flow of electrolyte ions into or removal from the graphene layers in a short diffusion pathway (Figure 4.11g).^{12,28} Moreover, the fabrication process of MPG-MSCs is simple, reliable, and can be scaled up to pattern hundreds to thousands of devices on one substrate in a relatively short period of time. Such microdevices manifest ultrahigh volumetric energy densities and power densities operable at ultrafast charge and discharge rates. Indeed, MPG-MSCs can also work collaboratively when connected in parallel or in series. This is very important when compared with micro-batteries whose finite lifetime could be a major problem when they have to be embedded in permanent structures, such as biomedical implants, active radio frequency identification tags and embedded micro-sensors where no maintenance or replacement is possible. As these micro-supercapacitors can be directly integrated on-chip, they may help to better extract the energy from solar, mechanical and thermal sources and thus make more efficient self-powered systems.³⁹ They could also be fabricated on the backside of solar cells in both portable devices and rooftop installations. Other applications could arise that take advantage of the flexible nature of the substrates, such as electronics embedded into clothing, large-area flexible displays and roll-up portable displays.^{40,41}

4.7 Conclusion

We demonstrate highly efficient reduction of GO films into large area, uniform, continuous, and conductive graphene films using methane plasma. Exposure of the GO film into the plasma only for a few seconds can effectively de-oxygenate and restore the π -conjugation of graphene. The plasma rGO has a high C/O ratio of 12.9 and hole transport mobility of $1.70 \text{ cm}^2 \text{ V}^{-1} \text{ s}^{-1}$. Moreover, the prepared graphene film reveals a sheet resistance of $4.12 \text{ k}\Omega/\text{sq}$. with $\sim 80\%$ transmittance only after 10 sec of plasma treatment. The sheet resistance is significantly lower than that of conventional thermal and/or chemically reduced GO films. This can be attributed to the efficient removal of oxygen functional groups by reactive ion species and radicals produced in the CH_4 plasma. Further, we fabricated graphene based in-plane interdigital MSCs on arbitrary substrates by using plasma rGO films. The resulting MSCs deliver an area capacitance of $80.7 \text{ }\mu\text{F cm}^{-2}$ and a stack capacitance of 17.9 F cm^{-3} . Further, they show a power density of 2.5 mWh cm^{-3} that is comparable to lithium thin-film batteries, in association with superior cycling stability. Such microdevices allow for operations at ultrahigh rate up to $1,000 \text{ V s}^{-1}$, three orders of magnitude higher than that of conventional supercapacitors. Nevertheless, compared with the CVD grown and/or mechanically exfoliated graphene, the quality of the reduced GO is still poor. In addition, as various hazardous chemicals have been used during the preparation of GO preparation which inhibits their industrialization. Thereby, alternative chemical exfoliation methods need to be developed in order to obtain high quality graphene in bulk-scale. Towards this end, electrochemical exfoliation of graphite is an environmentally friendly method to produce high-quality graphene that we will discuss in the next chapter.

4.8 References

- (1) Jung, I.; Dikin, D.; Park, S.; Cai, W.; Mielke, S. L.; Ruoff, R. S. *J. Phys. Chem. C* **2008**, *112*, 20264.
- (2) Eda, G.; Fanchini, G.; Chhowalla, M. *Nat. Nanotechnol.* **2008**, *3*, 270.
- (3) Gomez-Navarro, C.; Weitz, R. T.; Bittner, A. M.; Scolari, M.; Mews, A.; Burghard, M.; Kern, K. *Nano Lett* **2007**, *7*, 3499.
- (4) Park, S.; Hu, Y. C.; Hwang, J. O.; Lee, E. S.; Casabianca, L. B.; Cai, W. W.; Potts, J. R.; Ha, H. W.; Chen, S. S.; Oh, J.; Kim, S. O.; Kim, Y. H.; Ishii, Y.; Ruoff, R. S. *Nat. Commun.* **2012**, *3*.
- (5) Mattevi, C.; Eda, G.; Agnoli, S.; Miller, S.; Mkhoyan, K. A.; Celik, O.; Mostrogiovanni, D.; Granozzi, G.; Garfunkel, E.; Chhowalla, M. *Adv. Funct. Mater.* **2009**, *19*, 2577.
- (6) Yang, D.; Velamakanni, A.; Bozoklu, G.; Park, S.; Stoller, M.; Piner, R. D.; Stankovich, S.; Jung, I.; Field, D. A.; Ventrice, C. A.; Ruoff, R. S. *Carbon* **2009**, *47*, 145.
- (7) Gilje, S.; Han, S.; Wang, M.; Wang, K. L.; Kaner, R. B. *Nano Lett.* **2007**, *7*, 3394.
- (8) Wang, X.; Zhi, L. J.; Mullen, K. *Nano Lett.* **2008**, *8*, 323.
- (9) Pang, S. P.; Tsao, H. N.; Feng, X. L.; Mullen, K. *Adv. Mater.* **2009**, *21*, 3488.
- (10) Baraket, M.; Walton, S. G.; Wei, Z.; Lock, E. H.; Robinson, J. T.; Sheehan, P. *Carbon* **2010**, *48*, 3382.
- (11) Cheng, M.; Yang, R.; Zhang, L. C.; Shi, Z. W.; Yang, W.; Wang, D. M.; Xie, G. B.; Shi, D. X.; Zhang, G. Y. *Carbon* **2012**, *50*, 2581.
- (12) Moon, I. K.; Lee, J.; Ruoff, R. S.; Lee, H. *Nat. Commun.* **2010**, *1*, 73.
- (13) Fang, M.; Zhang, Z.; Li, J. F.; Zhang, H. D.; Lu, H. B.; Yang, Y. L. *J. Mater. Chem.* **2010**, *20*, 9635.
- (14) Tung, V. C.; Allen, M. J.; Yang, Y.; Kaner, R. B. *Nat. Nanotechnol.* **2009**, *4*, 25.
- (15) Stankovich, S.; Dikin, D. A.; Piner, R. D.; Kohlhaas, K. A.; Kleinhammes, A.; Jia, Y.; Wu, Y.; Nguyen, S. T.; Ruoff, R. S. *Carbon* **2007**, *45*, 1558.
- (16) Tuinstra, F.; Koenig, J. L. *J. Chem. Phys.* **1970**, *53*, 1126.

- (17) Yuan, G. D.; Zhang, W. J.; Yang, Y.; Tang, Y. B.; Li, Y. Q.; Wang, J. X.; Meng, X. M.; He, Z. B.; Wu, C. M. L.; Bello, I.; Lee, C. S.; Lee, S. T. *Chem. Phys. Lett.* **2009**, *467*, 361.
- (18) Wu, Z. S.; Parvez, K.; Feng, X.; Mullen, K. *Nat. Commun.* **2013**, *4*, 2487.
- (19) Bagri, A.; Mattevi, C.; Acik, M.; Chabal, Y. J.; Chhowalla, M.; Shenoy, V. B. *Nat. Chem.* **2010**, *2*, 581.
- (20) Lee, S. W.; Mattevi, C.; Chhowalla, M.; Sankaran, R. M. *J. Phys. Chem. Lett.* **2012**, *3*, 772.
- (21) Park, S.; An, J.; Potts, J. R.; Velamakanni, A.; Murali, S.; Ruoff, R. S. *Carbon* **2011**, *49*, 3019.
- (22) Compton, O. C.; Jain, B.; Dikin, D. A.; Abouimrane, A.; Amine, K.; Nguyen, S. T. *ACS Nano* **2011**, *5*, 4380.
- (23) Ohta, T.; Bostwick, A.; Seyller, T.; Horn, K.; Rotenberg, E. *Science* **2006**, *313*, 951.
- (24) Liu, H. T.; Zhang, L.; Guo, Y. L.; Cheng, C.; Yang, L. J.; Jiang, L.; Yu, G.; Hu, W. P.; Liu, Y. Q.; Zhu, D. B. *J. Mater. Chem. C* **2013**, *1*, 3104.
- (25) Wang, S.; Ang, P. K.; Wang, Z. Q.; Tang, A. L. L.; Thong, J. T. L.; Loh, K. P. *Nano Lett.* **2010**, *10*, 92.
- (26) Li, X. L.; Zhang, G. Y.; Bai, X. D.; Sun, X. M.; Wang, X. R.; Wang, E.; Dai, H. J. *Nat Nanotechnol* **2008**, *3*, 538.
- (27) Huang, L.; Liu, Y.; Ji, L. C.; Xie, Y. Q.; Wang, T.; Shi, W. Z. *Carbon* **2011**, *49*, 2431.
- (28) Wu, J. B.; Becerril, H. A.; Bao, Z. N.; Liu, Z. F.; Chen, Y. S.; Peumans, P. *Appl. Phys. Lett.* **2008**, *92*.
- (29) Sung, J. H.; Kim, S. J.; Jeong, S. H.; Kim, E. H.; Lee, K. H. *J. Power Sources* **2006**, *162*, 1467.
- (30) Chmiola, J.; Largeot, C.; Taberna, P. L.; Simon, P.; Gogotsi, Y. *Science* **2010**, *328*, 480.
- (31) Pech, D.; Brunet, M.; Durou, H.; Huang, P. H.; Mochalin, V.; Gogotsi, Y.; Taberna, P. L.; Simon, P. *Nat. Nanotechnol.* **2010**, *5*, 651.
- (32) Adriaanse, C. *Chem. Ind-London* **2011**, 11.

-
- (33) Rolison, D. R.; Long, J. W.; Lytle, J. C.; Fischer, A. E.; Rhodes, C. P.; McEvoy, T. M.; Bourga, M. E.; Lubers, A. M. *Chem. Soc. Rev.* **2009**, *38*, 226.
- (34) Heon, M.; Lofland, S.; Applegate, J.; Nolte, R.; Cortes, E.; Hettinger, J. D.; Taberna, P. L.; Simon, P.; Huang, P. H.; Brunet, M.; Gogotsi, Y. *Energ. Environ. Sci.* **2011**, *4*, 135.
- (35) Pech, D.; Brunet, M.; Taberna, P. L.; Simon, P.; Fabre, N.; Mesnilgrete, F.; Conedera, V.; Durou, H. *J. Power Sources* **2010**, *195*, 1266.
- (36) El-Kady, M. F.; Kaner, R. B. *Nat. Commun.* **2013**, *4*.
- (37) Nagasubramanian, G.; Jungst, R. G.; Doughty, D. H. *J. Power Sources* **1999**, *83*, 193.
- (38) El-Kady, M. F.; Strong, V.; Dubin, S.; Kaner, R. B. *Science* **2012**, *335*, 1326.
- (39) Wang, Z. L. *Adv. Mater.* **2012**, *24*, 280.
- (40) Miller, J. R.; Outlaw, R. A.; Holloway, B. C. *Science* **2010**, *329*, 1637.
- (41) Nishide, H.; Oyaizu, K. *Science* **2008**, *319*, 737.

Chapter 5

Electrochemically exfoliated graphene as solution processable, highly conductive electrodes for organic electronics

As described in Chapter 4, graphene obtained from chemical exfoliation of graphite via Hummers method (i.e. GO) possesses easy solution processability and can be produced in a large scale. However, the bottleneck of GO is their poor quality in terms of low electrical conductivity which depends largely on the removal of the functional groups through chemical or thermal reduction. In this chapter, we demonstrate that electrochemical exfoliation of graphite in acidic media furnishes graphene sheets in high quality. The electrochemically exfoliated graphene (EG) contains a high yield (> 80 %) of 1 to 3 layer graphene flakes with high C/O ratio of 12.3 and low sheet resistance ($4.8 \text{ k}\Omega \text{ sq.}^{-1}$ for a single EG sheet) compared to thermally and/or chemically reduced GO. Due to the solution-processability of EG, vacuum filtration method in association with dry transfer is introduced to produce large area and highly conductive graphene films on various substrates. Moreover, we demonstrate that the patterned EG can serve as high-performance source/drain (S/D) electrodes for organic field-effect transistor (OFETs).

5.1 Introduction

A major challenge of organic electronics is the development of robust techniques for fabricating highly-conductive, flexible, and transparent electrodes.¹ The most widely used transparent electrode is indium tin oxide (ITO) which has an optical transparency of more than 80% in the visible light range, a favorable work function (~ 4.8 eV), and a sheet resistance of 10 to 30 $\Omega \text{ sq.}^{-1}$.²⁻⁴ There are several limitations to ITO, however, such as sensitivity to acidic and basic environments, high surface roughness, and increasing cost due to the scarcity of indium. In addition, ITO is brittle which leads to microcracks when the material is bent as well as dramatically reduced conductivity. Many alternative materials have been developed to replace ITO such as conducting polymers like poly(3,4-ethylenedioxythiophene):poly(styrenesulfonate) (PEDOT:PSS),⁵ carbon nanotubes (CNTs),^{6,7} metal grids, and metallic nanowires.^{8,9} Among these materials, CNT films exhibit high transparency across the visible light spectrum, but the high resistance at the junctions between carbon nanotubes obstructs conductive pathways within the film.¹⁰

Graphene, which features high electrical conductivity, flexibility, and good mechanical and thermal stability, has emerged as a new-generation electrode material for organic electronic devices.¹¹⁻¹³ Graphene-based electrodes, obtained from either solution-processed reduced graphene oxide (rGO) or graphene grown by chemical vapor deposition (CVD) methods, have been used for organic photovoltaics,¹⁴ light-emitting diodes (OLEDs),¹⁵ field-effect transistors (OFETs),^{16,17} and photodetectors.¹⁸ Electrodes prepared from rGO require chemical and/or thermal treatment of GO to partially remove the oxygen-containing groups and to restore the electrical properties. Chemical reduction by toxic hydrazine generally introduces impurities in rGO¹⁹ while high-temperature treatment is

incompatible with plastic or glass substrates. Moreover, high-quality graphene directly grown on Ni or Cu substrates by CVD requires a multi-step transferring process involving the use of poly(methylmethacrylate) and/or polydimethylsiloxane.^{20,21} The latter are difficult to remove and may even damage the graphene film.^{22,23} Direct exfoliation of graphite in solution, such as electrochemical, sonochemical, and liquid-phase exfoliation,²⁴⁻²⁸ allows for the fabrication of high-quality graphene electrodes *via* a low temperature process. Nevertheless, the yields of graphene (typically 1 to 4 layers) synthesized by these protocols remain low (< 50%). In addition, due to the poor solution-processability of exfoliated graphene in high-boiling point solvents (such as *N*-Methyl-2-pyrrolidone (NMP) or *N,N'*-Dimethylformamide (DMF)), it is difficult to prepare graphene films of a large area using conventional solution-processing techniques such as dip-coating,¹⁴ drop casting,²⁸ spin coating,²⁹ spray casting,³⁰ ink-jet printing,³¹ and Langmuir-Blodgett deposition.³² Therefore, the development of a low-cost fabrication protocol leading to highly conductive, uniform graphene films based on solution-processable graphene is highly desirable.

In this chapter, we demonstrate that electrochemical exfoliation of graphite furnishes graphene sheets in high quality and high yield. The electrochemically exfoliated graphene (EG) has a large sheet size ($\sim 10 \mu\text{m}$), low oxygen content (*i.e.*, 7.5 at%), and a sheet resistance of only $4.8 \text{ k}\Omega \text{ sq.}^{-1}$ without any further chemical or thermal treatment. Moreover, the sheet resistance is significantly lower than that of reduced GO. Due to the solution-processability ($\sim 1 \text{ mg mL}^{-1}$ in DMF) of such graphene sheets, large and homogeneous graphene films can be fabricated on both rigid and flexible substrates by vacuum filtration and subsequent transfer to the desired substrates. The resulting graphene films exhibit sheet resistances of 4.1 and $2.4 \text{ k}\Omega \text{ sq.}^{-1}$ with transmittances of 85% and 73%,

respectively. Patterned graphene films can serve as high-performance source/drain (S/D) electrodes for OFETs. Nevertheless, the preparation of solution-processable high quality graphene is expected to play a critical role in the field of organic electronics and energy storage devices.

5.2 Electrochemical exfoliation of graphite

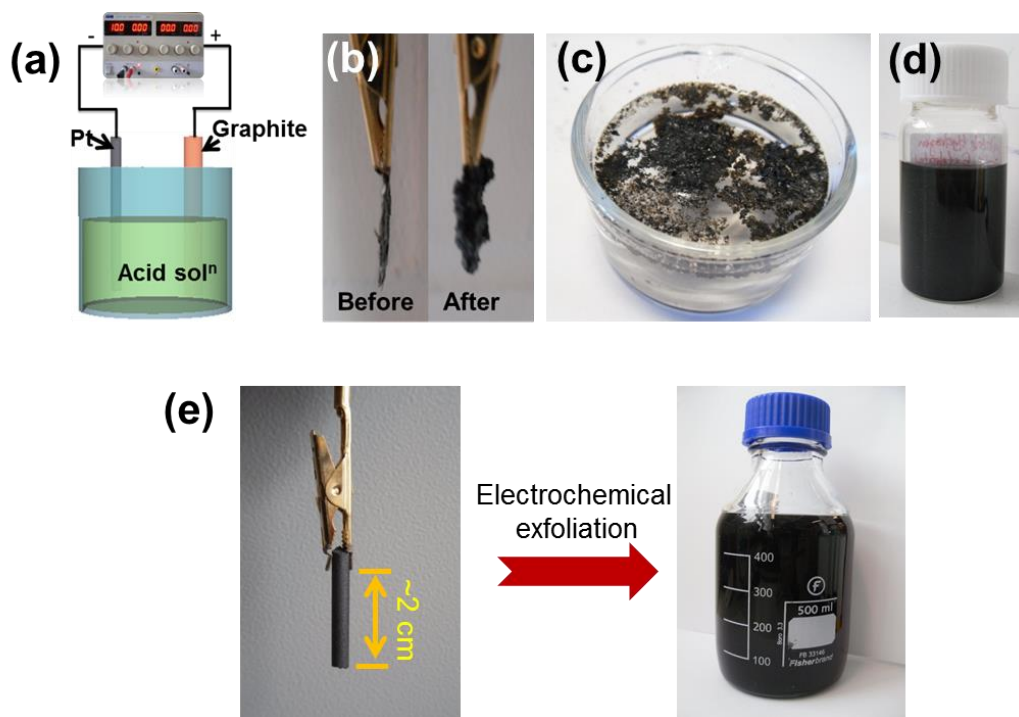


Figure 5.1 (a) Schematic illustration of the electrochemical exfoliation of graphite, (b) photographs of graphite flakes before and after exfoliation, (c) EG floating on top of water, (d) dispersed graphene sheets ($\sim 1 \text{ mg mL}^{-1}$) in DMF, and (e) Photographs representing large scale production of EG where, (left) graphite electrode used for electrochemical process and (right) dispersed EG (0.70 mg mL^{-1}) after exfoliation.

The experimental setup for electrochemical exfoliation of graphite is illustrated in Figure 5.1a. Typically, natural graphite flakes, platinum wire, and 0.1 M H₂SO₄ solution were used as working electrodes, counter-electrodes, and electrolytes, respectively. When a positive voltage (*i.e.*, +10 V) was applied to a graphite electrode, the graphite flakes begin to expand, quickly dissociate, and spread into the solution (Figure 5.1b and c). The bias voltage was kept constant for 2 min to complete the exfoliation process. Afterwards, the exfoliated graphitic materials was collected by vacuum filtration through a polytetrafluoroethylene (PTFE) membrane filter (pore size 0.2 μm) and washed repeatedly with DI water to remove the residual acid. Finally, the obtained powder was dispersed in DMF, resulting in EG sheets (Figure 5.1d). The yield of EG was generally higher than 60 % of the total amount of starting graphite materials. Notably, a dispersion of EG with a concentration up to 1.0 mg mL⁻¹ in DMF can be obtained and remains stable for several weeks without evidence of agglomeration. Moreover, the exfoliation process can be readily scaled up. For example, using only ~ 2 cm size graphite rod as an electrode, more than 350 mg of EG was obtained in less than 30 min (Figure 5.1e). Notably, from the starting of the exfoliation process to the stable dispersion of EG in DMF, takes less than an hour. Since, a stable dispersion of EG can only be obtained in solvents with a surface tension of ~40 mJ m⁻², such as DMF and/or NMP etc., one can expect that the produced EG is of high-quality (*i.e.* low defect density) which will be discussed later in this chapter. Nevertheless, the process opens up the possibility for the industrial production of graphene. This can be achieved by making electrochemical exfoliation a continuous process. For example, a series of several large sized graphite electrodes can be put together in a big tank filled with electrolyte and after the exfoliation process completes, then automatically replaced them with new graphite electrodes.

5.2.1 Exfoliation mechanism:

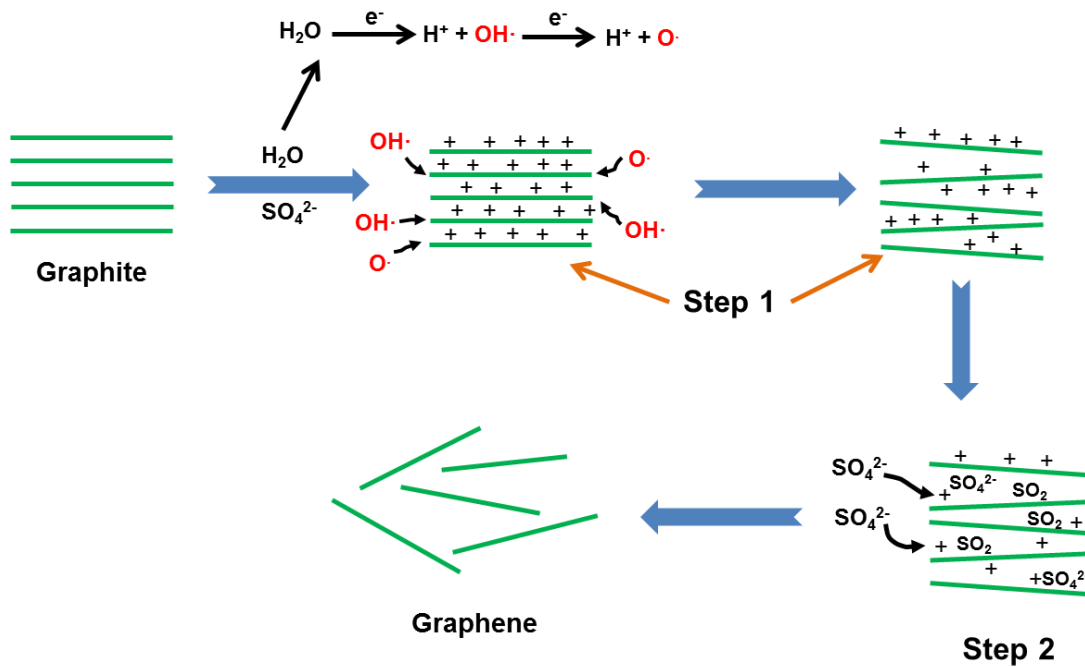


Figure 5.2 Schematic illustration of the proposed mechanism of electrochemical exfoliation.

The mechanism of graphite exfoliation in 0.1 M H_2SO_4 is depicted in Figure 5.2: first, applying bias voltage results in the oxidation of water, producing hydroxyl ($\text{OH}\cdot$) and oxygen radicals ($\text{O}\cdot$).³³ Oxidation or hydroxylation by these radicals initially occurs at edge sites and grain boundaries of the graphite electrode. Second, defective sites at the edges or grain boundaries open up due to oxidation which facilitates intercalation by anionic SO_4^{2-} . This process leads to the release of gaseous SO_2 and/or anion depolarization and causes expansion of the interlayer distance of graphite.³⁴ It should be noted that, the electrochemical intercalation and/or exfoliation of graphite in acidic electrolytes such as H_2SO_4 , also results in the overoxidation of graphite.^{35,36} A detailed graphite exfoliation mechanism will be discussed in the next chapter (i.e. Chapter 6).

5.2.2 Role of water and electrolyte concentration

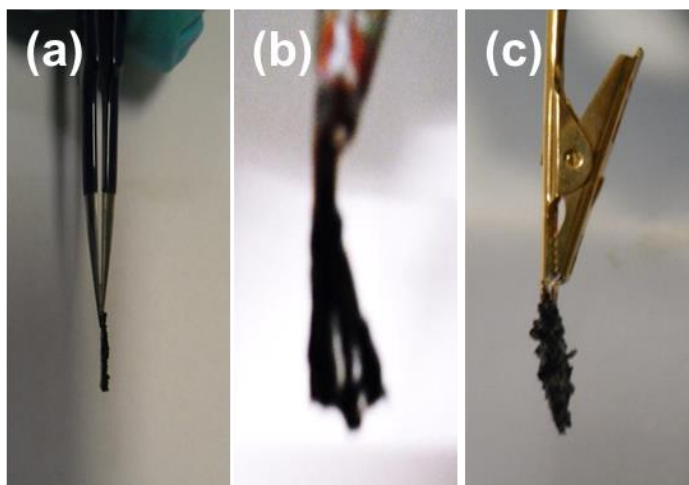


Figure 5.3 Photographs of graphite electrodes (a) before, (b) and (c) after electrochemical process in pure H_2SO_4 and $\text{CH}_3\text{COOH} : \text{H}_2\text{SO}_4$ (1:1) electrolytes, respectively. A bias voltage of + 10V was kept constant for 2h in each case.

To understand the role of electrolytes during the exfoliation process, controlled experiments using H_2SO_4 with higher concentrations (1.0 and 5.0 M) were performed. The exfoliation efficiency of graphite in 1.0 and 5.0 M H_2SO_4 was much lower than that in 0.1 M H_2SO_4 , and the corresponding yield of EG was ~25% and ~7%, respectively. Exfoliation in 5.0 M H_2SO_4 mainly generated fragments of graphite particle which rapidly suspends during exfoliation. Moreover, when a pure H_2SO_4 or H_2SO_4 /acetic acid mixture (1:1 in ratio) was used as the electrolyte, the graphite electrode remained intact or slightly expanded due to the intercalation of negative ions when a voltage was applied for 2 h (Figure 5.3). These findings suggest that the presence of water in the electrolyte is crucial for the generation of oxygen or hydroxyl radicals that can react with graphite at the initial stage. When diluted H_2SO_4 (*i.e.* 0.05 M and 0.01 M) was used, however, exfoliation only occurred at a higher voltage (+12.1 and +16.0 V for 0.05 M and 0.01 M, respectively) at a much lower rate

(several hours were required). The EG yield for 0.05 M and 0.01 M H₂SO₄ was ~34% and ~2% respectively. The low exfoliation efficiency of EG in diluted H₂SO₄ is most likely due to the inefficient intercalation of anions into the graphite.³⁵

5.3 Morphology of exfoliated graphene

The morphology and number of layers in the EG sheets were first investigated by atomic force microscopy (AFM) (Figure 3.4). The EG sheet was deposited on SiO₂ using the Langmuir-Blodgett (LB) technique (Figure 5.4a). For a typical experiment, the EG dispersion in 1:3 DMF/chloroform was added drop-wise onto the water surface. A faint black colored film was observed on the water surface after adding the EG dispersion. The film was compressed by LB trough barriers while the surface pressure was monitored using a tensiometer. Thus, EG sheets were uniformly deposited on SiO₂ by vertically dip-coating the substrate, followed by thermal annealing at 200 °C for 30 min to remove the residual solvent. A histogram acquired across the boundary (inset of Figure 5.4b) revealed a mean thickness of ~0.86 nm (Figure 5.4b) for monolayer graphene which is 0.6 to 0.7 nm higher than that of pristine graphene on SiO₂.³⁷ This result implies that a certain amount of oxygen-containing groups are decorated on the graphene surface. The measured thickness of bilayer graphene was ~1.5 nm (Figure 5.4c). The thickness distribution of 80 samples of EG sheets calculated from the AFM height profile is shown in Figure 3.4d. Remarkably, more than 80 % of the graphene sheets comprised 1 to 3 layers with bilayer graphene (~35%) as a dominant product (Figure 5.4d). The size of the EG sheets was 5 to 10 μm which is much larger than the size of previously reported exfoliated graphene.^{24,25,27}

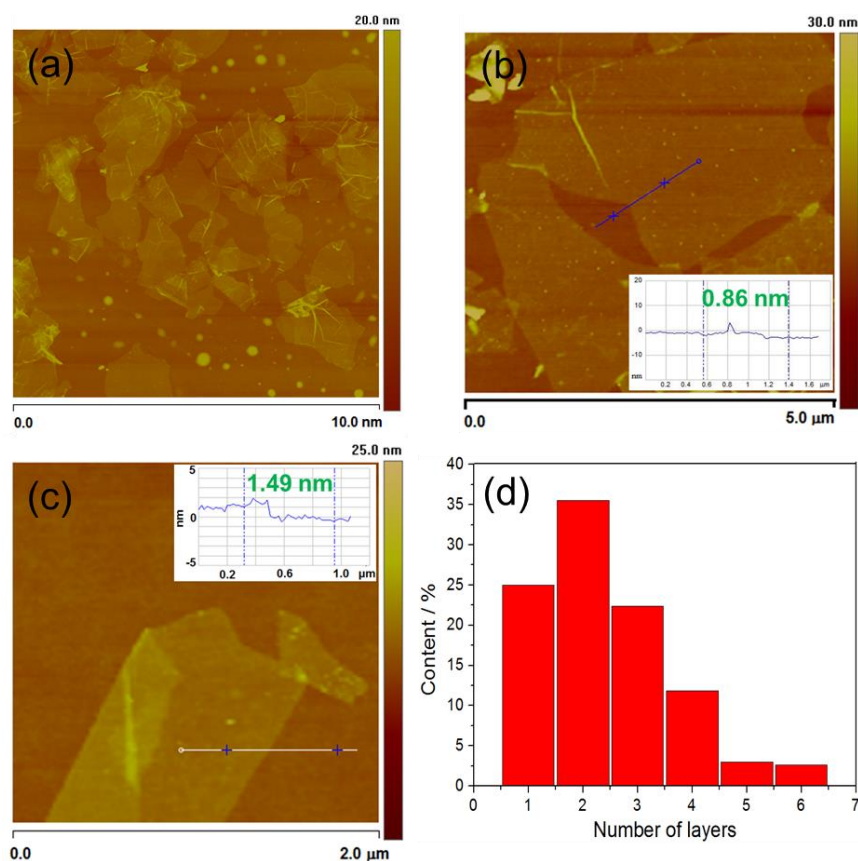


Figure 5.4 Typical AFM images of (a) EG sheets on SiO₂ substrates prepared by Langmuir-Blodgett (LB) assembly and, (b) single layer EG, (c) bi-layer EG and, (d) statistical thickness analysis of graphene sheets by AFM. Inset of (b) and (c) are the height profile of EG sheets.

Transmission electron microscopy (TEM) further confirmed a mean size of $\sim 10 \mu\text{m}$ for EG (Figure 5.5a, b). High-resolution TEM (HRTEM) studies provided further support that the EG sheets ranged from a single layer up to four layers (Figure 5.5c to e). A typical HRTEM image of bilayer graphene with an interlayer distance of $\sim 0.34 \text{ nm}$ is presented in Figure 2d. Moreover, the selected area electron diffraction (SAED) pattern (Figure 5.5f) of the graphene sheets exhibits the typical 6-fold symmetry, consistent with the hexagonal crystalline structure of a bilayer graphene sheet.³⁸

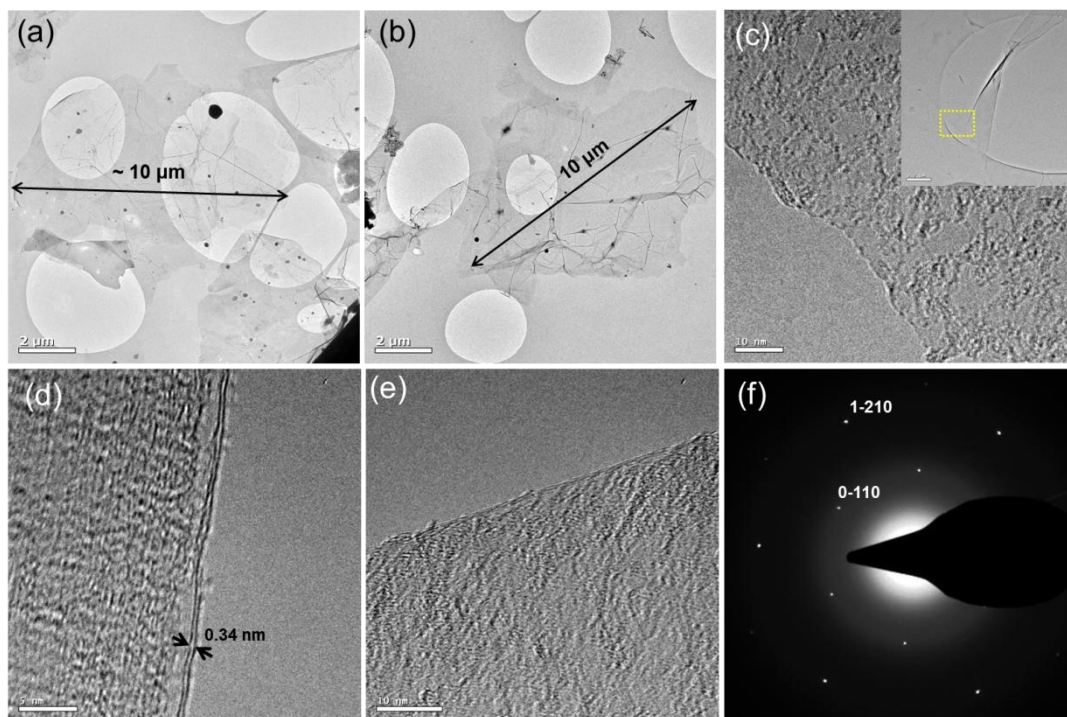


Figure 5.5 (a) and (b) TEM images of EG sheets indicating lateral size, (c), (d) and (e) HRTEM images of single-, bi- and four-layer graphene. Inset of (c) is the low magnification image of EG. To identify the number of graphene layers, the images are taken at the edge (as indicated by the dashed box). (f) SAED pattern of bi-layer graphene.

5.4 Structural characterizations

In order to investigate the chemical nature of the as-prepared EG sheets, X-ray photoelectron spectroscopy (XPS) characterization was performed by Dr. Shubin Yang in Rice University, USA. As shown in Figure 5.6a, approximately 7.5 % of oxygen is present in EG, attributable to the oxidation of graphene which was unavoidable during the electrochemical process. Nevertheless, a high C/O ratio of about 12.3 can be achieved for EG, in contrast to rGO (C/O ratio \sim 3-10) obtained by chemical or thermal reduction of

GO.^{39,40} The deconvoluted XPS spectra of the C 1s peak (~ 284 eV) in Figure 3.6b further shows the presence of 5.62 at% C-OH (285.4 eV) and 1.88 % C(O)-O (290.0 eV) functional groups (Figure 5.6b).

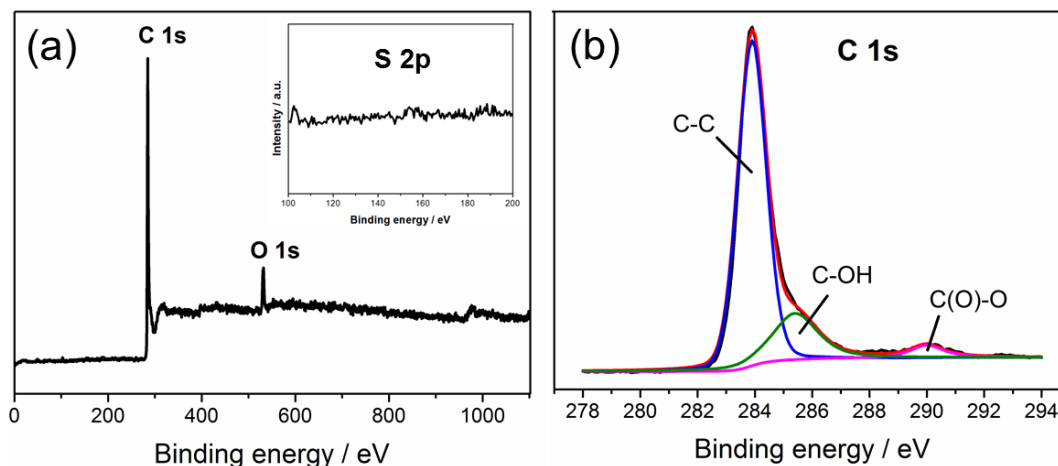


Figure 5.6 (a) XPS survey spectra and, (b) high-resolution XPS of the C 1s peak for EG. Inset of (a) indicates the absence of sulphur.

The Raman spectra (recorded with a Bruker RFS 100/S spectrometer) of a bilayer EG sheet displayed an intense 2D and G peak at ~ 2710 and ~ 1586 cm^{-1} , respectively (Figure 5.7a). Moreover, a defect-related D peak was observed at ~ 1356 cm^{-1} . The intensity ratio of D to G (*i.e.*, I_D/I_G) was calculated to be 0.40. This is much lower than that of chemically or thermally reduced GO (~ 1.2 to 1.5).^{41,42} The intensity ratio of 2D to G (*i.e.*, I_{2D}/I_G) is normally related to the graphitization degree (for C=C sp^2 bonds) in graphitic carbons.⁴³ The I_{2D}/I_G ratio (0.67) of bilayer EG graphene sheets produced in this work is significantly higher than that of rGO,^{44,45} further suggesting the high quality of the EG. Further, it is found that the exfoliation in higher concentration of H_2SO_4 (1.0 M and 5.0 M) resulted in an intense D peak with an I_D/I_G ratio of 0.96 and 1.12, respectively (Figure 5.7b). Moreover, the intensity of D' peak (~ 1620 cm^{-1}) which is attribute to the sp^3 type defects in

graphene increases with concentration of the electrolyte.⁴⁶ These results suggest that the electrochemical exfoliation in concentrated H_2SO_4 (> 0.1 M) leads to a decrease in average size of sp^2 domains and/or increase of structural defects, possibly due to the higher degree of oxidation.⁴⁷ Therefore, electrochemical exfoliation of graphite in concentrated H_2SO_4 (> 0.1 M) not only gives low yield of exfoliated product (discussed earlier) but also contains higher defect density in graphene resulting from the over-oxidation by acid.

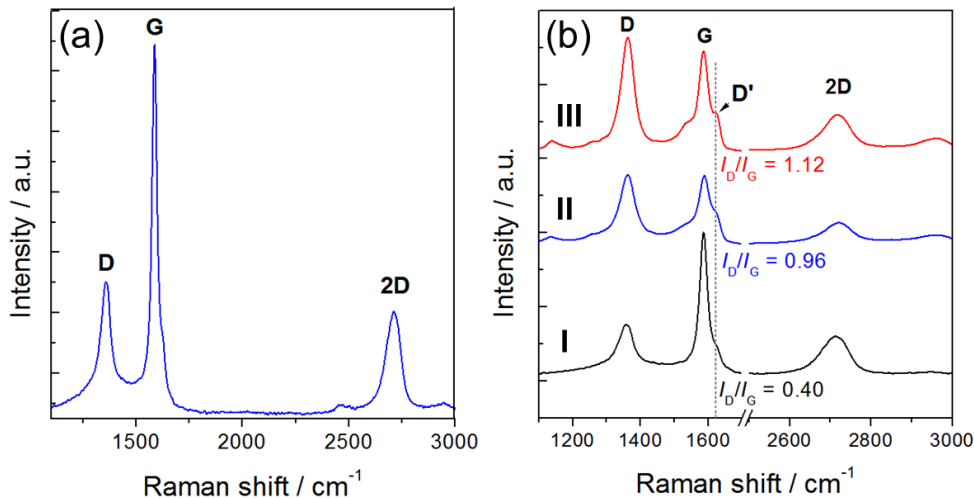


Figure 5.7 Raman spectrum (excited by 488 nm laser) of (a) bi-layer EG flake and (b) few layer EG sheets obtained in different concentration of electrolytes where, (I) 0.1 M, (II) 1.0 M and (III) 5.0 M of H_2SO_4 .

5.5 Electronic properties

The electronic properties of the resulting EG sheets were examined by bottom-gate, top-contact transistors based on a thin EG film or bilayer EG sheet. Thin-film and isolated sheets of EG on $\text{SiO}_2/\text{p-Si}$ were prepared by the LB method. Afterwards, a 60 nm thick Au was evaporated through a shadow mask to formulate S/D electrodes. To fabricate a single

EG sheet based FET device, 100 nm thick platinum (Pt) was deposited by focused ion-beam (FIB) to connect the isolated graphene sheet with Au electrodes. The thickness of the EG film ranged from 0.8 to 3.5 nm (roughness, R_a : 1.96 nm). The electrical properties of EG based transistors carried out inside a dry nitrogen glovebox with a Keithly 4200 semiconductor parameter analyzer. The field-effect mobility was extracted from the slope ($\Delta I_d/\Delta V_g$) of the linear regime of the transfer curves using the equation, $\mu = (L/WC_iV_d) \times (\Delta I_d/\Delta V_g)$, where ‘ L ’ and ‘ W ’ are channel length and width and ‘ C_i ’ (11 nF cm⁻²) is the capacitance.²⁸

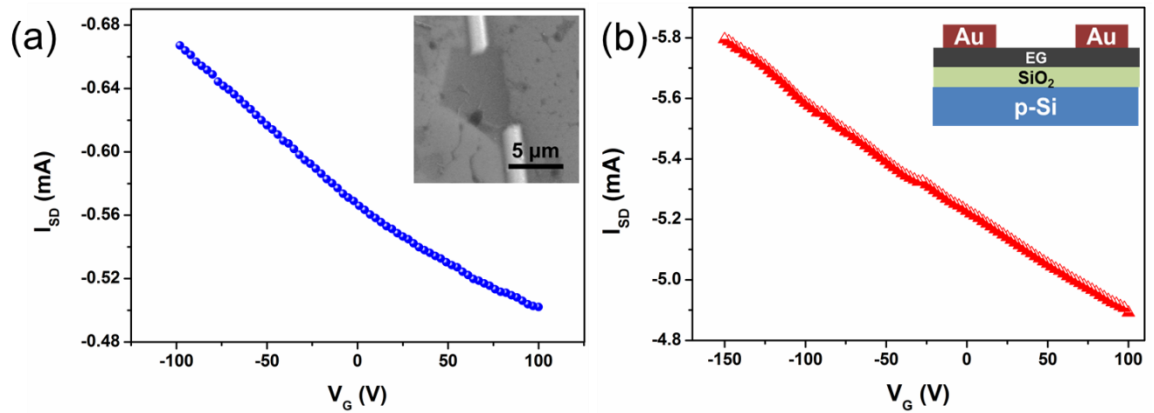


Figure 5.8 Transfer curve of the devices prepared from (a) bi-layer EG sheet and (b) a thin EG film. Inset of (a) is an SEM image and that of (b) is the cross-section scheme of the fabricated device.

The transfer curves of the devices are presented in Figure 5.8a and b. Remarkably, the bilayer EG sheets exhibited a mean hole mobility of ~ 233 cm²/Vs, which is several times higher than that reported for electrochemically derived graphene ($5.5 - 17$ cm² V⁻¹ s⁻¹)²⁸ and reduced graphene oxide ($\sim 0.01 - 12$ cm² V⁻¹ s⁻¹).^{29,45,48,49} Moreover, the devices based on EG thin-films delivered an average hole mobility of 34.6 cm² V⁻¹ s⁻¹ with a

maximum value of $47.3 \text{ cm}^2 \text{ V}^{-1} \text{ s}^{-1}$ (Figure 5.8b). The lower mobility of the EG thin-film compared to that of a single sheet can be attributed to the inter-junction resistance between EG sheets. The transfer curves of EG based devices fail to show the ambipolar effect which is common for high-quality graphene. The presence of hydroxyl groups in EG may inhibit n-type behavior. Presence of hydroxyl groups in graphene can act as electron traps and prohibit their function as free carriers.^{29,50} Further, the sheet resistance R_s ($R_s = RW/L$, where R is the resistance at 0.5V; W and L are the graphene width and channel length, respectively) of a single EG sheet was measured by a two-point probe system. The calculated R_s was $4.8 \text{ k}\Omega \text{ sq.}^{-1}$, (Figure 5.9a) which is much lower than that of rGO and comparable to that of CVD grown graphene.^{51,52}

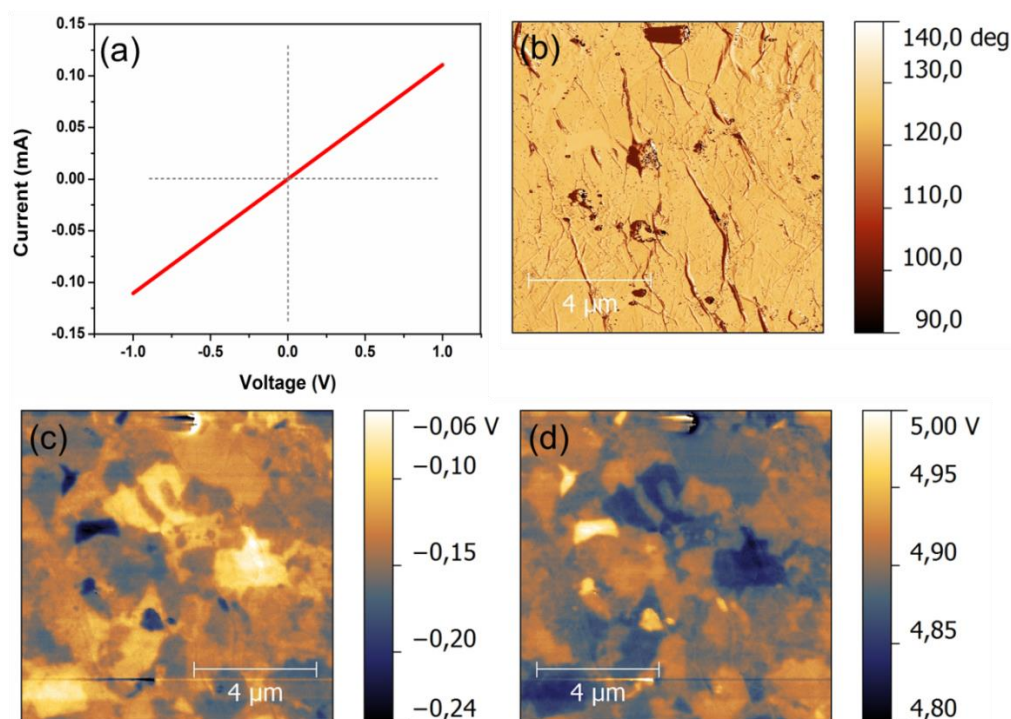


Figure 5.9 (a) Room temperature current-voltage (I - V) curve of a single bi-layer EG sheet; KPFM images of EG where, (b) phase image; (c) surface potential and; (d) work function of EG.

The work function of EG was investigated by Anna Domanski in Prof. Hans-Jürgen Butt group using a Kelvin Probe Force Microscopy (KPFM) equipped with a Nanosensors PPP-EFM Si cantilevers. The cantilevers with a nominal resonance frequency 70 kHz and a Pt/Ir coated were used. The work function of the tip ($\phi_{\text{tip}} = 4.761 \pm 0.008$ eV) was calibrated on freshly cleaved highly ordered pyrolytic graphite (HOPG). A mean value of 4.90 ± 0.05 eV (Figure 5.9d) was obtained which is slightly higher than that of pristine graphene (~ 4.6 eV).⁵³ The increased work function was due to the presence of oxygen-containing functional groups that produced surface $\text{C}^{\delta+}-\text{O}^{\delta-}$ dipoles *via* the extraction of π electrons from graphene.⁵⁴

5.6 Fabrication of transparent EG films

The high quality and solution-processability of the EG sheets led us to fabricate transparent graphene films on different substrates using a vacuum filtration and dry transfer method. The vacuum filtration method has several advantages: (i) homogeneity of the films is guaranteed by the process itself. As the graphene sheets accumulate, they generate a filter cake that acts to impede the permeation rate. If a region becomes thicker, the local permeation rate and the associated deposition rate slow down, allowing thinner regions to catch up. (ii) The film thickness is readily controlled with nanoscale precision by the concentration of graphene dispersion and volume of the dispersion filtered. To this end, an EG dispersion (~ 0.25 mg mL⁻¹) in DMF was first vacuum-filtered through a polytetrafluoroethylene (PTFE) membrane. The filtered EG film was then pressed on a target substrate such as glass or PET. When the PTFE membrane was peeled off, the EG film remained on the target substrate due to van der Waals interactions between the

graphene and substrate. Unlike the vacuum filtration method in which the filter membrane must be dissolved in organic solvents that may cause contamination,⁴⁹ the dry transfer method avoids dissolution of the filter membrane which can then be reused for further experiments. Moreover, the thickness of the transferred films can be adjusted through the filtration volume and the concentration of the graphene dispersion. For example, vacuum filtration of 5 and 10 mL of EG dispersion yields ~15- and 25-nm graphene films on substrates, respectively. The 15- and 25-nm thick graphene films (diameter 50 mm) on PET have a transmittance of 85 % and 73 %, respectively (Figure 5.10a). It can be seen from the optical microscopic (OM) images in Figure 5.10 b-e that the transferred film is uniformly covered on the substrates over large area.

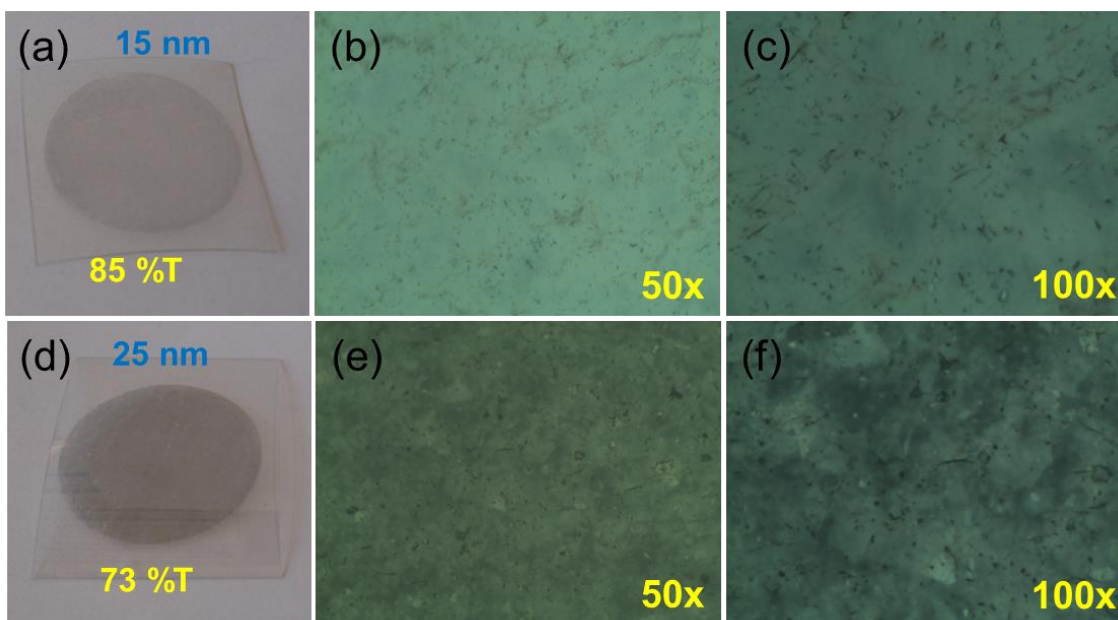


Figure 5.10 (a) and (d) Photographs of the 15 and 25 nm thick graphene films transferred on PET substrates, respectively. Optical microscopic images of the transferred EG films on PET substrates where, (b) and (c) are 15 nm; (d) and (e) are 25 nm thick films with different magnifications (50 and 100x), respectively.

The average sheet resistance of the transferred EG films measured using the four-point probe system (Keithly 2700 Multimeter) (Figure 5.11a) was 16.0 and 8.2 $\text{k}\Omega \text{sq}^{-1}$ for 15- and 25-nm EG films. Remarkably, after thermal annealing of the EG films at 200 °C for 30 min, the sheet resistance dropped dramatically to 4.1 and 2.4 $\text{k}\Omega \text{sq}^{-1}$, respectively, attributable to the evaporation of residual DMF. Further, a simple HNO_3 (65%) treatment of 15- and 25- nm EG films significantly reduced the sheet resistance to 0.49 and 0.27 $\text{k}\Omega \text{sq}^{-1}$, respectively (Figure 5.11b). This can be simply explained as the increase of carrier concentration with p-doping by HNO_3 and resulting in a decrease of the sheet resistance of EG films.^{48,55} The sheet resistance obtained without any further chemical and/or thermal reduction process is significantly lower than that of reduced GO thin films,^{56,57} again proving the superiority of the EG over reduced GO.

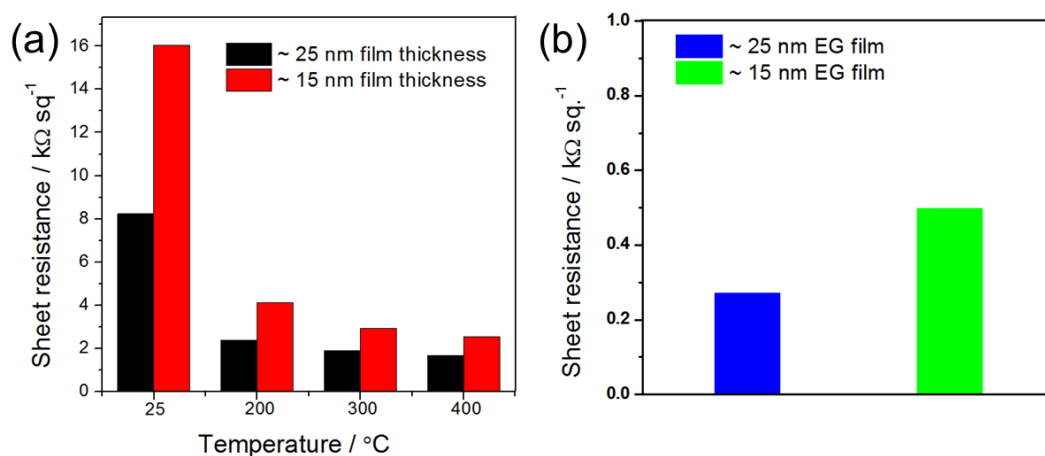


Figure 5.11 Sheet resistances of EG films where, (a) with different film thickness and, (b) after nitric acid (65% HNO_3) treatment.

5.7 Exfoliated graphene based electrodes for OFETs

The simple graphene film transfer process provides a major advantage for the solution fabrication of conductive electrodes for electronic devices. As a proof-of-concept, we demonstrated the fabrication of S/D electrodes for OFETs using patterned EG films. The fabrication process for patterned graphene electrodes from EG films is illustrated in Figure 5a. Briefly, an EG dispersion in DMF ($\sim 0.60 \text{ mg mL}^{-1}$) was vacuum-filtered through a PTFE membrane to obtain a 50-nm thick film and then transferred to a $\text{SiO}_2/\text{p-Si}$ substrate by a simple mechanical press (Figure S8a). Figure 5.12b and c presents the SEM and AFM image of uniformly transferred EG film on $\text{SiO}_2/\text{p-Si}$ substrate, respectively. The conductivity of the film is 590 S/cm which is higher than the previously reported 60-nm-thick rGO S/D electrodes (500 S/cm) produced *via* thermal treatment.¹⁷ The surface roughness (R_a) of the as-fabricated EG electrodes is high (*i.e.* $\sim 8.5 \text{ nm}$). Fortunately, unlike organic light-emitting diodes (OLEDs), and organic solar cells, in which the roughness of the electrodes influences the device performance dramatically, the roughness of the electrode surface does not pose major effect on OFETs. In fact, only the electrode/organic semiconductor interface at the end of the conductive channel has a great influence on the device performance. It has been reported previously that a rough electrode/organic layer interface could be beneficial to the OFETs performance.⁵⁸ Rough S/D electrodes can provide large surface area for the organic semiconductors. This large coverage of electrode/organic layer interface contributes to the decrease of the contact resistance and as a result improved device performance.⁵⁹

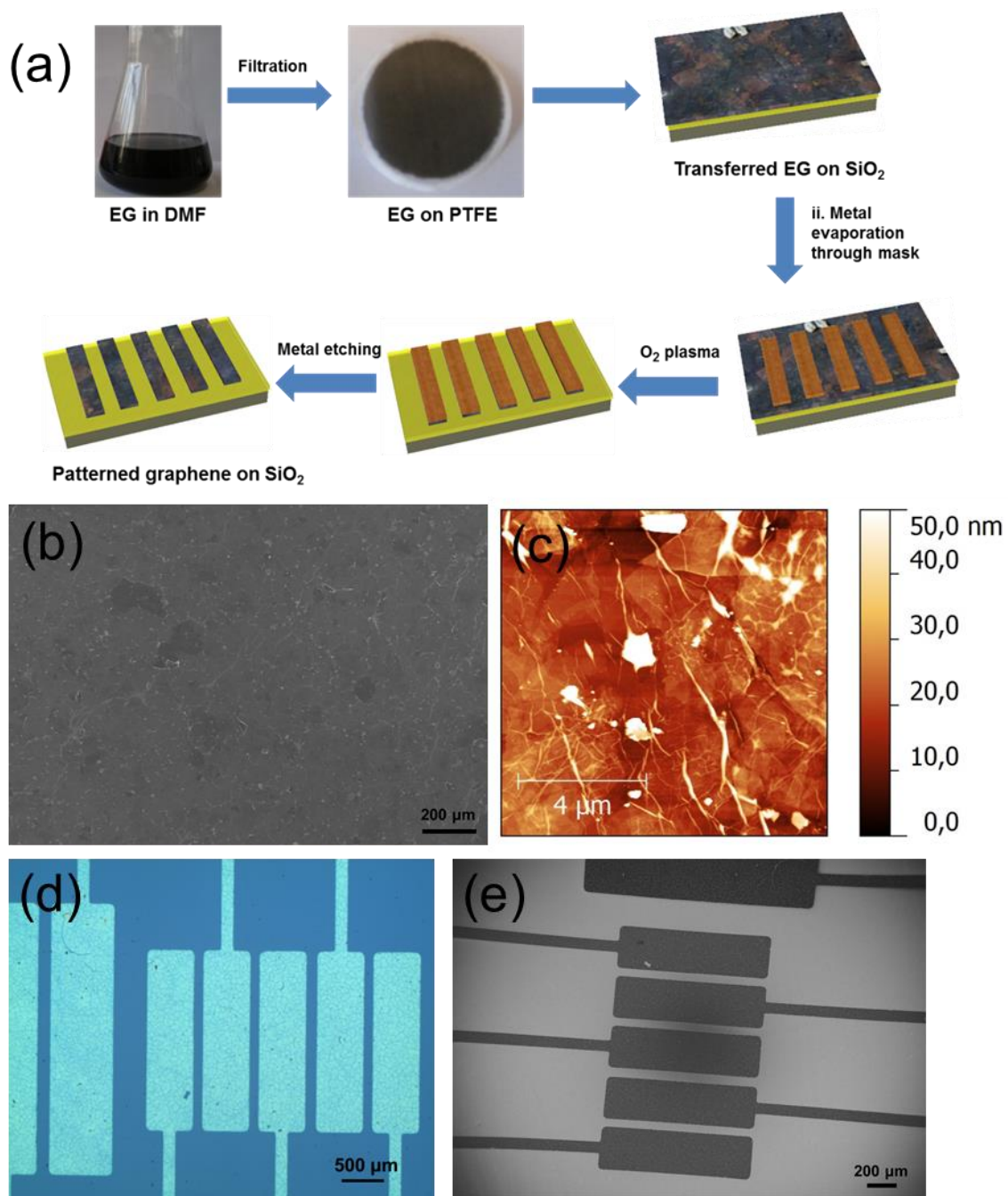


Figure 5.12 (a) Schematic illustration of the fabrication process of patterned EG S/D electrodes. (b) SEM and (c) AFM images of the transferred 50 nm thick EG film on SiO₂/p-Si substrates. (d) Optical microscopic and (e) SEM images of the patterned S/D electrodes.

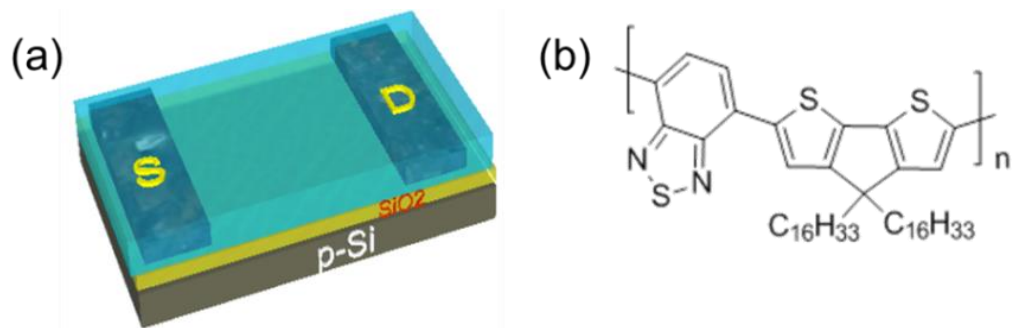


Figure 5.13 (a) Scheme of the fabricated EG-based OFETs. (b) The molecular structure of 4*H*-cyclopenta[1,2-*b*; 5,4-*b'*]dithiophene-benzo[*c*][1,2,5]thiadiazole (CDT-BTZ-C16).

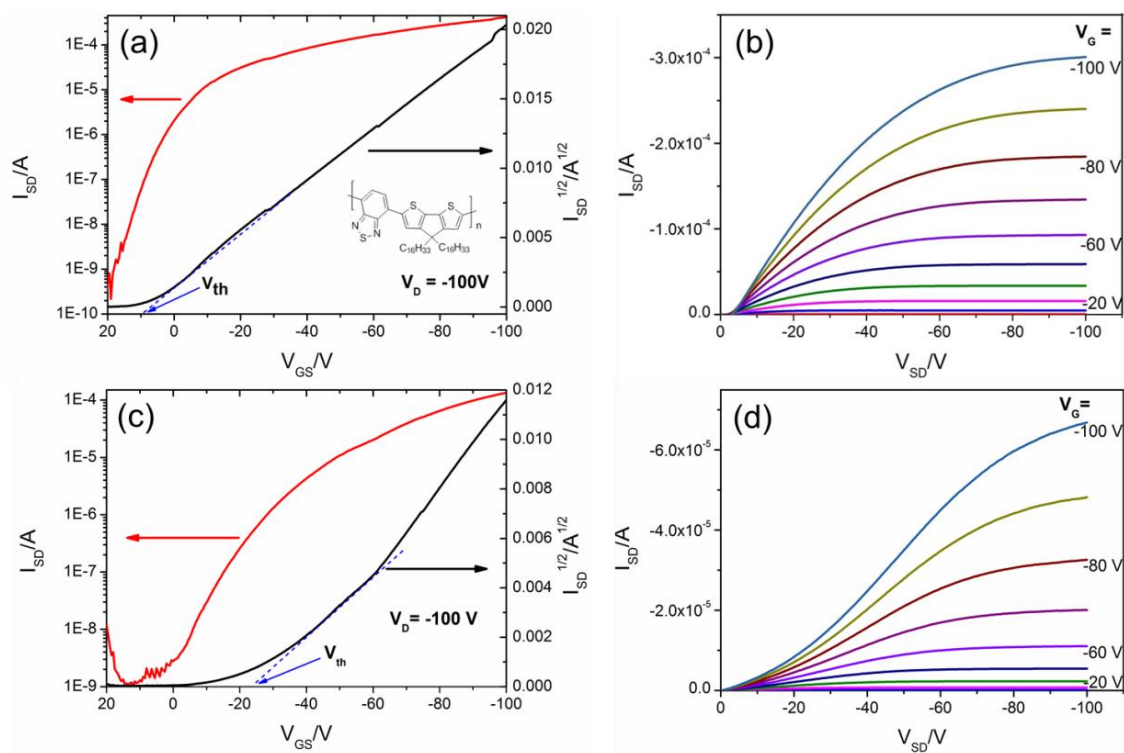


Figure 5.14 (a) Transfer characteristics of the CDT-BTZ-C16 based OFETs with EG S/D electrodes at a bias of $V_D = -100$ V. (b) Output characteristics for various gate bias V_G . (c) Transfer characteristics and (d) output characteristics of Au S/D based OFETs.

The patterned EG electrodes were obtained by thermally evaporating aluminum (Al) on top of the EG film through a mask with subsequent exposure to an O₂-plasma to remove the EG film from unmasked regions. Finally, Al was chemically etched and EG-based S/D electrodes were generated (Figure 5.12d and e). The channel length of the fabricated EG electrodes was 50 μm ($L/W = 1/18$). The p-doped silicon (p-Si) below 300 nm SiO₂ layer served as the gate (capacitance $C_i = 11 \text{ nF cm}^{-2}$). The patterned EG and/or Au electrodes were then treated with hexamethyldisilazane (HMDS). A conjugated donor-acceptor polymer (synthesized by Felix Hinkel in our group), 4*H*-cyclopenta[1,2-*b*; 5,4-*b'*]dithiophene-benzo[*c*][1,2,5]thiadiazole (CDT-BTZ-C16, Mw=10K Da, polydispersity index=2.67), was used as the semiconductor due to its good solution-processability, close π -stacking distance, and highly ordered lamellar packing structure on the surface (Figure 5.13).⁶⁰ Therefore, CDT-BTZ-C16 solution (2 mg mL⁻¹ in *o*-dichlorobenzene) was drop-casted on hexamethyldisilazane (HMDS) treated substrates and subsequently treated at 200 °C for 1h in nitrogen atmosphere. All the FET measurements were carried out inside a dry nitrogen glove box with a Keithly 4200 semiconductor parameter analyzer. Hole mobilities (μ) of all OFETs were calculated in the saturation regime by the following equation:

$$\mu = \frac{WC_i}{2L} (V_{GS} - V_T)^2$$

Where, C_i is the capacitance per unit area of the gate dielectric and V_T is the threshold voltage. The transfer and output characteristics are shown in Figure 5.14a and b, respectively. Remarkably, a mean hole mobility of 0.50 cm² V⁻¹ · s⁻¹ (maximum mobility up to 0.60 cm² V⁻¹ · s⁻¹) with an on/off ratio exceeding 10⁶ was achieved. In contrast, Au-based S/D electrodes produced a mean hole mobility of only 0.19 cm² V⁻¹ · s⁻¹ (maximum up to

$0.21 \text{ cm}^2 \text{ V}^{-1} \cdot \text{s}^{-1}$) with a lower on/off ratio (10^5) (Figure 5.14c and d).⁶¹ For EG-based S/D devices, the desirable linear and saturation regimes with apparent gate-voltage dependence (Figure 5.14b) can be identified,^{62,63} in marked contrast to the S-shaped output curves derived from Au-based devices (Figure 5.14d). This finding strongly suggests that graphene electrodes have a low contact resistance with organic materials resulting from low charge injection barrier between graphene and organic semiconductors,^{58,64} and is mainly responsible for the enhanced device performance.

5.8 Flexible OFETs based on graphene electrodes

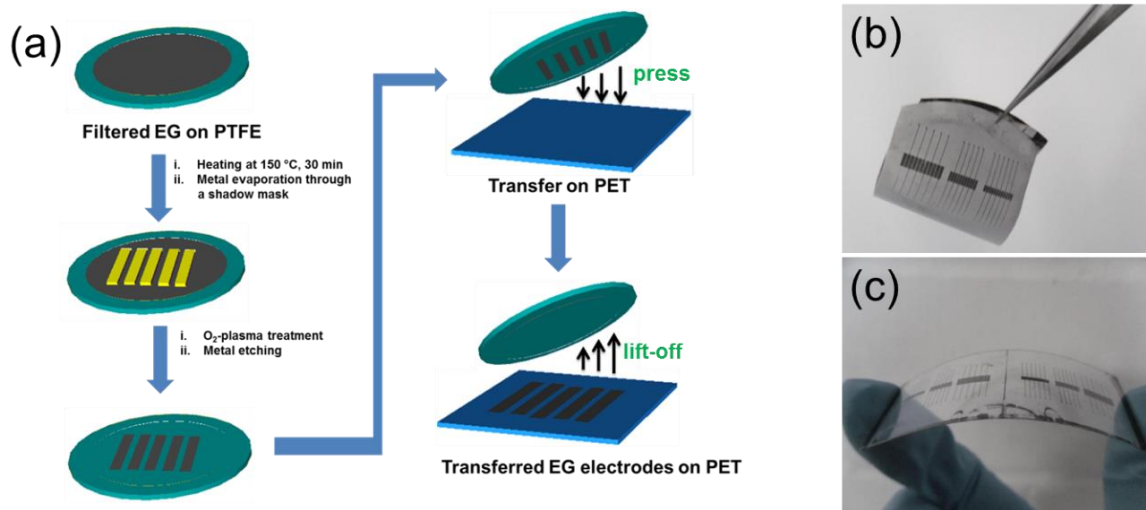


Figure 5.15 (a) Schematic illustration of the fabrication of patterned EG electrodes on PET substrates; (b) Photograph of EG electrodes patterned on PTFE membrane and; (c) transferred on PET substrate.

A novel and simple approach is also developed for the fabrication of flexible OFETs by patterning electrodes on filter membrane and subsequent dry transfer on the PET substrates. Our fabrication method can avoid the patterning of the electrodes directly on

PET substrates by exposing to oxygen plasma and the possibility of any contaminations during conventional photolithographic process. To this end, flexible OFETs based on EG S/D electrodes can be fabricated on a PET substrate. As shown in Figure 3.14a the electrodes were patterned on a filter (PTFE) membrane followed by a dry transfer process on a PET substrate. S/D electrodes (~50 nm thick) were fabricated on the PTFE filter by protective metal (Al) followed by O₂-plasma etching (Figure 5.15a). Afterwards, removal of the sacrificial Al layer in acidic solution afforded an EG film patterned on the PTFE filter (Figure 5.15b). The EG electrodes were then transferred to a PET substrate by mechanically pressing the PTFE filter containing the patterns (Figure 5.15c). Top-gate, bottom contact FETs were thus constructed by spin coating CDT-BTZ-C16 (2 mg mL⁻¹ in CHCl₃) on the substrate and subsequent annealing at 150 °C for 30 min. Afterwards, a dielectric layer of ~560 nm thick PMMA (15,000 g mol⁻¹, 12 wt% in toluene) was deposited by spin-coating at 1000 rpm for 30s ($C_i = 5.06 \text{ nF cm}^{-2}$) and dried in a vacuum oven at 80 °C for 4 h. Finally, 30 nm thick Au was evaporated on top of the PMMA layer and used as a gate electrode. The transfer and output characteristics of flexible OFET are shown in Figure 5.16. The field-effect mobility of the flexible OFET device was calculated to be 0.053 cm²/V·s, with a current on/off ratio of 10⁴ (Figure 5.16b). The relatively low performance of the flexible device compared to the SiO₂/Si based devices might be caused by the poor interface between organic semiconductor and PMMA dielectric layer. Although the performance of flexible OFET is inferior to the device based on SiO₂/p-Si substrate, further optimization of the fabrication process as well as the improvement of the interfaces between organic/dielectric materials can improve the performance of flexible OFETS. Nevertheless, this study shows that besides providing a suitable alternative to Au or other metal based S/D electrodes, these patterned EG electrodes allow for the fabrication of high

performance OFETs and complementary circuits that offer a viable route towards transparent organic electronics, fabricated by solution processing.

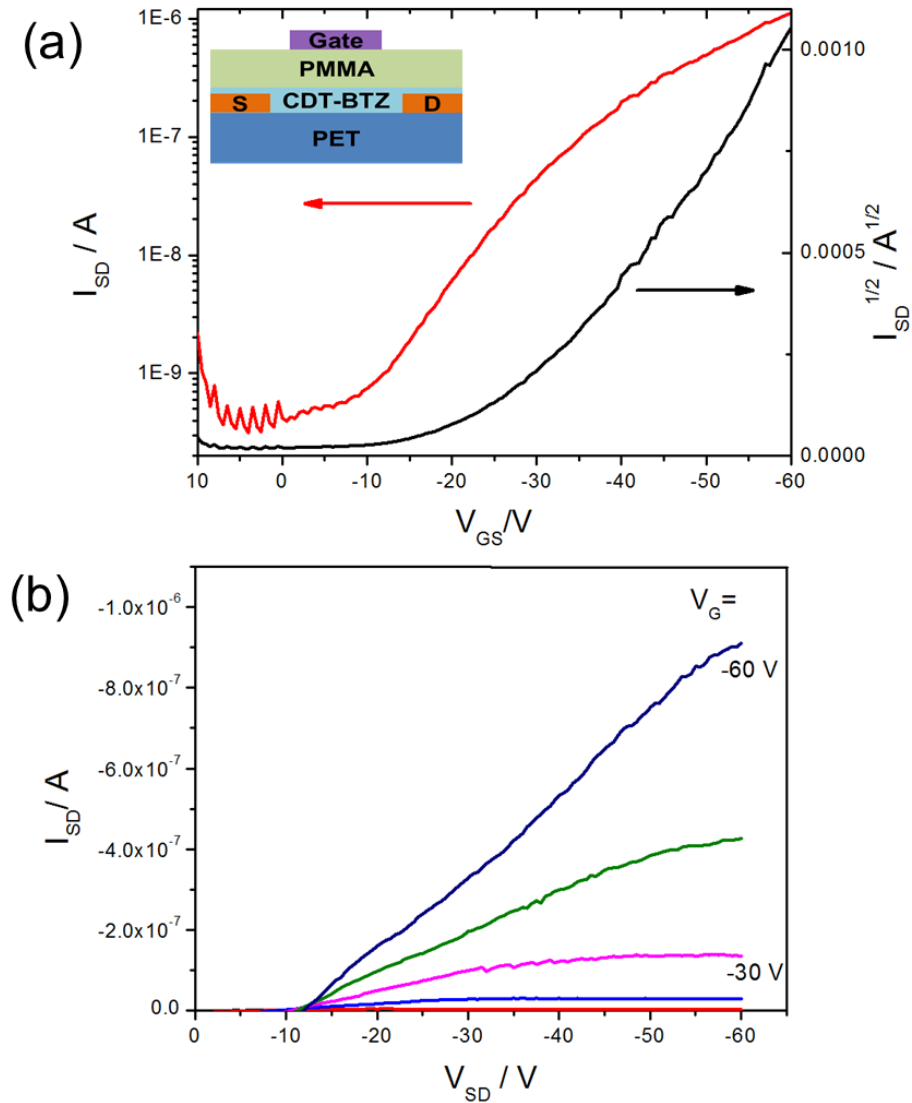


Figure 5.16 (a) Transfer and (b) output curves of flexible OFETs with EG electrodes ($L = 50 \mu\text{m}$, $W = 900 \mu\text{m}$) at a source-drain bias $V_{SD} = -60 \text{ V}$.

5.9 Conclusion

In conclusion, the present study demonstrates that electrochemical exfoliation of graphite is a promising method for the fabrication of graphene sheets in high quality and high yield. The as-prepared graphene has a large sheet size (average $\sim 10 \mu\text{m}$), low oxygen content (7.5%) and/or high C/O ratio as well as excellent electronic properties comparable to CVD graphene. In addition, we introduce a vacuum filtration method in association with the dry transfer method to produce highly conductive graphene films on various substrates. Due to the high quality along with their feasible solution-processability and large scale production in short time period, electrochemically exfoliated graphene sheets is expected to hold a great promise for graphene based organic electronic devices such as OFETs, LEDs, sensors, transparent conductors etc. Nevertheless, the prepared EG still contains significant amount of oxygen groups due to the over-oxidation by acid. Therefore, it is of great importance to avoid the over-oxidation process and to further improve the quality of EG. One possibility is to replace acidic electrolytes for the electrochemical exfoliation, which will be discussed in the following chapter.

5.10 References

- (1) Southard, A.; Sangwan, V.; Cheng, J.; Williams, E. D.; Fuhrer, M. S. *Org. Electron.* **2009**, *10*, 1556.
- (2) Wang, X.; Zhi, L. J.; Tsao, N.; Tomovic, Z.; Li, J. L.; Mullen, K. *Angew. Chem. Int. Ed.* **2008**, *47*, 2990.
- (3) Wassei, J. K.; Kaner, R. B. *Mater. Today* **2010**, *13*, 52.
- (4) Kim, J. Y.; Lee, K.; Coates, N. E.; Moses, D.; Nguyen, T. Q.; Dante, M.; Heeger, A. *J. Science* **2007**, *317*, 222.
- (5) Na, S. I.; Kim, S. S.; Jo, J.; Kim, D. Y. *Adv. Mater.* **2008**, *20*, 4061.
- (6) Wu, Z. C.; Chen, Z. H.; Du, X.; Logan, J. M.; Sippel, J.; Nikolou, M.; Kamaras, K.; Reynolds, J. R.; Tanner, D. B.; Hebard, A. F.; Rinzler, A. G. *Science* **2004**, *305*, 1273.
- (7) Rowell, M. W.; Topinka, M. A.; McGehee, M. D.; Prall, H. J.; Dennler, G.; Sariciftci, N. S.; Hu, L. B.; Gruner, G. *Appl. Phys. Lett.* **2006**, *88*.
- (8) Lee, J. Y.; Connor, S. T.; Cui, Y.; Peumans, P. *Nano Lett.* **2008**, *8*, 689.
- (9) De, S.; Higgins, T. M.; Lyons, P. E.; Doherty, E. M.; Nirmalraj, P. N.; Blau, W. J.; Boland, J. J.; Coleman, J. N. *ACS Nano* **2009**, *3*, 1767.
- (10) Ho, G. W.; Wee, A. T. S.; Lin, J. *Appl. Phys. Lett.* **2001**, *79*, 260.
- (11) De, S.; Coleman, J. N. *ACS Nano* **2010**, *4*, 2713.
- (12) Wang, Y.; Chen, X. H.; Zhong, Y. L.; Zhu, F. R.; Loh, K. P. *Appl. Phys. Lett.* **2009**, *95*.
- (13) Bae, S.; Kim, H.; Lee, Y.; Xu, X. F.; Park, J. S.; Zheng, Y.; Balakrishnan, J.; Lei, T.; Kim, H. R.; Song, Y. I.; Kim, Y. J.; Kim, K. S.; Ozyilmaz, B.; Ahn, J. H.; Hong, B. H.; Iijima, S. *Nat. Nanotechnol.* **2010**, *5*, 574.
- (14) Wang, X.; Zhi, L. J.; Mullen, K. *Nano Lett.* **2008**, *8*, 323.
- (15) Matyba, P.; Yamaguchi, H.; Eda, G.; Chhowalla, M.; Edman, L.; Robinson, N. D. *ACS Nano* **2010**, *4*, 637.
- (16) Liu, W.; Jackson, B. L.; Zhu, J.; Miao, C. Q.; Chung, C. H.; Park, Y. J.; Sun, K.; Woo, J.; Xie, Y. H. *ACS Nano* **2010**, *4*, 3927.
- (17) Pang, S. P.; Tsao, H. N.; Feng, X. L.; Mullen, K. *Adv. Mater.* **2009**, *21*, 3488.
- (18) Pang, S. P.; Yang, S. B.; Feng, X. L.; Mullen, K. *Adv. Mater.* **2012**, *24*, 1566.

-
- (19) Park, S.; An, J. H.; Jung, I. W.; Piner, R. D.; An, S. J.; Li, X. S.; Velamakanni, A.; Ruoff, R. S. *Nano Lett.* **2009**, *9*, 1593.
- (20) Kim, K. S.; Zhao, Y.; Jang, H.; Lee, S. Y.; Kim, J. M.; Kim, K. S.; Ahn, J. H.; Kim, P.; Choi, J. Y.; Hong, B. H. *Nature* **2009**, *457*, 706.
- (21) Lee, Y.; Bae, S.; Jang, H.; Jang, S.; Zhu, S. E.; Sim, S. H.; Song, Y. I.; Hong, B. H.; Ahn, J. H. *Nano Lett.* **2010**, *10*, 490.
- (22) He, M.; Jung, J. H.; Qiu, F.; Lin, Z. Q. *J. Mater. Chem.* **2012**, *22*, 24254.
- (23) Pirkle, A.; Chan, J.; Venugopal, A.; Hinojos, D.; Magnuson, C. W.; McDonnell, S.; Colombo, L.; Vogel, E. M.; Ruoff, R. S.; Wallace, R. M. *Appl. Phys. Lett.* **2011**, *99*.
- (24) Liu, N.; Luo, F.; Wu, H. X.; Liu, Y. H.; Zhang, C.; Chen, J. *Adv. Funct. Mater.* **2008**, *18*, 1518.
- (25) Wang, J. Z.; Manga, K. K.; Bao, Q. L.; Loh, K. P. *J. Am. Chem. Soc.* **2011**, *133*, 8888.
- (26) Xu, H. X.; Suslick, K. S. *J. Am. Chem. Soc.* **2011**, *133*, 9148.
- (27) Hernandez, Y.; Nicolosi, V.; Lotya, M.; Blighe, F. M.; Sun, Z. Y.; De, S.; McGovern, I. T.; Holland, B.; Byrne, M.; Gun'ko, Y. K.; Boland, J. J.; Niraj, P.; Duesberg, G.; Krishnamurthy, S.; Goodhue, R.; Hutchison, J.; Scardaci, V.; Ferrari, A. C.; Coleman, J. N. *Nat. Nanotechnol.* **2008**, *3*, 563.
- (28) Su, C. Y.; Lu, A. Y.; Xu, Y. P.; Chen, F. R.; Khlobystov, A. N.; Li, L. J. *ACS Nano* **2011**, *5*, 2332.
- (29) Tung, V. C.; Allen, M. J.; Yang, Y.; Kaner, R. B. *Nat. Nanotechnol.* **2009**, *4*, 25.
- (30) Gilje, S.; Han, S.; Wang, M.; Wang, K. L.; Kaner, R. B. *Nano Lett.* **2007**, *7*, 3394.
- (31) Shin, K. Y.; Hong, J. Y.; Jang, J. *Chem. Commun.* **2011**, *47*, 8527.
- (32) Li, X. L.; Zhang, G. Y.; Bai, X. D.; Sun, X. M.; Wang, X. R.; Wang, E.; Dai, H. J. *Nat. Nanotechnol.* **2008**, *3*, 538.
- (33) Lu, J.; Yang, J. X.; Wang, J. Z.; Lim, A. L.; Wang, S.; Loh, K. P. *ACS Nano* **2009**, *3*, 2367.
- (34) Kang, F. Y.; Leng, Y.; Zhang, T. Y. *J. Phys. Chem. Solids* **1996**, *57*, 889.
- (35) Beck, F.; Jiang, J.; Krohn, H. *J. Electroanal. Chem.* **1995**, *389*, 161.
- (36) Beck, F.; Junge, H.; Krohn, H. *Electrochim. Acta.* **1981**, *26*, 799.
- (37) Cheng, Z. G.; Zhou, Q. Y.; Wang, C. X.; Li, Q. A.; Wang, C.; Fang, Y. *Nano Lett.* **2011**, *11*, 767.

- (38) Sun, Z. Z.; Yan, Z.; Yao, J.; Beitler, E.; Zhu, Y.; Tour, J. M. *Nature* **2010**, *468*, 549.
- (39) Compton, O. C.; Jain, B.; Dikin, D. A.; Abouimrane, A.; Amine, K.; Nguyen, S. T. *ACS Nano* **2011**, *5*, 4380.
- (40) Park, S.; Ruoff, R. S. *Nat. Nanotechnol.* **2009**, *4*, 217.
- (41) Mattevi, C.; Eda, G.; Agnoli, S.; Miller, S.; Mkhoyan, K. A.; Celik, O.; Mostrogiovanni, D.; Granozzi, G.; Garfunkel, E.; Chhowalla, M. *Adv. Funct. Mater.* **2009**, *19*, 2577.
- (42) Lopez, V.; Sundaram, R. S.; Gomez-Navarro, C.; Olea, D.; Burghard, M.; Gomez-Herrero, J.; Zamora, F.; Kern, K. *Adv. Mater.* **2009**, *21*, 4683.
- (43) Krauss, B.; Lohmann, T.; Chae, D. H.; Haluska, M.; von Klitzing, K.; Smet, J. H. *Phys. Rev. B* **2009**, *79*.
- (44) Zhao, F.; Liu, J. Q.; Huang, X.; Zou, X.; Lu, G.; Sun, P. J.; Wu, S. X.; Ai, W.; Yi, M. D.; Qi, X. Y.; Xie, L. H.; Wang, J. L.; Zhang, H.; Huang, W. *ACS Nano* **2012**, *6*, 3027.
- (45) Su, C. Y.; Xu, Y. P.; Zhang, W. J.; Zhao, J. W.; Tang, X. H.; Tsai, C. H.; Li, L. J. *Chem. Mater.* **2009**, *21*, 5674.
- (46) Eckmann, A.; Felten, A.; Mishchenko, A.; Britnell, L.; Krupke, R.; Novoselov, K. S.; Casiraghi, C. *Nano Lett.* **2012**, *12*, 3925.
- (47) Ferrari, A. C. *Solid State Commun.* **2007**, *143*, 47.
- (48) Su, C. Y.; Xu, Y. P.; Zhang, W. J.; Zhao, J. W.; Liu, A. P.; Tang, X. H.; Tsai, C. H.; Huang, Y. Z.; Li, L. J. *ACS Nano* **2010**, *4*, 5285.
- (49) Eda, G.; Fanchini, G.; Chhowalla, M. *Nat. Nanotechnol.* **2008**, *3*, 270.
- (50) Ohta, T.; Bostwick, A.; Seyller, T.; Horn, K.; Rotenberg, E. *Science* **2006**, *313*, 951.
- (51) Reina, A.; Jia, X. T.; Ho, J.; Nezich, D.; Son, H. B.; Bulovic, V.; Dresselhaus, M. S.; Kong, J. *Nano Lett.* **2009**, *9*, 30.
- (52) Shi, Z. W.; Yang, R.; Zhang, L. C.; Wang, Y.; Liu, D. H.; Shi, D. X.; Wang, E. G.; Zhang, G. Y. *Adv. Mater.* **2011**, *23*, 3061.
- (53) Yu, Y. J.; Zhao, Y.; Ryu, S.; Brus, L. E.; Kim, K. S.; Kim, P. *Nano Lett.* **2009**, *9*, 3430.
- (54) Li, S. S.; Tu, K. H.; Lin, C. C.; Chen, C. W.; Chhowalla, M. *ACS Nano* **2010**, *4*, 3169.
- (55) Kasry, A.; Kuroda, M. A.; Martyna, G. J.; Tulevski, G. S.; Bol, A. A. *ACS Nano* **2010**, *4*, 3839.

-
- (56) Eda, G.; Lin, Y. Y.; Miller, S.; Chen, C. W.; Su, W. F.; Chhowalla, M. *Appl. Phys. Lett.* **2008**, *92*.
- (57) Pham, V. H.; Cuong, T. V.; Hur, S. H.; Shin, E. W.; Kim, J. S.; Chung, J. S.; Kim, E. *J. Carbon* **2010**, *48*, 1945.
- (58) Di, C. A.; Wei, D. C.; Yu, G.; Liu, Y. Q.; Guo, Y. L.; Zhu, D. B. *Adv. Mater.* **2008**, *20*, 3289.
- (59) Di, C. A.; Yu, G.; Liu, Y. Q.; Guo, Y. L.; Wu, W. P.; Wei, D. C.; Zhu, D. B. *Phys. Chem. Chem. Phys.* **2008**, *10*, 2302.
- (60) Tsao, H. N.; Cho, D. M.; Park, I.; Hansen, M. R.; Mavrinskiy, A.; Yoon, D. Y.; Graf, R.; Pisula, W.; Spiess, H. W.; Mullen, K. *J. Am. Chem. Soc.* **2011**, *133*, 2605.
- (61) Zhang, M.; Tsao, H. N.; Pisula, W.; Yang, C. D.; Mishra, A. K.; Mullen, K. *J. Am. Chem. Soc.* **2007**, *129*, 3472.
- (62) Moore, V. C.; Strano, M. S.; Haroz, E. H.; Hauge, R. H.; Smalley, R. E.; Schmidt, J.; Talmon, Y. *Nano Lett.* **2003**, *3*, 1379.
- (63) Gomez-Navarro, C.; Weitz, R. T.; Bittner, A. M.; Scolari, M.; Mews, A.; Burghard, M.; Kern, K. *Nano Lett.* **2007**, *7*, 3499.
- (64) Lee, S.; Jo, G.; Kang, S. J.; Wang, G.; Choe, M.; Park, W.; Kim, D. Y.; Kahng, Y. H.; Lee, T. *Adv. Mater.* **2011**, *23*, 100.

Chapter 6

Electrochemical exfoliation of graphite into graphene in aqueous solutions of inorganic salts

As discussed in Chapter 5, electrochemical exfoliation of graphite in aqueous acid electrolyte yields thin graphene sheets with relatively lower defect density compared to reduced GO. However, the prepared graphene sheets contains significant amount of oxygen functional groups mostly due to the over-oxidation by acidic electrolytes. To further improve the quality of graphene, the over-oxidation process must be suppressed. Here we present a highly expeditious electrochemical exfoliation of graphite in aqueous inorganic salt electrolytes such as ammonium sulfate, sodium sulfate, potassium sulfate etc. The exfoliation in electrolyte under neutral pH condition leads to graphene with high yield of one to three layers (>80%), large flake size (up to 44 μm) and low oxidation degree. The as-prepared graphene shows a C/O ratio of 17.2, which is the highest value reported to date for graphene by chemical synthesis. Moreover, a single layer graphene exhibits a remarkable hole mobility of $310 \text{ cm}^2 \text{ V}^{-1} \text{ s}^{-1}$ which is several times higher than that of chemically reduced graphene oxide (rGO). High solution processability of EG also ensures their wide applications from window electrodes to conductive ink for printable electronics as well as high performance energy storage devices, such as supercapacitors. Therefore, this electrochemical exfoliation method provides an environmentally benign route to prepare high quality few layer graphene on large scale.

6.1 Introduction

Electrochemical exfoliation of graphite has attracted much attention due to its easy, fast and environmental friendly approach to produce high quality graphene with only a small amount of defects in comparison with GO and/or rGO.¹⁻⁴ By far, the electrochemical exfoliation of graphite was performed mainly in two different types of electrolytes i.e. in ionic-liquids (ILs)^{3,5} and in aqueous acids (*i.e.* H₂SO₄).^{1,4} The exfoliation in ILs suffers from low yield of graphene, small flake size (less than 5 μm) and often functionalized with ILs which disrupt the electronic properties of graphene.^{3,6} On the other hand, as we discussed in Chapter 5, exfoliation in acidic electrolytes can produce graphene in better quality and larger flake size, but a significant amount of oxygen containing functional groups cannot be avoided due to the over-oxidation of graphite by acid.^{1,4} A proper electrolyte system which can balance the high-quality and large quantity synthesis of exfoliated graphene is still missing.

In this chapter, we demonstrate a highly efficient electrochemical exfoliation of graphite in aqueous sulfate salts such as ammonium sulfate ((NH₄)₂SO₄), sodium sulfate (Na₂SO₄), potassium sulfate (K₂SO₄) etc. Under the neutral pH condition for electrochemical exfoliation, graphene sheets with the highest C/O ratio 17.2 (*i.e.* oxygen content of 5.5 at%) and lowest defect density. The exfoliated graphene (EG) sheets can be produced on tens of gram scale in less than an hour. Large-size, highly conductive graphene films (11 Ω sq.⁻¹ at ~ 0.74 mg cm⁻² graphene loading) on A4-size paper fabricated by simple brush painting of graphene ink (10 mg mL⁻¹ in DMF) shows promising application as highly flexible solid-state supercapacitors with an area capacity of 11.3 mF cm⁻² and high rate capability up to 5000 mV s⁻¹. The present environment friendly exfoliation

method to produce large-scale graphene with very low defect density opens up a whole new vista of potential applications from electronic devices to window electrodes etc. and is expected to advance the research on graphene-based practical applications.

6.2 Electrochemical exfoliation of graphite in aqueous inorganic salt

The electrochemical exfoliation of graphite was performed in a two electrode system where platinum was used as a counter electrode and graphite as a working electrode. The graphite electrode was prepared by adhering graphite flakes on a conductive carbon tape and thereby making a pellet. The distance between two electrodes was 2 cm. Different types of aqueous inorganic salt electrolytes were examined in this work and among them sulfate containing salts such as, $(\text{NH}_4)_2\text{SO}_4$ exhibited the best exfoliation efficiency. The electrolyte was prepared by dissolving 1.06 g of $(\text{NH}_4)_2\text{SO}_4$ in 80 mL water (concentration of 0.1 M and pH ~6.5-7.0). When a DC voltage of +10 V was applied to graphite electrode, the graphite flakes started to dissociate and spread into the electrolyte solution (Figure 6.1a). The voltage was kept constant for 3 to 5 minutes to complete the exfoliation process. Afterwards, the exfoliated product was collected by vacuum filtration through a polytetrafluoroethylene (PTFE) membrane (pore size 0.2 μm) and repeatedly washed with DI water to remove any residual salts. The resulting powder was then dispersed in *N,N'*-dimethylformamide (DMF) by sonicating for 10 min. The dispersion was kept for 48 h for the sedimentation of un-exfoliated graphite flakes or particles. The yield of EG flakes was more than 75% relative to the total weight of starting graphite electrode. A dispersion of

$\sim 2.5 \text{ mg mL}^{-1}$ in DMF was obtained which could be stable for three weeks without apparent agglomeration (Figure 6.1b). Remarkably, the exfoliation process can be readily scaled up depending upon the type and size of the graphite electrode used (Figure 6.1c-g). For example, using three $11.5 \text{ cm} \times 2.3 \text{ cm}$ size graphite foils simultaneously (Figure 6.1c-f) in a series of electrochemical experiments, $\sim 16.3 \text{ g}$ of graphene sheets were obtained (Figure 6.1g) within 30 min.

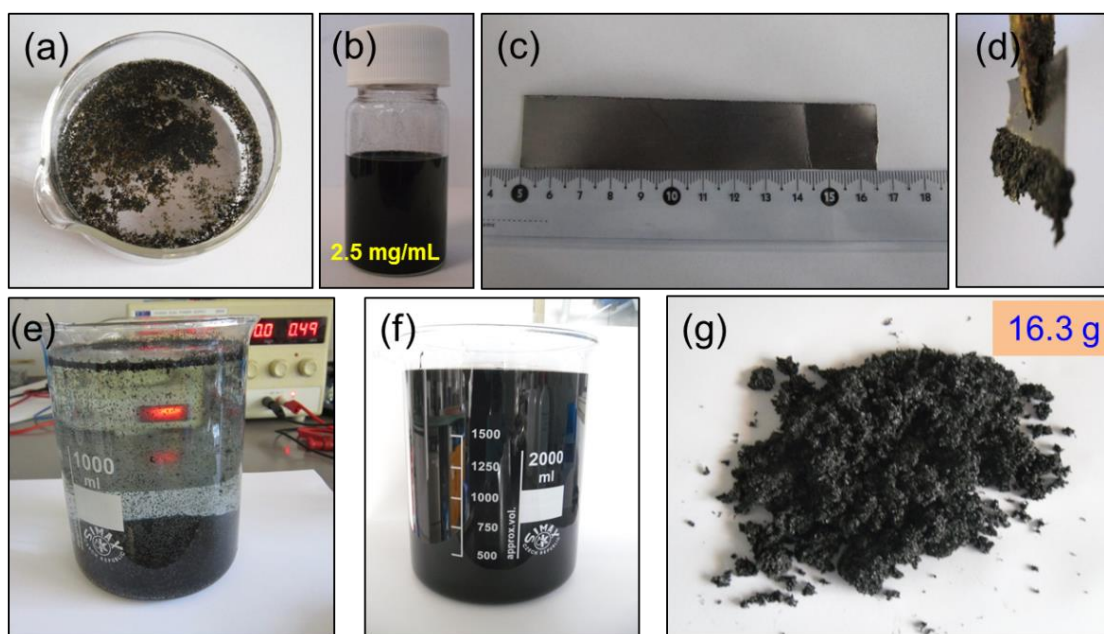
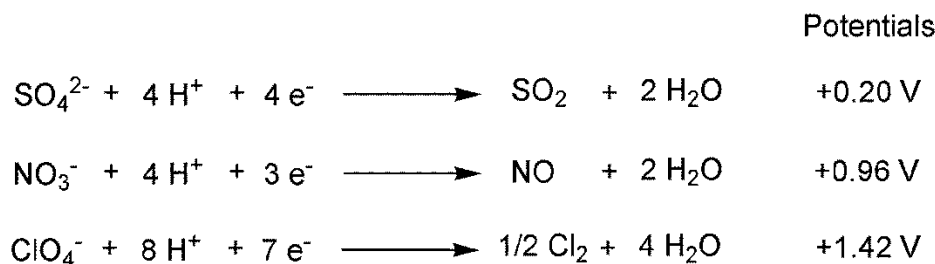


Figure 6.1 Photograph of (a) graphene flakes after electrochemical exfoliation, (b) dispersed EG in DMF (concentration 2.5 mg mL^{-1}). (c)-(g) demonstration of large-scale preparation of EG where, (c) and (d) graphite foil before and after exfoliation. (e) exfoliated graphene in aqueous $(\text{NH}_4)_2\text{SO}_4$ electrolyte. Majority of the product is suspended at the bottom of solution. (f) Large-scale EG dispersion in DMF (total volume of 2 liters) with a concentration of $\sim 3 \text{ mg mL}^{-1}$ and, (g) dried EG powder in bulk scale (16.3 g).

6.2.1 Exfoliation in different types of salt electrolytes

In addition to $(\text{NH}_4)_2\text{SO}_4$, various electrolytes based on aqueous solution of inorganic salts such as, NH_4Cl , Na_2SO_4 , NaNO_3 , K_2SO_4 , NaClO_4 were also examined for the electrochemical exfoliation and the results are summarized in Table 6.1. The salts containing anions such as, ClO_4^- , Cl^- , NO_3^- did not exert apparent exfoliation. Only the expansion of graphite electrode was observed in the case of ClO_4^- and NO_3^- anions (Figure 4.2b and c). In contrast, the salts containing sulfate anions (i.e. SO_4^{2-}) exhibited high exfoliation efficiency.

Thin graphene sheets could be readily exfoliate from graphite flakes in less than 5 min (Figure 6.2d and e). The superior exfoliation efficiency of sulfate anions compared to other anions can be explained by the following redox reactions:



It can be seen from above reactions that the SO_4^{2-} anions possesses lowest reduction potential (i.e. +0.20 V). Whereas, the reduction potential of ClO_4^- and NO_3^- ions to produce Cl_2 and NO gas are as high as 1.42 and 0.96 V, respectively. Therefore, SO_4^{2-} ions are expected to produce gaseous SO_2 much faster than the NO or Cl_2 gas in between the graphite layers, resulting in a fast electrochemical exfoliation.

Table 6.1: Summary of the inorganic salt based electrolytes investigated in electrochemical exfoliation of graphite.

Electrolyte	Electrolyte concentration (M)	Voltage	Time	Results
NH₄Cl	0.1	+ 10V	5 to 10 min	No exfoliation
Na₂SO₄	0.1	+ 10V	3 to 5 min	Efficient exfoliation
NaNO₃	0.1	+10 V	5 to 10 min	Poor exfoliation. Product yield very low. Graphite electrode expands due to intercalation
K₂SO₄	0.1	+ 10V	3 to 5 min	Efficient exfoliation
NaClO₄	0.1	+10V	5 to 10 min	No exfoliation. Intercalation of graphite electrode occurs as evident by the expansion of the electrode
(NH₄)₂SO₄	0.1	+ 10V	3 to 5 min	Efficient exfoliation.

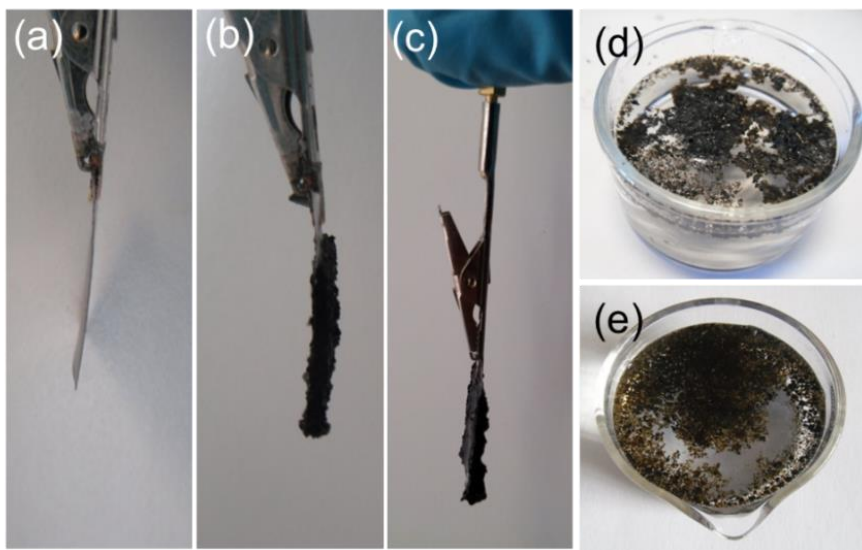


Figure 6.2 Photographs of (a) graphite electrode before electrochemical process. (b) and (c) expanded graphite electrode after electrochemical processes in 0.1 M NaNO_3 and NaClO_4 , respectively. After applying +10 V for 10 min, the electrodes displays only expansion without any obvious exfoliation. (d)-(e) exfoliated graphene in 0.1 M Na_2SO_4 and K_2SO_4 electrolytes, respectively.

6.2.2 Exfoliation mechanism

We propose the mechanism of electrochemical exfoliation as depicted in Figure 6.3: (i) applying bias voltage results in reduction of water at the cathode, producing hydroxyl ions (OH^-) which act as a strong nucleophile in the electrolyte. The nucleophilic attack of graphite by OH^- ions initially occurs at the edge sites and grain boundaries. (ii) the oxidation at the edge sites and grain boundaries then leads to depolarization and expansion of graphite layers and thereby facilitating the intercalation of sulfate ion (SO_4^{2-}) within graphitic layers. During this stage, water molecules may co-intercalate with SO_4^{2-} anions.

(iii) the reduction of SO_4^{2-} anions and self-oxidation of water produces gaseous species like SO_2 , O_2 etc., as evidenced by vigorous gas evolution during the electrochemical process.^{7,8} These gaseous species can exert large forces on graphite layers which are sufficient enough to separate weakly bonded graphite layers from one another.⁹

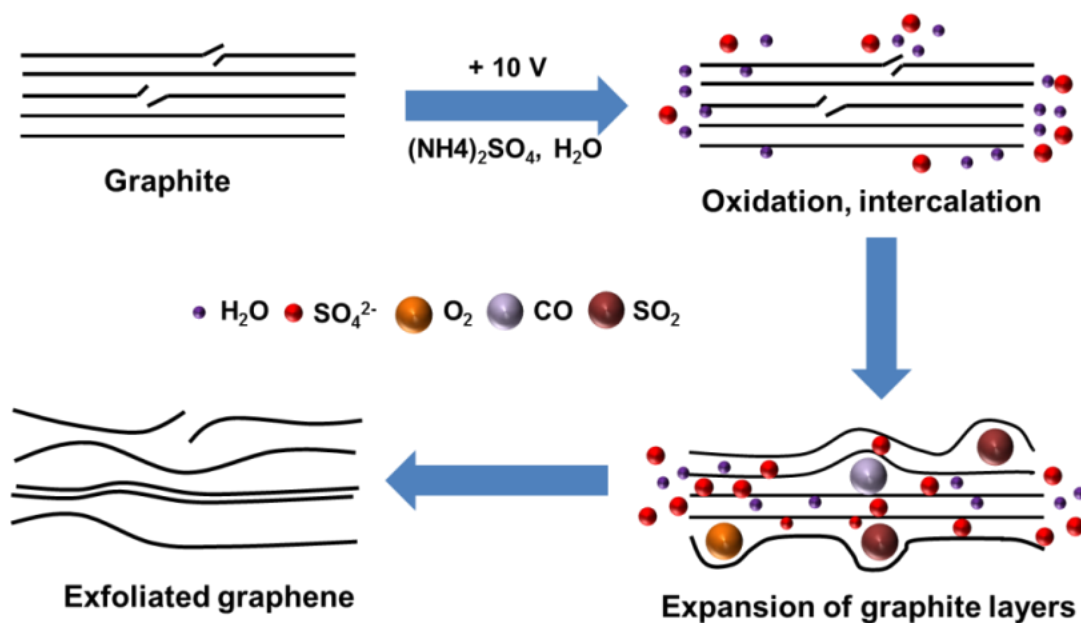


Figure 6.3 Schematic illustration of the mechanism of electrochemical exfoliation.

This hypothesis was further confirmed by control experiments where a constant bias voltage (i.e. +10 V) was applied to graphite electrodes for different time periods, from 5 s to 60 s, and the morphology changes of graphite foil were monitored by the scanning electron microscopy (SEM) and optical microscopy (OM) (Figure 6.4 and 6.5).

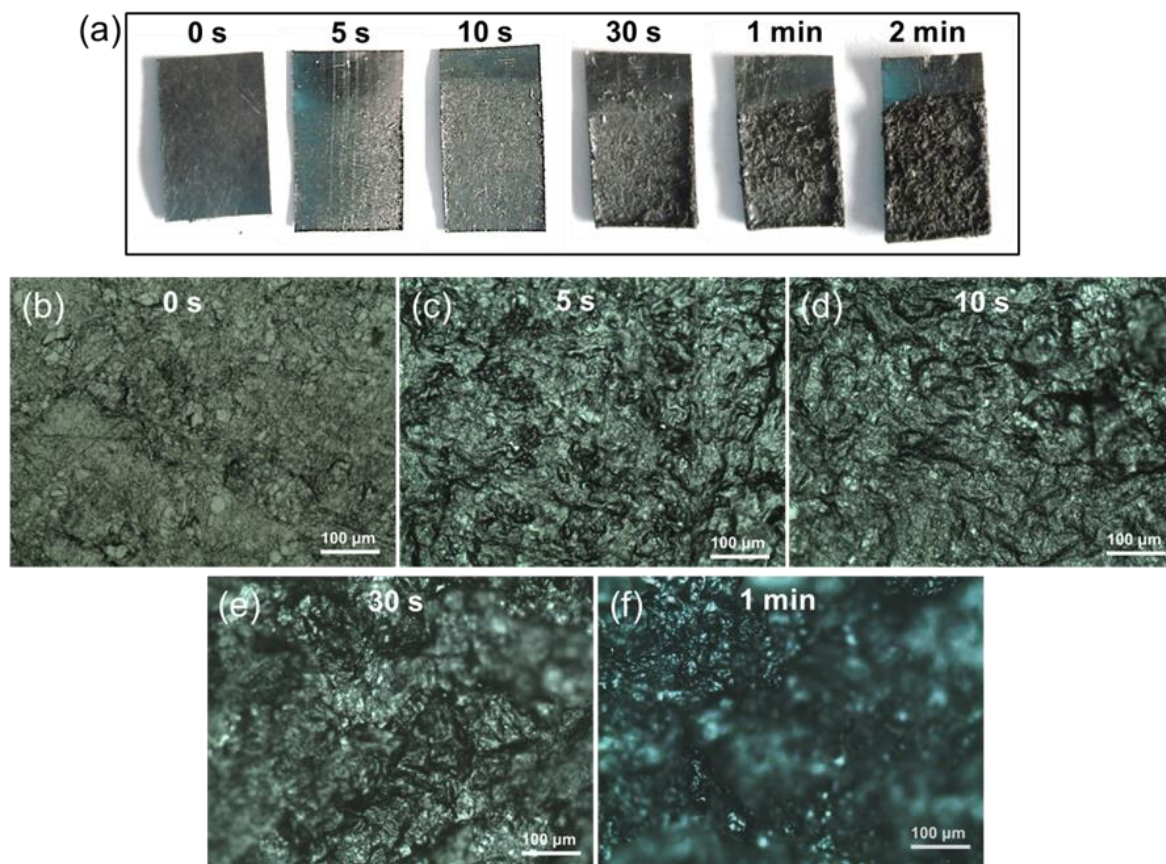


Figure 6.4 (a) Photographs and (b-f) optical microscopic images of graphite foil exfoliated at different time intervals revealing morphology changes on the electrode surface. The graphite electrodes with different morphology were obtained by applying a DC bias of +10 V in $(\text{NH}_4)_2\text{SO}_4$ electrolyte. As indicated in (b-f), the voltage was switched off after a certain period of time and subjected to OM analysis to monitor the morphological changes.

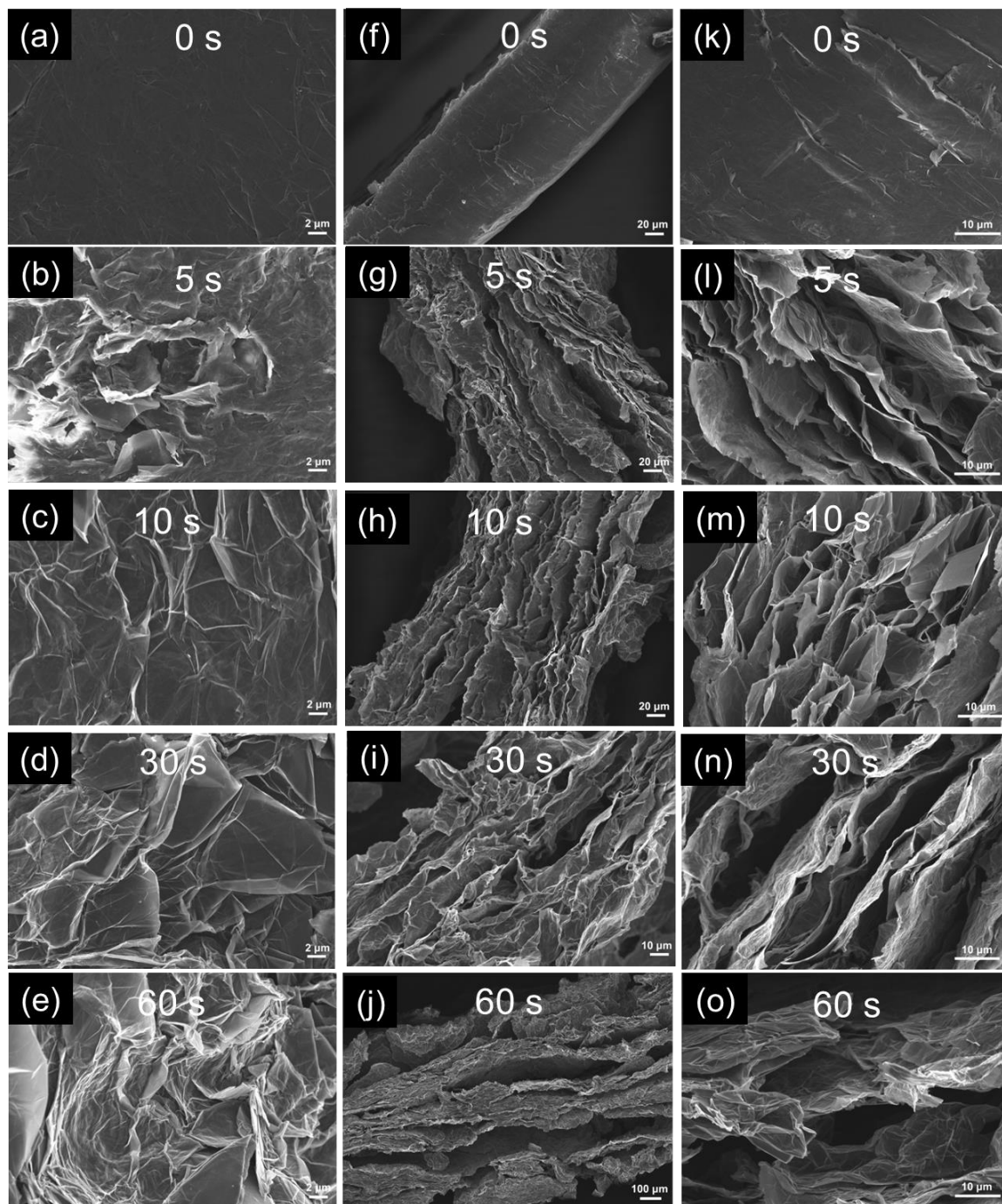
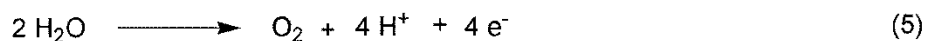
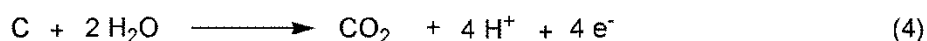
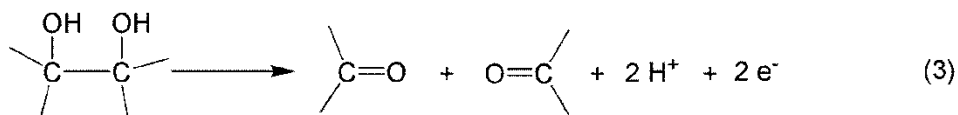
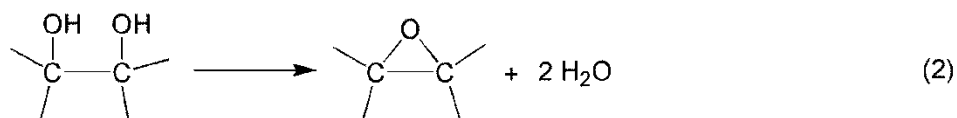
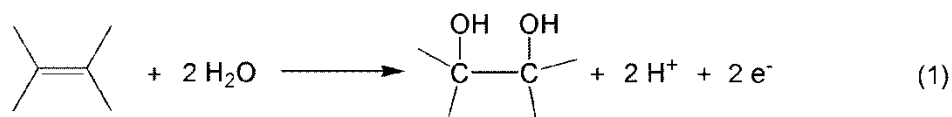


Figure 6.5 SEM images of (a-e) surface; (f-j) edge and; (k-o) magnified edge morphology of the graphite foil after applying a bias voltage of + 10V for 0 s to 60 s in aqueous $(\text{NH}_4)_2\text{SO}_4$ electrolyte.

The SEM images of both the surface and edge of original graphite foil exhibits closely packed layers (Figure 6.5). However, when the voltage was applied, the surface and edge morphology changed drastically within few seconds (Figure 6.4). After applying the voltage for 5 sec, the expansion of the edge of graphite foil and the increased crack of the graphite layers were observed (Figure 6.5g and l). When the time increased from 5 to 60 sec, a significant amount of graphene flakes were exfoliated and spread into the electrolyte. The edge of the graphite foil expanded almost 10 times after 60 s compared to the initial state (Figure 6.5j and o). Moreover, a network of ripples on the surface of graphite were clearly identified in SEM images (Figure 6.5b to e), which might be attributed to the visible gas evolution that caused expansion and swelling of graphite layers. Therefore, these observations strongly support our hypothesis that during the electrochemical process, edge and grain boundaries of graphite electrode first open up which facilitate anion intercalation and result in exfoliated graphene sheets. In addition, the electrochemical oxidation process i.e. oxide bond formations can be summarized as follows:



When a positive bias voltage is applied to the graphite electrode, nucleophilic water molecules attack on sp^2 carbon introducing C-OH groups followed by the formation of vicinal OH groups (reaction (1)).⁷ As the electrochemical process continues, epoxy rings might form (reaction 2). Furthermore, the diol can be further oxidized via C-C cleavage to form carbonyl groups (reaction 3). The C-O covalent bond formation can be accompanied by evolution of CO_2 (reaction 4) and self-oxidation of water, which producing O_2 (reaction 5).^{7,10,11} The formation of these oxygen containing groups on graphene is supported by the XPS analysis (discussed later on).

6.2.3 Effect of electrolyte concentration

We further investigated the effect of electrolyte concentration on the applied potential for graphite exfoliation. Figure 4.6a presents the voltage or potential for the graphite exfoliation which decreased upon increasing the concentration of $(NH_4)_2SO_4$. When the concentration of $(NH_4)_2SO_4$ was lower than 0.01 M, the yield of EG was less than 5 wt%, implying the limited amount of ions available for graphite intercalation. In sharp contrast, when the concentration increased from 0.01 M to 1.0 M, high yield of EG (~70 wt%) was achieved. Nevertheless, further increase in concentration. (i.e. 3.0 and 5.0 M) did not result in better yield of graphene (less than 50%, Figure 6.6b). As discussed above, initial oxidation of graphite by OH^- ions at the edge and/or grain boundaries causes depolarization and expansion of graphite layers and facilitates the anion intercalation. Increase of $(NH_4)_2SO_4$ concentration results in lowering the formation of OH^- ions due to low water content. Therefore, the graphite edge oxidation, expansion and SO_4^{2-} ion intercalation process is expected to be relatively slow at high salt concentration. Thus the

168

inefficient intercalation of SO_4^{2-} ions into graphite is likely to result in low yield of exfoliated product.

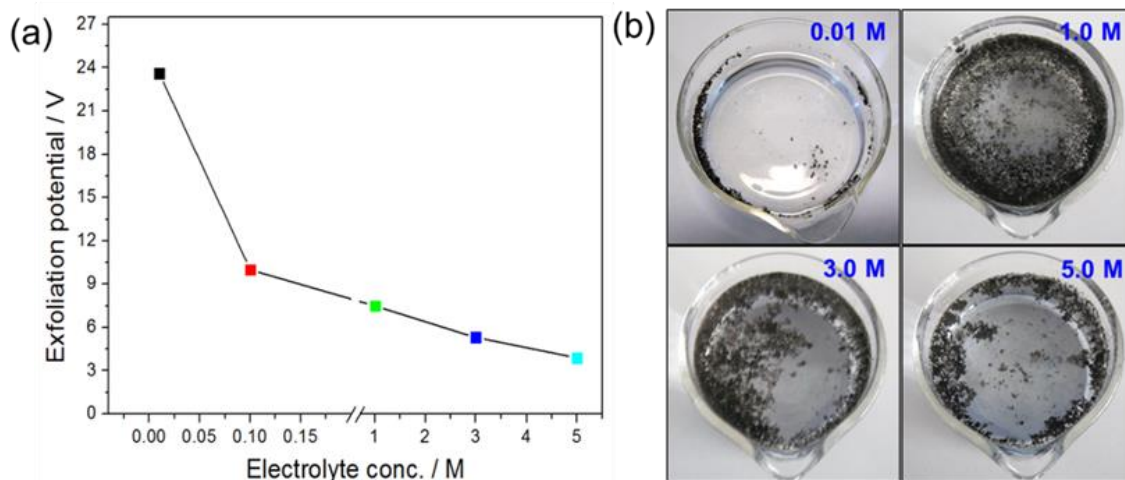


Figure 6.6 (a) Relationship of graphite exfoliation potential with different $(\text{NH}_4)_2\text{SO}_4$ concentration and (b) photographs of exfoliated product in $(\text{NH}_4)_2\text{SO}_4$ electrolyte of different concentration. For all cases, both the applied DC voltage (*i.e.* +10 V) and exfoliation time (3 min) were kept constant.

6.3 Morphology characterizations

The morphology of the EG sheets was investigated by SEM (Gemini 1530 LEO) and atomic force microscope (AFM) (Veeco Dimension 3100). EG flakes were deposited on SiO_2 substrates by employing Langmuir-Blodgett (LB) technique. Briefly, the EG dispersion in DMF (conc. $\sim 0.2 \text{ mg mL}^{-1}$) was mixed with chloroform (1:3 ratio of DMF: CHCl_3) and carefully dropped onto water surface using a 100 μL glass syringe. Dropwise addition of 3 mL of EG dispersion resulted in a faint black colored film on

water surface. Afterwards, the film was compressed by LB trough barriers while monitoring the surface pressure by a tensiometer. The EG film was then collected by vertically dip-coating SiO₂ (300 nm) substrates followed by annealing at 200 °C for 30 min under vacuum to evaporate residual solvents. Figure 6.7a, b and c display the SEM images of EG flakes obtained from electrochemical exfoliation in (NH₄)₂SO₄, Na₂SO₄ and K₂SO₄ electrolytes, respectively. Measuring the lateral size over hundreds of EG flakes reveals that over 80% of EG flakes were larger than 5.0 μm size (Figure 6.7d), and the largest flake size observed was ~ 44.0 μm (inset of Figure 6.7a).

A histogram acquired across the EG flake by AFM revealed a mean thickness of ~ 0.69 nm (Figure 6.8a), confirming a monolayer nature which is comparable with the thickness of pristine graphene on SiO₂¹². The measured thickness of a bi-layer and a four-layer EG is 1.30 and 3.11 nm, respectively (Figure 6.8b and c). Moreover, the thickness distribution of more than 50 flakes calculated from AFM height profile is presented in Figure 6.8d. Remarkably, 85% of EG flakes comprise thin graphene layers (1 to 4 layers) where, single and bi-layer graphenes are the dominant products (together ~ 70%). High resolution transmission electron microscopic (HRTEM) images further support that the EG flakes range from single layer to four layers (Figure 6.9a-c). A selected area electron diffraction (SAED) pattern in Figure 6.9d exhibits a typical six-fold symmetric diffraction, indicating the high crystallinity of a bi-layer EG.¹³

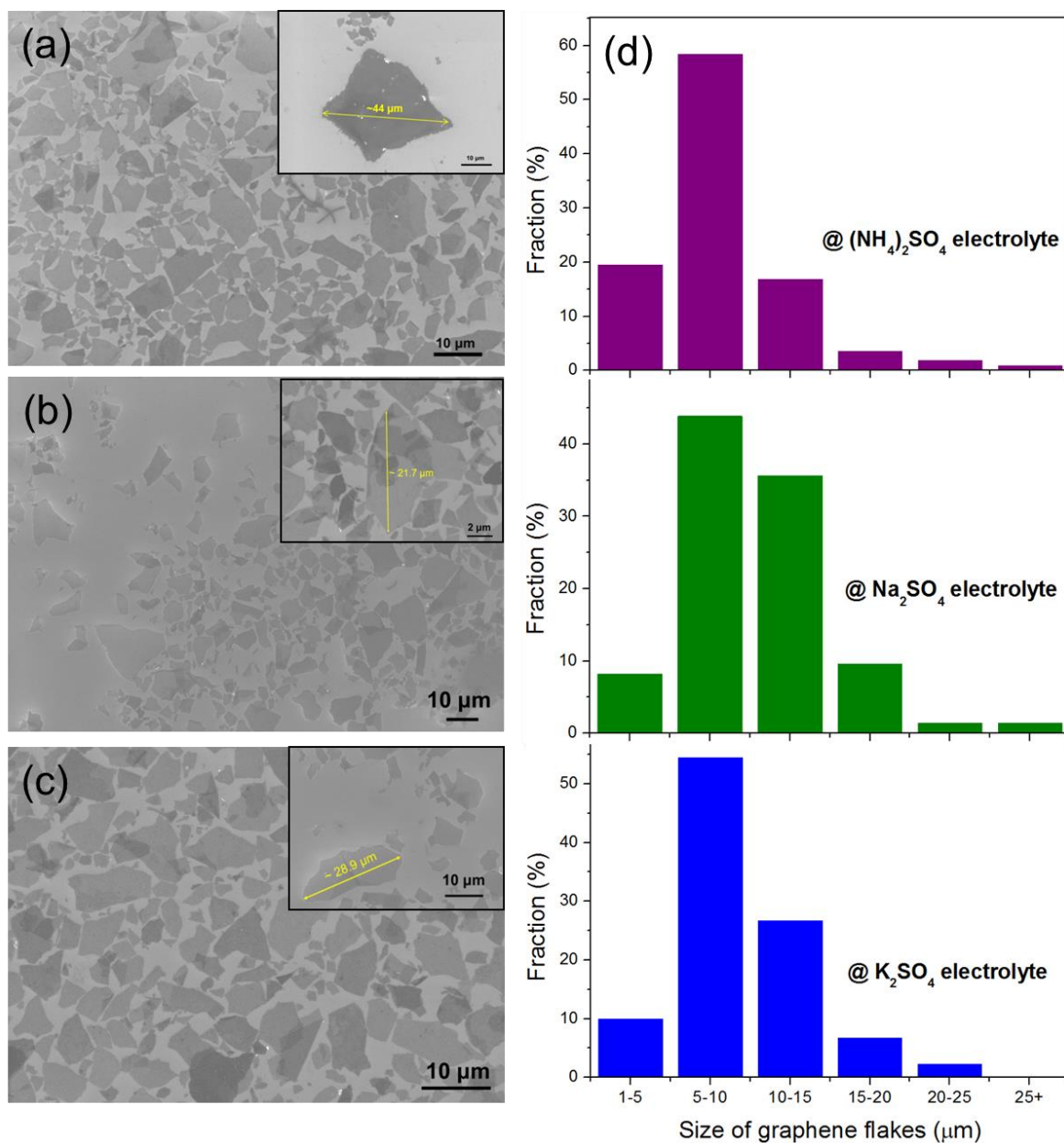


Figure 6.7 (a), (b) and (c) SEM images of EG flakes obtained in aqueous $(\text{NH}_4)_2\text{SO}_4$, Na_2SO_4 and K_2SO_4 electrolytes, respectively. The inset presents the largest EG flake observed in the corresponding electrolyte system; (d) statistical flake size analysis of EG sheets from $(\text{NH}_4)_2\text{SO}_4$, Na_2SO_4 and K_2SO_4 electrolytes, respectively.

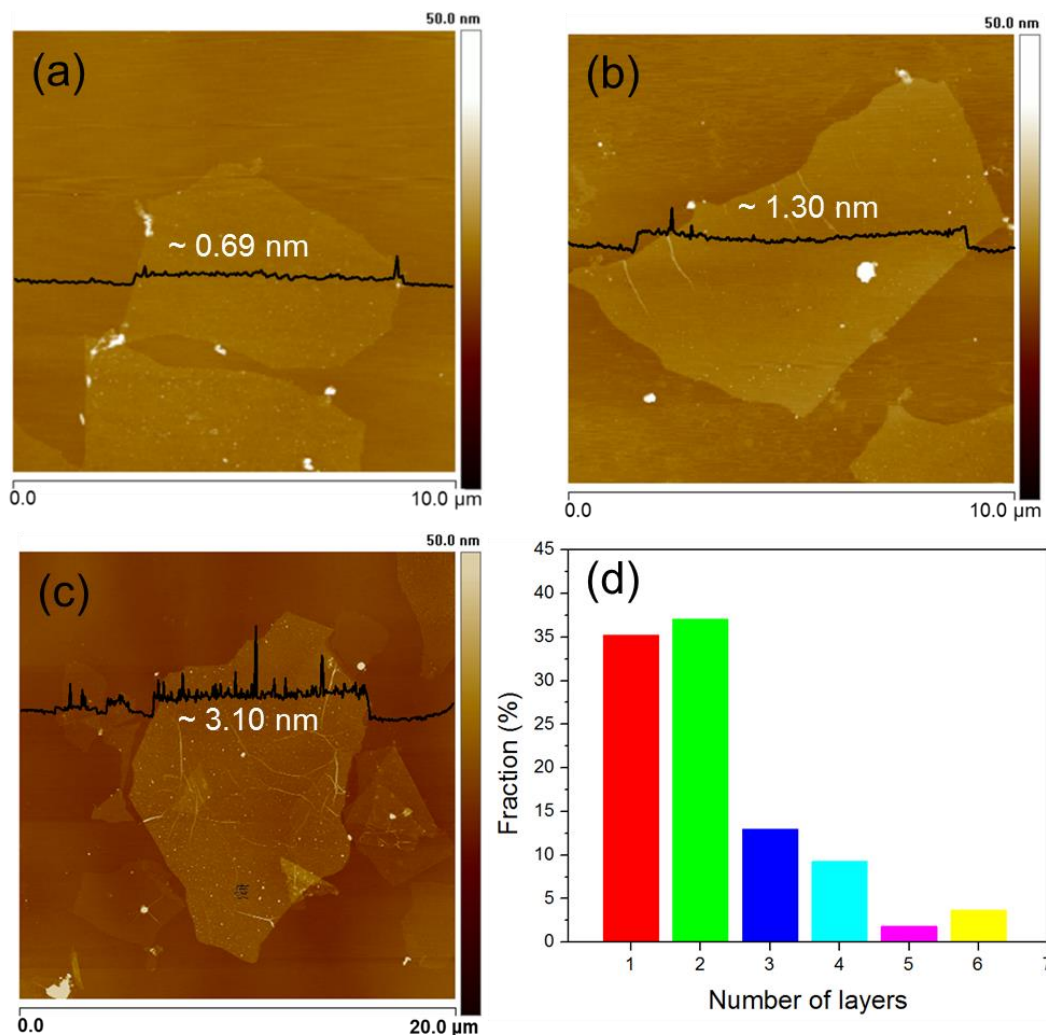


Figure 6.8 AFM images of (a) single layer (b) bi-layer, (c) multi-layer EG flakes on silicon wafer. The corresponding height profiles with the thickness are shown inside each image. (d) Statistical thickness analysis of EG by AFM.

The Raman spectroscopy has been extensively used as a nondestructive tool to probe the structural characteristics of graphene.^{14, 15} Thus, we performed Raman spectroscopy and mapping with a 532 nm excitation laser on EG deposited on SiO₂/Si substrates. Raman mapping of D and G peaks from a few layer EG flake (2 to 4 layers) (selected are in Figure 6.10a) was extracted and plotted in Fig. 3b and c, respectively. The D peak ($\sim 1350 \text{ cm}^{-1}$) is caused by the breathing mode of sp^2 carbon atom and activated by

the existence of defects such as edges, functional groups or structural disorders.¹⁶ The intensity contrast in the color scale in Figure 6.10b and c reveals that the intensity of G peak is more than twice than that of D peak (average I_D/I_G ratio is 0.42), indicating low defect content. The corresponding Raman spectra in Figure 6.10d (measured nearby the center of the graphene flake) indicate that the I_D/I_G ratio is 0.25, which is much smaller than the chemically or thermally rGO (~ 1.1 to 1.5),¹⁷ and electrochemically exfoliated graphene (0.4)¹ in acidic electrolyte.

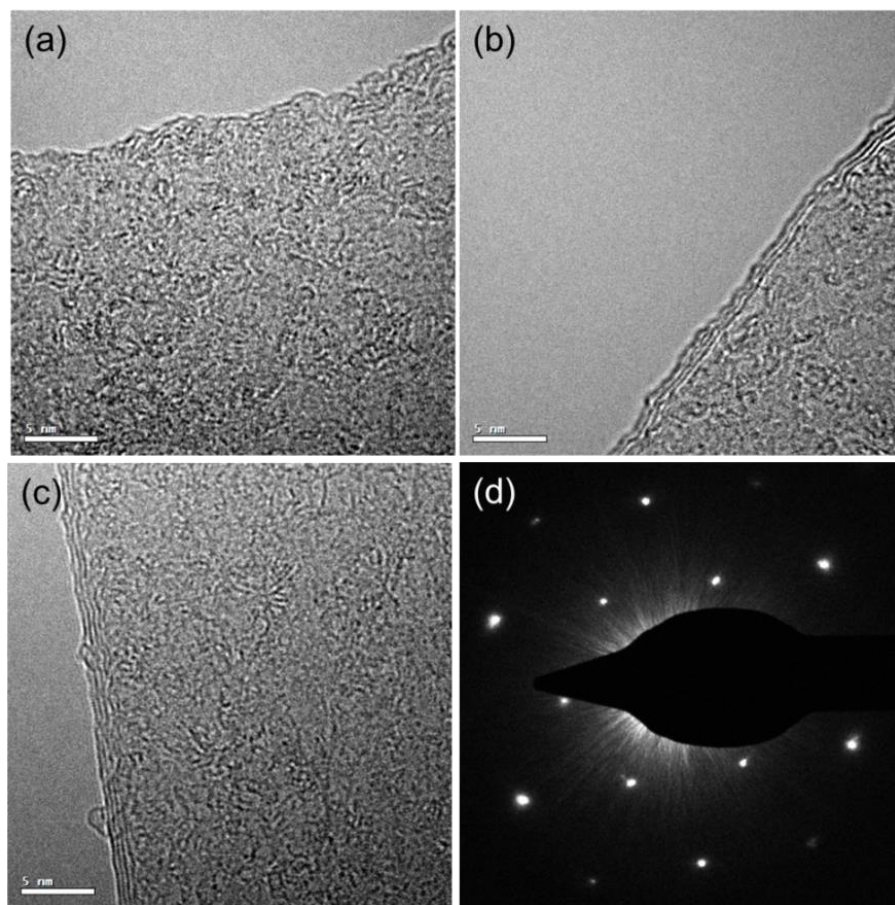


Figure 6.9 HRTEM images of (a) single layer, (b) three layer and (c) four layer EG. (d) SAED pattern of a bi-layer EG.

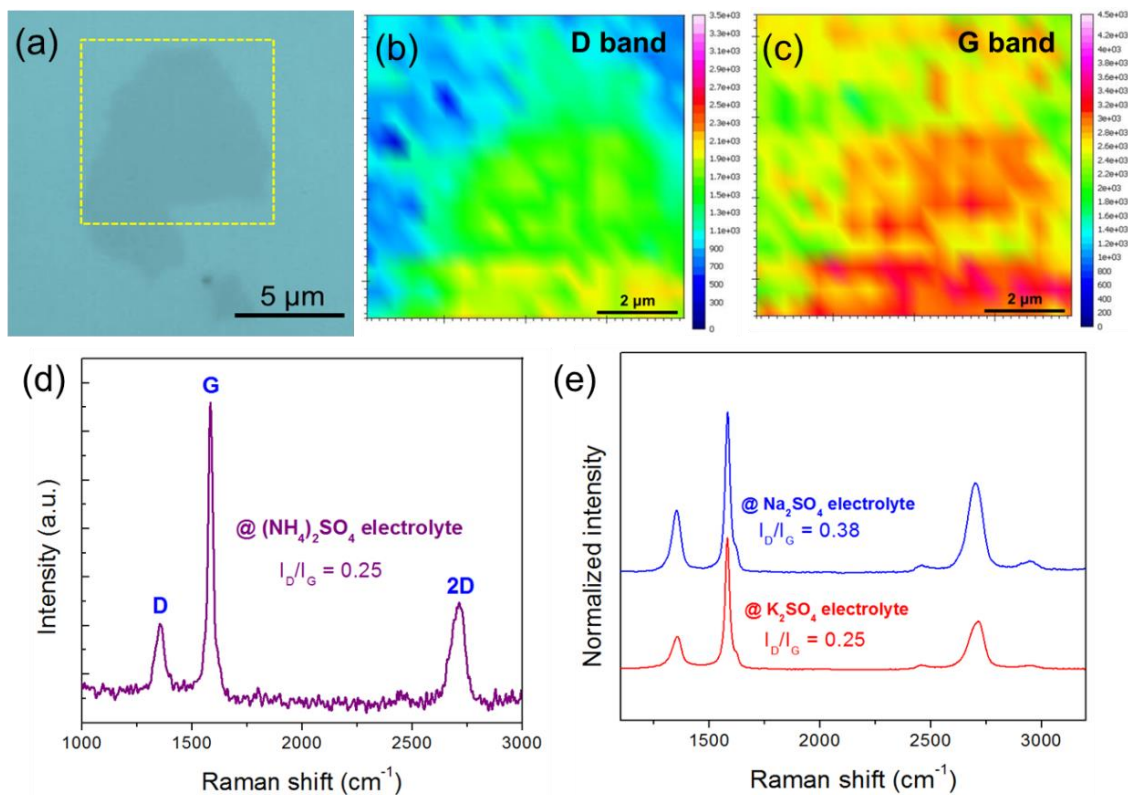


Figure 6.10 (a) Optical microscopic image of an EG flake obtained in $(\text{NH}_4)_2\text{SO}_4$ electrolyte; (b) and (c) Raman intensity maps for D and G peak resulted from EG flake shown in (a), respectively; (d) and (e) representative Raman spectra of EG flakes from different electrolyte systems. The wavelength of the Raman excitation laser is 532 nm.

6.4 Structural characterizations

X-Ray photoelectron spectroscopy (XPS) was used to probe the chemical composition of the prepared EG in aqueous $(\text{NH}_4)_2\text{SO}_4$ electrolyte. The XPS measurements were carried out by Dr. Xianjie Liu in the group of Prof. Mats Fahlman at Linköping University, Sweden. The EG revealed approximately 5.5 at% oxygen content on graphene (Figure 6.11a), which is much lower than that obtained in acidic electrolytes (*i.e.* 7.5 at%).

Despite the presence of a tiny amount of oxygen originated from the oxidation of graphite by OH^- ions during electrochemical process, the C/O ratio of 17.2 for EG is significantly higher than the exfoliated graphene and rGO reported to date.^{1,18,19} The deconvoluted XPS spectra of C1s peak (Figure 6.11b) display the presence of 3.64 at% of C-OH (285.5 eV), 0.38 at% of C=O (287.6 eV) and 1.48 at% of C(O)-O (290.1 eV) groups.

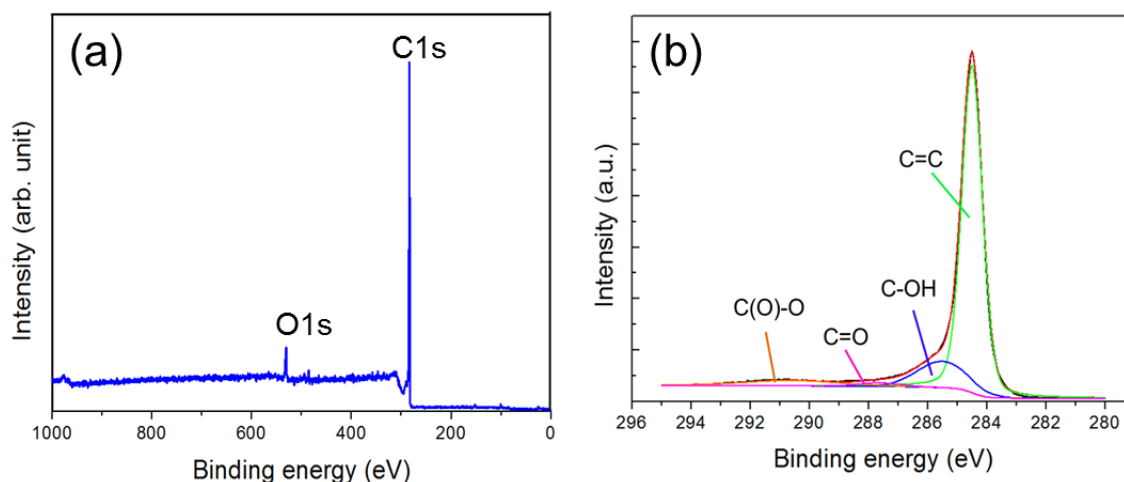


Figure 6.11 (a) XPS survey spectra and (b) deconvoluted high-resolution C1s spectra of EG.

Solid-state NMR studies were conducted by Dr. Robert Graf in our institute to gain structural analysis of EG. The ^{13}C magic angle spinning (MAS) NMR revealed a broad signal centered at 122 ppm (graphitic, C sp^2) indicating the presence of pure sp^2 hybridized carbon sites (Figure 6.12a). In contrast, the NMR spectrum of GO shows an additional signal of sp^3 hybridized carbons bound to oxygen (C-OH or C-O-C) in the range from 60 - 70 ppm. It should be noted that the signal at 122 ppm is substantially broader in the graphene compared to the GO and might be due to high conductivity of EG resulting in higher number of perturbing magnetic moments of the free charges. The spinning of EG sample in the magnetic field was found to be difficult because of high conductivity of EG

which also limits the filling of MAS rotors. As a result, ^{13}C MAS NMR spectra of EG has a poor spectral resolution and low signal to noise ratio than that of GO. Note that, due to the strong paramagnetic properties and the high electrical conductivity of the EG sample, only approximately 3-4 mg of graphene was placed in 2.5 mm MAS rotor such that they were located in the center of the NMR detection coil when the rotor is spinning in the probe, while both ends of the rotor were filled with KBr.

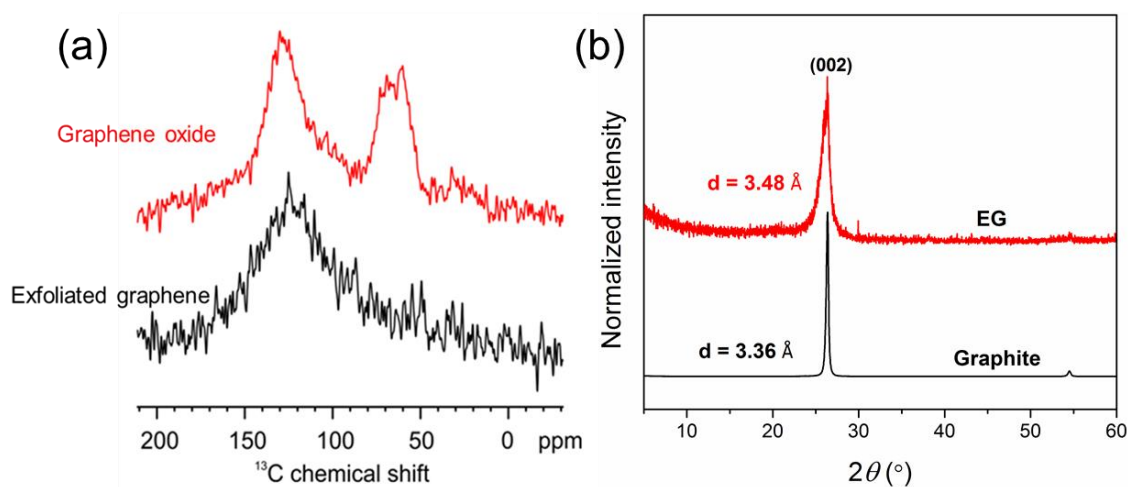


Figure 6.12 (a) Solid-state ^{13}C MAS NMR spectra of graphene oxide and exfoliated graphene recorded at 30 kHz MAS and 176 MHz ^{13}C Larmor frequency. (b) Powder XRD of exfoliated graphene.

The powder X-ray diffraction (XRD) measurements of EG were performed by Michael Steiert in our institute using a Bruker D4 X-ray scattering system with Ni-filtered Cu K α radiation, shows a peak at 26.3° (d -spacing 3.48 \AA) (Figure 6.12b). Presence of small amount of functional groups in EG acts as a spacer between layers and results in

lower 2θ angle with large d -spacing compared to graphite (26.5° , d -spacing 3.36 \AA), but significantly higher than the reduced GO (25.0° , d -spacing $\sim 3.56 \text{ \AA}$).¹⁸

6.5 Electronic properties

To examine the electronic properties of the as-prepared EG flakes, we fabricated FET devices based on thin EG film (thickness ~ 0.5 to 4 nm) and a single layer EG sheet (thickness $\sim 0.71 \text{ nm}$) (Figure 6.13d). Both thin EG film and isolated single layer EG on SiO_2/Si substrates were prepared by Langmuir-Blodgett (LB) method. The transfer curves of the FET devices based on EG thin film and single layer are shown in Figure 6.13a and c, respectively. Notably, the device based on thin EG film (Figure 6.13a) shows a maximum hole mobility of $98.2 \text{ cm}^2 \text{ V}^{-1} \text{ s}^{-1}$. Whereas, a single-layer graphene (Figure 6.13c) delivers a hole mobility of $\sim 310 \text{ cm}^2 \text{ V}^{-1} \text{ s}^{-1}$ and a sheet resistance of $1.96 \text{ k}\Omega \text{ sq.}^{-1}$ (Figure 6.14a) that is comparable with un-doped CVD grown graphene ($1.05 \text{ k}\Omega \text{ sq.}^{-1}$).²⁰ The lower mobility of the thin film device can be attributed to the interjunction resistance between EG flakes. It should be emphasized that the hole mobility values of single-layer EG achieved in this work are significantly higher than the chemically reduced GO ($123 \text{ cm}^2 \text{ V}^{-1} \text{ s}^{-1}$)²¹, electrochemically exfoliated graphene in acidic electrolytes ($233 \text{ cm}^2 \text{ V}^{-1} \text{ s}^{-1}$).¹ Table 6.2 summarizes a comparison of the mobility of the EG with different types of graphene.

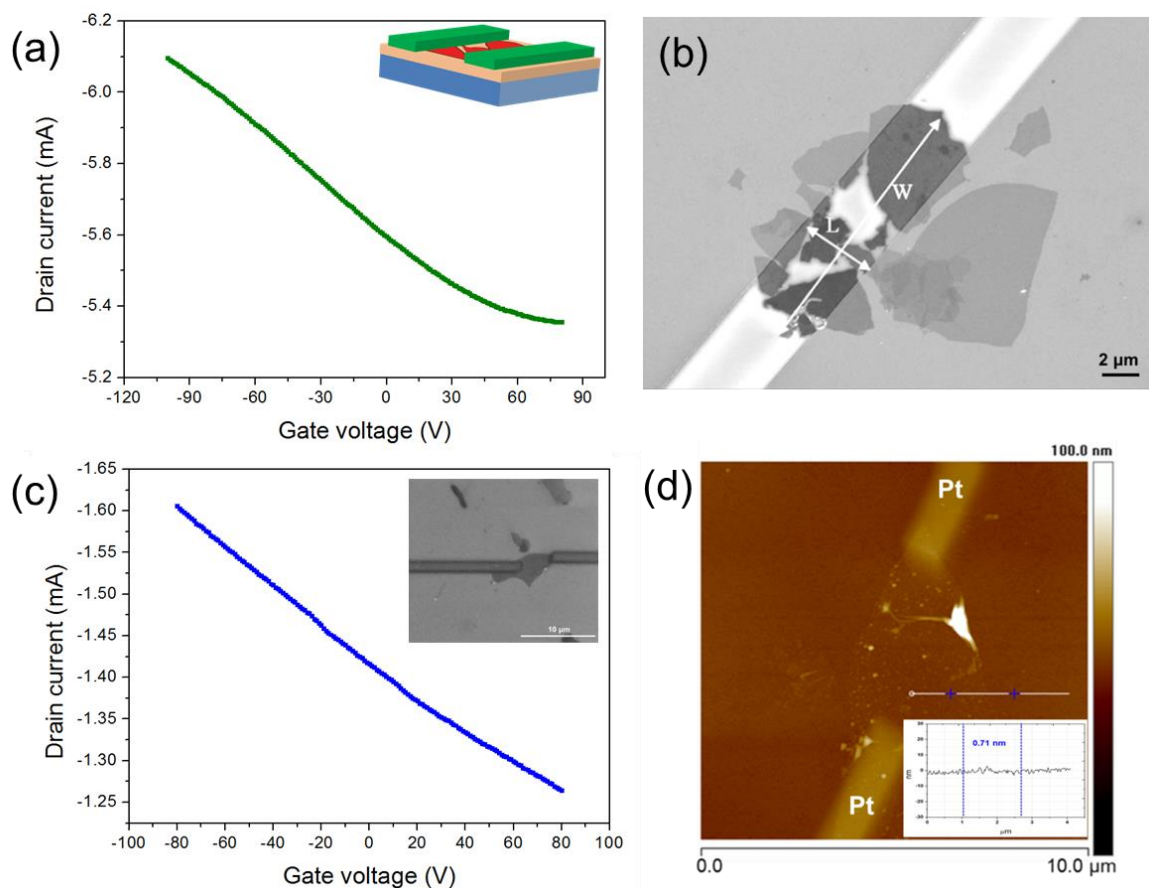


Figure 6.13 (a) Transfer curve for a field-effect transistor (FET) devices based on thin EG film; (b) SEM images of the fabricated device exhibiting the EG flakes between the Au electrodes. Channel length (L) and width (W) is indicated by arrows; (c) transfer curve of a FET device based on a single layer EG (inset is the SEM image of the fabricated device); (d) AFM image of the single layer EG based FET device. Platinum (Pt) electrodes deposited by focused ion-beam was used to connect EG flake. Inset presents the corresponding height profile of EG flake.

Table 6.2 Comparison of mobility values of FET devices based on different types of graphene.

Types of graphene	Sample type	Hole mobility (cm ² /V·s)	Electron mobility (cm ² /V·s)	Reference
Reduced GO (Hydrazine vapor, 80 °C and thermal annealing at 200 °C)	Film	1	0.2	<i>Nat. Nanotechnol.</i> 3 (2008) 270
rGO (thermal annealing at 1000 °C)	Film	5.1	1.1	<i>Nano Lett.</i> 10 (2010) 92
rGO (hydrazine vapor reduction at 80 °C, 24 h)	Sheets	43.55	14.91	<i>Adv. Mater.</i> 24 (2012) 2299
Liquid-phase exfoliated graphene	Film	95	-	<i>ACS Nano</i> 6 (2012) 2992
Electrochemically exfoliated in H ₂ SO ₄ electrolyte	Film	47.3	-	<i>ACS Nano</i> 7 (2013) 3598
	Bi-layer sheet	233		
Electrochemically exfoliated in H ₂ SO ₄ + KOH electrolyte	Single graphene sheet	5.5 - 17	-	<i>ACS Nano</i> 5 (2011) 2332
rGO (Na-NH ₃ reduction at -33 °C, 30 min)	Single sheet	123	-	<i>Nat. Commun.</i> 4 (2013) 1539
Electrochemically exfoliated in (NH₄)₂SO₄ electrolyte	Film	98.16		This work
	Single layer sheet	310		

The work function of the EG was measured by ultraviolet photoelectron spectra (UPS) (ESCA 200 spectrometer) with a He discharge lamp providing photon energy of 21.22 eV. The work function was calculated using the equation, $\Phi = h\nu - E_F + E_{\text{cutoff}}$, where $h\nu$, E_F and E_{cutoff} are the photon energy of the excitation light, the Fermi level edge and the measured secondary electron cutoff. As shown in Figure 6.14b, the measured work function (Φ_{EG}) of EG is 4.57 eV, slightly higher than the work function of pristine graphene (~ 4.50 eV)²², which can be attributed to the presence of oxygen containing functional groups that can produce surface dipoles via the extraction of π electrons from graphene²³.

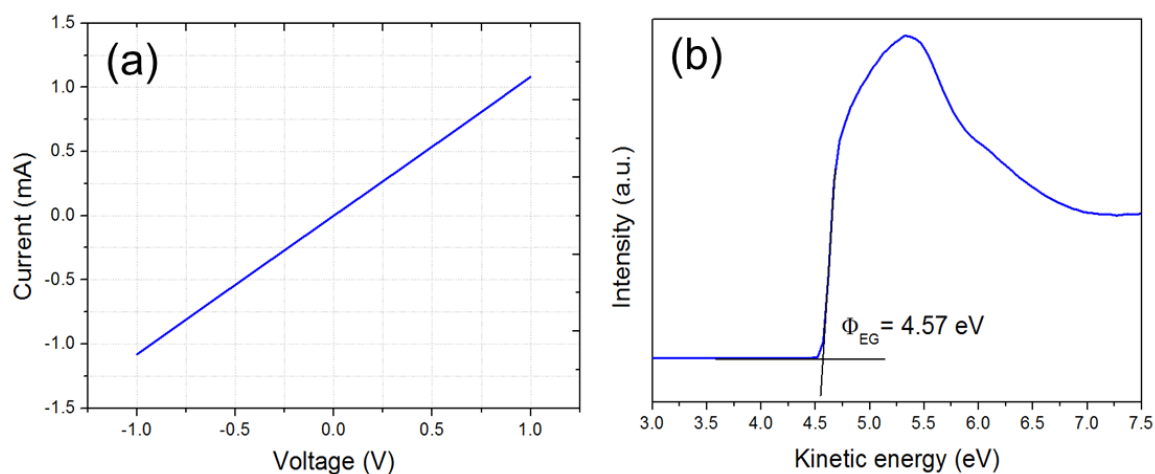


Figure 6.14 (a) Current-voltage (I - V) curve of an isolated single layer EG flake; (b) ultraviolet photoelectron spectra of EG.

6.6 Fabrication of exfoliated graphene based thin films

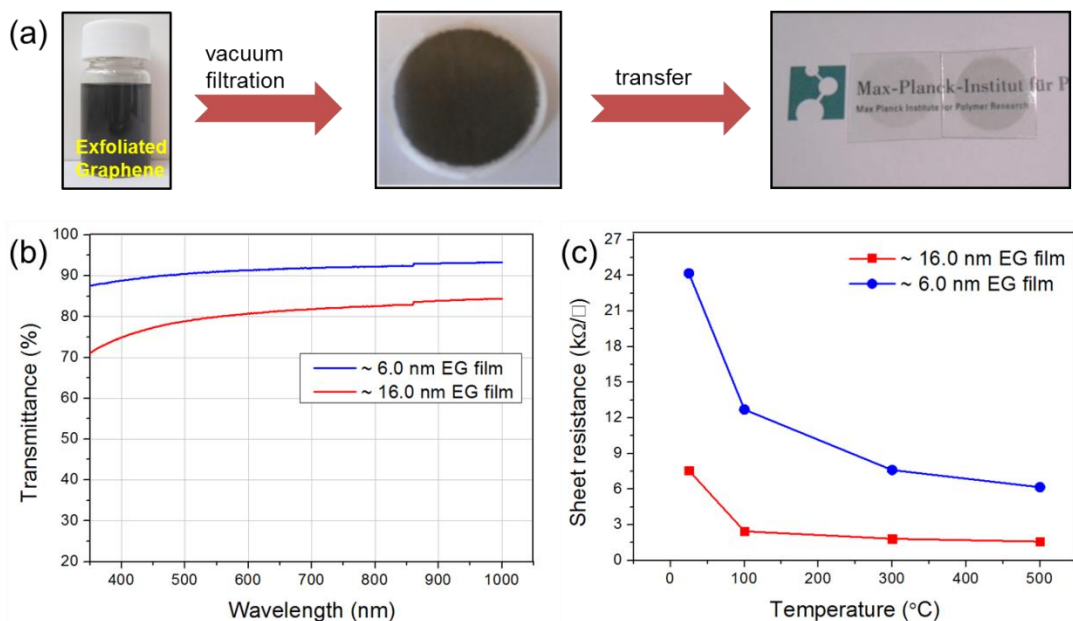


Figure 6.15 (a) Illustration of the fabrication process of transparent, conductive EG films on PET substrates, (b) transmittance of the fabricated films and, (c) sheet resistance (R_s) of EG films with different thickness.

The high-quality and solution processability of EG allow for fabricating transparent graphene films on flexible polyethylene terephthalate (PET) substrates by a vacuum filtration and dry transfer method (Figure 6.15a).¹ Briefly, an EG dispersion of 0.1 mg/mL in DMF was vacuum filtered through a polytetrafluoroethylene (PTFE) membrane followed by mechanically pressing the filtered film against a PET substrate. Afterwards, the PTFE membrane was peeled off, leaving the transferred EG film on the substrate due to van der Waals interaction between the substrate and graphene. The thickness of the transferred EG film can be adjusted via controlling the filtration volume and the concentration of EG

dispersions. For instance, vacuum filtration of 3 and 9 mL of EG dispersion resulted in ~ 6.0 and ~ 16.0 nm graphene films on PET with ~ 91.0 and ~ 79.9% transparency (Figure 6.15b), respectively.

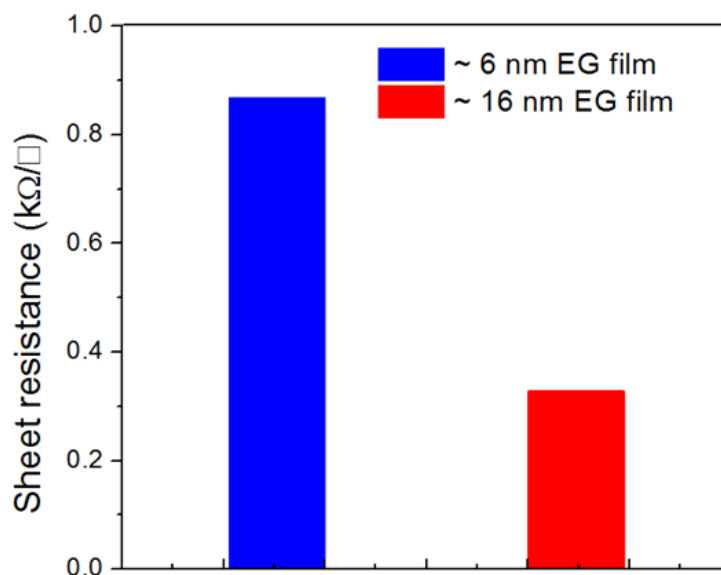


Figure 6.16 Sheet resistance of EG films with different thickness after HNO₃ (65%) doping.

The sheet resistance (R_s) measured by a four-point probe system revealed an average value of 24.2 and 7.56 kΩ sq.⁻¹ for ~ 6.0 and ~ 16.0 nm films, respectively. Low temperature annealing (*i.e.* 300 °C) of the EG films decreased the R_s to 7.61 and 1.81 kΩ sq.⁻¹ (Figure 6.15c), respectively. Remarkably, further doping the EG films with 65% HNO₃ for 2 h, over 80% reduction of R_s was achieved without any significant change in transparency. The final R_s values for ~ 6.0 and ~ 16.0 nm EG films were 0.87 and 0.33 kΩ sq.⁻¹, respectively (Figure 6.16). Notably, R_s of the EG films fabricated from the electrochemical exfoliation in inorganic salt electrolytes is significantly lower than that of

the EG obtained in acidic electrolytes,^{1,4} liquid-phase exfoliated graphene films,^{24,25} and thermally and/or chemically reduced GO.^{26,27} The low R_s might be attributed to the large flake size (which minimizes the inter-junctions resistance)²⁸ and low defect density of EG sheets.

6.7 Graphene-ink

Furthermore, we demonstrate the use of EG as conductive-ink which is an important requirement for next-generation printable electronics. Towards this end, conductive graphene-ink was prepared by dispersing 1 g of EG powder in 100 mL DMF (*i.e.* concentration 10 mg/mL) followed by sonication for 20 min (Figure 6.17a). As-prepared EG dispersion was then brush painted on commercial A4 size paper. Afterwards, the painted paper was dried at 120 °C for 2 to 3 min. The brush painting and drying process was repeated several times. Thus, an A4 size paper simply transforms the paper into an electrically conductive sheet (Figure 6.17b). The bonding of cellulose fiber in paper produces many air passages or pores throughout the paper (Figure 6.17d). Thus, the highly porous nature of paper provides strong capillary force for the EG ink, which can enhance the solvent absorption and lead to a conformal coating of EG ink on paper (Figure 6.17e). Moreover, a simple film adhesion test with a Scotch tape demonstrates the strong adhesion between EG onto and paper, confirming high film stability against damage, such as scratching or peeling off (Figure 6.17c).

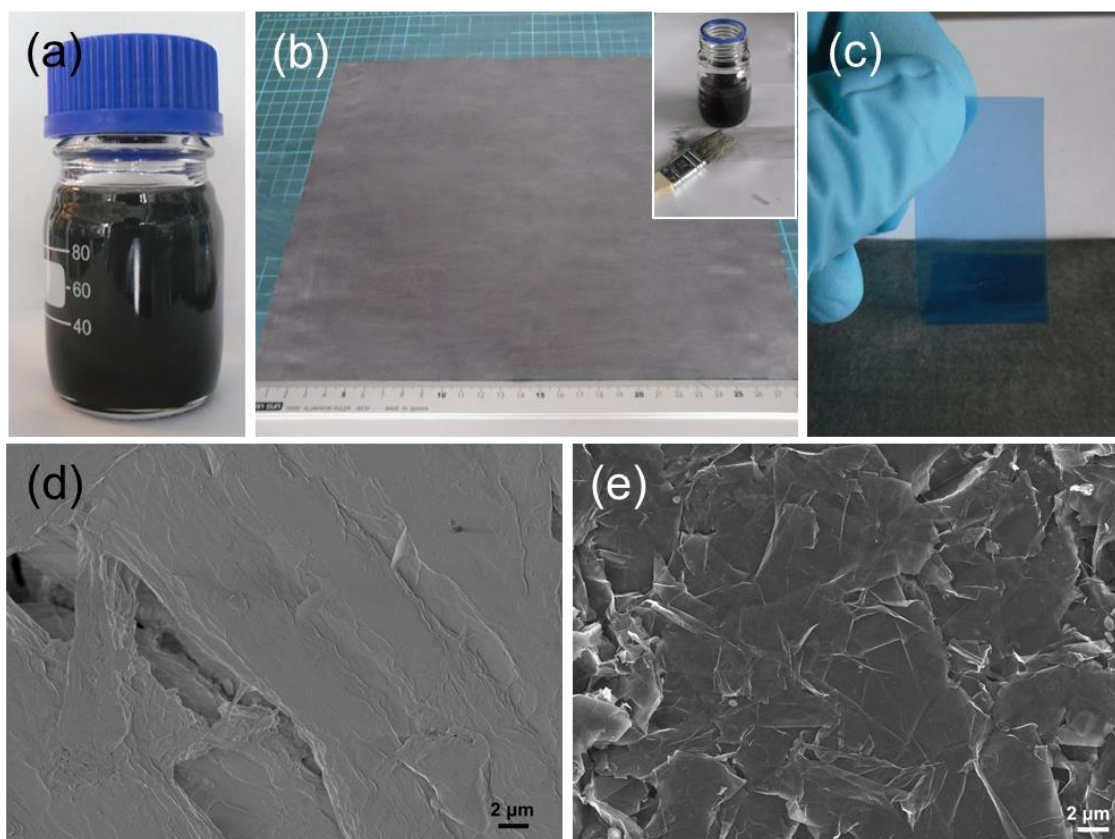


Figure 6.17 (a) Photograph of EG in DMF (10 mg/mL) used as an ink; (b) commercial A4 paper coated with EG using a painting brush (inset); (c) film adhesion test with Scotch tape; (d) and (e) SEM images revealing surface morphology of Xerox paper and EG on paper fabricated by brush painting, respectively.

The relationship between the paper resistance and the amount of EG loading (in mg cm^{-2}) is presented in Figure 6.18. A sheet resistance of $\sim 11 \Omega \text{ sq.}^{-1}$ was obtained with an EG loading of 0.74 mg cm^{-2} , comparable to carbon nanotube (CNT) paper.²⁹ Moreover, the graphene paper exhibits excellent mechanical properties. After bending down to 4 mm radius, the EG paper shows no significant change in electrical conductivity (Figure 6.18b).

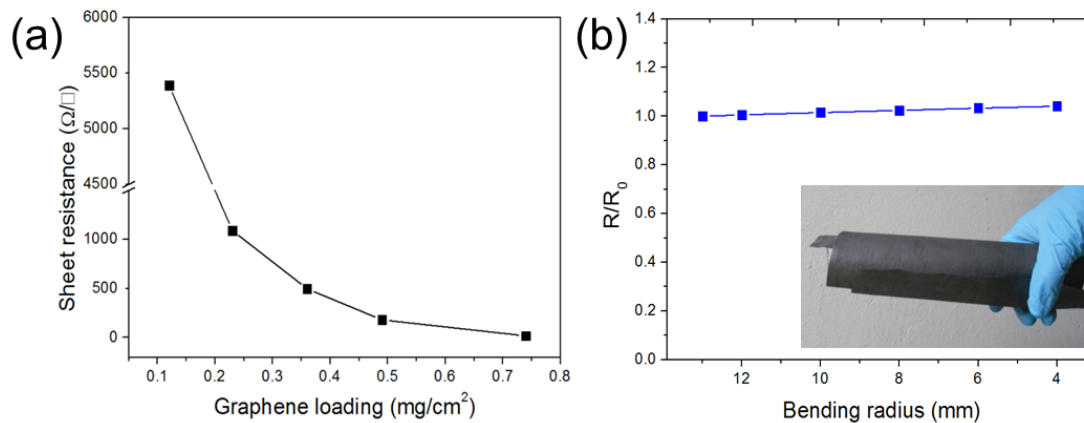


Figure 6.18 (a) Relationship between the resistances of the paper with graphene loading and; (b) changes in sheet resistance after bending the conductive paper into different radii.

6.8 Graphene paper based supercapacitors

To demonstrate the multifunction of the EG paper, we have explored the potential of EG coated paper for all solid-state flexible supercapacitors. For this purpose, a polyvinyl alcohol (PVA)/ H_2SO_4 gel was drop-cast onto the top surface of EG coated paper (with a loading of $\sim 0.60 \text{ mg cm}^{-2}$) and solidified for overnight. The active area of the supercapacitor device was $2 \text{ cm} \times 2 \text{ cm}$. Afterwards, two pieces of EG paper electrodes were integrated to a solid-state supercapacitor without using any additional current collector. The electrochemical properties of as-fabricated device were investigated by Dr. Zhong-Shuai Wu in our group using cyclic voltammetry (CV). The area capacitance value was calculated from CV data according to the following equation:

$$C_{\text{area}} = \frac{1}{v(V_f - V_i)A} \int_{V_i}^{V_f} I(V) dV$$

Where C_{area} is denoted as the area capacitance based on graphene electrodes ($F\text{ cm}^{-2}$), ν is the scan rate ($V\text{ s}^{-1}$), V_f and V_i are the integration potential limits of the voltammetric curve, and $I(V)$ is the voltammetric discharge current (A), and A refers to the total area (cm^2) of device.

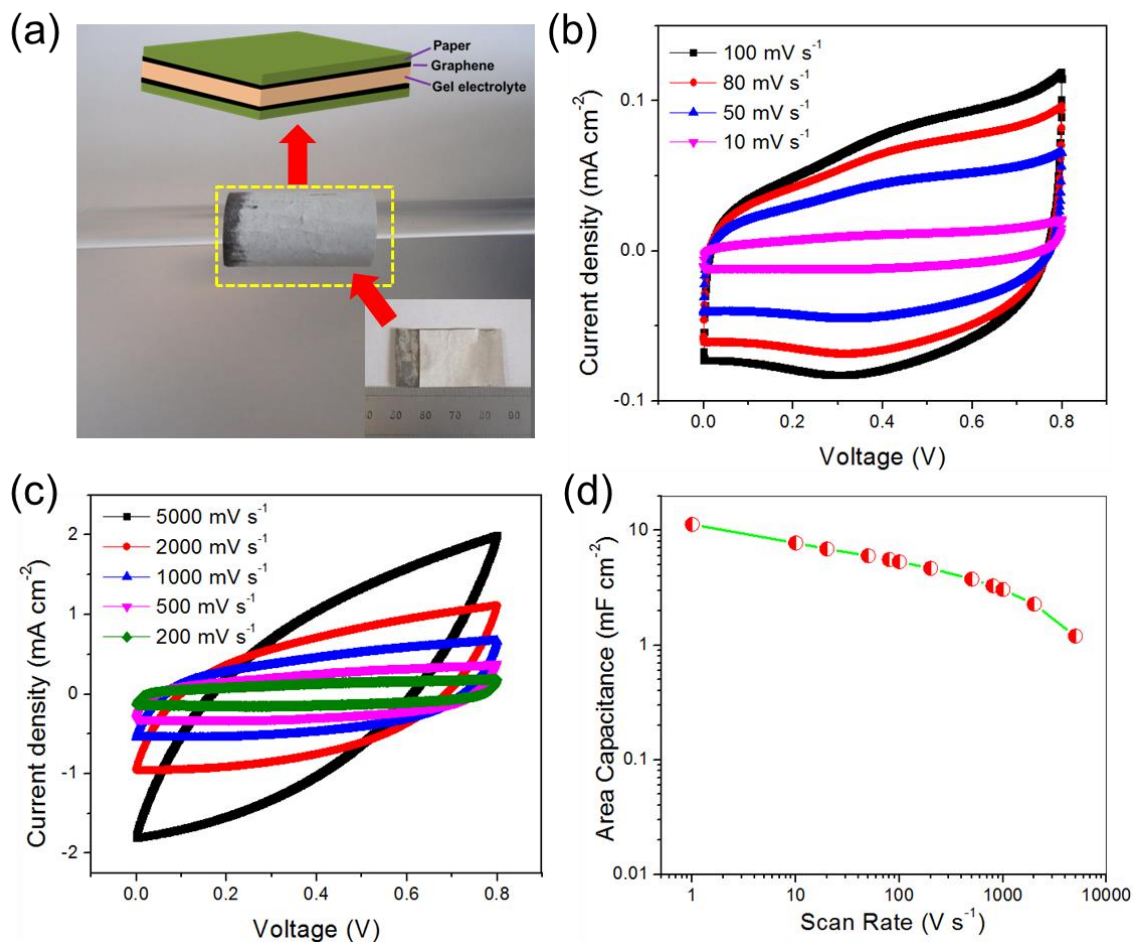


Figure 6.19 (a) Photographs of supercapacitor based on EG ink coated paper, where the device is rolled around a glass rod. The inset presents the photograph of the device prior rolling; (b) and (c) cyclic voltammetry curves obtained at scan rates from 0.01 to 0.1 V s^{-1} and from 0.2 to 5.0 V s^{-1} ; (d) evolution of area capacitance versus scan rate.

The fabricated all solid-state supercapacitor from graphene coated paper can be easily rolled onto a glass rod demonstrating its high flexibility (Figure 6.19a). Moreover, the binder- and additive-free fabricated EG electrode based supercapacitor exhibited a typical double-layer capacitive behavior at various scan rates (Figure 4.19b). The area capacitances of the fabricated device were 11.3 mF cm^{-2} at a scan rate of 1 mV s^{-1} (Figure 6.19d) comparable to or even higher than thin-film rGO,³⁰ CNTs,³¹ ZnO nanowires,³² and carbon nanoparticles/MnO₂ hybrid³³ supercapacitors on flexible substrates. In addition, the gravimetric capacitance calculated on the basis of the area capacitance ranges from 18.8 to 56.6 F g^{-1} , depending on the loading of EG on paper varying from 0.6 to 0.2 mg cm^{-2} , respectively (Figure 6.20). Remarkably, the device exhibited high rate capability which could be operated up to 5000 mV s^{-1} (Figure 6.19c). The rate capability achieved in this work is of the highest value when compared with CNT and/or rGO coated solid-state paper supercapacitor, reported to date.^{30,34-37}

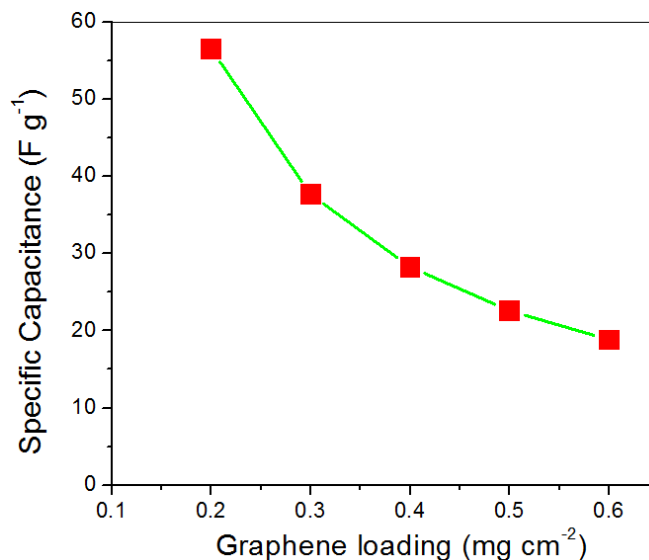


Figure 6.20 Specific capacitance of EG paper based supercapacitors as a function of EG loading on paper.

6.9 Conclusion

In summary, electrochemical exfoliation of graphite in aqueous sulphate salt electrolytes effectively reduce the oxidation and thereby significantly improve the chemical and electronic properties of graphene prepared by chemical methods. The yield of thin layer graphene is higher than 85% with large flake size (up to 44 μ m) and can be produced in tens of gram scale in less than an hour demonstrating the potential for industrial scale-up production. The EG has highest C/O ratio (17.2) and charge carrier mobility ($\sim 310 \text{ cm}^2 \text{ V}^{-1} \text{ s}^{-1}$) of all solution processed reduced GO and exfoliated graphene in acidic electrolytes. The solution processability of high-quality EG in organic solvents permits their direct use in transparent films and conductive ink, offering a great deal in the creation of graphene based materials and devices. The low cost and environment friendly production of such high-quality graphene represent an important breakthrough in graphene production and is of great importance not only for future generation electronics but also for large-scale applications such as, composite materials, supercapacitors, fuel-cells, batteries etc.

6.10 References

- (1) Parvez, K.; Li, R. J.; Puniredd, S. R.; Hernandez, Y.; Hinkel, F.; Wang, S. H.; Feng, X. L.; Mullen, K. *ACS Nano* **2013**, *7*, 3598.
- (2) Lee, J. H.; Shin, D. W.; Makotchenko, V. G.; Nazarov, A. S.; Fedorov, V. E.; Kim, Y. H.; Choi, J. Y.; Kim, J. M.; Yoo, J. B. *Adv. Mater.* **2009**, *21*, 4383.
- (3) Liu, N.; Luo, F.; Wu, H. X.; Liu, Y. H.; Zhang, C.; Chen, J. *Adv. Funct. Mater.* **2008**, *18*, 1518.
- (4) Su, C. Y.; Lu, A. Y.; Xu, Y. P.; Chen, F. R.; Khlobystov, A. N.; Li, L. J. *ACS Nano* **2011**, *5*, 2332.
- (5) Lu, J.; Yang, J. X.; Wang, J. Z.; Lim, A. L.; Wang, S.; Loh, K. P. *ACS Nano* **2009**, *3*, 2367.
- (6) Shang, N. G.; Papakonstantinou, P.; Sharma, S.; Lubarsky, G.; Li, M. X.; McNeill, D. W.; Quinn, A. J.; Zhou, W. Z.; Blackley, R. *Chem. Commun.* **2012**, *48*, 1877.
- (7) Beck, F.; Jiang, J.; Krohn, H. *J Electroanal. Chem.* **1995**, *389*, 161.
- (8) Beck, F.; Junge, H.; Krohn, H. *Electrochim. Acta* **1981**, *26*, 799.
- (9) Goss, C. A.; Brumfield, J. C.; Irene, E. A.; Murray, R. W. *Anal. Chem.* **1993**, *65*, 1378.
- (10) Noel, M.; Santhanam, R. *J. Power Sources* **1998**, *72*, 53.
- (11) Alsmeyer, D. C.; McCreery, R. L. *Anal. Chem.* **1992**, *64*, 1528.
- (12) Cheng, Z. G.; Zhou, Q. Y.; Wang, C. X.; Li, Q. A.; Wang, C.; Fang, Y. *Nano Lett.* **2011**, *11*, 767.
- (13) Sun, Z. Z.; Yan, Z.; Yao, J.; Beitler, E.; Zhu, Y.; Tour, J. M. *Nature* **2010**, *468*, 549.
- (14) Yu, Q. K.; Jauregui, L. A.; Wu, W.; Colby, R.; Tian, J. F.; Su, Z. H.; Cao, H. L.; Liu, Z. H.; Pandey, D.; Wei, D. G.; Chung, T. F.; Peng, P.; Guisinger, N. P.; Stach, E. A.; Bao, J. M.; Pei, S. S.; Chen, Y. P. *Nat. Mater.* **2011**, *10*, 443.
- (15) Malard, L. M.; Pimenta, M. A.; Dresselhaus, G.; Dresselhaus, M. S. *Phys. Rep.* **2009**, *473*, 51.
- (16) Ferrari, A. C.; Meyer, J. C.; Scardaci, V.; Casiraghi, C.; Lazzeri, M.; Mauri, F.; Piscanec, S.; Jiang, D.; Novoselov, K. S.; Roth, S.; Geim, A. K. *Phys. Rev. Lett.* **2006**, *97*.

- (17) Buglione, L.; Chng, E. L. K.; Ambrosi, A.; Sofer, Z.; Pumera, M. *Electrochem. Commun.* **2012**, *14*, 5.
- (18) Feng, H.; Cheng, R.; Zhao, X.; Duan, X.; Li, J. *Nat. Commun.* **2013**, *4*, 1539.
- (19) Moon, I. K.; Lee, J.; Ruoff, R. S.; Lee, H. *Nat. Commun.* **2010**, *1*, 73.
- (20) Kholmanov, I. N.; Magnuson, C. W.; Aliev, A. E.; Li, H. F.; Zhang, B.; Suk, J. W.; Zhang, L. L.; Peng, E.; Mousavi, S. H.; Khanikaev, A. B.; Piner, R.; Shvets, G.; Ruoff, R. S. *Nano Lett.* **2012**, *12*, 5679.
- (21) Feng, H. B.; Cheng, R.; Zhao, X.; Duan, X. F.; Li, J. H. *Nat. Commun.* **2013**, *4*.
- (22) Shin, H. J.; Choi, W. M.; Choi, D.; Han, G. H.; Yoon, S. M.; Park, H. K.; Kim, S. W.; Jin, Y. W.; Lee, S. Y.; Kim, J. M.; Choi, J. Y.; Lee, Y. H. *J. Am. Chem. Soc.* **2010**, *132*, 15603.
- (23) Li, S. S.; Tu, K. H.; Lin, C. C.; Chen, C. W.; Chhowalla, M. *ACS Nano* **2010**, *4*, 3169.
- (24) Blake, P.; Brimicombe, P. D.; Nair, R. R.; Booth, T. J.; Jiang, D.; Schedin, F.; Ponomarenko, L. A.; Morozov, S. V.; Gleeson, H. F.; Hill, E. W.; Geim, A. K.; Novoselov, K. S. *Nano Lett.* **2008**, *8*, 1704.
- (25) Oh, S. Y.; Kim, S. H.; Chi, Y. S.; Kang, T. J. *Appl. Surf. Sci.* **2012**, *258*, 8837.
- (26) Wang, X.; Zhi, L. J.; Mullen, K. *Nano Lett.* **2008**, *8*, 323.
- (27) Wu, J. B.; Agrawal, M.; Becerril, H. A.; Bao, Z. N.; Liu, Z. F.; Chen, Y. S.; Peumans, P. *ACS Nano* **2010**, *4*, 43.
- (28) Kobayashi, T.; Kimura, N.; Chi, J. B.; Hirata, S.; Hobar, D. *Small* **2010**, *6*, 1210.
- (29) Hu, L.; Choi, J. W.; Yang, Y.; Jeong, S.; La Mantia, F.; Cui, L. F.; Cui, Y. *Proc. Natl. Acad. Sci.* **2009**, *106*, 21490.
- (30) Yoo, J. J.; Balakrishnan, K.; Huang, J. S.; Meunier, V.; Sumpter, B. G.; Srivastava, A.; Conway, M.; Reddy, A. L. M.; Yu, J.; Vajtai, R.; Ajayan, P. M. *Nano Lett.* **2011**, *11*, 1423.
- (31) Kaempgen, M.; Chan, C. K.; Ma, J.; Cui, Y.; Gruner, G. *Nano Lett.* **2009**, *9*, 1872.
- (32) Bae, J.; Song, M. K.; Park, Y. J.; Kim, J. M.; Liu, M. L.; Wang, Z. L. *Angew. Chem. Int. Edit.* **2011**, *50*, 1683.
- (33) Yuan, L. Y.; Lu, X. H.; Xiao, X.; Zhai, T.; Dai, J. J.; Zhang, F. C.; Hu, B.; Wang, X.; Gong, L.; Chen, J.; Hu, C. G.; Tong, Y. X.; Zhou, J.; Wang, Z. L. *ACS Nano* **2012**, *6*, 656.

-
- (34) Hu, S.; Rajamani, R.; Yu, X. *Appl. Phys. Lett.* **2012**, *100*.
- (35) Weng, Z.; Su, Y.; Wang, D. W.; Li, F.; Du, J. H.; Cheng, H. M. *Adv. Energy. Mater.* **2011**, *1*, 917.
- (36) Kang, Y. J.; Chun, S. J.; Lee, S. S.; Kim, B. Y.; Kim, J. H.; Chung, H.; Lee, S. Y.; Kim, W. *ACS Nano* **2012**, *6*, 6400.
- (37) Kang, Y. J.; Chung, H.; Han, C. H.; Kim, W. *Nanotechnology* **2012**, *23*.

Chapter 7: Conclusion and Outlook

7.1 Conclusion

In this PhD work, solution production of high-quality graphene sheets by wet-chemical exfoliation methods as well as their applications for high performance fuel cell catalysts, supercapacitors and OFETs have been demonstrated. Chemical exfoliation of graphite into graphene oxide (GO) has been achieved by well-known oxidation process (i.e. Hummers method). Taking advantage of the high solution processability of GO due to the presence of oxygen containing functional groups, both metal free and non-precious transition metal containing nitrogen doped graphene for the oxygen reduction reaction (ORR) have been prepared. For the fabrication of electrically conductive graphene films, a novel methane plasma assisted reduction of GO was developed. The high electrical conductivity of plasma reduced GO films revealed an excellent electrochemical performance in terms of high power and energy densities when used as an electrode in the micro-supercapacitors. To overcome the intrinsic limitations of poor quality of GO and/or reduced GO, we established a novel protocol for mass production of high-quality (i.e. with low defect density) graphene sheets by means of electrochemical exfoliation of graphite.

The most commonly used catalyst for the ORR in fuel cells is platinum (Pt). Unfortunately, Pt based catalysts suffer from sluggish electron transfer kinetics, surface oxide formation during long term electrochemical process. On the other hand, nitrogen-doping in graphene networks is known to enhance not only electrical conductivity but also long-term operational stability towards ORR. Towards this end, a simple, cost-effective and scalable method for the preparation of nitrogen doped graphene (NG) as a metal-free

catalyst was developed by using cyanamide as nitrogen source and GO as graphene precursor. Thermal annealing of the surfactant modified GO with cyanamide at 550 °C produced graphene-carbon nitride (G-CN) composites, while further annealing of G-CN at 800~1000 °C resulted in NG. As-prepared NG manifested a high surface area and nitrogen content up to 12.0%. The NG prepared at 900 °C (i.e. NG-900) revealed an electron transfer number of 3.70 with high current density and superior durability compared to that of Pt-based catalysts in alkaline condition.

The ORR performance of NG samples is generally poor in acidic media mainly due to the protonation of pyridinic-N in acidic environment. Therefore, to stabilize the active sites of NG, non-precious iron (Fe) was incorporated into NG. The Fe nanoparticles embedded into NG were prepared with the aid of Fe salt during the synthesis of NG from G-CN composites. The NG supported with only 5 wt% Fe nanoparticles (named as NG/Fe_{5.0}) displayed stable methanol cross-over effect, almost four electron transfer process and two times higher current density than that of Pt-based catalysts in alkaline conditions. More importantly, NG/Fe_{5.0} catalysts exhibited pronounced catalytic behavior with four electron transfer process and low onset potential (0.47 V vs Ag/AgCl) in acidic conditions. Although the current density of NG/Fe_{5.0} catalyst (1.47 mA cm⁻²) was lower than Pt/C, the stability of catalyst in acidic media was significantly higher than that of Pt/C.

Graphene films with high electrical conductivity are one of the most important requirements for their application in electronic devices and thin-film technologies. A critical challenge for using GO is to restore its electronic properties by removal of oxygen-containing groups. However, most of the reported reduction processes of GO rely on time consuming chemical treatment with toxic chemicals and/or high temperature (~ 1100 °C)

thermal annealing. In this work, a novel protocol has been developed for the reduction of GO employing methane (CH_4) plasma treatment. The CH_4 plasma can facilitate the deoxygenation of GO and restore π -conjugation of graphene within few seconds. As the consequence, the plasma reduced GO (i.e. PrGO) exhibited a high C/O ratio of 12.9. Moreover, only few seconds of plasma treatment is found to be a very efficient method for GO reduction compared with that of thermal and/or chemical reduction methods. In addition, to achieve high power and energy density of graphene based micro-supercapacitors, a novel class of all-solid-state in-plane micro-supercapacitors (MSCs) was developed based on the PrGO films. Due to the high electrical conductivity of PrGO films and in-plane geometry, the fabricated MSCs delivered an area capacitance of $80.7 \mu\text{F cm}^{-2}$ and a stack capacitance of 17.9 F cm^{-3} . Remarkably, the MSCs showed a power density of the 2.5 mWh cm^{-3} that is comparable to lithium thin-film batteries, in association with superior cycling stability. Such micro-devices allowed for operations at ultrahigh rate up to $1,000 \text{ V s}^{-1}$, three orders of magnitude higher than that of conventional supercapacitors. The superior performance PrGO based MSCs is attributed to the cooperative effects of high electrical conductivity of graphene materials and the in-plane geometry of the devices.

Although significant progress has been made for the reduction of GO, it should be emphasized that the intrinsic bottleneck of GO and rGO is the poor quality in terms of structural defects. To overcome the limitations of GO, an environmentally friendly method has been developed to produce high-quality graphene by electrochemical exfoliation in acidic media. The as-prepared electrochemically exfoliated graphene (EG) revealed a low defect density with an oxygen content of only 7.5%, compared to that of GO and rGO and therefore, ensuring the high quality nature of EG. The EG sheets also exhibited a hole

transport mobility of $233 \text{ cm}^2 \text{ V}^{-1} \text{ s}^{-1}$ demonstrating the superiority of EG over GO and/or rGO for electronic applications. Moreover, due to the good solution processability of EG in DMF, vacuum filtration in association with dry transfer method has been developed to manufacture highly conductive graphene films on various substrates. Patterned graphene films were demonstrated to serve as high-performance source/drain (S/D) electrodes for OFETs.

Despite the successful electrochemical exfoliation of graphite in aqueous acid electrolyte which yields graphene sheets with high-quality compared to reduced GO, a significant amount of oxygen groups are still introduced on EG sheets mainly due to the over-oxidation by acidic electrolytes. To suppress the over-oxidation of graphite, more efficient electrochemical exfoliation of graphite has been achieved in aqueous inorganic salts such as, ammonium sulfate, sodium sulfate, potassium sulfate etc. The exfoliation in electrolyte under neutral pH conditions led to graphene with high yield of thin layers (>80 % one to three layers), large flake size up to $44 \mu\text{m}$ and can be produced in tens of gram scale, highlighting the potential for industrial scale-up production. More importantly, as prepared graphene shows a C/O ratio of 17.2, which is the highest value reported to date for graphene prepared by wet-chemical exfoliation. A single layer EG shows an excellent hole transport mobility of $310 \text{ cm}^2 \text{ V}^{-1} \text{ s}^{-1}$ which is several times higher than that of chemically reduced GO. Taking advantage of the high solution processability of as-prepared EG, we further demonstrate the use of EG as conductive ink, which is an important requirement for next-generation printable electronics. Towards this end, large size, electrically conductive graphene films ($11 \Omega \text{ sq.}^{-1}$ at $\sim 0.74 \text{ mg cm}^{-2}$ graphene loading) on A4-size paper fabricated by simple brush painting of graphene ink (10 mg mL^{-1} in DMF) shows promising

application as highly flexible all-solid-state supercapacitors with an area capacity of 11.3 mF cm^{-2} and high rate capability up to 5000 mV s^{-1} . The low cost and environment friendly production of such high-quality graphene is of great importance not only for future generation electronics but also for large-scale applications such as, composite materials, supercapacitors, fuel-cells etc.

7.2 Outlook

The scope of this thesis has been centered on the chemical exfoliation of graphene and their applications in organic electronics and/or energy conversion/storage devices. The findings achieved in this thesis would contribute to a deeper insight into the graphene preparation, solution-processing of graphene and fabrication of graphene based devices.

Nevertheless, there remains a long way to achieve practical applications of graphene. For instance, the performance of graphene and/or graphene composite based catalysts for fuel cell applications is still poor especially in acidic environment. Therefore, significant attention must be paid in order to improve the catalytic property of graphene based materials. Within the scope of the synthetic method for the preparation of NG and NG/Fe composites discussed in this thesis, several issues need to be investigated for the further development of graphene based catalysts such as, i) control the synthesis of other heteroatom (such as S, B, and P) doped graphene with pronounced ORR performance ii) although the type of nitrogen such as, pyridinic- or graphitic-N responsible for facilitating ORR is still controversial, there is no doubt that either one or both types of nitrogen are catalytically active site. Therefore, to enrich the catalytic performance, NGs with various amount and types of nitrogen needs to be synthesized. This can be achieved by selecting

different nitrogen containing precursors such as, polyaniline, polypyrrole, ammonia etc. iii) Various Fe precursors should be examined for further optimization of NG/Fe composites, to achieve higher catalytic performance in acidic media. This is due to the fact that different Fe precursors might result in diverse microstructure, morphology, elemental state as well as the ORR performance. iv) It is well known that a binary catalysts involving cobalt (Co) and Fe provide benefits with excellent intrinsic ORR activity than the respective catalysts containing single metals. Therefore, the preparation of a binary transition metal (Fe and Co) incorporated NG catalysts would provide enormous opportunities to achieve high performance ORR catalysts. v) control the size, morphology and compositions of metals on NG to enhance the ORR performance.

The specific surface area and porous structure determine the accessible part of the active sites and transport properties of ORR active species (H^+ , e^- , O_2 , H_2O), and thus govern the performance of a catalyst. The traditional method for preparing metal nanoparticles containing catalysts usually involves direct pyrolysis of the mixture of carbon, nitrogen and transition metal precursors and frequently fails in controlling the porous structure, thus leading to limited exposure of the ORR active sites and relatively poor transport properties. Therefore, the surface area of the catalysts might be increased by the formation of three-dimensional (3D) graphene networks and/or template assisted synthesis of the catalysts with well-defined mesoporous structures which would allow the utilization of the unique features of graphene sheets, such as their rich micro- and mesoporosity and multidimensional electron transport pathway.

The electrochemically exfoliated graphene (EG) already holds a great promise for replacing the chemically and/or thermally reduced GO as it offers a fast and

environmentally benign method to produce high-quality graphene on a large scale. Nevertheless, the EG still contains a small amount of defects associated with decoration of few percent of oxygenated groups. In order to obtain defect-free EG sheets further optimization of the exfoliation process is necessary. First, water based electrolyte system must be replaced. As discussed in Chapter 5 and 6, oxygen and hydroxyl radicals and/or ions produced by the dissociation of water cause the oxidation of graphite during electrochemical process. Therefore, use of organic solvents such as propylene carbonate might be an alternative of water. Second, the DC voltage applied for the exfoliation has to be minimized (i.e. <10 V) to avoid redox reaction of the electrolyte itself. This can be achieved by increasing the concentration of electrolyte materials. Third, the EG can only be dispersed in high boiling point solvents such as DMF, NMP etc. which limits the use of conventional film deposition methods such as spin coating, drop casting, ink-jet printing etc., which are particularly important for fabricating graphene based electronic devices. The in-situ or post functionalization of EG with small organic molecules or polymers can be utilized to disperse EG in low boiling point solvents. Moreover, functionalization also enables one to tune the electronic properties of EG such as work function, conductivity etc. Last but not least, nanocomposites based on EG remain a less explored area, such as for additives or supporting matrix in electrode materials in lithium ion batteries, supercapacitors, fuel cells, solar cells etc. Both the optimization of the electrochemical exfoliation methods for graphene preparation and improvement of the solution processability of EG are still urgently required.

List of Publications

Scientific publications

- (1) **K. Parvez**, Z. S. Wu, R. Li, X. Liu, R. Graf, X. Feng, K. Müllen, Exfoliation of Graphite into Graphene in Aqueous Solutions of Inorganic Salts. *J. Am. Chem. Soc.*, **2014**, *136*, 6083–6091.
- (2) Z. S. Wu, **K. Parvez**, X. Feng, K. Müllen, Photolithographic fabrication of high-performance all-solid-state graphene-based planar micro-supercapacitors with different interdigital fingers. *J. Mater. Chem. A*, **2014**, *2*, 8288-8293.
- (3) Z. S. Wu, **K. Parvez**, A. Winter, H. Vieker, X. Liu, S. Han, A. Turchanin, X. Feng, K. Müllen, Layer-by-layer Assembled Heteroatom-Doped Graphene Films with Ultrahigh Volumetric Capacitance and Rate Capability for Micro-Supercapacitors. *Adv. Mater.* **2014**, doi: 10.1002/adma.201401228
- (4) W. Wei, H. Liang, **K. Parvez**, X. Zhuang, X. Feng, K. Müllen, Nitrogen-Doped Carbon Nanosheets with Self-Defined Mesopores as Highly Efficient Metal-Free Catalysts for the Oxygen Reduction Reaction. *Angew. Chem.Int. Ed.*, **2014**, *53*, 1570-1574.
- (5) C. Christodoulou, A. Giannakopoulos, M. V. Nardi, G. Ligorio, M. Oehzelt, L. Chen, L. Pasquali, M. Timpel, A. Giglia, S. Nannarone, P. Norman, M. Linares, **K. Parvez**, K. Müllen, D. Beljonne, N. Koch, Tuning the work function of graphene-on-quartz with a high molecular acceptor. *J. Phys. Chem. C* **2014**, *118*, 4784-4790.
- (6) **K. Parvez**, R. Li, S. R. Puniredd, Y. Hernandez, F. Hinkel, S. Wang, X. Feng, K. Müllen, Electrochemically Exfoliated Graphene as Solution-Processable, Highly Conductive Electrodes for Organic Electronics. *ACS Nano*, **2013**, *7*, 3598–3606.
- (7) Z. S. Wu, **K. Parvez**, X. Feng, K. Müllen, Graphene-based in-plane micro-supercapacitors with high power and energy densities. *Nat. Commun.*, **2013**, *4*, 2487-2494.
- (8) Y.-Z. Tan, B. Yang, **K. Parvez**, A. Narita, S. Osella, D. Beljonne, X. Feng, K. Müllen, Atomically precise edge chlorination of graphenes. *Nat. Commun.*, **2013**, *4*, 2646.
- (9) R. Li, **K. Parvez**, F. Hinkel, X. Feng, K. Müllen, Bioinspired Wafer-Scale Production of Highly Stretchable Carbon Films for Transparent Conductive Electrodes. *Angew. Chem. Int. Ed.*, **2013**, *125*, 5645-5648.
- (10) Z. S. Wu, L. Chen, J. Liu, **K. Parvez**, H. Liang, J. Shu, R. Graf, X. Feng, K. Müllen, High-Performance Electrocatalysts for Oxygen Reduction Derived from

- Cobalt Porphyrin-based Conjugated Mesoporous Polymer. *Adv. Mater.* **2013**, *26*, 1450-1455.
- (11) L. Chen, K. S. Mali, S. R. Puniredd, M. Baumgarten, **K. Parvez**, W. Pisula, S. D. Feyter, K. Müllen, Assembly and Fiber Formation of a Gemini-type Hexathienocoronene Amphiphile for Electrical Conduction. *J. Am. Chem. Soc.* **2013**, *135*, 13531-13537.
- (12) M. A. Mamun; M. Poostforush; S. A. Mukul; K. Parvez; M. A. Subhan; Biosorption of As(III) form aqueous solution by *Acacia auriculiformis* leaves. *Scientia Iranica* 2013, *20*, 1871-1880.
- (13) **K. Parvez**, S. Yang, Y. Hernandez, A. Winter, A. Turchanin, X. Feng, K. Müllen, Nitrogen-Doped Graphene and Its Iron-Based Composite as Efficient Electrocatalysts for Oxygen Reduction Reaction. *ACS Nano*, **2012**, *6*, 9541-9550.
- (14) Z. S. Wu, S. Yang, Y. Sun, **K. Parvez**, X. Feng, K. Müllen, 3D Nitrogen-Doped Graphene Aerogel-Supported Fe₃O₄ Nanoparticles as Efficient Electrocatalysts for the Oxygen Reduction Reaction. *J. Am. Chem. Soc.* **2012**, *134*, 9082-9085.
- (15) **M. K. Parvez**; I. In; J. M. Park; S. H. Lee; S. R. Kim; Long-term stable dye-sensitized solar cells based on UV photo-crosslinkable poly(ethylene glycol) and poly(ethylene glycol) diacrylate based electrolytes. *Solar Energ. Mater. Solar Cells* **2011**, *95* 318-322.
- (16) S. R. Kim; **M. K. Parvez**; Oxygen Ion-Beam Irradiation of TiO₂ Films Reduced Oxygen Vacancies and Improves Performance of Dye-Sensitized Solar Cells. *J. Mater. Res.* **2011**, *26*, 1012-1017.
- (17) D. W. Seo; **M. K. Parvez**, S. H. Lee; J. H. Kim; S. R. Kim; Y. D. Lim; W. G. Kim; Synthesis of Acetyl Imidazolium-Based Electrolytes and Application for Dye-Sensitized Solar Cells. *Electrochim. Acta* **2011**, *57*, 285-289.
- (18) **M.K. Parvez**; G.M. Yoo; J.H. Kim; S.R. Kim; Comparative study of plasma and ion-beam treatment to reduce oxygen vacancies in TiO₂ and recombination reactions in dye-sensitized solar cells. *Chem. Phys. Lett.* **2010**, *495*, 69-72.
- (19) S.R. Kim; **M.K. Parvez**; I. In; H.Y. Lee; J. M. Park; Novel photo-crosslinkable polymeric electrolyte system based on poly(ethylene glycol) and trimethylolpropanetriacrylate for dye-sensitized solar cells with long-term stability. *Electrochimica Acta* **2009**, *54*, 6306-6311.
- (20) S.R. Kim; **M.K. Parvez**; M. Chhowall; UV-reduction of graphene oxide and its application as an interfacial layer to reduce the back transport reactions of dye-sensitized solar cells. *Chem. Phys. Lett.* **2009**, *483*, 124-127.
(Selected as Top 25 Hottest articles in Chemistry from Oct. 2009 to Dec. 2012).

-
- (21) Z. Mics; S. A. Jensen; **K. Parvez**; I. Ivanov; K. J. Tielrooij; F. H. L. Koppens; X. Feng; K. Müllen; M. Bonn; D. Turchinovich; Hot Carriers in Graphene: Consequences for Ultra-High Speed Electronics. *Nat. Nanotechnol.* **2014**, under review.
- (22) Z. Liu; **K. Parvez**; R. Li; N. Yang; S. Li; X. Feng; K. Müllen; Spray-coating of Graphene/PH1000 hybrid thin films: Towards large area production of transparent conductive electrodes for ultrathin organic photodetectors. In preparation, **2014**.

Patents

- (1) **K. Parvez**, X. Feng, K. Müllen, Electrochemical exfoliation of graphite (Preparation of two dimensional carbon materials by electrochemical exfoliation). App. No. MI-0903-4785-LC-JK, **2014**.
- (2) S. Venkataraman; T. Kurkina; T. Nathan-Walleser; **K. Parvez**; X. Feng; K. Müllen; Preparation of two dimensional carbon materials by electrochemical exfoliation. WO patent No. 14165214.9-1360, **2014**.
- (3) **K. Parvez**; X. Feng; K Müllen; G. M. Schwab; Nitrogen-doped graphene and metal-composites for applications in electrocatalysts, WO Patent No. EP2687483 (A1), **2012**.
- (4) S.R. Kim, **M. K. Parvez**, I. In, Polymer electrolyte with long-term stability and dye-sensitized solar cells using polymer electrolyte. Korean Patent No. KR20110059148 (A), **2011**.

Book chapters

- (1) **K. Parvez**; R. Li; X. Feng; K Müllen; Graphene as Transparent Electrodes for Solar Cells, chapter in “Advanced Nanocarbons for Energy Conversion”. Publisher: WILEY-VCH, **in preparation, 2014**.

Curriculum Vitae

Personal Details

Name: Md. Khaled Parvez
Date of birth: 11 October 1981
Place of birth: Gazipur, Bangladesh
Nationality: Bangladeshi
Marital status: Married

University Education

September 2010 – June 2014	PhD studies, Max Planck Institute for Polymer Research, Mainz Research adviser: Prof. Dr. Klaus Müllen
September 2007 – February 2010	Master thesis, Department of Polymer Science and Engineering, Graduate School of Science, Chungju National University, South Korea Research adviser: Prof. Dr. Sung-Ryong Kim Thesis title: <i>Surface-Interface Modification of TiO₂ Film Structure and Development of Novel Type Polymeric Electrolytes for Dye-Sensitized Solar Cells.</i>
September 2007 – February 2010	Master course, Department of Polymer Science and Engineering, Graduate School of Science, Chungju National University, South Korea
April 2007 – March 2008	Bachelor thesis, Department of Chemistry, Faculty of Science, Shah Jalal University of Science and Technology, Sylhet, Bangladesh Research adviser: Prof. Dr. Abdus Subhan Thesis title: <i>Synthesis, Characterization and Spectroscopic Studies of Some Novel Luminescent Cerium (III) Complexes.</i>
October 2000 – June 2005	Bachelor course, Department of Chemistry, Faculty of Science, Shah Jalal University of Science and Technology, Sylhet, Bangladesh

School Education

August 1996 – July 1998	Notre Dame College, Dhaka, Bangladesh
January 1985 – June 1996	Safiuddin Sarker Academy School and College, Tongi, Bangladesh.